PhD Dissertation

Optoelectronic studies of strongly correlated 2D materials

Rafael Luque Merino

Supervisor:
Prof. Dmitri K. Efetov

Thesis committee:
Prof. Päivi Törmä
Prof. Nicola Poccia
Prof. Frank Koppens

Universitat Politècnica de Catalunya, Spain
June 2024

Abstract

The study of strongly-correlated matter in two-dimensional materials has emerged as a exciting prospect for the exploration of condensed matter physics, as well as the design of novel device platforms. Moiré engineering, where the 2D layers feature an interlayer twist angle, has proven to be a powerful tool to engineer electronic correlations. In magic angle twisted bilayer graphene, a twist angle of 1.1° between the graphene layers generates a moiré superlattice potential. A flat electronic band appears at the Fermi level, in which a variety of interaction-driven, many-body quantum phases can emerge. Another avenue to study strong electronic correlations in two dimensions is the exfoliation of intrinsically correlated bulk crystals into the atomic limit.

The optoelectronic response of strongly-correlated systems in 2D heterostructures stands out as a powerful probe, as it can provide insight into both the electronic transport properties and the fundamental light-matter interaction in these systems. In this thesis, we study two strongly correlated 2D materials: MATBG and the cuprate superconductor $Bi_2Sr_2CaCu_2O_{8-\delta}$ (BSCCO-2212). We leverage different optoelectronic techniques to study the fundamental properties of the correlated electrons in the MATBG flat bands and the potential of two-dimensional BSCCO-2212 layers for applications in quantum sensing.

First, we investigate the electronic spectrum of the MATBG flat bands through their thermoelectric transport. We use an optical excitation to induce a thermal gradient in the flat band electrons, which in turn generates a charge current. We report anomalous thermoelectricity which provides strong evidence for the coexistence of localized and de-localized electronic states in the strongly-interacting flat bands.

Next, we study the dynamics of hot carrier cooling in the MATBG flat bands using a frequency-resolved photomixing technique. Strikingly, we find that hot carriers can efficiently relax their energy down to cryogenic temperatures; in contrast to the case of bilayer graphene samples. We propose a novel Umklapp electron-phonon scattering mechanism for hot carriers in MATBG, enabled by the moiré superlattice potential.

Lastly, we explore the development of superconducting photodetectors with high-T_c based on ultrathin BSCCO-2212 flakes. We fabricate high quality samples that exhibit remarkable performance at telecom wavelengths. We observe fast and sensitive bolometric response at $T = 77$ K in free-space and waveguide-coupled devices, as well as single-photon sensitivity at $T = 20$ K through a non-bolometric, avalanche detection mechanism.

Resum

L'estudi de la matèria fortament correlacionada en materials bidimensionals ha sorgit com una perspectiva engrescadora per a l'exploració de la física de la matèria condensada, així com el disseny de nous dispositius. L'enginyeria de moiré, on les capes 2D presenten un angle de gir intercapa, ha demostrat ser una potent eina per a induir correlacions electròniques. En el grafè bicapa torçada d'angle màgic (MATBG en anglès), un angle de gir de 1.1◦ entre les capes de grafè genera un patró de moiré o superxarxa. Una banda electrònica plana apareix a nivell de Fermi, en la qual poden sorgir una varietat de fases quàntiques de molts cossos impulsades per la interacció.Una altra via per a estudiar correlacions electròniques en 2D és l'exfoliació al límit atòmic de materials 3D intrínsecament correlacionats.

L'estudi optoelectrònic de sistemes fortament correlacionats en heteroestructures 2D destaca com una eina molt útil, ja que pot proporcionar informació tant sobre les propietats de transport electrònic com sobre la interacció fonamental llum-matèria en aquests sistemes. En aquesta tesi, estudiem dos materials 2D fortament correlacionats: MATBG i el cuprat superconductor $Bi_2Sr_2CaCu_2O_{8-\delta}$ (BSCCO-2212). Aprofitem diferents tècniques optoelectròniques per estudiar les propietats fonamentals dels electrons correlacionats en les bandes planes MATBG i el potencial de les capes bidimensionals BSCCO-2212 per a aplicacions en la detecció quàntica.

En primer lloc, investiguem l'espectre electrònic de les bandes planes MATBG mitjançant l'estudi del seu transport termoelèctric. Utilitzem una excitació òptica per induir un gradient tèrmic, que al seu torn genera un corrent de càrrega. L'anomalia observada en la termoelectricitat de MATBG constata la coexistència de portadors de càrrega localitzats i deslocalitzats en les bandes planes correlacionades.

A continuació, estudiem la dinàmica de refrigeració per portadors calents a les bandes planes de MATBG, una tècnica de mescla de làsers continus amb resolució de freqüència. Observem que els portadors calents poden relaxar la seva energia eficientment a temperatures criogèniques, al contrari que en les mostres de grafè bicapa. Proposem un mecanisme nou per a la dispersió entre electrons i fonons en MATBG, basat en un procés Umklapp que sorgeix a conseqüència del potencial de moiré.

Finalment, explorem el desenvolupament de fotodetectors superconductors d'alta temperatura basats en flocs ultrafins de BSCCO-2212. Fabriquem mostres d'alta qualitat que exhibeixen un notable rendiment en longituds d'ona de telecomunicacions. Observem una resposta bolomètrica ràpida i sensible a $T = 77$ K, tant en guies d'ones com en espai lliure. A més, vam demostrar la detecció de fotó únic a altes temperatures ($T = 20$ K) a través d'una resposta d'allau no bolomètrica.

Resumen

El estudio de materia fuertemente correlacionada en materiales 2D ha surgido como una oportunidad para el estudio fundamental de la materia condensada y el diseño de dispositivos novedosos. La ingeniería de moiré, donde las capas 2D son desalineadas rotacionalmente, es una herramienta poderosa para inducir correlaciones electrónicas. En el grafeno bicapa rotado de ángulo mágico (MATBG en inglés), un ángulo de 1.1° entre las capas de grafeno crea un patrón de moiré o superred. En consecuencia, se forman bandas electrónicas planas en el nivel de Fermi, donde aparecen una multitude de fases cuánticas de varios cuerpos, generadas por correlaciones electrónicas. Otra vía para estudiar correlaciones electrónicas en 2D es la exfoliación al límite atómico de materiales 3D intrínsicamente correlacionados.

El estudio optoelectrónico de heterostructuras 2D fuertemente correlacionadas destaca como una herramienta muy útil, ya que permite tanto la exploración de las propiedades de transporte electrónico como de la interacción luz-materia en el material. En esta tesis, estudiamos dos materiales 2D fuertemente correlacionados: el MATBG y el cuprato superconductor $Bi_2Sr_2CaCu_2O_{8-\delta}$ (BSCCO-2212). Utilizamos diferentes técnicas optoelectrónicas para estudiar las propiedades fundamentales de los electrones en las bandas planas de MATBG, e investigar el potencial de las capas 2D de BSCCO-2212 para aplicaciones en detección cuántica.

Primero, investigamos las bandas planas de MATBG a través de su transporte termoeléctrico. Utilizamos una excitación óptica para inducir un gradiente térmico en MATBG, que a su vez genera un potencial eléctrico. La anomalía observada en la termoelectricidad de MATBG constata la coexistencia de portadores de carga localizados y de-localizados en las bandas planas con correlaciones

A continuación, estudiamos la dinámica de enfriamiento de electrones fotoexcitados en MATBG utilizando una técnica de mezcla de láseres continuos con resolución de frecuencia. Observamos que los electrones fotoexcitados pueden relajar su energía eficientemente a temperaturas criogénicas, al contrario que en muestras de grafeno bicapa. Proponemos un mecanismo nuevo para la dispersión ente electrones y fonones en MATBG, basado en un proceso Umklapp que surge a consecuencia del potencial de moiré.

Por último, desarrollamos fotodetectores superconductores de alta temperatura basados en capas ultrafinas de BSCCO-2212. Las nanostructuras fabricadas presentan propiedades fotodetectoras sobresalientes a frecuencias de telecomunicaciones. Observamos fotorespuesta bolométrica con sensibilidad y velocidad récord a $T = 77$ K, tanto en guías de ondas como en espacio libre. Además, demostramos detección de foton único a altas temperaturas ($T = 20$ K) a través de una respuesta de avalancha no bolométrica.

Acknowledgments

The research comprised in these pages represents several years of work for me and many others. From those who have had direct, hands-on participation in my doctoral studies (all my colleagues) to those who have been engaged (often from afar) in the emotional aspect of it. I cannot thank them enough for their help and support; it is the main thing I will take away from this time in my life. For once, I will keep things short and not speak much.

I've been fortunate to cross paths with many colleagues with remarkable scientific and personal qualities, both in Barcelona and in Munich. I shall begin thanking my supervisor, Dmitri Efetov, as none of this would have been possible without him. Thank you for giving me this great opportunity and providing structure and guidance during my PhD.

I'm also grateful for the former group members that received me when I first joined: Aamir, Nick, Xiaobo, Petr, José and Paul. I learned a lot from them in many aspects. In particular, I'd like to thank Paul for continuing to help me and serve as a mentor.

My PhD colleagues in the group have been invaluable during this experience. Going through the PhD with Ipsita, Jaime, Andrés and Giorgio has been a pleasure and a privilege; learning a lot of physics together and also learning non-scientific aspects of life, teamwork, personal development, etc... We have lived challenging situations, including moving the group from sunny Barcelona to green Munich. These were only easier thanks to our mutual bond. I wish you all the best.

I shall also thank PostDocs that came later: particularly Alex and Martin. You've both forgotten more physics than I will ever know, but it's your personal qualities that I admire the most.

Between ICFO in Barcelona and LMU in Munich, I had the pleasure of meeting a lot of great people, doing research in other groups. I thank all of them for their friendship, as it also helped me get through the rougher aspects of the PhD. Playing padel, football and basketball, plus the occasional beers was a great escape valve from the demanding research life. To my friends and colleagues in Tenerife, Madrid and Barcelona, thank you for your friendship, I hope to reconnect with you sometime soon.

Sometimes forgotten, I would like to thank all the great technicians and supporting staff at ICFO and LMU. From the cleaning staff, to the kitchen

workers, to the maintenance and logistic teams, to the cleanroom staff (Luis Enrique, Johann, Javi, Paula, Helena / Christian, Philipp). Even if it's not obvious, whatever we achieve as researchers is also your achievement, thank you. Special thanks to Carlos Dengra and Bert Lorenz for making everything easier.

Now I must express gratitude to my family, who have supported me unconditionally during my PhD and during my entire life. This would have never been possible without you, your support, your wisdom and your love. To my mother: thank you for pushing me in your caring way, help me become a better person and teach how to love myself and others. To my father: thank you for encouraging me to be myself, to be playful and not take life for granted. To my brother: thank you for caring for me in every possible way, even if we are many kilometers apart. You always were, and continue to be, a role model for me. This thesis is not for me, it's for the entire family.

To Laura: thank for being there during all these years, going through this process with me . Without your support, without your smile, this moment would have never come. I cannot find the words to properly thank you in this limited space and time; but I can only hope to have many more years to express my love and appreciation, day by day, moment to moment. You should know that this thesis and everything that has happened in my life in the last 8 years, has revolved around you, me, and what we are together.

To my extended family in Barcelona, thank you for making me feel at home from the first day. Over the years, we have gotten to know each other better and I could not be happier to have you all in my life. Thank you for hosting many Sundays and helping me through adverse circumstances. To Francisco, Dolors, Cristina, David, Antonia, Montse, Alex; thank you.

When I first decided to do research in physics, I hoped to study and understand the laws that govern nature. I don't know if I have managed to do that, but I have realized other things along the way. Science is not about the equations or the experiments. Science is about the people who do science, the people you meet while doing science, it's also about the working environments we create for (young!) scientists. One can fall in love with physics, but one may also fall in love with doing physics. I would know, as I fell for both. I'm grateful for these years doing physics, surrounded by so many people that I deeply care about, I shall not take it for granted.

Contents

List of publications

Publications as first author

1. **Rafael Luque Merino**, Dumitru Călugăru, Haoyu Hu, Jaime Díez Mérida, Andrés Díez Carlón, Takashi Taniguchi, Kenji Watanabe, Paul Seifert, B. Andrei Bernevig and Dmitri K. Efetov. 'Evidence of heavy fermion physics in the thermoelectric transport of magic angle twisted bilayer graphene', *arXiv:2402.11749*, 2024
   Contributions: Sample characterization, measurements, data analysis, paper writing.

2. **Rafael Luque Merino**, Paul Seifert, José Ramón Durán Retamal, Roop K. Mech, Takashi Taniguchi, Kenji Watanabe, Kazuo Kadowaki, Robert H. Hadfield, Dmitri K. Efetov. 'Two-dimensional cuprate nanodetector with single telecom photon sensitivity at T = 20 K', *2D Materials* **10**, 021001, 2023
   Contributions: Sample fabrication & characterization, measurements, data analysis, paper writing.

Other works

1. Jake D. Mehew, **Rafael Luque Merino**, Hiroaki Ishizuka, Alexander Block, Jaime Díez Mérida, Andrés Díez Carlón, Kenji Watanabe, Takashi Taniguchi, Leonid S. Levitov, Dmitri K. Efetov, Klaas-Jan Tielrooij. 'Ultrafast Umklapp-assisted electron-phonon cooling in magic-angle twisted bilayer graphene', *Science Advances*, **10**, adj1361, 2024
   Contributions: Sample characterization, measurements, data analysis.

2. Dumitru Călugăru, Haoyu Hu, **Rafael Luque Merino**, Nicolas Regnault, Dmitri K. Efetov, B. Andrei Bernevig 'The Thermoelectric Effect and Its Natural Heavy Fermion Explanation in Twisted Bilayer and Trilayer Graphene', *arXiv:2402.14057*, 2024
   Contributions: Data analysis, insight into the theoretical modelling.

3. Paul Seifert, José Ramón Durán Retamal, **Rafael Luque Merino**, Hanan Herzig Sheinfux, John N. Moore, Mohammed Ali Aamir, Takashi

Taniguchi, Kenji Watanabe, Massimo Artiglia, Marco Romagnoli, Dmitri K. Efetov . 'A high-Tc van der Waals superconductor based photodetector with ultra-high responsivity and nanosecond relaxation time', *2D Materials*, **8**, 035053, 2021
Contributions: Sample fabrication & characterization, measurements.

4. Shuoying Yang, Andrés Díez Carlón, Jaime Díez Mérida, Alexandre Jaoui, Ipsita Das, Giorgio di Battista, **Rafael Luque Merino**, Roop K Mech, Dmitri K. Efetov . 'Plethora of many body ground states in magic angle twisted bilayer graphene', *Low. Temp. Phys.*, **49**, 631, 2023
Contributions: Sample characterization.

Chapter 1

Introduction

Advancements in technology, spanning from primitive stone tools to today's digital era based on semiconducting transistors, consistently rely on the discovery of new materials. Over the past two decades, crystalline two-dimensional (2D) materials have attracted significant interest, thanks to their exceptional properties that stem from their atomically thin structure[1]. Moreover, 2D materials can be assembled into van der Waals (vdW) heterostructures, where emergent properties arise from the close proximity of the constituent layers[2]. This layer-by-layer assembly offers a method to engineer artificial materials with tailored properties.

The concept of moiré engineering, based on the rotational misalignment of 2D materials to create a moiré superlattice potential, has emerged as a powerful tool to further engineer the electronic and optical properties of vdW heterostructures[3]. Moiré 2D materials, in particular, facilitate the study of one of condensed matter's most intriguing aspects: the physics of strongly-correlated electron matter. Electronic correlations augment the ever-expanding toolkit of 2D materials, which serves as a versatile platform to explore condensed matter physics and develop novel materials for technological applications.

In this thesis, we describe optoelectronic studies of 2D heterostructures that host strong electronic interactions. In this introduction, we aim to provide context into the history of strongly correlated electron systems and the recent developments in the study of two-dimensional, crystalline materials. We first describe free-electron models and band theory, which appropriately describe non-interacting electrons in crystalline solids. Next, we consider the case of weakly-interacting electrons at low temperatures and then illustrate the effects of strong electron interactions through the 1D Mott insulator. Then, we present an overview of the rich phenomenology of two families of strongly-correlated electron systems: heavy fermion compounds

and cuprate superconductors.

We then shift our focus to 2D moiré heterostructures, mainly on magic angle twisted bilayer graphene (MATBG) where strongly correlated phenomena were first observed in 2018[4, 5]. We provide an outline of its history and the plethora of many-body quantum states observed in this system. Lastly, we highlight the possibility of harnessing strong correlations in other 2D-based heterostructures and the use of optoelectronic techniques to study these materials.

Electronic transport in crystalline solids

The properties of electrons in crystals constitute one of the central areas of study in condensed matter physics. In contrast to free electrons, which have a continuous energy spectrum, the energy levels for a bound electron (for example, to an atom's nucleus) are discrete. This concept extends to crystalline solids, where electrons reside inside a periodic lattice of nuclei. In a real crystalline solid, an electron will experience interactions with the ionic lattice and other electrons. Still, the electronic properties of most materials are often described adequately considering the movement of nearly-free electrons. This is a consequence of the conceptually simple, yet powerful ideas behind free-electron transport models and band theory.

The Drude model[6], first proposed in 1900, describes the electronic properties of metals. It considers the movement of a free electron gas where the electrons can scatter off the static ions that form the lattice(1.1a). From Newton's second law of motion, Drude derived the equation of motion for the electron gas. The scattering processes between electrons and the ion lattice were described through a characteristic mean free time between collisions τ. From the Drude model, the current density $\mathbf{J}$ generated in the presence of an electric field $\mathbf{E}$ is given by:

$$\mathbf{J} = \frac{nq^2\tau}{m}\mathbf{E} \tag{1.1}$$

where n, q and m are the electron density, charge and mass, respectively. This expression provided a semi-quantitative expression for the phenomenological Ohm's law. Despite the wide-ranging validity of the Drude model, it does not consider the periodic arrangement of ions in a crystal or the quantum-mechanical nature of electrons. Most notably, the Drude model failed to explain the experimentally observed temperature dependence of the heat capacity.

Following the derivation of Fermi-Dirac statistics in 1926, Sommerfeld and Bethe revised the Drude model to account for the fermionic character of

electrons[7]. From Pauli's exclusion principle, the ground state of an electron gas (or Fermi gas) occupies all the low energy states up to the Fermi energy E_F (or Fermi momentum p_F). Above the Fermi energy, all electronic states are unoccupied. Still, the predictions from the now-quantum Sommerfeld model for electron transport did not deviate much from those of the Drude model. In a Fermi gas, the electrons occupying states near E_F can still be described as free electrons with a quadratic relation between their energy and momentum.

While these models successfully describe electronic and thermal transport in many systems, a crucial question remains unsolved: what makes a material a good conductor (metal) or a bad one (insulator)? To resolve this issue, a closer look into the periodic lattice of a crystalline solid was needed. In 1929, Felix Bloch showed that one could solve Schrödinger's equation for electrons in a periodic potential using plane waves that are modulated by a periodic function that reflects the lattice periodicity[8].

$$\psi(\mathbf{r}) = e^{i\mathbf{kr}}u(\mathbf{r}) \tag{1.2}$$

where ψ is the electron wavefunction, $\mathbf{r}$ is the position, $\mathbf{k}$ is the crystal momentum and $u(\mathbf{r})$ is a periodic function with the lattice's period. Thus, electrons in a crystal can be described as nearly-free electron waves.

Crucially, the periodicity of the lattice splits the free-electron spectrum into different bands that electrons can occupy. These energy bands arise from the dense packing of individual atoms in a crystal. The discrete energy levels of individual atoms start to split as other atoms are in proximity. In a real crystal, which hosts a huge number ($\sim 10^{23}$) of atoms, the splitting of the energy levels leads to continuous energy bands. The modification of the free-electron dispersion into energy bands is pictured in reciprocal space in Fig. 1.1b.

The continuous electronic bands are separated by energy gaps, where no electronic states are available. The energy gaps appear at the edges of the Brillouin zone (unit cell equivalent in reciprocal space) due to Bragg scattering of the electron waves. The location of these forbidden energy intervals determines the electrical properties of uncorrelated solids. If the Fermi energy of the electron gas lies inside one of the allowed energy bands, the material will be a metal characterized by high electrical and thermal conductivity. On the contrary, if the Fermi energy lies inside an energy gap, the material will not be a good conductor. Depending on the size of the energy gap, these materials are classified as insulators ($E_g > 4$ eV) or semiconductors ($E_g < 4$ eV).

So far, we have described the behaviour of nearly-free electrons, where the free-electron dispersion is split into different energy bands by the periodic

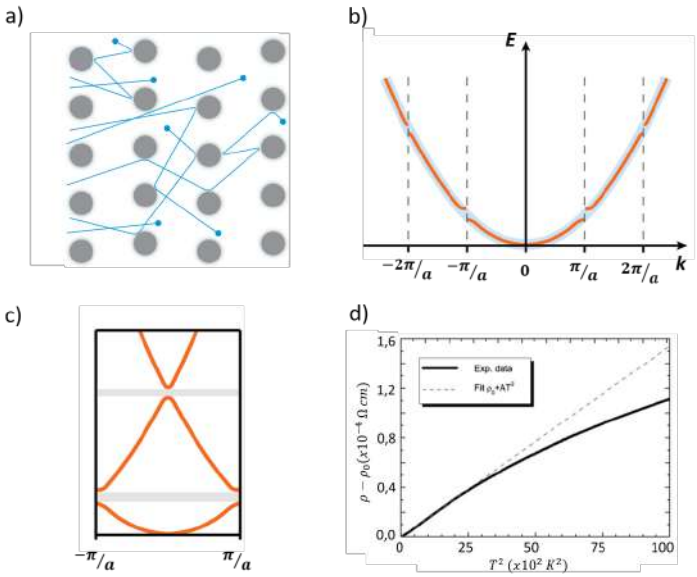

Figure 1.1: a) Illustration of electron movement in a classical, free electron gas picture such as the Drude model. b) Formation of electronic energy bands (orange) from the free-electron dispersion (light blue) in the presence of a periodic lattice. c) Band structure from panel (b) depicted in a reduced zone scheme. d) T^2 dependence of the low-temperature resistivity ρ (after substracting the residual resistivity ρ_0) for semimetallic $MoTe_2$. Note that the X-axis corresponds to units of T^2. In this material, the scattering mechanism giving rise to the T^2 dependence is Baber scattering. Panel (d) adapted from Ref. [9]

lattice. To explain the transport properties of real materials, like their electrical resistance, one must consider the microscopic scattering mechanisms that affect electron transport, including scattering between electrons.

At high temperatures, the (electrical) resistivity evolves linearly with temperature due to scattering with phonons (collective lattice vibrations). As the lattice temperature is decreased, the number of thermally active phonons (or phonon phase space) decreases as $1/T$. Below the Debye temperature, the effects of phonon scattering are expected to be greatly reduced. However, the material's resistivity does not vanish at low temperatures. Instead, a quadratic temperature dependence ($\rho \propto T^2$) is observed across a vast range of materials. Electronic interactions (although weak) must be investigated to understand this low-temperature behaviour.

In 1956, Lev Landau introduced the Fermi liquid theory to describe the low-energy excitations of a (weakly) interacting Fermi gas[10]. In particular, he aimed to explain the confounding properties of ^{3}He. In Fermi liquid theory, electrons interact via Coulomb repulsion and obey Pauli's exclusion principle.

Landau's key insight was that for an adiabatic electron-electron interaction, the low-energy physics of the interacting particles could be described as those of a non-interacting system of 'dressed particles' or quasiparticles. In a Fermi liquid, the result of the complex, many-body correlation effects is the renormalization of the dynamical properties of the electrons near the Fermi level. The resulting quasiparticles exhibit different masses and susceptibilities, but their charge, spin and momentum are unchanged. Notably, the physics of a weakly interacting Fermi gas could now be modeled as a non-interacting ensemble of the newly formed quasiparticles.

Regarding the resistivity of the Fermi liquid, scattering events only involve quasiparticles near E_F, within a $\sim k_B T$ energy window. For a scattering event involving two quasiparticles, the probability of finding two available quasiparticles in the allowed energy window goes as T^2 (each quasiparticle contributes $k_B T$). Thus, the Fermi liquid theory successfully explains the ubiquitous quadratic temperature dependence of ρ across different solids. We note that different microscopic processes, such as Umklapp electron-electron scattering[10] or Baber scattering[11], can give rise to the T^2 dependence of the resistivity.

Strong electronic correlations

Despite the wide success of non-interacting or weakly-interacting pictures for the electronic properties of solids, some materials exhibit unconventional behaviour that requires finer treatment of electron correlations. These materials are often labeled as non-Fermi liquids, as Landau's quasiparticle picture fails to explain their phenomenology. The Hubbard model[12–14], first proposed in the 1960s, is the simplest model that captures some of the physics of strongly-correlated electron systems. To illustrate the Hubbard model, we describe here the scenario of a Mott-Hubbard insulator in a two-dimensional lattice. Consider a condensed matter system consisting of N mono-orbital atoms arranged in a 2D lattice where each atom hosts one electron (see Fig. 1.2a). In other words, the system is half-filled, as Pauli's principle allows for 2N electrons to occupy the lattice. From single-particle band theory, one expects this system to exhibit metallic behaviour as its Fermi energy lies in the middle of a non-filled energy band (Fig. 1.2b).

The Hamiltonian for the Hubbard model can be written as:

$$\hat{H} = -t \sum_{\langle i,j \rangle \sigma} (\hat{c}^{\dagger}_{i\sigma} \hat{c}_{j\sigma} + \hat{c}^{\dagger}_{j\sigma} \hat{c}_{i\sigma}) + U \sum_{i} \hat{n}_{i\downarrow} \hat{n}_{i\uparrow} \tag{1.3}$$

where $\hat{c}^{\dagger}_{i,j\sigma}$ is the creation operator at site i or j of an electron with spin σ, $\hat{c}_{i,j\sigma}$ is the annihilation operator at site i or j of an electron with spin

σ and $\hat{n}_{i\downarrow,\uparrow}$ is the number operator at site i for electrons in the spin down or spin up states. The sum is performed only between nearest-neighbours. Typically, both t and U are taken to be positive. The Hubbard model comprises two competing energy scales. First, the hopping term t describes the energy gained by the system through electrons hopping from one atom to another (we consider here only nearest-neighbour hopping, $j = i + 1$). This term represents the overlap between the electronic orbitals and sets the bandwidth of the resulting energy bands in the solid. Second, the on-site repulsion energy U represents the Coulomb repulsion between two electrons that occupy the same atom. Therefore, double occupancy of an atomic site has an energetic cost U. The on-site repulsion parametrized by U is the only electronic interaction that we consider here.

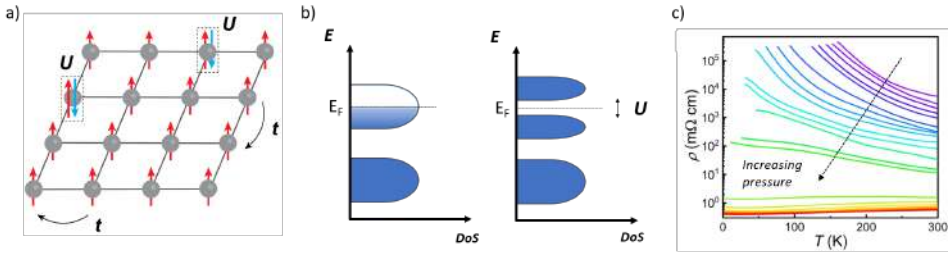

Figure 1.2: a) Schematic of the half-filled 2D Hubbard model. Parameters t and U denote the hopping energy and the on-site repulsion energy, respectively. b) Opening of a gap driven by Coulomb repulsion in the half-filled Hubbard model. The half-filled band splits into the lower and upper Hubbard bands, separated by energy U. c) Mott-Hubbard transition driven by pressure in ferromagnetic Weyl metal $La_2O_3Fe_2Se_2$. Increasing pressure brings the atoms closer, effectively increasing the electronic interaction strength. Panel (c) adapted from Ref. [15].

The physics of weakly interacting systems described so far correspond to the limit $U << t$, where the on-site Coulomb interaction is weak. Then, the material hosts large energy bands and its electronic properties are well described by Fermi liquid theory. However, when $U \geq t$ the electronic spectrum of the system changes dramatically. Because of the large energy cost of double occupation, it is unfavourable for electrons to hop between atoms, even though there are available states. As a consequence, the density of states (DoS) is reconstructed by the Coulomb repulsion, with an interaction-induced gap proportional to U appearing at the Fermi energy (see Fig. 1.2b). The original energy band is now split by interactions into the so-called upper and lower Hubbard bands[16].

Materials that undergo such a metal-insulator transition are known as Mott insulators or, more generally, correlated insulators. It's important to note that this phase transition is not driven by a change in temperature.

Instead, the transition is triggered by other parameters, such as doping, pressure (Fig. 1.2b) or applied magnetic fields. Continuous phase transitions at zero temperature, known as quantum phase transitions, are one of the hallmarks of strongly correlated materials[17].

Despite the apparent simplicity of the Hubbard model, it captures many of the striking properties that appear in strongly correlated systems. We note that the limit of strong interactions of the Hubbard model (large U/t ratios) can also be seen as the limit of low bandwidth (low t). Consequently, the physics dominated by strong electronic interactions are prominent in flat electronic bands. Lastly, we point out that analytically solving the Hubbard model for arbitrary dimensions, lattices or specific U/t values remains an outstanding challenge in condensed matter theory[18]. All in all, the Hubbard model represents a testbed for the exploration of electronic correlation effects in crystalline solids.

Next, we will outline the phenomenology of two families of strongly-correlated materials: heavy fermion compounds and cuprates. We do not intend to provide a comprehensive view of their phenomena, as this falls outside the scope of this thesis. Not one, but hundreds of doctoral theses have been devoted (and continue to be) to the study of these intriguing materials.

Heavy fermion compounds

Heavy fermion materials are clear examples of strongly correlated matter that exhibits non-Fermi liquid behaviour[19, 20]. These compounds contain rare-earth and actinide elements, such as cerium (Ce), ytterbium (Yb) or uranium (U) that feature highly-localized orbitals (4f, 5f, 3d, etc...). Heavy fermion compounds exhibit both localized moments and delocalized, free electrons near the Fermi level. The complex phenomena of heavy fermion materials can be boiled down to the interaction between these two distinct electronic species. First, let's look at how a single localized moment may interact with a conduction electron.

Motivated by the intriguing observation of a low-temperature resistance minima in metals doped with magnetic impurities[21], Jun Kondo put forward in 1964 that conduction electrons could interact with local moments, temporarily exchanging their spin state[22]. Crucially, Kondo showed that the interaction strength grew logarithmically as the temperature was lowered. Thus, below a certain temperature, the Kondo temperature T_K, a new (inelastic) scattering mechanism appeared for the conduction electrons, leading to the increase of the resistivity below T_K[21].

In a heavy fermion material, the single impurity Kondo problem must be extended to the so-called Kondo lattice. Here, the aforementioned single-

particle inelastic scattering mechanism becomes coherent and elastic, where the momentum conservation is enabled by the crystal lattice. Below a certain coherence temperature ($T_{coh} < T_K$), the coherent scattering of conduction electrons off the magnetic moments gives rise to correlated phenomena[23].

Depending on the degree of hybridization between the localized and itinerant electrons (known as f- and c-electrons, respectively), heavy fermion materials exhibit a wide range of properties. When the c-f hybridization is weak, the local moments can polarize the spin of the surrounding conduction electrons, which in turn interact with the neighbouring local moments. In this way, the localized moments develop an antiferromagnetic order through the non-magnetic c-electrons via the Ruderman-Kittel-Kasuya-Yosida (RKKY) interaction[24–26]. Such antiferromagnetic order has been observed in neutron scattering experiments[27], as well as anomalies of the specific heat[28].

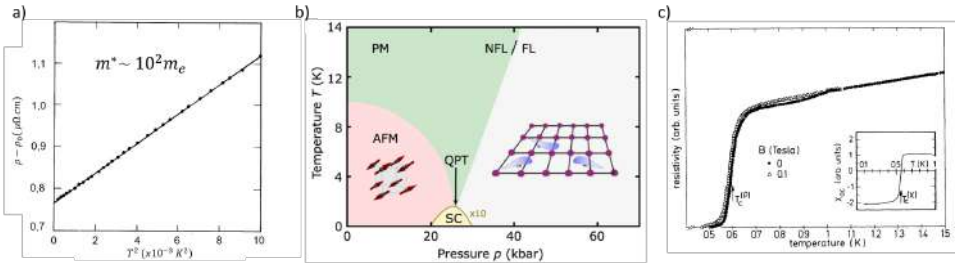

Figure 1.3: a) Heavy Fermi liquid behaviour in heavy fermion compound $CeAl_3$. The extracted effective mass is approximately a hundred times the bare electron mass. b) Pressure-dependent phase diagram for a representative heavy fermion superconductor. The hybridization strength between localized f-orbitals and itinerant electrons increases with increasing pressure, tuning the system from an RKKY-mediated antiferromagnet to a heavy Fermi liquid. Here, PM stands for paramagnet, AFM for antiferromagnet, QPT is quantum phase transition, SC is superconductor, and NFL/FL stands for Non-Fermi liquid and Fermi liquid, respectively. c) Superconductivity in heavy fermion compound $CeCu_2Si_2$. Note that the resistivity decreases linearly with temperature before the superconducting transition, exhibiting strange metal behaviour. Furthermore, in $CeCu_2Si_2$ the superconductivity emerges in the vicinity of an antiferromagnetic instability (see panel (b)). Panels (a), (b) and (c) adapted from Refs. [29], [30] and [31] respectively.

On the contrary, when the hybridization is strong, the coherent scattering off f-electrons leads to new, emergent properties such as the formation of a heavy Fermi liquid[32]. At sufficiently large interaction strength, the conduction electrons can screen the magnetic local moments via the Kondo effect. Then, heavy quasiparticles are formed, with effective masses that can reach a hundred times the bare electron mass. This effect was observed in

the specific heat and resistivity of Ce-based compounds such as $CeCu_2Si_2$[31] or $CeAl_3$[29] (Fig. 1.3a). Notably, the onset of coherent scattering below T_{coh} leads to a decrease in the resistivity, contrary to the single impurity Kondo problem.

It is worth noting that Landau's quasiparticle picture can account for the properties emerging from (then-unknown) scattering mechanisms by simply renormalizing the dynamical properties of the carriers. Nevertheless, as we will show, the heavy fermion phenomenology cannot be fully rationalized in the Fermi liquid picture.

Coherence of the Kondo scattering processes can be controlled by non-thermal parameters, such as pressure or doping. Thus, the heavy fermion phase diagram generally features a quantum phase transition between these magnetic phases[19, 20]. Furthermore, an unconventional superconducting state appears in the vicinity of the quantum phase transition in some heavy fermion compounds. The unconventional nature of the superconducting state is evidenced by several observations: for one, the state lies close to a magnetically-ordered state[31] and it implies the condensation of large-mass quasiparticles, which are expected to interact weakly with the lattice. Lastly, the existence of nodes in the superconducting order parameter has been observed in several experiments[33–35]. Generally, the superconducting state of heavy fermions is believed to be mediated by magnetic fluctuations.

In addition, the quantum critical point (which indicates the location of the quantum phase transition in the phase diagram) evolves from a non-Fermi liquid state at high temperatures. This anomalous state exhibits a linear temperature dependence of the resistivity ($\rho \propto T$) that defies Landau's quasiparticle picture. This state is often referred to as a 'strange metal', as the $\rho \propto T$ dependence persists well below the Debye temperature and cannot be linked to electron-phonon scattering[36].

The existence of a non-Fermi liquid, strange metal that evolves from a zero-temperature quantum critical point is a general feature of strongly-correlated electrons. We note that for strong interaction strengths, other ground states besides the heavy Fermi liquid can be formed below T_{coh}, such as Kondo insulators[37]. Today, the study of the interplay between localized and itinerant electrons in heavy fermion compounds remains an important paradigm in condensed matter physics.

Cuprate superconductors

Cuprate compounds exhibit a layered perovskite-like crystal structure and are composed of copper-oxide (CuO_2) two-dimensional planes sandwiched between layers of other metal oxides. Cuprates attracted huge attention after the discovery of high-temperature superconductivity (HTS),

with $T_c \approx 30$ K in $Ba_{0.75}La_{4.25}Cu_5O_5$ by Bednorz and Müller in 1986[38] (Fig. 1.4a). Shortly after, other cuprate compounds such as $YBa_2Cu_3O_{7-\delta}$[39] or $Bi_2Sr_2CaCu_2O_{8-\delta}$ [40] were found to exhibit remarkable superconducting critical temperatures in the order of $\sim$ 90 K. These findings warranted Bednorz and Müller the Nobel prize of Physics in 1987. Since then, the physics of cuprates have been extensively studied to understand the nature of the unconventional superconductivity and its connection to neighbouring ground states[41].

The physics of cuprates are dominated by the CuO_2 planes, which realize a 2D Hubbard model (see Fig. 1.4b). The surrounding oxide layers act as charge reservoirs for these CuO_2 planes. When each lattice site of the CuO_2 plane is occupied by a copper atom, the system is an antiferromagnetic Mott insulator. As illustrated in Fig. 1.4b, the correlated physics of the CuO_2 plane are dominated by the in-plane $3d_{x^2-y^2}$ orbitals in the copper atoms and the in-plane $2p_{x,y}$ orbitals of the oxygen atoms. At the intrinsic doping level, the Cu sites are occupied by a single unpaired electron, while 2 electrons (of opposite spin) occupy the $2p_{x,y}$ orbitals of oxygen. In this system, conduction through the hopping of the Cu electrons is prohibited by the large on-site repulsion energy U and the $3d_{x^2-y^2}$ orbital is split into Hubbard bands (inset Fig. 1.4b). Furthermore, the unpaired electrons at the Cu sites develop long-range antiferromagnetic order across the CuO_2 plane via super-exchange interaction mediated by the oxygen $2p_{x,y}$ orbitals.

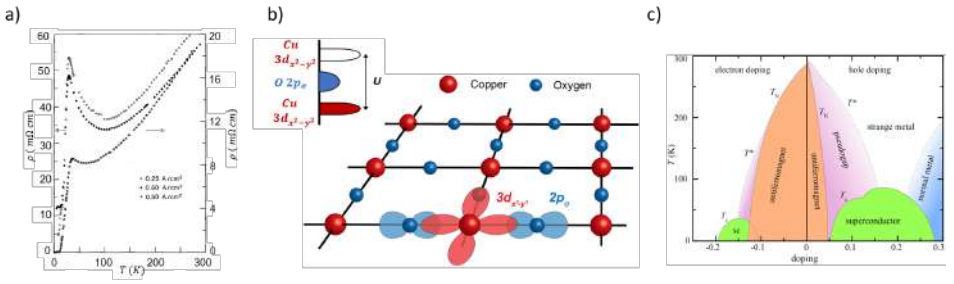

Figure 1.4: a) High-temperature superconductivity (T_c $\sim$30 K) in $Ba_{0.75}La_{4.25}Cu_5O_5$. b) Copper oxide plane in a cuprate superconductor. The lattice of copper and oxygen atoms realizes the 2D Hubbard model. We illustrate here the main orbitals involved in the electronic spectrum at the Fermi level. The on-site interactions split the $3d_{x^2-y^2}$ band of copper, creating a Mott-Hubbard gap. c) Phase diagram for electron and hole-doped cuprates. Note the overall similarity with the phase diagram for heavy fermion superconductors shown in Fig. 1.3b. Panels (a) and (c) adapted from Ref. [38] and Wikimedia Commons, respectively.

Crucially, doping this Mott insulator state (we focus here on hole-doping) modifies the energy balance in the Hubbard lattice and leads to the emergence

of more many-body quantum states[41], including the aforementioned high-T_c superconductivity. As shown in Fig. 1.4c, the electronic properties of cuprates depend critically on the doping of the CuO_2 unit cell which is set by the oxygen concentration. Depending on the doping level, the system can exhibit various phases, including insulating, superconducting and metallic phases. Many of these states are separated by a quantum phase transition, whose quantum critical point generally lies at a critical doping level of $p^* \approx 0.16$ holes per CuO_2 unit cell[42]. A strange metal phase also appears above the quantum critical point, as in heavy fermion materials and other correlated electron systems[43].

Other intriguing phases appear in the vicinity of the superconducting dome for a multitude of cuprates, including charge density waves and the so-called 'pseudogap' phase[44, 45]. The pseudogap phase is characterized by the suppression of electronic states at the Fermi energy, reminiscent of the superconducting gap, at $T > T_c$. Many scenarios have been proposed to explain the pseudogap phase, including the pre-formation of Cooper pairs above the condensation temperature. The nature of the pseudogap phase and its central role in the phase diagram is one of the key questions in the cuprate phenomenology[46].

Regarding the superconducting state of cuprates, it has been well-established that it does not comply with the conventional BCS picture. For one, the BCS theory sets a theoretical limit for $T_c \leq 30$ K[47], which is surpassed in cuprate superconductors. Also, the superconducting state of cuprates lies in the vicinity of other ground states and depends strongly on the stoichiometry of the compound, unlike in BCS superconductors. Moreover, the normal state above the superconducting dome does not behave as a Fermi liquid. The strongest evidence for non-BCS superconductivity in the cuprates is their anisotropic superconducting order parameter. As famously observed in tunneling[48] and calorimetric[49] experiments, the order parameter exhibits strong spatial dependence with nodal directions (where the superconducting gap is null) and opposite signs at opposite k_x, k_y points. Overall, the confounding properties of cuprate superconductors are a consequence of the strong electron interactions in the Hubbard-like CuO_2 planes.

Other strongly-correlated systems and limitations

It's important to stress that there are other condensed matter systems whose properties are profoundly affected by electronic correlations. These include iron pnictides[50], transition metal dichalcogenides[51], organic superconductors[52] or even the fractional quantum hall states[53]. However, all these platforms share some limitations that hamper the study of

strongly-correlated electrons. Namely, they are not easily tuned (one needs to chemically dope the bulk crystals) and they generally feature complex chemical compositions and crystal structures. In the case of the fractional quantum hall effect, the sample quality of the 2D films must be extremely high. Therefore, preparation of these samples is often a challenge in itself and it is sometimes hard to track the effect of external parameters, such as doping or applied pressure.

The last two decades have witnessed the emergence of two new platforms for the study of strongly correlated physics. First, the advances in the control of atomic gases paved the way for the development of optical lattices[54, 55], where laser fields are used to manipulate and cool down single atoms. Arrays of atoms with on-demand spatial configurations and highly tunable interactions can now be used for the simulation of the Hubbard model. One can use fermionic atoms to study the conventional (Fermi-)Hubbard model[55, 56] or bosonic atoms to realize the so-called Bose-Hubbard model[54, 57]. What's more, a mixture of bosonic and fermionic atoms can be used to explore the interplay between the atomic species[58, 59]. Overall, optical lattices have attracted great interest and are positioned as excellent simulators of condensed matter systems[60, 61]. Compared to real crystalline solids that host correlated physics, the length scales of optical lattices are larger, with atoms separated by a few microns (compared to sub-nm distances in crystals). In addition, optical lattices can access very low energy scales (~ 1 K) and must be operated at exceedingly low temperatures, often below 1 nanoKelvin.

The second novel platform for the study of correlated physics is moiré 2D materials. The isolation of crystalline 2D layers, kickstarted by graphene[62] (single layer graphite), opened the door for the assembly of 2D heterostructures that exhibit novel physical properties. Then, the concept of moiré engineering, where an interlayer twist angle between the 2D layers creates a superlattice potential that profoundly modifies the electronic spectrum[63–65], paved the way for the study of moiré-reconstructed bands hosting strong electron correlations[4, 5, 66–68].

In 2D moiré materials, a vast range of quantum many-body ground states have been observed, reproducing nearly all the key phenomena in the field. These materials offer unprecedented tunability via external parameters such as electrostatic gates or the dielectric environment, owing to their 2D nature. The typical length scale of the moiré superlattice is ~ 10 nm and strongly correlated physics can be observed up to $T \sim 100$ K. Compared to optical lattices, moiré correlated matter offer a wider range of accessible temperatures and density, which can be tuned with ease. In addition, correlated physics in moiré 2D matter can take place at large energy scales, such as those associated with, for example, high-T_c superconductivity in the

cuprates.

In the following, we will introduce the correlated physics of 2D moiré materials through the description of its most prominent realization, magic-angle twisted bilayer graphene (MATBG). First, we will briefly review the basics of 2D materials that enabled the development of MATBG. Then, we describe the concepts behind the formation of the moiré superlattice and recap the vast phenomenology of the MATBG flat bands. Lastly, we will discuss other 2D-based platforms and the experimental techniques used to study strongly-correlated phenomena in these systems.

MATBG and correlated electrons in 2D materials

Graphene, vdW heterostructures

The mechanical exfoliation of graphene from a bulk graphite crystal, first reported by Geim and Novoselov in 2004[62], opened the door for the study of graphene and a myriad of other 2D materials. Most of the striking properties of 2D materials originate from their low dimensionality. In addition, all these 2D layers can be isolated from the bulk crystals with a high degree of crystallinity.

Graphene, a one-atom-thick honeycomb lattice of carbon atoms, has received great interest due to its remarkable electronic, optical and mechanical properties. The crystal structure of graphene can be described as two interlocked triangular lattices, labeled as atoms A and B in the upper panel of Fig. 1.5a. Both the primitive lattice vectors and the Wigner-Seitz unit cell (shaded rhombus) are indicated in the figure. The length of the primitive lattice vectors is $|a_i| \sim 2.46$ Å. In reciprocal space, the Brillouin zone of graphene is hexagonal (lower panel Fig. 1.5a) and features 4 main high-symmetry points: Γ, K, M and K'. It is important to note that K and K', known as the two valleys, are inequivalent points in reciprocal space[69]. The Fermi surface of monolayer graphene exhibits linearly-dispersing bands at the Fermi level, occurring at the K, K' points. These low-energy bands are known as Dirac cones and are pictured in Fig. 1.5b. The electronic properties of graphene, which have been intensively studied since its discovery[70], are dominated by the Dirac cones. The linear dispersion arises from the presence of identical atoms in the A and B sublattices. The gapless Dirac cones are topologically protected by the combined C_2 and T symmetries of the system. The linear dispersion directly implies that the carriers populating the Dirac cones are massless and must be described through the relativistic Dirac equation[71].

The dispersion relation near the K (or K') can be written as:

$$E(\boldsymbol{K}+\boldsymbol{q}) = \hbar v_f \boldsymbol{q}\boldsymbol{\sigma} \tag{1.4}$$

, where $\mathbf{q}$ is a small momentum such that $\mathbf{K} + \mathbf{q} \approx \mathbf{K}$, $v_f \approx 10^6$ m/s is the so-called Fermi velocity of graphene carriers and $\boldsymbol{\sigma} = (\sigma_x, \sigma_y)$ is the vector of Pauli matrices.

We note that the Dirac nature of the low-energy carriers in monolayer graphene already brings about exotic physics. For instance, at very low carrier densities, the system does not behave as a Fermi liquid and is best described by a hydrodynamic transport regime[72]. Also, the quantum hall effect can be observed at room temperature in graphene[73], thanks to the extremely high carrier mobility enabled by the Dirac dispersion. A crucial factor in the study of graphene transport is the possibility of moving the chemical potential across the Dirac cones using an electrostatic potential.

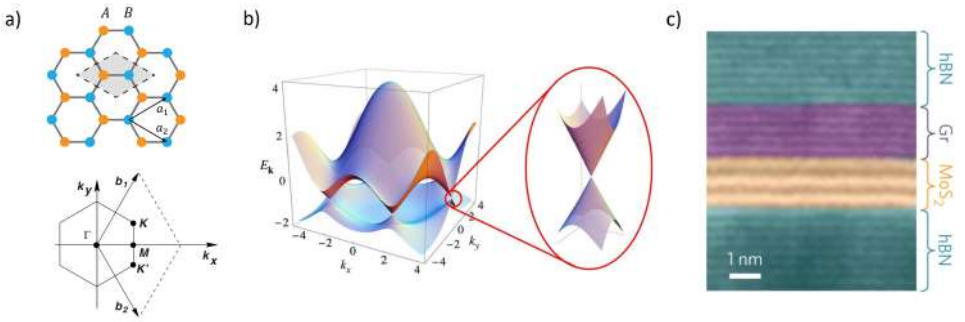

Figure 1.5: a) Upper panel: Crystal structure of graphene, formed by two triangular lattices labeled A and B. The shaded rhombus depicts the unit cell. The length of the lattice vectors a_1, a_2 is 0.246 nm. Lower panel: Hexagonal Brillouin zone of graphene, with two inequivalent valleys K and K'. b) Fermi surface of graphene. Also shown is a zoom-in into the Dirac cones appearing at the K, K' points. c) Cross-sectional transmission electron microscope image of a van der Waals heterostructure. The interfaces between the different 2D materials are atomically sharp and independent of lattice matching. Panels (b) and (c) adapted from Refs. [70] and [74], respectively.

In addition, graphene has enticing mechanical, thermal and optical properties. We outline here its optical properties, as they are relevant to the presented work. First, absorption in graphene is broadband, from visible range to terahertz[75], owing to its gapless spectrum. Different optical transitions (intraband and interband) intervene in the absorption of different wavelengths. Second, the optical absorption is quite large (2.3 %) for an atomically thin layer of carbon atoms. The absorption increases linearly with the number of layers and is determined by the fine structure

constant[76]. Lastly, light-matter interaction in graphene can occur in an ultrafast timescale and holds promise for the design of photonic devices such as broadband, saturable absorbers[77].

We also note that AB bilayer graphene, where the two layers are stacked in their energetically favourable configuration, also features remarkable electronic properties[78]. Like monolayer graphene, AB bilayer graphene is a zero-gap semimetal. However, in this case, the low-energy dispersion is not linear, but quadratic. Furthermore, unlike monolayer graphene, an out-of-plane displacement field can break inversion symmetry in AB bilayer graphene, opening a gap at the Fermi level. Thus, AB bilayer graphene has a tunable bandgap[79], in contrast to conventional semiconductors where the bandgap is fixed. The tunability of the AB bilayer graphene bandgap (up to mid-infrared energies) positions this system as a promising platform for a multitude of applications[80].

The principle of mechanical exfoliation used for graphene can be expanded to a wide variety of layered bulk crystals[81]. Nowadays, a multitude of 2D materials have been isolated and their properties cover nearly all the spectrum of electronic ground states: from semiconducting transition metal dichalcogenides (TMD)[82, 83], insulators like hexagonal boron nitride (hBN)[84], to ferromagnets[85, 86], semimetals[62], superconductors[87–89] or topological insulators[90]. What's more, 2D materials can be vertically assembled into heterostructures without the need for any lattice matching. Instead, the 2D layers are bonded via van der Waals forces, allowing for the assembly of heterostructures with arbitrary layers and stacking orders. These vertical stacks of 2D materials are known as van der Waals (vdW) heterostructures[1, 2].

The possibility of creating vdW heterostructures with extremely clean interfaces (see Fig. 1.5c) has drastically expanded the scope of the field of 2D materials. Due to their atomically-thin nature, 2D materials are extremely sensitive to their environment and their properties can be significantly modified by proximity effects with neighbouring 2D layers. Therefore, it is possible to design heterostructures with emergent properties as new, artificial materials that do not exist in nature. For example, one may vertically interface graphene with a superconducting 2D layer to induce a superconducting proximity effect in the Dirac electrons[91], or combine semiconducting and metallic 2D layers to design efficient optoelectronic devices[92].

The versatile toolkit of 2D materials, based on the exfoliation of different ultrathin crystals and the assembly of gate-tunable heterostructures, was revamped once more with the discovery of twist-angle engineering of vdW heterostructures. Thanks to the vdW bonding between 2D layers, their crystalline structures can be rotationally misaligned. As we describe next,

this interlayer twist angle brings about new possibilities in the design of novel 2D materials[3].

Magic angle twisted bilayer graphene

The role of rotational misorientation in graphite had been explored in the context of turbostratic few-layer graphene films, where tunneling experiments observed electronic decoupling of the constituent layers due to a large interlayer twist angle[93–96]. Advancements in the fabrication techniques for exfoliated graphene motivated the theoretical exploration of moiré effects in small-angle twisted graphene stacks[97, 98]. In addition, at small twist angles, tunneling spectroscopy in the moiré sites revealed the presence of two van Hove singularities (vHs) near the Fermi level[63, 64].

In this context, Bistritzer and Macdonald proposed in 2011 that a heterostructure of misaligned graphene monolayers at a 'magic' twist angle of $\theta = 1.1^\circ$ would host a flat electronic band at the Fermi level[65]. Their model, which we briefly outline here, is known as the continuum model or BM model. The slight misalignment of two periodic lattices gives rise to an interference pattern that results in an emergent, large-scale moiré superlattice (see upper panel Fig. 1.6a). In momentum space, the Brillouin zones are also rotated with respect to each other, and a new hexagonal mini-Brillouin zone is formed between the adjacent valleys of each layer (lower panel of Fig. 1.6a).

The formation of a large-scale superlattice in real space, or a small mini-Brillouin zone in momentum space, leads to the renormalization of the low-energy electronic spectrum of the twisted bilayer. The band renormalization results from the destructive interference between the intralayer and interlayer tunneling pathways for electrons in the bilayer. This effect can also be pictured through the hybridization of the Dirac cones of each layer, as they come closer in momentum space.

Then, the hybridization of the two Dirac cones forms 2 sets of bands: two Dirac-like bands far from the Fermi level and two bands with flat dispersion near the Fermi level (right panel of Fig. 1.6a and Fig. 1.6b). Crucially, the bandwidth of the flat bands (≤ 10 meV), as well as their separation from the dispersive bands depend critically on the twist angle θ.

The electrons populating the flat bands at the Fermi level experience a large reduction of their Fermi velocity v_F[65]. Consequently, their kinetic energy is quenched and Coulomb repulsion can become the dominant energy scale in the flat band. Figure 1.6c illustrates the relative magnitude of the kinetic energy (parametrized by the bandwidth W) and the Coulomb interaction (parametrized by U) in the flat band. At the magic angles, we focus here on the first one $\theta = 1.1^\circ$, the bandwidth is minimized and the flat

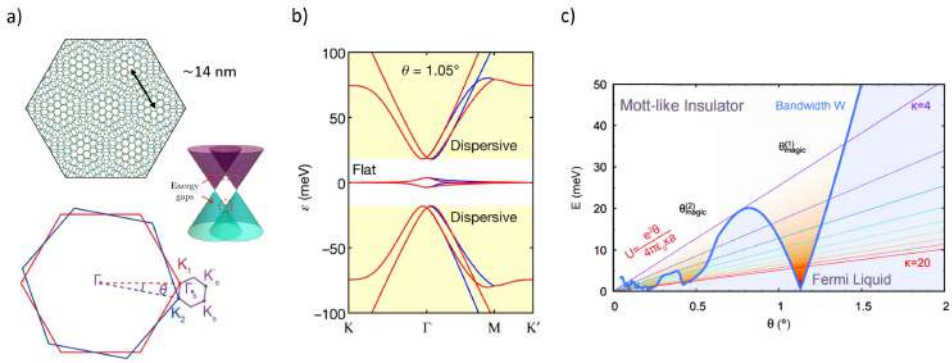

Figure 1.6: a) Upper panel: Moiré superlattice formed in a magic angle twisted bilayer graphene. Note that the new lattice constant is ~ 100 times larger than the lattice vectors of graphene. Lower panel: Rotated Brillouin zones in momentum space and generation of a mini-Brillouin zone. Pictured here is only the one at the K valley. Right panel: Illustration of the Dirac cone hybridization for small-angle twisted bilayer graphene. b) Band structure for MATBG computed from the BM model. Each of the two flat bands at low energy is fourfold degenerate (spin and valley). c) Comparison between Coulomb energy and bandwidth of the flat bands for different twist angles. Regions where $U > W$ are expected to host strongly-correlated physics at the Fermi level. Panels (b) and (c) adapted from Refs. [99] and [4], respectively.

band realizes the strongly-correlated limit of the Hubbard model as $U > W$.

The flat band electrons exhibit a reduced four-fold degeneracy (compared to the eight-fold degeneracy of non-twisted bilayer graphene[78]). The four-fold degeneracy originates from the spin and valley degrees of freedom. It's worth noting that the valley degeneracy persists due to the large separation in momentum space of the mini-Brillouin zones associated with the original K and K' valleys. Therefore, for each of the two flat bands, a moiré unit cell can host up to 4 charge carriers. Akin to the Hubbard model, interaction effects become prominent at integer occupations of the moiré unit cells. The phase diagram of MATBG is often parametrized by the filling factor $\nu = 4\frac{n}{n_s}$, where n is the carrier density and n_s is the number of charge carriers needed to fill a moiré unit cell, given by $n_s \approx \frac{8\theta^2}{\sqrt{3}a^2}$ where a is the lattice constant of graphene (see Fig. 1.5a)

Thus, the physics of the MATBG flat bands are characterized by strong electronic interactions[100]. As we show next, a multitude of many-body electronic ground states have been observed in this system. It's worth noting that while the BM model[65] predicted the emergence of the isolated flat band near the Fermi level, it did not treat the electronic interactions within the flat band. The strong correlations break the degeneracies of the non-interacting

flat bands and lead to a variety of symmetry-breaking ground states. Several years later, a comprehensive understanding of electron correlations in the flat bands has not been established.

Phenomenology of the MATBG flat bands

Following the prediction of a flat electronic band for twisted bilayer graphene at $\theta = 1.1°$, the first experimental demonstration came in 2018 from the group of Pablo Jarillo-Herrero. In back-to-back papers, the first direct evidence of strongly-correlated physics in the flat bands of MATBG was reported. First, authors demonstrated the appearence of a Mott-like correlated insulator at half-filling of the flat bands[4] (Fig. 1.7a). This behaviour evidences the strong electronic interactions in the system, which produce an emerging gap in what should be a metallic system (recall the previous discussion on the Hubbard model). Next, they reported a superconducting phase near half-filling of the flat bands[5] (Fig. 1.7a). This state, with critical temperatures in the order of $T = 1$ K, exhibited zero resistance and could be quenched by a perpendicular magnetic field (see Fig. 1.7b).

These striking findings underscored the immense potential of the MATBG flat bands as a tunable platform for the study of strongly correlated physics. Note that, unlike traditional correlated condensed matter systems, here all the atoms are carbon atoms and the electronic correlations stem solely from the formation of a superlattice potential via the twist angle. In the following years, the electronic properties of the MATBG flat bands have been extensively explored, mainly through quantum transport measurements. We highlight here some of the key findings that characterize the MATBG phenomenology and link it to the physics of strongly correlated materials.

First, it is important to highlight the similarities between the phase diagram for MATBG near half-filling ($\nu = \pm 2$), shown in Fig. 1.7a, and the phase diagram for heavy fermion and cuprate superconductors, shown in Figs. 1.3b and 1.4c, respectively. This parallelism underscores the strongly-correlated nature of the flat bands and suggests the existence of a quantum critical point that separates these different ground states. Second, magnetotransport studies of the flat bands demonstrated the interaction-driven reconstructions of the Fermi surface at integer fillings, as distinct sets of Landau fans emerge from every integer filling $\nu = \mathbb{Z}$[4, 5, 103, 104]. Often, the Landau fans not coming from charge-neutrality exhibit reduced degeneracy, signaling the breaking of the system's symmetries. These observations supported the picture of the many-body ground states at integer ν as symmetry-broken correlated insulators[105].

Further transport and thermodynamic studies revealed the existence of a strange metal phase ($\rho \propto T$) in samples twisted near the magic angle[101,

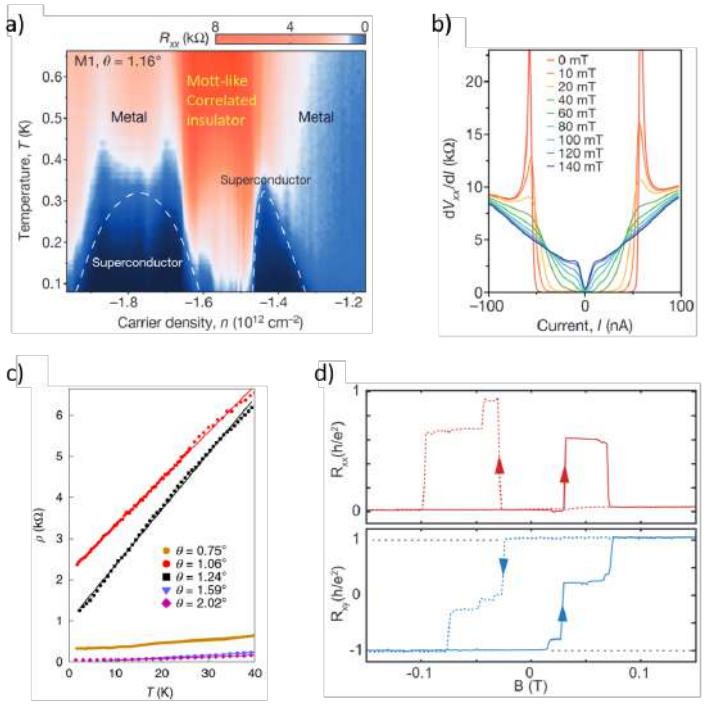

Figure 1.7: a) Phase diagram of the longitudinal resistance of MATBG near half-filling of the valence flat band. A superconducting state appears in the vicinity of a Mott-like correlated insulator, flanked by Fermi-liquid-like regions. Note the similarity with the phase diagrams shown in Figs. 1.3b and 1.4c. b) Suppression of the superconducting phase by an out-of-plane magnetic field in MATBG. c) Strange metal behaviour for twisted bilayer graphene samples near the magic angle. Fermi level lies near half-filling of the conduction flat band. d) Quantum anomalous Hall state with Chern number $C = 1$ near $\nu = +3$ filling of the flat bands in MATBG. Panels (a) and (b) adapted from Ref. [5], panels (c) and (d) adapted from Refs. [101] and [102], respectively.

106, 107] (Fig. 1.7c). This phase, reflective of strong correlations, appears in the vicinity of $\nu = \pm 2$ in the flat bands, above the superconducting dome, just as in heavy fermion compounds and cuprates[36, 43]. The strange metal phase poses questions about the scattering mechanisms for electrons, as well as the nature of superconductivity in the system. The superconducting phase was already thought to be unconventional, due to the extremely low carrier density at which it appeared[5].

The flat bands of MATBG host one more crucial ingredient in modern condensed matter physics: non-trivial topology[108]. The flat bands are endowed with topological character by the Dirac cones of the constituent graphene layers, which are known to be monopoles of Berry curvature.

Indeed, close to $\nu = +3$, a topological state with vanishing longitudinal resistance (R_{xx}) and quantized Hall resistance (with Chern number $C = 1$) was observed at zero magnetic field[109] (Fig. 1.7d). Since then, many other topological states have been reported, including integer[110] or even fractional Chern insulators[111].

All in all, the MATBG flat bands constitute an exceptional platform for the study of strong electronic interactions and their interplay with non-trivial band topology[100]. The elegant concept of twist angle engineering allows for complex physics to arise in a relatively simple material platform, made entirely out of carbon atoms. Crucially, the gate tunability of the system allows for the study of the various many-body ground states in a single device. Thus, the flat bands of MATBG stand out as a rich and versatile playground for the study of strongly-correlated phenomena.

Correlated 2D materials beyond twisted bilayer graphene

The prospect of exploring strongly-correlated electrons in 2D vdW heterostructures is not limited to twisted bilayer graphene. The principle of twist angle engineering can be applied to many other heterostructures, including other graphene-based moiré heterostructures. Correlated phases and superconductivity have been observed in twisted trilayer, quatrilayer, and pentalayer graphene at their respective magic angles[112] (Fig. 1.8a). Moiré patterns between graphene layers and the encapsulating hBN layers also bring about new correlated states[66–68, 113]. Even higher-order moiré patterns (moiré of a moiré) have been experimentally demonstrated[114, 115].

Other 2D materials such as semiconducting TMD's also have magic angles for which the low energy bands are drastically flattened. Twisted TMD heterostructures host correlated insulators[116, 117] (Fig. 1.8b), novel topological phases[118, 119] and act as a faithful simulators of the Hubbard model[120, 121]. What's more, heterostructures of different TMD's (heterobilayers) do not require a precise twist angle for the emergence of the superlattice potential. Instead, at zero twist angle (which is energetically favourable), the small lattice mismatch between different TMD compounds gives rise to the moiré interference pattern. In addition to the transport properties, the superlattice potential also modifies the excitonic spectrum in TMD's, creating so-called moiré excitons[122, 123].

An alternative to the assembly of vdW heterostructures is the exfoliation of layered bulk crystals which intrinsically host strongly-correlated physics. Correlated states such as Wigner crystals[124] (Fig. 1.8c), fractional quantum Hall phases[125] and excitonic insulators[126] have been observed in monolayer TMD's. Other states such as the elusive quantum spin liquid are currently being explored in other crystalline monolayers[51, 127]. Some

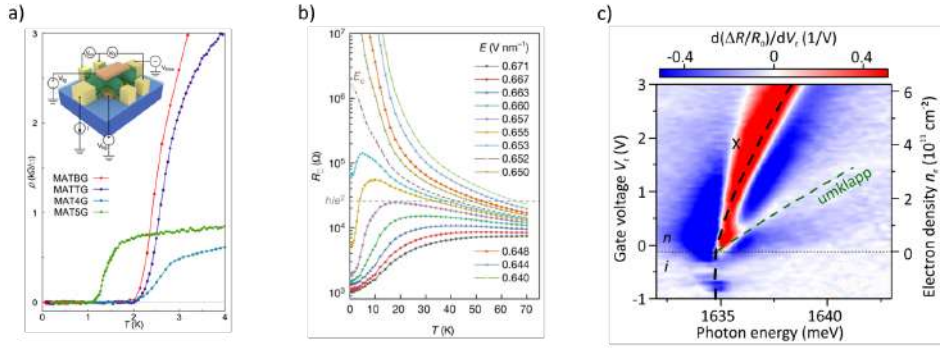

Figure 1.8: a) Superconducting transitions for magic angle multilayer graphene samples. For more than 2 layers, the twist angle is alternated ($\theta_{n-1,n} = -\theta_{n,n+1}$). b) Continuous Mott transition driven by an applied displacement field in $MoTe_2/WSe_2$ heterostructure. c) Exciton spectrum of monolayer $MoSe_2$ imaged by differential reflectivity. Next to the main trion peak X, an additional umklapp resonance appears, signaling the formation of a Wigner crystal. Panels (a), (b) and (c) adapted from Refs. [112], [128] and [124], respectively.

cuprate superconductors and heavy fermion compounds also feature a layered structure, allowing for their mechanical exfoliation down to the monolayer level. In the latter part of this thesis (Chapter 5), we explore the use of an exfoliated cuprate superconductor for the development of high-temperature superconducting sensors.

Optoelectronic studies in these systems

In this thesis, we will explore the optoelectronic response of strongly-correlated 2D systems as a way to explore both their fundamental properties and their suitability for applications. Therefore, we conclude this introduction motivating the optoelectronic studies of these novel, 2D-based strongly-correlated materials. Historically, optical and optoelectronic techniques have been useful tools to unveil correlated phenomena[129]. In the case of MATBG, the flat bands have been thoroughly investigated through quantum transport techniques. Local probe studies (mainly tunneling and magnetic) have also shed light on the spatial properties of the correlated phases. However, the optoelectronic response of the flat band electrons remains mostly unexplored, even though light-matter interaction is a widely studied topic in graphene-systems[77, 130]. As we show in this work, optoelectronic experiments can be used to improve on certain transport measurements, such as thermoelectric effects; or to investigate otherwise inaccessible physics, such as the dynamics of light-matter interaction in the presence of a moiré super-

lattice potential. Here, we will explore these effects in the strongly-correlated flat bands of magic-angle twisted bilayer graphene[131].

Furthermore, electronic correlation effects are not only relevant to fundamental studies; they can also be harnessed for the development of new technologies[132–140]. For example, colossal magnetoresistance in correlated oxides can be used to design magnetic memories or magnetometers[133, 134]; while HTS in the cuprates is widely employed in superconducting magnets[141]. Regarding the novel platforms based on 2D materials, some examples include the use of the low-carrier-density superconducting state to create gate-tunable superconducting devices and photodetectors[137, 138, 140, 142, 143], or the opening of interaction-driven gaps in twisted graphene systems to develop broadband photodetectors[139, 144]. In addition, going to the 2D limit in cuprate superconductors creates new possibilities to create nanoscale, HTS devices[145].

Outline of the thesis

In this introduction, we have introduced the aspects of strongly-correlated electrons and their realization in vdW heterostructures of 2D materials. In Chapter 2, we describe the experimental methods for the fabrication and measurement of the samples used in this doctoral thesis. In Chapter 3, we report on the study of thermoelectricity in the flat bands of MATBG using optical excitation. At low temperatures, we find an anomalous response which we interpret as direct evidence for the coexistence of light and heavy fermions in the MATBG flat bands. In Chapter 4, we explore the cooling dynamics of photoexcited electrons in the MATBG flat bands. We uncover a novel mechanism for electron-phonon scattering at low temperatures, which is enabled by the superlattice potential. In Chapter 5, we switch material platforms to demonstrate ultra-sensitive photodetection at elevated temperatures using an exfoliated, 2D cuprate superconductor. We obtain record-response in terms of sensitivity, operation temperature, and detection speed in two different device concepts. Finally, in Chapter 6, we summarize the findings of this doctoral thesis and provide a specific outlook on each one of the presented research projects.

This work encompasses several topics involving different materials, measurement techniques, and physical processes. Therefore, we will introduce in each chapter the necessary concepts relevant to the presented work.

Chapter 2

Experimental Methods

In this section, I will describe all the experimental techniques used in the projects that are comprised in this doctoral thesis. These include both the fabrication of samples and the measurement techniques used to characterize said samples. First, the fabrication procedure for the samples will be presented. Given the contrasting nature of the two types of van der Waals heterostructures used in these studies, we separate this discussion in separate sections on the fabrication of MATBG samples and the fabrication of heterostructures based on the exfoliated cuprate superconductor $Bi_2Sr_2CaCu_2O_{8-\delta}$ (BSCCO-2212).

We note that for the former, a large amount of pre-existing knowledge exists in the group and I will briefly describe the standard procedure for the fabrication of MATBG samples designed for optoelectronic experiments. I refer the reader to the PhD thesis of my colleagues Ipsita Das and Jaime Díez-Mérida for an in-depth discussion of this fabrication process. On the other hand, I did contribute significantly to the development of the fabrication process of high-quality BSCCO-2212 heterostructures inside a glovebox setup. Thus, this second subsection contains more detailed information about this very challenging, often frustrating process.

2.1 Fabrication of MATBG samples

The general fabrication method for high-quality heterostructures of 2D materials was first developed at Columbia University in 2013[146]. Since then, many incremental improvements have been introduced to accommodate more complex heterostructures[147] and other 2D materials whose properties are more restrictive than graphene or hBN. For air-sensitive materials, as will be discussed in the next section, an alternative method was also developed that bypasses the use of any solvent[148, 149]. The fabrication of MATBG

samples can be divided into three different stages: the exfoliation and flake selection process, the stacking or assembly process, and the Hall bar fabrication through standard nanolithography. The samples used in the projects presented here feature one additional step, the splitting of the top graphite gate that enables the creation of a gate-defined *pn*-junction.

2.1.1 Exfoliation and flake selection

Exfoliation onto silicon chips

A MATBG sample comprises layers of monolayer graphene, hBN and thicker, multilayer graphite that will serve as metallic gates. In terms of exfoliation, slightly different strategies can be used to optimize the exfoliation of each one of these target materials. All the exfoliation is performed on Si/SiO_2 chips (generally with 285 nm thickness of the oxide layer) which are cut into small pieces ($\sim$ 8x8 mm) using a diamond tip cutter. Then, to clean the surface of the chips and also increase the adhesive force between the chip and the flakes of 2D materials[81], we do O_2 plasma etching of the chips. Usual parameters are 100 Watts power, O_2 flow rate of 50 sccm and a duration of 3 minutes. This plasma etching process may be skipped for certain 2D layers, depending on the specific device structure. Further discussion on this point will be presented in the next subsection. Once the chips are etched, we proceed to the exfoliation of the layered crystals.

We start by uniformly pressing the bulk layered crystal onto a freshly prepared piece of scotch tape. The bulk crystal is then carefully removed from the tape and stored; from this point on we will use this 'mother' scotch tape. Successive exfoliation of the crystal in the same tape or onto another fresh scotch tape is performed until the bulk crystals have been significantly thinned down. We aim to uniformly cover the piece of tape, which will be then used to exfoliate onto the silicon chips. Figure 2.1a shows an exemplary graphite tape ready for exfoliation onto silicon chips. The number of exfoliations from the 'mother' tape will largely determine the type of flakes we obtain. This choice offers a clear trade-off between the thickness and the size of the resulting 2D layers, as well as the amount of tape residues on the chip. Excessive repetitions will lead to generally thinner layers that will be smaller and/or surrounded by tape residues and might be broken. On the other hand, not enough exfoliations of the tape will yield more uniform, sparsely distributed flakes without so many tape residues but few-layer flakes are less likely to be isolated.

After tape exfoliation, we carefully place the etched silicon chips (their polished side) onto the scotch tape, which is then flipped. Through a piece of lint-free tissue, we now press the tape strongly on each chip in a stable,

uniform manner for about 1-2 minutes. Finally, we place the scotch tape with the attached chips on a hot plate at 110°C for approximately 2 minutes. Applying some uniform pressure on the chips during the heating process can increase the yield of flakes on the chip. We finally release the chips from the tape slowly, with the non-sticky side of the tape facing us. Using tweezers, we hold in place each chip as we slowly peel the tape upwards while keeping the chip in contact with the work surface. After repeating this for each chip and each 2D material being exfoliated, we store the chips in small chip boxes and proceed with an additional step before the vertical assembly of the heterostructures: the preparation of polymer stamps.

Polymer stamps

In short, we will subsequently pick up the exfoliated flakes from the silicon chips using a temperature-sensitive polymer stamp that sits on a standard glass slide. A variety of polymers can be used, in our lab we use a combination of commercial polydimethylsiloxane (PDMS, Gelpak) and a homemade polycarbonate (PC) film on top of the PDMS. The former will provide mechanical stability while the PC film will be the active polymer in the stacking process. Crucially, its mechanical properties can be controlled through temperature. This feature is leveraged to, for example, make the PC film adhere strongly to the 2D flakes to pick them up or melt the PC film to drop the finalized heterostructure onto the silicon chip. A small ($\sim$ 6x6) mm piece of PDMS is placed on the glass slide in a uniform manner. Afterwards, the PC film will be carefully laid on top of the PDMS square using a scotch tape 'window' as support. The scotch tape 'window' is stuck to the glass slide to keep the PC film stable on the glass slide[146]. It's important for the stacking process that the PC film and also the PC/PDMS interface are highly uniform and free of defects. Figure 2.1b shows one such polymer stamp. Once we have the exfoliated silicon chips and some clean polymer stamps, we can proceed to the stacking process.

2.1.2 van der Waals assembly process

Transfer stage

Vertical assembly of 2D materials is performed using a transfer stage. We use a custom-made transfer stage pictured in Figure 2.2. The main components of the transfer stage are: a sample stage, a stamping stage and a microscope. The entire transfer stage sits on a heavy metal plate that serves to dampen mechanical vibrations. The purpose of the transfer stage is to offer complete control over the alignment and approach between the stamping stage (where the polymer stamp lies) and the transfer stage

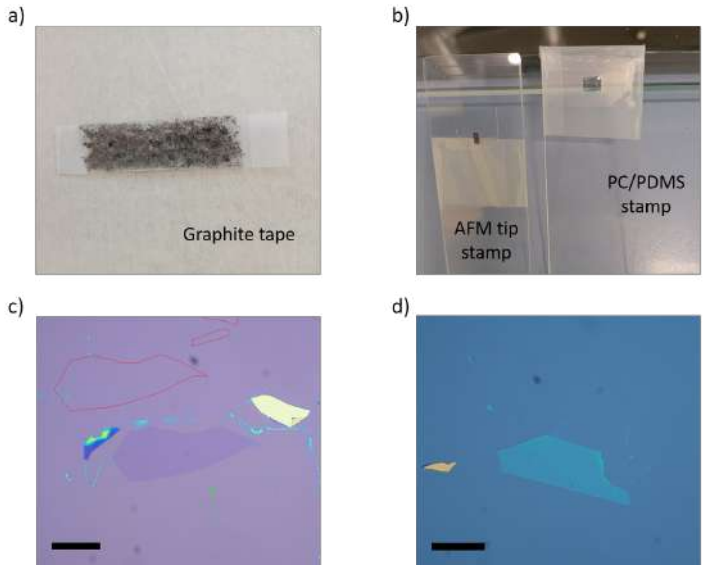

Figure 2.1: a) Graphite exfoliation tape. b) Stamps for flake cutting (left) and polymer stamp for pickup (right). c) Exemplary clean graphene flake with large size. d) Exemplary hBN flake of medium thickness ($\sim$ 12-16 nm) and high uniformity. The scale bars in (c) and (d) correspond to 10 μm.

(where the silicon chips are placed), while the microscope optics allow us to monitor the process in real-time. The spatial control includes the three spatial directions (XYZ) plus tilt angles both in the XY and Z planes. The

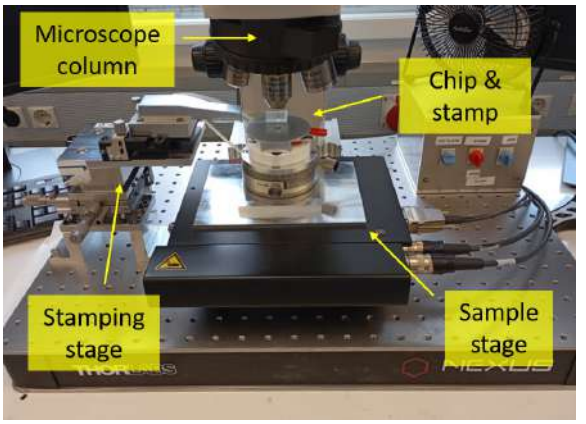

Figure 2.2: Custom transfer stage for the assembly of MATBG heterostructures.

sample stage features automated in-plane movements (both fine and coarse) controlled through a joystick. In addition, it includes a high-precision,

manual rotation stage (with both standard and Vernier scales). The chips, which may be heated in the sample stage, are held in place through a small vacuum chuck. The stamping stage, which is operated manually, features micro-manipulators for XYZ as well as the aforementioned tilt control. A stamp leg sticks out from the stamping stage, held in contact with it by another vacuum chuck, to facilitate the approach between stamp and chip. The glass slide containing the polymer stamp is then attached to the stamp through a last vacuum chuck. The microscope column contains 4 different objective lenses (5x, 10x, 20x and 50x) along with multiple optical filters, including a dark field filter. The entire column can be moved in the vertical direction to focus on the different surfaces. The image can be captured live by a CMOS camera attached to the column, or the user can employ the eyepiece from the microscope.

Flake selection

The assembly process starts with the identification of suitable flakes for the desired heterostructure. As a general rule, we aim to identify 2D flakes that are large and uniform, ideally isolated from other flakes and accumulations of tape residue. The following discussion is focused on the assembly of a particular type of MATBG heterostructure: a top-and-bottom graphite-gated MATBG Hall bar. This heterostructure comprises, in the following order, a graphite layer (serves as a top gate), an hBN layer, a twisted bilayer of graphene, another hBN layer and a final graphite layer (serves as a bottom gate). With this in mind, the criteria for the identification of suitable flakes (both in size, thickness and shape) are described here:

For graphene:: For the assembly of MATBG heterostructures, we aim to find large ($\sim$ 40x40 μm) monolayer graphene flakes with a clean surface and straight edges (Fig. 2.1c). Crucially, the optical absorption of graphene increases linearly with the number of layers. Each layer absorbs ($\sim$ 2.3%) of the incident light in the optical range[76]. Thus, after some training, it becomes easy for the user to identify monolayer, bilayer or multilayer graphene flakes.

For hBN: We generally utilize hBN flakes with thicknesses between 10 and 25 nm and of larger area than the graphene layer. We note that for thin hBN, below 10 nm, one should use silicon chips with 90 nm of SiO_2 thickness; as they offer much higher optical contrast. Having a uniform thickness of the hBN flake is crucial, as it will define the dielectric in the parallel plate capacitor gating scheme. The targeted hBN flakes have different hues of blue in their optical image (Fig. 2.1d), they become greener for thicker layers.

For graphite gates: The width and length of the eventual Hall bar will be largely defined by the shape of the graphite gates. Thus, we search for rectangle-shaped graphites that have an approximate width of a few microns and lengths approximately half the length of the initial graphene flake. The criteria for their shape and length will become clearer once we discuss the nanofabrication of the Hall bar. Regarding the thickness of these graphite gates, we aim for approximately 5-10 layer graphite, which will act as a good metallic gate. One important distinction must be made here between the top and bottom graphite gates. The top graphite gate will be the first layer picked up in the assembly process, through the adhesion to the PC film, not by van der Waals forces. Given that, during the exfoliation process, some chips should not be etched for graphene/graphite exfoliation, from which we will select a suitable top graphite gate.

Cutting the graphene flake

Before proceeding to the stacking of the 2D layers, one should have a clear design of the heterostructure, considering the size and shape of the flakes. The active area of the eventual device will be the twisted bilayer graphene, where a precise rotational misalignment is required. Importantly, these two graphene layers will be obtained from a single graphene flake. In this way, as the crystallographic axes of the component graphene layers are perfectly parallel to begin with, we can produce a precise rotational misalignment between the two layers.

An AFM tip may be used to cut the target graphene flake. Generally, the flake will be cut approximately in half, so that the area of the twisted interface is maximized. A glass slide with a PDMS stamp will be used as the 'arm' to manipulate the AFM tip. We place an AFM tip on the PDMS stamp at an angle, with the tip facing away from the glass slide. Using scotch tape, we fix its position with the glass slide so it doesn't move during the cutting process (see the left stamp in Fig. 2.1b). Then, we mount this glass slide on the stamp leg connected to the stamping stage micro-manipulators. We roughly align the position of the graphene flake (moving the sample stage) and the position of the AFM tip, playing with the focus of the microscope as each object lies at a very different focal distance. After this rough alignment, we lower the AFM tip using the Z-control knob on the stamping stage until it lies close to the focal plane of the graphene. To choose the position of the tip with respect to the graphene, one must consider the desired direction of the cut. We usually 'cut' horizontally, from left to right, so the AFM tip is oriented to the left of the graphene flake, pointing along the direction of the desired cut. Now, the AFM tip is carefully lowered to the plane of the

silicon chip, using the optical contrast and focus of the tip as an indication of the height. Once in contact or near contact with the substrate, the silicon chip is swiftly moved from right to left and the graphene flake is cleanly cut by the AFM tip. If successful, we lift the AFM tip away from the substrate and remove it from the stamp leg. This simple process routinely produces clean cuts with widths of one or few microns (Fig. 2.3a). Repeated sweeps of the sample stage to repeat the cut are sometimes needed but can result in very wide cuts, ripping or even folding of the graphene. Once the cut has been performed, the design and alignment of the heterostructure should be revised once more, considering the exact shape of the two graphene flakes (Fig. 2.3b).

vdW vertical assembly

We now describe the sequential alignment and pickup of the 2D layers that compose a double-gated MATBG device. This process can begin only when all the component layers have been identified in the different silicon substrates.

As mentioned before, we start by picking up the top graphite gate using the PC film. The optimal temperature for the pickup of 2D layers using this polymer is approximately 110°C. This temperature will be (although weakly) dependent on the exact composition of the PC film and its thickness. Once the sample stage has been heated to the target pickup temperature, we lower the polymer stamp towards the sample stage by using the Z control knob on the stamping stage. Generally, one should keep the stamp parallel to the silicon chip to avoid strain and mechanical stress during the assembly. Monitoring this first contact between the polymer and the substrate is crucial. During the pickup process, the microscope must always be focused on the plane of the silicon chip. The contact will become apparent through the optical image as a change in colour. In addition, at the point of contact between the polymer stamp and the substrate, a series of optical fringes (like oil on water) will appear. These fringes contain crucial information about the 'wavefront' that determines the stacking process, such as the direction, the speed, the angle of contact and the overall smoothness of the pickup process. A wavefront that does not evolve smoothly will lead to significant strain on the 2D layers during the stacking process.

The target graphite gates have a rectangular shape with a high aspect ratio (their length is approximately 5-10 times their width). It is beneficial to align the approaching wavefront parallel to the short side of this rectangle shape. We smoothly lower the stamp stage until the PC film is in full contact with the entire flake, keeping care of the formation of bubbles or imperfections. One should stop the wavefront once it's some distance ($\sim$

10-20 μm) past the graphite flake. We now retract the wavefront, by slowly lifting the stamping stage, picking up the graphite layer in the process. If successful, we will observe a clear change in the contrast of the graphite layer as the wavefront passes over it, signaling that it has been picked up and it's no longer at the focal plane of the substrate. We coarsely lift the stamping stage, having completed the first step in our assembly process. The chip on the sample stage is replaced by the chip containing the top hBN flake. We place the chip according to the target alignment of our 2D layers (Fig. 2.3c). Lowering the stamp leg, we repeat the process to pick up the hBN flake. One should avoid aligning the wavefront to a long, straight edge of the hBN flake, as this may result in ripping of the flake and an unsuccessful pickup process.

The two graphene layers are sequentially picked up using the same process. It's important to reset the rotation stage of the sample stage to the origin of the Vernier scale before picking up the first graphene layer. Note that the eventual twisted graphene interface should be correctly aligned with the top gate and completely covered by both hBN layers. Alignment of the wavefront with the direction of the cut simplifies the pickup process. In this way, one can fully contact the first graphene layer with the PC film and stop the wavefront before touching the second layer. Again, we smoothly contact the graphene flake and pick it up.

At this point, we lift the stamp and rotate the sample stage to the target twist angle (1.1° for the first magic angle of twisted bilayer graphene). We then lower the polymer stamp again, align the two graphene layers to maximize the twisted interface area and pick up the second flake. Such small rotational misalignment produces a meta-stable configuration: the two graphene layers will relax to their untwisted configuration (Bernal stacking) if enough energy is provided (through temperature, vibrations, etc...). Therefore, once the twisted interface is picked up, one must be exceedingly careful and smooth with the remaining stacking process. The bottom hBN is picked up following the same process, making sure it fully covers the twisted bilayer graphene. As mentioned before, it's of crucial importance that the two hBN layers are uniform in thickness, at least in the area that will cover the graphene flakes. Lastly, the bottom graphite is picked up. One should aim to align the two graphite gates as much as possible, in order to have a well-defined area that will be the active channel of the fabricated Hall bar. In addition, the two graphite gates should stick out from the twisted interface, ideally on opposite sides. This will simplify the fabrication of electrical contacts to each gate and avoid cross-talk. Figure 2.3c shows a finished vdW heterostructure following the design in Fig. 2.3b.

Note that after the first and second pickup steps, the adhesion force allowing us to pick the 2D layers is the van der Waals force between the

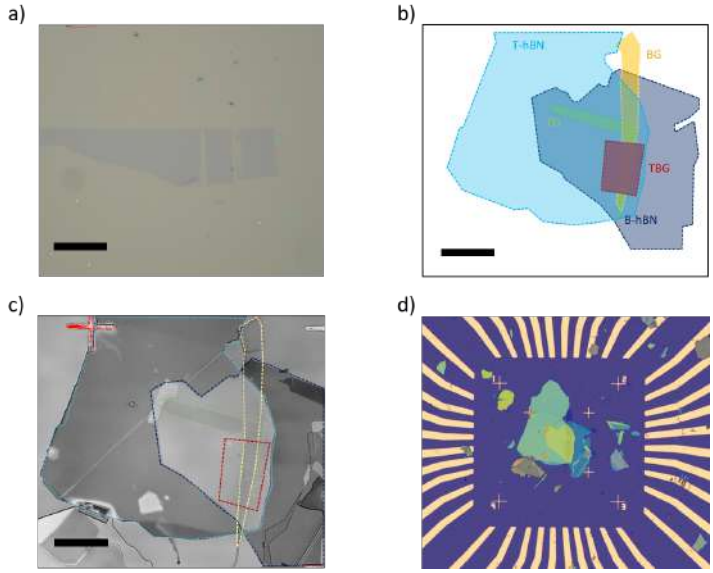

Figure 2.3: a) Graphene flake after AFM cutting. b) Target design for the heterostructure. c) Optical image of the assembled heterostructure, overlaid with the original design. The scale bars in (a), (b), (c) correspond to 10 μm. d) Dropped heterostructure on SiO_2 substrate with pre-patterned electrodes.

clean 2D interfaces. This process lies at the heart of the fabrication of ultraclean interfaces in these van der Waals heterostructures. In particular, the interfaces between the graphene layers and the encapsulating hBN layers should be extremely clean. Furthermore, bubble formation during the stacking process is naturally counteracted. The contact between the flat interfaces of the 2D materials tends to bunch up the bubbles and push them to the edges of the flakes, away from the active area[150].

Before performing further cleanroom fabrication, we must drop the heterostructure on a silicon chip. Here, the temperature-dependent properties of the PC film will be particularly useful. A pre-patterned silicon chip with multiple electrical contacts is placed on the sample stage. The polymer stamp, containing the entire heterostructure, is lowered to make contact with the pre-patterned chip. We place the heterostructure in the center of the prepatterned chip and advance the wavefront further (by several millimeters). We now increase the temperature of the sample stage, from 110°C to 180°C, monitoring the wavefront for possible temperature-induced movement. Once we reach this temperature, the PC film will start to melt and stay attached to the silicon chip. At this point, the stamp stage is slowly raised to break up the PC film, leaving the contacted part on the chip while raising the uncontacted film away. In this manner, the PC film will be ripped at the

wavefront interface and the heterostructure will now lie on the pre-patterned silicon chip, fully covered by the PC film. Lastly, the PC film is chemically removed by placing the chip in a beaker with chloroform for 3-5 minutes. The chip is then immersed in IPA for another 3-5 minutes and dried using an N_2 gun. The assembly process for magic-angle twisted bilayer graphene is now completed 2.3d.

2.1.3 Fabrication of MATBG Hall bar devices

The cleanroom fabrication process for MATBG Hall bars is rather standard. It involves several steps of electron beam lithography, reactive ion etching and metal evaporation; accompanied by the required spin coating, developing, lift-off and cleaning processes. Of course, one must use lithography software to design the various lithography masks needed. For the double-gated MATBG Hall bars, there are in total three cycles of lithography, etching and evaporation (one of these cycles can forego the etching process). The goal of each subsequent cycle is, in chronological order: (1) defining a Hall bar geometry in MATBG, (2) making electrical edge contacts to both the twisted bilayer graphene and bottom graphite gate and (3) contacting the top graphite gate. Here's a sequential rundown of the entire process:

1. Spin coating the sample. Standard parameters for the e-beam resist PMMA 950K (0,27 μm) are 30 seconds at 4000 rpm, followed by baking the chip in the hot plate for 2-3 minutes at 150°C.

2. Exposure of the first lithography mask (Hall bar geometry) in the electron-beam lithography (EBL) system. Developing using MIBK:IPA (1:3) for 40-50 seconds (depending on e-beam dose). Cleaning in IPA for 2 minutes.

3. Etching of the defined Hall bar structure. As etching gas, we use a mixture of CHF_3 and O_2 at a 10:1 ratio. This etching gas will remove hBN layers at a much faster rate than the graphite/graphene layers, making it reasonably selective. The etching rates must be calibrated for each RIE machine and combination of etching parameters. In this step, we etch down to the surface of the silicon chip. After etching, we optically check that the process was successful and clean the chip with acetone and IPA.

4. Second spin coating of the sample, same parameters as in the first step

5. Exposure of the second lithography mask in the EBL. This mask comprises contacts to the Hall bar arms, as well as a lithographic

window to the bottom graphite gate. The exposed resist is developed using the same parameters as before

6. Etching of the exposed areas. The contacts in the Hall bar arms are re-etched here to ensure that the graphene interface there is clean. Etching process should reach the bottom graphite gate.

7. Inmediately load the etched chip into the metal evaporator for e-beam evaporation of a Cr/Au (3 nm/50 nm). Chromium will adhere well to the substrate (and the graphite flake) and serve as support for the gold atoms. A chamber pressure of approximately 10^{-7} mbar in the evaporator is desirable for good electrical contacts

8. Lift-off process of the evaporated metal. Usually done in room-temperature acetone overnight. A syringe filled with acetone can be used to help the process after several hours. After successful lift-off, the chip is cleaned again using fresh acetone and IPA.

9. Third spin coating process, same parameters.

10. Exposure of the third lithographic mask, which consists of a simple lithographic window into the top graphite gate. One may define multiple windows to the top graphite along its length. The purpose of these multiple contacts will become apparent at the end of this section. Subsequent development using the same parameters stated above.

11. Directly load into the metal evaporator. As the top graphite gate is not covered in hBN, one can forego etching in this step. Standard evaporation of Cr/Au bilayer (3 nm /50 nm).

12. Final lift-off process in acetone. This sequence describes standard fabrication of a double-graphite-gated MATBG Hall bar. The contact to the exposed (not covered in hBN) graphite gate can be performed as the first or last cycle in this sequence. Figure 2.4 depicts the different lithographic masks for the heterostructure described in 2.3 and the finalized device.

    The particular devices used for the experiments described in this thesis feature one more characteristic: the top graphite gate is split into two, allowing us to operate the device as a *pn*-junction. This fabrication process was developed by my colleagues Jaime Díez Mérida and Andrés Díez Carlón and is detailed in Ref. [138]. This fabrication step is performed after the sample has been characterized in transport, to define the junction in the region with the best transport characteristics. However, I will succinctly describe it here as it also constitutes a process of cleanroom fabrication.

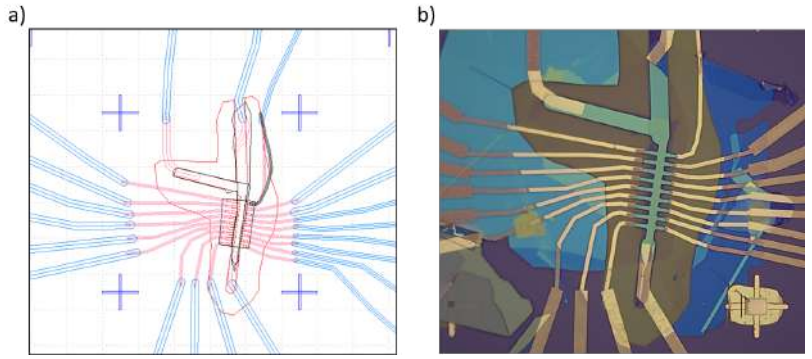

Figure 2.4: a) Lithographic masks (both etching and contact definition) for a MATBG Hall bar device. Design and visualization software is KLayout. Distance between adjacent crosses is 50 μm. b) Optical image of fabricated Hall Bar device.

13. Spin coating of the sample, with the same parameters.

14. Exposure of the lithographic mask, which consists of one (or multiple) highly aligned segments perpendicular to the Hall bar channel (parallel to the Hall bar arms). Typical widths for these segments range between 80 - 300 nm.

15. Etching of the lithographically-defined segment in the top graphite gate. In this step, the etching time must be well calibrated, as not to etch into the layers below and destroy the Hall bar. For this, measuring the thickness of the top graphite using AFM is very important.

16. Cleaning of the etched chip using acetone and IPA.

    After all these fabrication steps: 4 cycles of lithography, 3 cycles of etching and 2 cycles of metal evaporation; the double-gated MATBG Hall bar samples are prepared for transport and optoelectronic studies.

2.2 Fabrication of BSCCO-2212 heterostructures

In this section, I will describe the fabrication process for hBN-encapsulated BSCCO-2212 heterostructures. The devices should provide a good electrical contact to the superconducting 2D layer, while it remains encapsulated by a top hBN. In addition, we aim to nano-pattern the superconducting flake to restrict the supercurrent flow to a small active area, which will be used to sensitively detect near-infrared photons in our experiment.

The fabrication for these samples is more straightforward than for twisted bilayer graphene, but very challenging due to the unstable nature of the

BSCCO-2212 flakes. As described in the introduction, the superconducting properties of the material depend strongly on the hole doping (oxygen doping) in its unit cell. The entire fabrication process will be centered around avoiding sample oxidation (via oxygen out-diffusion) during the assembly and nanopatterning of the BSCCO-2212 flakes. Thus, nearly all steps of the fabrication will differ from those presented in the previous section: we will use pre-patterned metallic electrodes for contact, we will work inside an inert-atmosphere glovebox, we will use a dry-transfer method for the vdW assembly and novel non-invasive patterning method will be employed.

All these techniques are geared towards one goal: minimize the exposure of BSCCO-2212 to air or moisture and shorten the processing time between BSCCO-2212 exfoliation and device loading as much as possible. Some steps, like the contact preparation or the hBN exfoliation, can be done in advance. Once we exfoliate the BSCCO-2212 layer, we aim to fully finish our device and have it ready to load in the cryostat in 90-120 minutes. Such time constraint presents a challenge, requiring large amounts of practice in this fabrication process.

2.2.1 Development of bottom contact electrodes

We start from a silicon wafer with 285 nm of SiO_2 thickness, which is diced into large squares of 2x2 mm. Afterwards, these squares are thoroughly cleaned through strong ultrasonication in acetone, IPA and lastly DI water, 5 minutes in each of them. We optically check the removal of the resist used for wafer dicing. Using the dark field mode in the microscope helps detect any impurities. We then spin coat the square chips, using the same recipe described in the e-beam lithography of MATBG stacks. We load into the EBL system and expose the lithography mask overnight. The mask comprises a 4x4 matrix of the contact design, which will be distributed over the entire millimeter-scale chip. Such lithography is normally done on laser writers or mask aligners, since it is less time-consuming. However, photoresist polymers are known to produce more residues than, for example, PMMA resist. As these are bottom contact electrodes, the cleanliness of the substrate and the surfaces of the evaporated metals will be crucial. Therefore, we elect to use long EBL sessions (between 6-10 hours) to create 16 chips at a time. The typical design for our bottom contacts is shown in Figure 2.5a-b.

On the contact design

We use a rather simple contact design, featuring only 4 inter-digitated contacts arranged in a square. Two main design principles set this design: maximize the contact area with the BSCCO-2212 layer and maximize the number of 2-probe channels between contacts. The first principle is based on a material characteristic: as shown in Fig. 5.4a, the unit cell of BSCCO-2212 features (super)conducting planes that are sandwiched between non-conducting layers of bismuth and strontium oxide. Therefore, one can expect that electrical bottom contact may not be Ohmic and uniform, but rather tunneling-like and probabilistic. Maximizing the contact area will give us the best chance to have an area where electron tunneling is efficient and an Ohmic percolation path might be established. Furthermore, the inter-digitated shape of each electrode (Fig. 2.5a) aims to maximize the area of contact where the electrode and the BSCCO-2212 layer are not perfectly parallel. The (small) corrugations induced in the BSCCO-2212 layer sitting

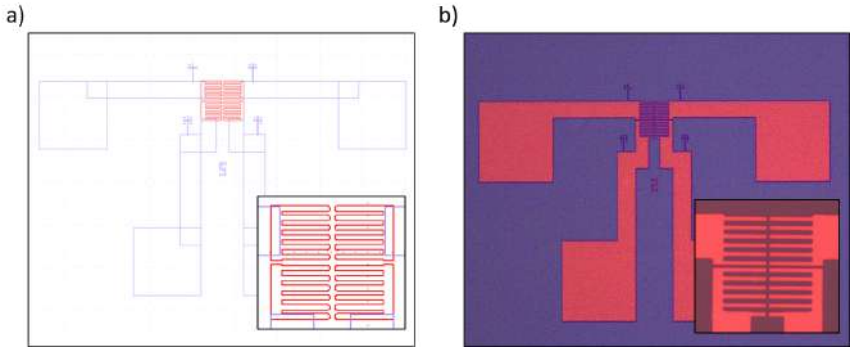

Figure 2.5: a) Design for 4-terminal electrodes for bottom contact of BSCCO-2212 heterostructures. b) Optical image of the electrodes after lift-off. Insets show the interdigitated central area.

on top of such an electrode will offer areas of contact that are not perfectly planar, but rather at an angle. In addition, the electric field lines in such electrodes under electrical bias will be strongest at the edges of the contact 'fingers', giving us the best chance to establish good electrical contact. The second principle, maximizing the number of available 2-probe channels, allows us the possibility to write multiple superconducting channels in the same flake. This is very important, as the yield of high-quality BSCCO-2212 heterostructures with high-temperature superconductivity will not be large. Furthermore, it will allow us to measure nanostructures of different lengths and widths within the same BSCCO-2212 flake. We note that the nanostructures will be written in the micron-scale gaps between the electrode

pairs, not between the 'fingers' of each electrode. The nano-patterning of the 2D flakes will be discussed in a later section.

After e-beam lithography, we develop the expose patterns using MIBK:IPA (1:3) ratio as described in the previous section. Subsequently, we use the dark field mode of the optical microscope to check for newly formed defects, areas that were not well-developed or the presence of 'fences' in the edges of the resist. Then, the chip is loaded into a Lesker evaporator, where we will deposit a Ti/Au bilayer. The titanium layer, generally 2-4 nm in thickness, helps the gold 'stick' to the silicon chip. Titanium is evaporated using e-beam evaporation. The gold layer is immediately deposited, without breaking the vacuum in the chamber. A quick transition between the two evaporation steps helps avoid the oxidation of the titanium layer into titanium oxide TiO_2.

On the characteristics of the gold film

Initially, we considered that the gold film should be very thin and extremely smooth, in analogy to the sharp and clean interfaces of 2D materials. Some effort went into developing recipes to achieve this, generally involving the deposition of 6-10 nm Au films at a very slow evaporation rate (0.3-0.5 Å/ s). We didn't find any significant correlation between low contact resistance and extremely smooth films, so we decided to use standard evaporation rates (1 Å/ s). What's more, having some small roughness of the gold film can help establish good electrical contact, as it provides the chance for non-planar contact (as discussed regarding the inter-digitated electrodes). We note here that other colleagues in ICFO did develop ultrathin and ultrasmooth gold films for different projects, not related to the bottom contact of 2D materials. Intriguingly, they found that faster evaporation rates ($\sim$ 2 Å s) tended to yield smoother gold films in this evaporator.

Regarding the thickness of the evaporated film, we eventually moved to medium thicknesses between 20 and 25 nm. Very thin films are more prone to suffer from imperfections or even have a lowered conductivity. Given the low success rate of fabricating these devices, it is not worth to risk having a bad gold film in the electrodes. Thicker gold films can create significant gaps between the stacked 2D materials and the silicon substrate, allowing for the entry of air or moisture through these gaps. We find that such medium thicknesses offer a good balance between low-dimensionality and stable metallic properties of the film.

After metal evaporation, we proceed to standard lift-off in a large beaker filled with acetone at room temperature. Leaving the chip at an angle inside the beaker (not sitting horizontally at the bottom of the beaker) can help facilitate the lift-off process. Once lift-off is completed, we thoroughly clean

the chips under ultra-sonication in a cycle of acetone, IPA and DI water. Then, we use a diamond tip cutter and pliers to divide the large chip into 16 parts, which will be the chips we use in the assembly process. After cutting, we repeat the same sonication and cleaning process, making sure that the chips don't collide into each other during sonication.

Afterwards, we inspect the 16 chips under the microscope, making sure that the metal evaporation has been successful (Fig. 2.5b). Again, the dark field mode will help us detect any significant impurities in the contacts. The electrodes must be extremely clean near the channels, as well as the lack of defects in the channels themselves. We classify the fabricated chips into different groups, namely 'perfect', 'good' and 'bad' depending on the density of defects. We preferably use only the 'perfect' chips, while the 'good' ones can be used as long as we know where the few defects are. This concludes the fabrication of pre-patterned bottom contacts for their use in hBN/BSCCO-2212 heterostructures.

2.2.2 Inert atmosphere setup for air-sensitive 2D materials

Here, we describe the glovebox setup used for the assembly of BSCCO-2212 heterostructures. Glovebox systems provide an isolated atmosphere in which one can manipulate materials which are highly sensitive to ambient conditions, as well as chemicals which are toxic or dangerous. In our case, we work inside this protected atmosphere to avoid oxidation (and loss of superconductivity) in 2D BSCCO-2212 flakes.

Description of the glovebox setup

The glovebox, shown in Figure 2.6, consists of 3 main parts: two argon-filled boxes (left and right) and one central transferring area (loadlock). The central transfer area is crucial for the operation of a glovebox, as it serves as an intermediate step between the ambient conditions outside the glovebox and the inert atmosphere inside it. It comprises two chambers (one large and one small) which can be put in vacuum conditions or flushed with argon to ambient pressure. I briefly describe here the transfer method to bring samples into the glovebox (particularly through the small loadlock).

Initially, the transfer chambers are in vacuum conditions, at around 50 mbar. One should note that for the idle status of the loadlock, the highest vacuum conditions are not always desirable, as they can impose significant strain on the silicone O-rings and reduce their lifetime.

1. To bring samples into the glovebox, we first flush the small transfer chamber with argon until reaching a pressure of 600 mbar.

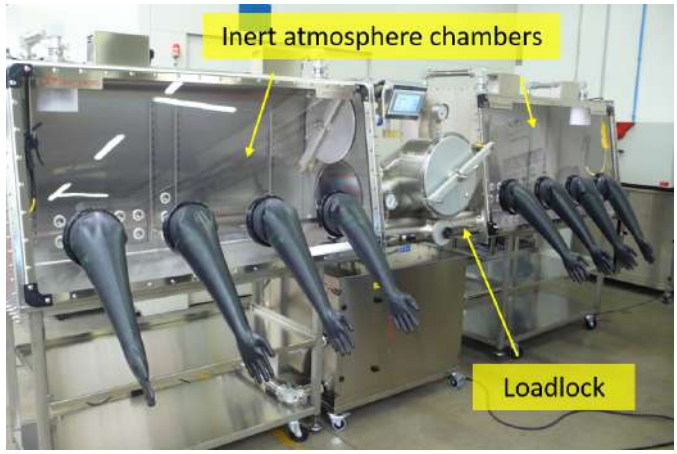

Figure 2.6: General view of the Jacomex glovebox system.

2. We subsequently pump down the chamber again down to 10 mbar.
3. Repeat this flushing/pumping cycle two more times, end with flushing, leave the chamber at ambient-pressure.
4. Open the loadlock to the ambient conditions, introduce the objects, close the loadlock.
5. Repeat the pumping/flushing cycle 3 more times, end with flushing of the chamber.
6. Open the transfer chamber from the inside of the glovebox, take out the samples, close the chamber once more.
7. Perform 2 more cycles of pumping/flushing, ending with the pumping step and leaving the chamber in ambient conditions.

To take samples out of the glovebox, we will simply repeat this process in the inverse order; always taking care to pump/flush the chamber multiple times before opening it. This glovebox system works in over-pressure mode, meaning that the argon pressure inside it is higher than the atmospheric pressure. This is clearly visible through the gloves, which stick out from the chamber to the outside. We work at 10 mmHg pressure. Thus, even in a total failure state where the loadlock is opened on both sides and connects the two atmospheres directly, no air should leak into the chamber.

Focusing on the argon-filled boxes, these feature a closed cycle of argon flow fixed at the aforementioned over-pressure value. As part of this cycle, each box features two filters that help mitigate any contamination: a high-efficiency particle-absorbing filter (HEPA) H13 open filter and an HEPA H13

+ charcoal-activated filter. The box is isolated from the environment through metal walls, a plastic screen with gloves in the front (Piercan 13800) and epoxy-filled, KF-40 flanges (used to interface connecting cables into the box) in the back. The box also includes an N_2 gun inside it and multiple shelves for storage. This glovebox system presented oxygen and water concentrations of $O_2 < 1$ppm and $H_2O < 0.5$ ppm. Lower values can be achieved if one reduces the load of instruments mounted inside the glovebox.

Here we outline and describe the work stations on the right box of the glovebox system, depicted in Figure 2.7:

1. A 4-probe, room-temperature probe station on the left side (Fig. 2.7a). It features optical imaging (through a CMOS camera), as well as 4 micro-manipulators that control tungsten tips for contact with the bonding pads in the pre-patterned chips. These 4 electrodes are interfaced with a lock-in amplifier outside the glovebox, used to measure the 2-probe and 4-probe resistance across different contact pairs.

2. An exfoliation and storage station in the center (Fig. 2.7b). It includes a plastic container, whose top surface is as working surface, storage for all the air-sensitive 2D materials, basic tools and consumables for the exfoliation and a hot plate for pre-baking of the pre-patterned chips.

3. A custom transfer stage on the right side, which will be described next.

4. Outside the glovebox, a work station with PC, mouse, keyboard, joysticks and multiple adjustable screens

The custom transfer stage, pictured in Figure 2.8, comprises the same main elements as the transfer used outside the glovebox for the assembly of graphene devices: an microscope column, a sample stage and a stamping stage. This transfer stage features 3 long-working-distance Mitutoyo objectives (2x, 10x, 50x) mounted on a wheel for their (automated) exchange. The entire microscope column can be actuated (electronically) in the Z direction to adjust the focus. White light illumination is also provided through the microscope column. The images are captured by an Amscope CMOS camera and monitored live via PC.

The sample stage features 2 Newport micro-manipulators for movement in the XY direction. Unlike the previously described transfer stage, the sample stage is manual. This stage also includes a heater/thermometer combination for control of the stage temperature; as well as a vacuum chuck to fixate the chips during transfer. Lastly, the sample stage includes a rotation stage without a Vernier scale.

Lastly, the stamping stage features coarse horizontal movement along one direction (it's mounted on a rail). Tilt control with respect to the XY

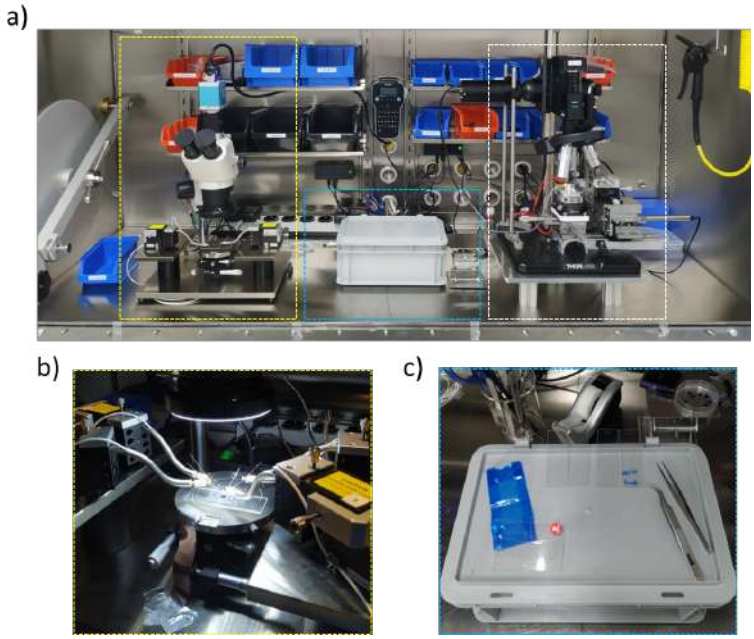

Figure 2.7: a) Overview of the right chamber of the glovebox. Dashed lines highlight the 3 main work stations in the chamber. b) Device testing with the 4-terminal probe station. c) Exfoliation station.

plane and the Z direction is provided by Thorlabs micro-manipulators; as well as automated Z control through a Newport micro-manipulator. Overall,

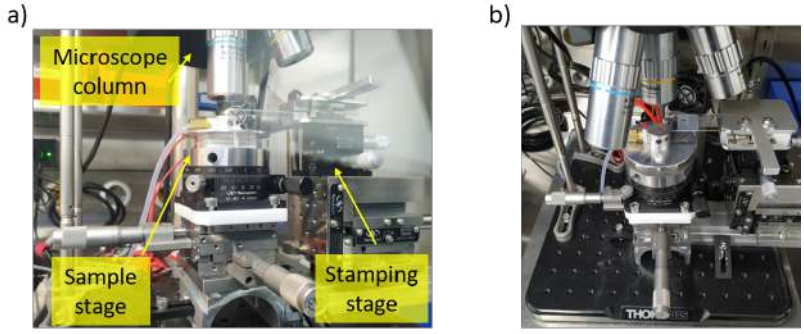

Figure 2.8: a) Main stages of the glovebox transfer stage. b) Top view of the transfer stage.

this transfer stage is well-suited for the manual control of most parameters (placement of the substrate, coarse movement of the stamp stage, lateral alignment and tilt control), except those which require fine control: Z

movement of the stamping stage and adjustment of the focal plane. This tool allows an experienced user to minimize the processing time during vdW assembly of unstable 2D materials[149].

2.2.3 Exfoliation and stacking methodology for BSCCO-2212 heterostructures in an inert atmosphere

For the fabrication of hBN/BSCCO-2212 heterostructures, some steps must be performed in advance to shorten the processing time once the BSCCO-2212 flakes are exfoliated.

Polymer stamps

The polymer stamps are prepared beforehand. As we want to avoid chemical post-processing of the samples, we avoid using PC (which requires removal with chloroform). Instead, we use the dry-transfer technique using PDMS stamps. We combine two types of PDMS: thick, high-retention PDMS film for structural support and thin, low-retention PDMS film to minimize the residues on the flake. A typical stamp, prepared on a glass slide, features a thick PDMS square of 1x1 cm and a smaller thin PDMS square (5-7 mm each side) in the center of the thick PDMS. We will prepare two sets of PDMS stamps, one will be used for exfoliation of hBN in ambient conditions and the other set will be saved for BSCCO-2212 flakes once we are ready to exfoliate them. For this second set, one should keep the topmost protection layer of the thin PDMS square until the last moment.

hBN exfoliation

Before exfoliating BSCCO-2212 and assembling the heterostructure, we exfoliate hBN on multiple PDMS stamps. The stamps should be optically inspected for flakes with large size (it should fully cover the BSCCO-2212 layer, of which we want to maximize the area for electrical contact) and thicknesses between 10 and 30 nm (Fig. 2.9). Unlike the case of MATBG, hBN flakes with non-uniform thicknesses can be used for encapsulation of BSCCO-2212 (see 2.9d). The main bottleneck will be the large size of the target flakes, ideally larger than 70x70 μm. The exfoliation technique with PDMS stamps is the same for hBN and BSCCO-2212, and will be described shortly after.

In order to shorten the processing time of the stacking process, one should thoroughly classify all the viable hBN flakes in each PDMS stamp; labeling them and indicating where they appear on the stamp (center, top right, bottom left, etc...) and their dimensions. This will save us significant time once: once we identify a good BSCCO-2212 flake, we can measure its

dimensions, check this index of hBN flakes and quickly prepare the hBN stamp for encapsulation. Once we have prepared sufficient PDMS stamps with viable hBN flakes, we load them into the glovebox and we proceed with the exfoliation and stacking of BSCCO-2212. Figure 2.9 shows some exemplary good hBN flakes exfoliated on PDMS.

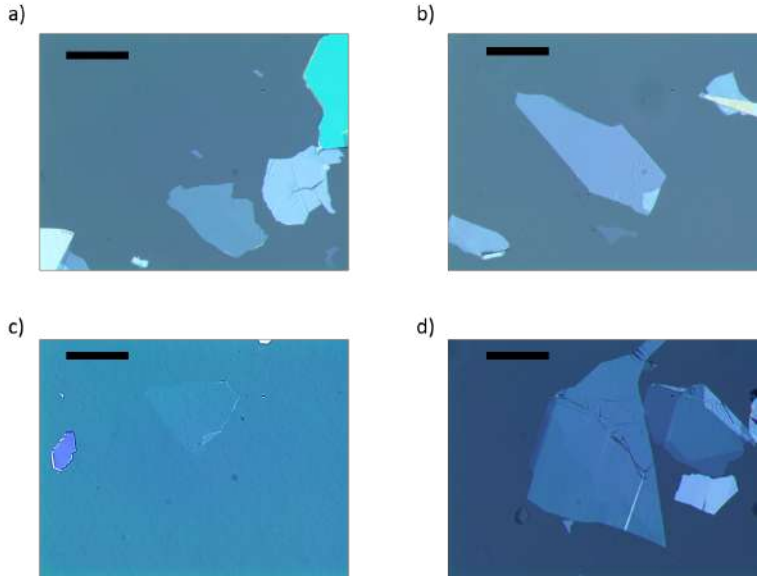

Figure 2.9: Viable hBN flakes for the top encapsulation of BSCCO-2212. (a) and (b) have medium thickness but their size and uniformity is good. (c) is a very thin hBN flake ($\sim$ 4-6 nm) and (d) is a very large, inhomogeneous flake. The lower left area of the flake (rectangle-shaped) is viable for encapsulation. The scale bar in all images corresponds to 75 μm.

BSCCO-2212 exfoliation

Now inside the glovebox, we exfoliate the bulk BSCCO-2212 crystal (of shiny black color) onto a clean, uniform piece of scotch tape. As we aim to obtain large BSCCO-2212 flakes, we will not exfoliate this scotch tape many times. Depending on the thickness of the crystal in the 'mother' tape, one should exfoliate this tape onto itself (without repeating the same area) between 3-5 times. Although hard to explain, we aim to see regions of silver-ish color in the tape; often still connected to darker BSCCO-2212 regions. For the repeated tape-on-tape exfoliation, a medium speed and force is advisable, if the exfoliation is too slow there will be very low transfer, while very rapid exfoliation will strain or break the 2D layers. Once we find a suitable area of the tape, one should quickly take a clean PDMS stamp

(whose cover we have removed shortly before BSCCO-2212 exfoliation) and make contact with the tape. We press the stamp onto the target area with our fingers by pushing on the glass slide. Here, one should again use a medium force, enough to ensure complete and uniform contact. Afterwards, one should flip the tape and glass slide, leaving the non-adhesive side of the tape facing up and the glass slide below. We proceed to exfoliate the tape away from the PDMS stamp, hopefully leaving good BSCCO-2212 flakes in the stamp. This step is of paramount importance, yet hardly tractable. I found the best yield using the procedure outlined below:

1. We place the glass slide + scotch tape combination as mentioned above.

2. Using the not dominant hand (left hand for me), we hold the glass slide on its opposite side.

3. Using the other hand, we grab the scotch tape by the bottom left corner (bottom right if left-handed). Also, if possible, we keep some pressure on the flake area by pressing on the glass slide using the not dominant hand.

4. We now switfly detach the tape from the PDMS stamp, following a diagonal trajectory (from bottom left corner of the tape towards upper right corner). Along with the diagonal trajectory, one should pull the tape up as it moves from left to right, i.e. the hand should end higher than it started. Lastly, the speed of this exfoliation should be relatively fast. I think a good way to indicate the speed is 75 % of the maximum speed you could use to detach the tape. All in all, the tape is detached from the PDMS diagonally (the wavefront of contact is not parallel to the edge of the PDMS stamp) and the user's hand performs a swift movement. This movement is, in my experience, the key to reliable exfoliation of large, relatively thin BSCCO-2212 flakes. I believe it's best described as a whip-like movement.

5. We inspect by eye the PDMS stamp, where a significant portion of the BSCCO-2212 crystal should have been transferred. If done correctly, other areas of the tape should remain untouched and can be used for further exfoliations onto PDMS stamps. One can now turn to the search of suitable flakes in the microscope.

Identification of BSCCO-2212 flakes

We now mount the glass slide on the stamping stage. Unlike the MATBG process, we will mount the glass slide with the PDMS surface pointing up, towards the microscope. This will facilitate flake identification, as one can

focus directly on this surface without passing through other focal planes. We also place the pre-patterned chip on the sample stage, off-centered, to have a uniform SiO_2 background while looking for flakes.

As mentioned before, once we exfoliate the BSCCO-2212 layers, the process must be optimized to save time and avoid degradation. Fastest flake identification involves: (1) rapid scanning of the PDMS stamp at 2x magnification to identify the area with the highest flake density, (2) inspection of the resulting flakes at 10x magnification, moving from one corner of the stamp to the opposite corner, (3) closer look at 50x on potentially viable BSCCO-2212 flakes and (4) precise measurement of the dimensions of the flake at 10x or 50x magnification. Ideally, for sub-centimeter exfoliation areas, one would fully check the stamp within 5 minutes. Figure 2.10 shows

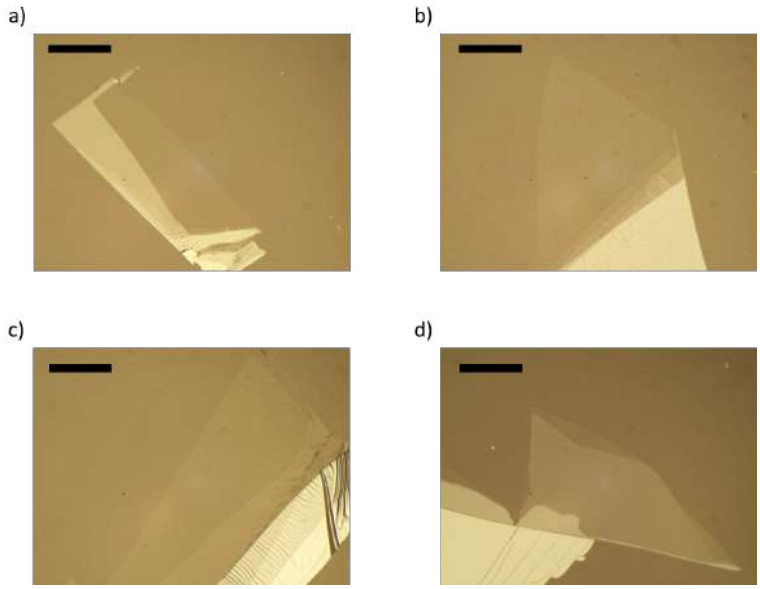

Figure 2.10: a) Bilayer ($\sim$ 3 nm) BSCCO-2212 flake, attached to a thicker surrounding flake. b) Trilayer ($\sim$ 4.5 nm) BSCCO-2212 flake. This flake could be easily detached from the surrounding thicker flakes. c) 4-layer ($\sim$ 6 nm) BSCCO-2212 flake. d) BSCCO-2212 flake of medium thickness ($\sim$ 15-18 nm). The scale bars in (a) and (d) represent 50 μm. The scale bars in (b) and (c) represent 75 μm.

exemplary BSCCO-2212 flakes that may be used in our heterostructures. As mentioned before, we want flakes to be large (not excessively, as hBN must fully cover it), uniform and relatively thin (10 layers or below). The optical contrast of the flakes will not necessarily scale linearly with the number of layers, but a solid intuition can be developed by measuring different flakes with an AFM. For each flake on Figure 2.10, we include an approximate (or known) thickness, so as to help the reader build this intuition.

Importantly, AFM cutting of the BSCCO-2212 flakes is not viable in this fabrication process. First, they sit on top a flexible substrate which difficults making straight, clean cuts. Second, the BSCCO-2212 flakes are thicker than the graphene flakes we cut using this technique. Therefore, it is likely for the AFM tip to rip or fold the BSCCO-2212 flakes, instead of cutting them. Nevertheless, this doesn't imply that one cannot use a good, thin flake attached to a larger, thicker BSCCO-2212 flake (see Fig. 2.13). One can play with the angle of approach and the tilt of the stamping stage to separate the 2 areas by selectively dropping only one of them on the chip. This process requires practice and does not guarantee 100 % success rate, but is surprisingly useful. Furthermore, even if a large surrounding area of BSCCO-2212 is not covered by hBN, the protected area can remain protected. However, the larger BSCCO-2212 area must not short the electrodes. As a last resort, it could be cut using an AFM tip or the tungsten tips of the probe station after encapsulation.

Dry-transfer process

The transfer process[148] is described here for the BSCCO-2212 flakes, although the procedure will be largely identical for the hBN flake. The temperature is not varied, both transfers take place at room temperature. Controlling the wavefront evolution through the angle and speed of contact, as well as the direction of contact will enable us to achieve clean dry-transfers. In Figures 2.11, 2.12 we show the sequential assembly of a clean BSCCO-2212/hBN heterostructure. Also, in Figures 2.13, 2.14 we demonstrate the fabrication process for another heterostructure based on thinner flakes.

1. Flip the glass slide, making the PDMS stamp face downwards, towards the silicon chip. Center the PDMS stamp under the white light spot.

2. Go to the focal plane of the chip and move the sample stage to center the electrodes in the optical image. The microscope objective should be fixed at 10x in the following.

3. Depending on the shape of the flake, and its position within the PDMS stamp, choose the direction of contact. If the flake is located near one edge of the stamp, it's often advisable to approach from the opposite side, to avoid possible sudden, uncontrolled contact.

4. Staying on the focal plane of the chip, lower the stamp stage coarsely. At this stage, the separation between stamp and substrate should be macroscopically large, so one can monitor this step with the naked eye.

5. Once the stamp and the chip are close, stop lowering the stamp and search for the focal plane of the lowest PDMS surface (that which hosts the flakes and will touch the chip).

6. Scan the stamp to locate the chosen flake. Double check its position and orientation, rotating the chip if necessary to achieve the desired wavefront direction.

7. The final step of the approach is quite sensitive. One must play around with the Z control of the stamp and the focus of the microscope to identify the relative distance between stamp and chip. The best way to do it is to focus on the chip, then go slightly off-focus in the direction of the stamp's focal plane. Then, slowly lower the stamp until the flakes come into focus.

8. Repeat this process sequentially until both focal planes nearly coincide.

9. In the focal plane of the chip, align the BSCCO-2212 flake with the inter-digitated electrodes, trying to maximize the contact area equally across the 4 electrodes.

10. Switch to 2x and slowly lower the stamp. Observe the formation of the wavefront, confirming that the contact takes place along the desired direction.

11. Switching back to 10x, check the alignment between electrodes and flake and continue to lower the stamp. Check that the wavefront evolves smoothly as it approaches the flake.

12. Transfer the BSCCO-2212 flakes onto the electrodes. In the case of the inter-digitated electrodes, it's advisable to align the wavefront parallel to the long dimension of the 'fingers'. This will minimize the formation of bubbles or excessive strain on the flake.

13. Once the entire flake is in contact with the electrodes, start peeling back the PDMS slowly. Both when transferring and peeling, the first contact of the wavefront with the flake edge is crucial and will determine the success of the process. If this first contact is not smooth, it's worth retracting the wavefront and adjusting its angle (through the tilt control in the stamping stage).

14. Peel back the PDMS over the BSCCO-2212 flake, which should remain on focus if successfully transferred onto the electrodes.

15. Raise the stamp stage to fully detach the PDMS stamp from the chip surface.

16. Remove the glass slide from the stamping stage, adjust the focus and capture images of the transferred flake.

17. Repeat this process for the hBN flake, making sure that the BSCCO-2212 flake is fully encapsulated. Capture images of the finalized stack.

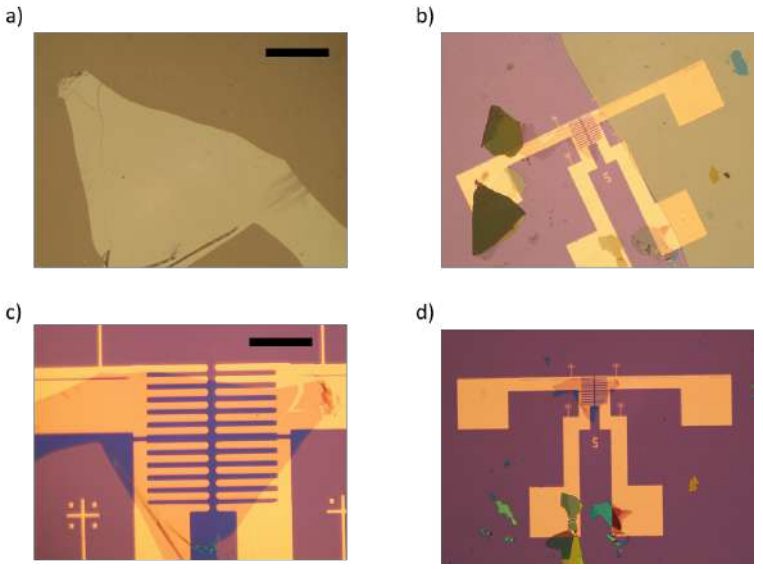

Figure 2.11: a) Exfoliated BSCCO-2212 flake of thickness d = 16.5 nm. b) Stacking of the flake depicted in (a). Note that the thicker, opaque flakes are not in contact with the substrate. c) Optical image of the dropped BSCCO-2212 flake. d) General view of the device after BSCCO-2212 stacking. The scale bars in (a) and (c) correspond to 50 μm

Isolating thin BSCCO-2212 flakes from 'bulk' areas

One final note on this process involves the aforementioned separation of thin flakes from 'bulk' connected flakes. Two strategies are possible here. First, if the thin and 'bulk' parts are separated by a clear boundary, one can try to stack the latter on an empty area of the chip, or just in an empty silicon chip. It's important to stop the wavefront after the thick flake is fully contacted, but before the thin flake makes contact. If the two areas are connected, a riskier (but faster) process must be employed. This process is depicted in Fig. 2.13, as well as the encapsulation of that same flake in Fig. 2.14. We follow the same procedure described above, but this time we stop the wavefront precisely at the boundary between the two flakes. Here, the thin flake will be pressed onto the electrodes while the thicker part is not.

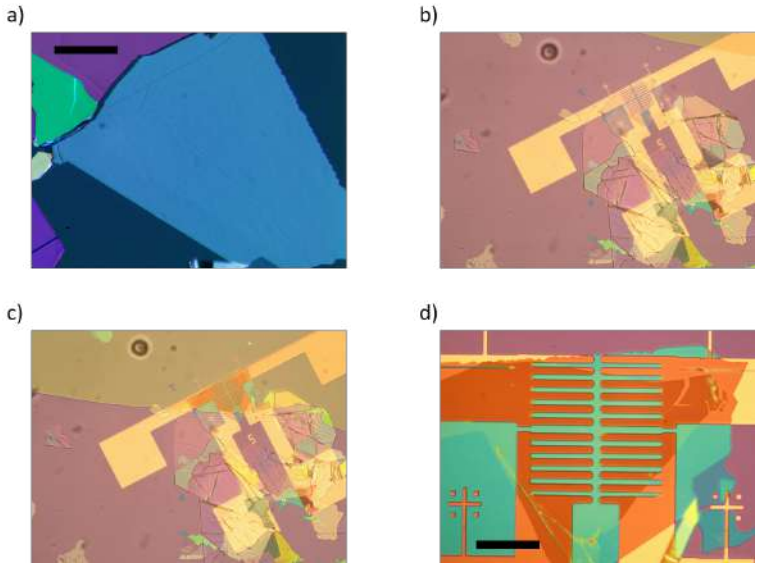

Figure 2.12: a)Exfoliated hBN flake used for top encapsulation of the device shown in 2.10. b) Approaching wavefront for the stacking of the hBN flake. In most of the images, the PDMS and substrate are not in contact. c) Stacking of the hBN flake. The greenish color signifies the contact between PDMS and the substrate. We selectively stop the wavefront at the boundary between the target flake and the surrounding, thicker hBN flakes. d) Optical image of the BSCCO-2212/hBN heterostructure right after assembly. The scale bars in (a) and (d) correspond to 50 μm

Aligning the wavefront exactly along this boundary line between the two flakes can be challenging, but can be achieved by careful adjustment of the tilt control. Once the wavefront is aligned, we transfer very slowly up to the precise boundary. If the 'terrace' at the boundary is high enough (see Fig 2.13a), the wavefront will tend to stay put unless we press down further. At this point, we can move back and forth the tilt controls around their original position, helping the wavefront fill out this boundary line. Finally, we peel back the PDMS, leaving the thin BSCCO-2212 flake on the electrodes while the thick flake remains on the PDMS.

Device pre-characterization and vacuum storage

After repeating the transfer process for both BSCCO-2212 and hBN, our superconducting BSCCO-2212 heterostructure is finalized. Before transferring it out of the glovebox, we can use the probe station to pre-characterize the device. In short, we measure the 2-probe resistance across all electrode combinations, as well as the 4-probe resistance of the flake. At this stage,

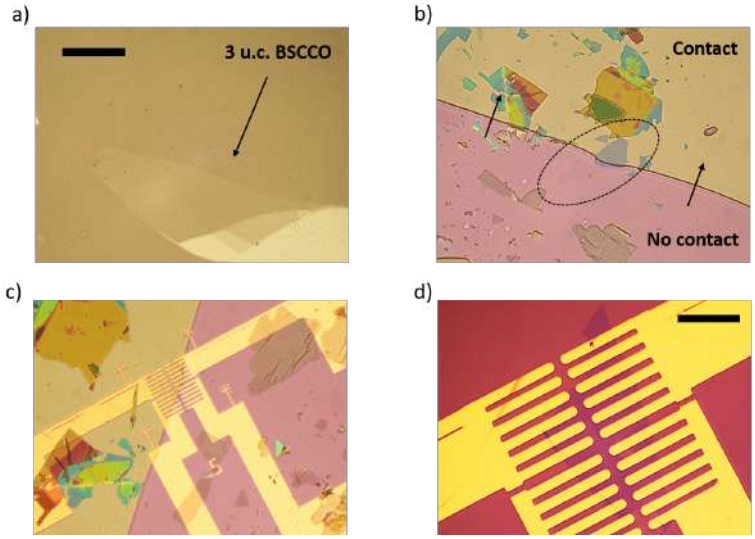

Figure 2.13: a) Optical image of a 3-unit cell thick BSCCO-2212 flake. b) Stacking of thicker flakes directly connected to the target, thin flake. This is done directly on the final chip but away from the metalized areas, taking care not to contact the electrodes. c) Re-stacking of the thin flake onto the electrodes. d) Optical image of the re-stacked thin BSCCO-2212 flake. Some cracks can be observed in the flake surface, due to the strain applied during the stacking of the thicker flakes. The scale bars in (a) and (d) correspond to 50 μm

we don't aim to precisely quantify the contact resistance, as one can do that in the cryostat. Instead, the goal is to discriminate between bad devices (for which we should not continue with the next fabrication steps) and good, promising devices. We contact the bonding pads in the chip using the tungsten probes.

A good device will show 2-probe resistances below 10-20 kΩ and 4-probe resistances in the order of 100 Ω. Of course, these quantities may vary depending on the quality and area of the electrical contact. On the other hand, bad devices will yield 2-probe resistances between 100 kΩ and few MΩ and should be discarded. In the case of ultrathin flakes (4 or fewer layers), 2-probe resistances in the order of 100 kΩ may not imply that there is no electrical contact. However, in our experience, even if the flake is superconducting, these resistance values indicate that the resulting nano-structured device won't be usable, as one cannot properly operate a zero-resistance device over a huge contact resistance. Also note that once the device is cooled down in the cryostat, the contact resistance will increase.

We can now transfer the vdW heterostructure out of the glovebox, for the final step of nanofabrication. Even though the BSCCO-2212 flake is

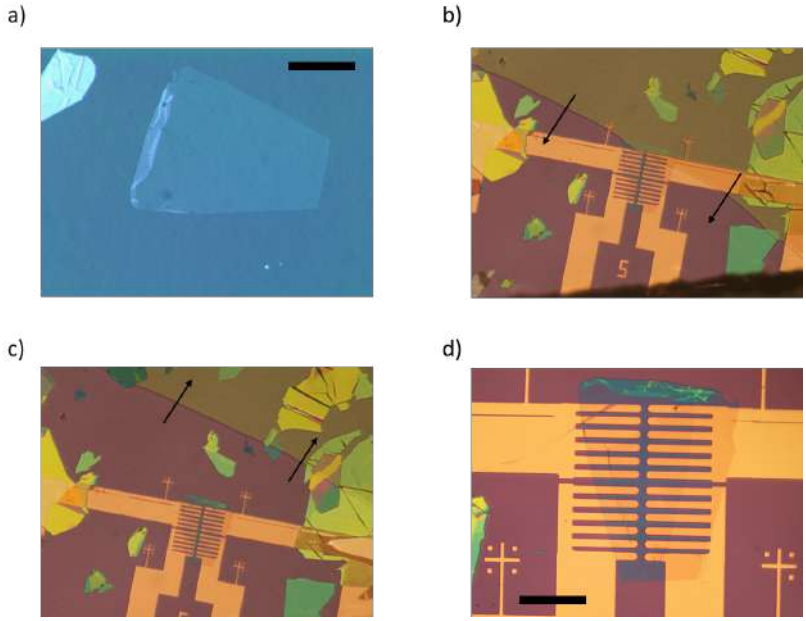

Figure 2.14: a) Thin hBN flake used for top encapsulation of the device shown in Fig. 2.13. b) Stacking of the hBN flake, wavefront approaching the target area. c) Stacking of the hBN flake, wavefront receding from the target area, leaving behind the hBN flake on the substrate. d) Optical image of the finalized BSCCO-2212/hBN heterostructure. The scale bars in (a) and (d) correspond to 50 μm

encapsulated with hBN, it's reccommendable to use a vacuum container to bring the sample out of the glovebox. We use a small vacuum desiccator (Pelco SEM stub desiccator), which we pump down inside the glovebox. Finally, we take the vacuum container out of the glovebox.

2.2.4 Non-invasive nanopatterning of air-sensitive 2D materials using a Helium Focused Ion Beam

Challenges in BSCCO-2212 nanofabrication

Fabricating practical superconducting devices often relies on the creation of a region with reduced dimensionality or weakened superconductivity. Whether it's a Josephson junction, where the tunneling across the weak link depends on the phase of the superconducting condensate; or a superconducting sensor, where one leverages the sharp phase transition between the superconducting and normal states. In the case of thin film, low T_C superconductors, micro- and nano-patterning can be achieved using conventional fabrication techniques as those described in the cleanroom fabrication of MATBG samples. These include lithography, etching and metal evaporation

processes.

However, the patterning of BSCCO-2212 (and cuprate superconductors in general) presents a major challenge[151]. On the one hand, the high critical temperature of cuprates also implies very large values of superconducting critical current density J_C and critical magnetic field H_C. Thus, a non-patterned piece of BSCCO-2212 cannot be biased at its superconducting phase boundary in practical conditions. On the other hand, due to their chemical instability, conventional cleanroom processing is not viable as the material would be exposed to air, moisture and any number of chemicals. Thus, alternative fabrication methods are required to create high quality, nano-patterned BSCCO-2212 areas that can be used as, for example, quantum sensors[145].

The helium Focused Ion Beam

First developed in 2009[152–154], the helium ion microscope appeared as an alternative to other scanning microscopy technologies, such as the scanning electron microscope (SEM) or the field ion microscope (FIM). The achievable resolution in all these systems depends on the volume of interaction between the beam and sample. While SEM systems can provide tightly focused beams, the interaction between the electron beam and the sample is generally weak. Conversely, FIM systems based on heavy ions (most notably Ga^+ and Ne^+) offer large beam-sample interactions but are rather invasive: they induce significant atom sputtering and ion implantation. As a middle ground, the He Focused Ion Beam (He-FIB) can provide a highly focused beam with larger interaction strength than the electron beam, while being comparatively non-perturbative, thanks to the very low mass of the He^+ ions[154, 155]. The He-FIB combines both high depth of field and high-resolution imaging, while most scanning microscope systems must face a trade-off between the two.

Here, we will briefly describe the main components of the He-FIB (Zeiss Orion NanoFab) and its working principle. However, our focus will remain on its operating procedure and how one can use it to create high-quality BSCCO-2212 nanostructures without breaking encapsulation. The He-FIB system comprises three main parts: a high vacuum chamber with a 5-axis motorized sample stage, a field ion source column (with He^+ and Ne^+) and a secondary electron detector. An additional electron flood gun will counteract the charging effect. During the processing, the sample stage is fixed, the ion beam is scanned using electromagnetic lenses and deflectors and the secondary electron detector (like in an SEM) will provide the necessary imaging.

The He-FIB is centered around a gas field ion source, in which He atoms

are ionized at the tip of a tungsten needle and then extracted using a large voltage difference to create a focused He^+ ion beam. To create a well-defined narrow beam, the tungsten needle is thinned at its tip down to the formation of a trimer (3 single tungsten atoms arranged in a triangular shape). The large voltage applied at the trimer will ionize the He atoms and create an extremely narrow beam. The beam is further controlled through multiple electrostatic lenses and deflectors before reaching the sample. The basic structure of the SEM and an image of the tungsten trimer are shown in Fig. 2.15. Once the focused beam reaches the sample surface, its interaction

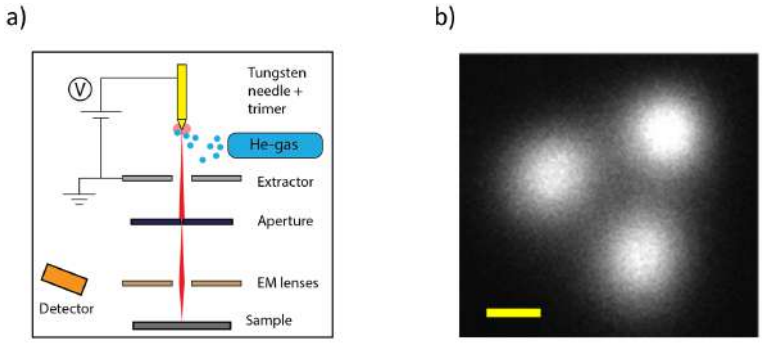

Figure 2.15: a) Schematic representation of the He-FIB system. Helium atoms are ionized at the tip of the needle by the large electric field between the needle and the extractor plates. Then, the He-ion beam is scanned and focused onto the sample using electrostatic lenses. A detector for secondary electrons provides the sample imaging. b) Image of the atomic trimer at the tip of the needle. The yellow scale bar corresponds to 0.25 nm.

will have 4 main effects: (1) the generation of secondary electrons, (2) the sputtering of atoms from the sample surface, (3) the implantation of He^+ ions and (4) amorphization of the irradiated sample. Compared to heavy ions FIB's, the He-FIB will have a significantly reduced sputtering rate ($\sim$ 50 times lower) and sputtering radius (about 2 nm). This enables high-resolution, low-damage writing of nanostructures. Furthermore, the implantation of He^+ ions occurs at a much larger depth, away from the sample's surface (about 500 nm for 30 keV), as the light He^+ ions have a much lower stopping range than the heavier Ga^+ ions (see Fig. 2.16). The properties of the He-FIB set it as an ideal tool for the non-invasive nanopatterning of air-sensitive heterostructures. The combination of low sputter rate, high-depth beam-sample interaction and implantation at large depths (see Fig. 2.16b-c) will allow us to irradiate the BSCCO-2212 flake without milling the encapsulating hBN layer. Importantly, the implanted ions will lie deep in the silicon chip. Furthermore, the high resolution enables the direct writing of patterns in the nanometer range. In 2015, Cybart *et*

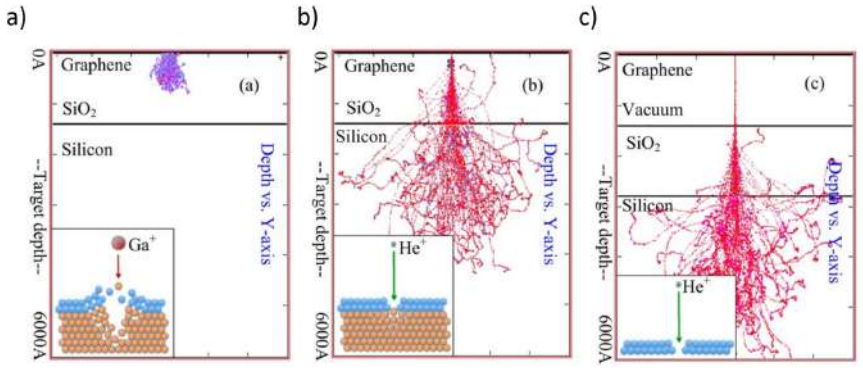

Figure 2.16: a) Simulation for the trajectories of incident Ga^+ ions onto a graphene layer on a Si/SiO_2 substrate. b) Simulation for the trajectories of incident He^+ ions onto a graphene layer on a Si/SiO_2 substrate. Compared to (a), the lateral size of the irradiated region is much smaller in the first few nanometers (where the active layer lies). Furthermore, the ions are implanted tens of nanometers deep into the chip, away from the graphene layer. c) Simulation for the trajectories of incident Ga^+ ions onto a suspended graphene layer. The back-scattering of ions from the substrate is strongly reduced, and the irradiation profile is extremely sharp in the active layer. For all panels, the ions are accelerated using 30 kV. Figure adapted from Ref. [155]

al demonstrated the local suppression of superconductivity in YBCO thin films using the He-FIB[156, 157]. The beam-sample interaction of the He^+ ion beam led to local amorphization of the YBCO crystal structure and allowed the direct writing of non-superconducting regions[158]. Using this technique, they demonstrated various HTS nanodevices directly written onto thin films[156–166]. Although the beam-sample interaction is not perfectly understood, the high-energy He^+ ions are believed to scatter off oxygen atoms, kicking them out of the unit cell and changing the local doping level. Since then, multiple groups have used this technique to pattern cuprates, including through an encapsulating layer[167, 168].

Process workflow

We aim to directly nano-pattern the hBN/BSCCO-2212 heterostructures by locally modifying the oxygen doping in the BSCCO-2212 layer without breaking the hBN encapsulation. One important note is that we cannot perform standard imaging of the sample. As in e-beam lithography, imaging the sample will expose it to the beam and affect its properties (here there's no resist, but BSCCO-2212 would be irradiated). Furthermore, as the He^+ are charged, the sample must be grounded to avoid charge accumulation and/or a discharge that would destroy the sample. This will also have

implications on the imaging and dose testing of the samples.

We describe here the exact process flow we employ:

1. Remove the sample from the vacuum container, mount it on an SEM stub and glue it using silver paste.
2. Connect the bonding pads and the stub using wire bonds to ensure the sample is grounded.
3. Load the SEM stub into the He-FIB through its loadlock.
4. Pump down the chamber and turn on the He^+ source (keep it blocked).
5. Move the beam to one of the edges of the chip, do a quick focus calibration.
6. Reduce the field of view and move towards the center of the chip.
7. Identify the big features on the chip (alignment marks or bonding pads).
8. Rotate the sample accordingly, to align the horizontal and vertical features of the electrode design at the XY directions of the software.
9. Carefully navigate, with a reduced field of view, to the alignment marks close to the inter-digitated contacts. Large scans should be done with the beam blocked.
10. Align with all the 4 marks.
11. Introduce the coordinates for the alignment marks in the patterning software. Check the optical image of the device to confirm the relative position of the BSCCO-2212 flake.
12. Navigate to one of the alignment marks, adjust focal distance and optical aberrations.
13. Navigate to a BSCCO-2212 area away from the center of the electrodes with the beam blocked.
14. Open the beam and perform dose testing (detailed in the next paragraph).
15. Once the right dose is chosen, load the design of the pattern and align it in the software relative to the alignment marks.
16. Navigate to the center of the active area (beam blocked) and start the patterning process.

17. Once finished, start unloading the sample. Take out from the vacuum chamber.

18. Remove the wire bonds and the silver paste from the SEM stub.

19. Glue the chip to a conventional 28-pin chip carrier using silver paste. Store in vacuum container.

20. With a long-working distance optical microscope, check that the patterning was successful.

Dose testing protocol

Dose testing is crucial to select the optimal dose for the patterning process. The optimal dose is the minimum dose needed to turn the irradiated BSCCO-2212 area insulating. Higher doses will increase the lateral size of the patterned features and increase the risk of damaging the encapsulating layer. We describe here a dose testing protocol, developed by my colleague Paul B. Seifert, to find the optimal dose *in situ* for the target BSCCO-2212 flake. Such *in situ* dose tests are very powerful, as they remove the variables of BSCCO-2212 thickness, hBN thickness or overall changes in the He-FIB system from day to day.

At the dose test stage of the process workflow (steps 13 and 14 above), one should navigate the tool to a BSCCO-2212 area away from the designed patterns. Importantly, the target area should have the same cross-section as the area where we will pattern. Therefore, it must be a region where the hBN-covered BSCCO-2212 does not lie on top of the metallic contacts. Both laters must also have the same thickness as in the area we will pattern. The dose test will occupy a small area, so this region does not need to be very large.

The dose testing procedure is based on the charging of the sample under ion irradiation. When the sample remains conductive, the added charge from the impinging ions will be compensated, as the flake is grounded through the SEM stub. Then, the hBN/BSCCO-2212 region will appear bright under the imaging system (which captures secondary electrons from the surface). However, if the sample becomes electrically isolated from the ground, the charging cannot be compensated and it will eventually charge positively. Then, no secondary electrons will be generated in this region, yielding a dark contrast in the imaging system. Our goal will be to write a closed pattern with a given dose. If the lines closing that pattern become insulating, the enclosed area (which has not been irradiated) will become disconnected and appear dark (see Figure 2.17). Generally, we fix both the ion energy (at 30 keV) and the emission current (between 2-5 pA) and calibrate the ion dose

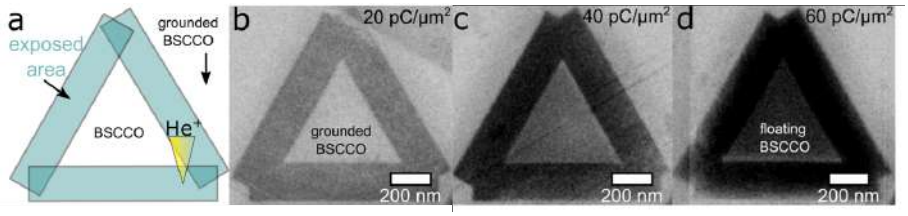

Figure 2.17: a) Schematic representation of the dose test process. b) Secondary electron image from the testing triangle for a low dose, the interior remains grounded. c) Secondary electron image for another triangle at higher dose, still not enough to isolate the central part. d) Secondary electron image of a triangle for an optimal dose, where the central area shows dark contrast, signaling it has been electrically isolated from the surroundings.

through the number of repetitions of the beam exposure. We proceed to write the dose test structure, which is a simple triangle shape. The width and shape of the lines forming the triangle should be representative of the pattern we aim to write later on. We write 3 identical triangles of increasing ion dose and then image them. Imaging should be done in a single snapshot, not continuously, so as to minimize the sample exposure. Figure 2.17 depicts such a dose test procedure for typical doses, between 10 and 100 pC/μm^{-2}. Once we identify the lowest dose for which the center region becomes dark, we can continue with the patterning process. Keep in mind that at low temperatures, one expects the irradiated lines to become more insulating.

Nanopattern designs

The He-FIB patterning software allows the user to write any pattern based on polygons and/or round shapes. We aim to define constrictions in which the supercurrent flow will be confined. These constrictions will have widths between 50 and 300 nm, while their length varies between two different designs: a rounded nanochannel and a meandering nanowire.

The rounded nanochannel (see Figs. 2.18a 2.19a) features long, straight segments which act as barriers for the supercurrent, and small ellipses separated by nanometric distances which define the device's active area. Thus, the nanochannels have short lengths (approximately 1-3 microns) and very narrow widths. Importantly, the rounded shape of the channel helps avoid current crowding effects that would limit the critical current of the device.

In Figure 2.19b-c we show an AFM image of one He-FIB patterned nanochannel, as well as a linecut of the sample's topography. The He-FIB patterning induces minor changes in the sample topography. The regions thaat have been irradiated appear as 'dips' in the surface with depths of

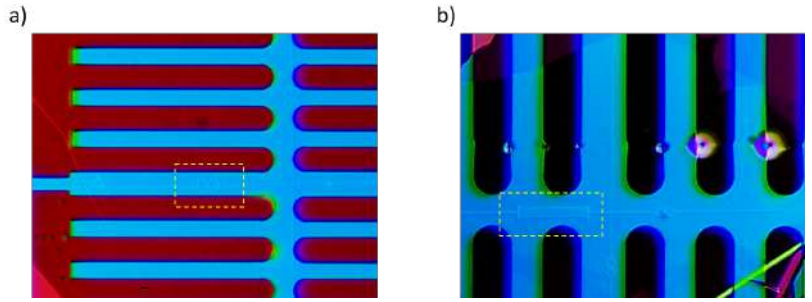

Figure 2.18: a) Optical image of He-FIB patterned nanochannels in a BSCCO-2212/hBN heterostructure. One of them is highlighted by the dashed yellow box. Also visible on the left side are the dose-testing triangles. b) Optical image of HE-FIB patterned meandering nanowire (highlighted by the dashed yellow box) and nanochannels in the same heterostructure. For both (a) and (b), the width of the gap where the patterns are written is 5 μm.

$\sim$ 4-5 nm. Crucially, the thickness of the encapsulating hBN layer is much larger, around 20 nm. Therefore, we conclude that this patterning method can simultaneously modify the properties of the underlying BSCCO-2212 layer and preserve the encapsulating hBN layer.

The meandering nanowire, widely utilized in commercial nanowire photodetectors, is based on a narrow, straight segment that meanders in a maze-like shape. It offers the advantage of larger active area compared to the nanochannels, but is much more prone to defects that will block the supercurrent flow along the meander. The total length of the nanowire is much larger (up to hundreds of microns) and its width is sub-micron scale, as one needs to pack multiple of these nanowires between the electrodes.

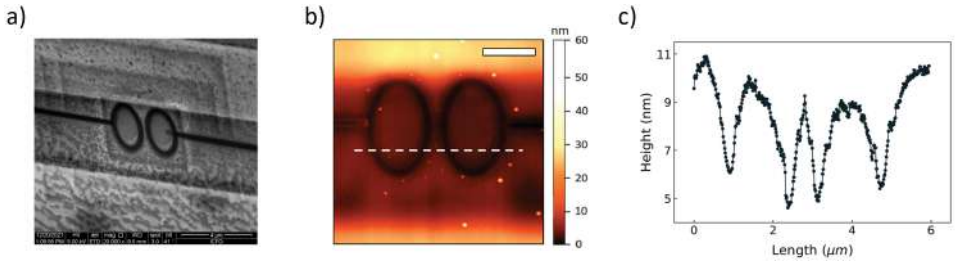

Figure 2.19: a) SEM image of a 250 nm wide BSCCO-2212 nanochannel. b) Topographic map of the nanochannel pictured in (a). The white scale bar corresponds to 2 μm. c) Height profile along the dashed line in (b). The irradiated areas show a decrease in height of $\sim$ 4-5 nm, much smaller than the hBN thickness ($\sim$ 20 nm)

In our experience, we find the nanochannels to be much more reliable and convenient. The meanders exhibit more current crowding effects and

are more sensitive to defects. Their main advantage, a larger device area, is not a crucial aspect of these proof-of-concept devices. In addition, the hugely increased normal state resistance of the long nanowire can hinder the operation of such a device.

Challenges in He-FIB nanopatterning

All in all, the He-FIB tool acted as a double edged sword in our projects. On the one hand, it's a remarkably powerful tool for a variety of applications and it's perfectly suited for the nanopatterning of encapsulated BSCCO-2212 devices. For 2D cuprate devices, the next best options after the He-FIB (which some groups have explored) are markedly worse than this technology. Perhaps this project could not have been possible without having access to the He-FIB tool, of which only a few exist in the world.

On the other hand, as the He-FIB is a young technology it also suffers from its novelty. Often, the system can be non-operative due to some unknown error which requires a technician's visit. This is not particularly uncommon, but the novelty of the technology also implies that the manufacturing company (and its technicians) are not nearly as experienced with the He-FIB as they are with, for example, a standard SEM. Thus, during my PhD work, this system was down for more than a year with no real timeline or prospects of fixing it. In this case, the use of a cutting-edge technique did cut both ways.

2.3 Transport measurements

The focus of the experiments described in this doctoral work resides in the optoelectronic measurements of different vdW heterostructures based on correlated 2D materials. It does not lie in the low-temperature transport study of their electric or magnetoelectric properties. However, all samples were characterized in transport, as their transport properties will inform the optoelectronic studies (about the underlying electronic ground state we want to optically probe, or about how to optimally bias a superconducting sensor). I will outline here the different setups used to characterize the devices in transport and describe the central technique behind these transport measurements.

Measurement setups

These are the different setups used to perform transport experiments:

- Room-temperature, ambient-pressure probe station located inside the

inert atmosphere setup, used to pre-characterize the electrical contact to the BSCCO-2212 heterostructures.

- Room-temperature, vacuum probe station used to pre-characterize the MATBG Hall bar samples.

- Variable temperature insert cryostat (ICEOxford) with a base temperature of 1.55 K and an 8 Tesla magnet. Samples can be mounted in the insert probe oriented perpendicularly or parallely to the magnetic field. Cooling power is attained through a circulating flow of He^4. To cool below 4 K, He^4 is pumped to reduce its vapor pressure, which allows further cooling down to 1.55 K.

- Dilution refrigerator (BlueFors) with base temperature of 35 mK and an 8 Tesla magnet. 2 samples can be mounted simultaneously perpendicular to the magnetic field. In addition, one can use an alternative mount, compatible with fiber optics for low-temperature optoelectronic measurements. However, there are no scanning capabilities for the optical mount. Down to $\sim$ 1 K, the cooldown procedure relies on the pumping of He^4. Below 1 K, further cooldown is achieved through a mixture of two helium isotopes: He^4 (of bosonic character) and He^3 (of fermionic character). This mixture will be separated into two phases, differentiated by the density of He^3. The two phases will be separated by a phase boundary, which can be leveraged to achieve higher cooling power and reach T $\sim$ 35 mK.

- Optical cryostat (Attodry 800) with free space optical access and base temperature of 6 K. In the sample space, a 3-axis piezoelectric stage enables spatial scanning of the sample. The system is anchored to an optical table. It features connections for 20 DC lines and 4 RF lines. Cooling power is attained thanks to a circulating flow of He^4 that reaches a so-called 'cold finger' in which the sample is mounted. This system will be described further in the next section.

For the MATBG *pn*-junctions, we generally pre-characterize them in the vacuum probe station and study their transport properties in both the ICEOxford and BlueFors systems. For the BSCCO-2212 superconducting devices, we pre-characterize them in the inert-atmosphere probe station and then use the Attodry system to measure their transport properties.

The basic toolkit for the transport measurements in these projects comprises DC transport and the low-frequency AC lock-in technique. DC biasing is used to gate the devices and/or pass large currents; while the low-frequency AC signals allow us to efficiently isolate the desired signal from a noisy environment, as we will describe next.

Low-frequency AC lock-in technique

This technique is based on the concept of homodyne detection. The main tool that enables these measurements is called the lock-in amplifier. An excitation signal of amplitude R and phase ϕ is generated at a given (low) frequency f_0 and fed to the sample. We are interested in the sample's response to this particular excitation, even if other biases or inputs (at different frequencies) are being applied at the same time. These include both extrinsic effects (environmental noise) and intrinsic, physical effects (which are not caused by our excitation). Then, the response from the sample is collected and demodulated with the reference local oscillator (at f_0) that was used to generate the excitation. The lock-in amplifier will demodulate the signal at its input (with all the frequencies present in the response) by frequency downconversion. Essentially, it will electronically mix the reference and input signal (let's say it contains two frequencies f_0 and f_1) and downconvert to the new, demodulated frequencies $f_0' = f_0 - f_0$ and $f_1' = f_1 - f_0$. It will then integrate all the demodulated signals over a time window much longer than $1/f_0$. The first frequency component, which we are interested in, is now downconverted to a DC signal, while the 'spurious' component remains at a finite frequency f_1'. Then, a low pass filter is applied to the demodulated signals and the response at DC is retrieved. In this way, one can isolate the response of the sample to the applied excitation, increasing the signal-to-noise ratio in the experiment. The signal obtained through this method is described in terms of its amplitude R, phase ϕ and quadratures (in-phase and out-of-phase components) X and Y, which are related according to:

$$\begin{aligned} R &= \sqrt{X^2 + Y^2} \\ \phi &= \arctan\left(\frac{Y}{X}\right) \end{aligned} \tag{2.1}$$

In these transport measurements, the excitation frequency is set by the lock-in amplifier and usually lies in the range between 15 Hz and 30 Hz. However, in the optoelectronic measurements, this same technique can be applied to isolate the optical response of the device to the laser excitation. There, we use an optical chopper to modulate the laser beam and use its reference frequency to electronically read out the device response using the lock-in amplifier. Both demodulation strategies can be done simultaneously (in separate lock-in amplifiers). The modulation of the laser beam is generally performed at higher frequencies (100-300 Hz). The optical chopper and further demodulation strategies in the optoelectronic measurements are described in the next section.

2.4 Optoelectronic techniques

In this section, I will describe the optical setup and measurement techniques employed in the optoelectronic studies comprised in this thesis. The main goal of the free space optical setup is the excitation and imaging (through the collection of reflected light) of the samples. The optical setup is schematically represented in Fig. 2.20. We choose to work at telecom wavelength ($\lambda = 1550$ nm) because of its technological relevance. In addition to the near-infrared optics, we utilize white light imaging for coarse imaging and positioning of the samples. We will describe the different parts of the optical setup in a self-contained manner, stating their purpose and optical elements.

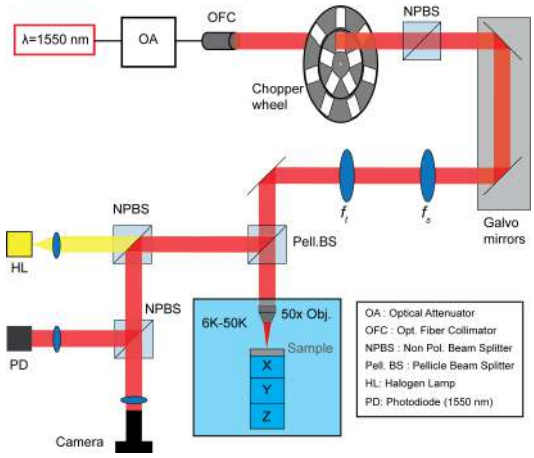

Figure 2.20: General schematic of the optoelectronic setup for telecom wavelength used in this thesis. Each part of the optical path is detailed in the following subsections. All symbols are specified in the legend.

2.4.1 Description of the optical setup

Generation and modulation of near-infrared light

In our optoelectronic experiments, we mostly employ two different continuous-wave (CW) near-infrared laser sources. Namely, a fibre-coupled diode laser (Thorlabs SFL1550P, $\lambda = 1550$ nm) with 40 mW maximum output power and a fibre-coupled, tunable laser source (Thorlabs TLX1, $\lambda = 1528$ - 1566 nm) with 100 mW maximum output power. The tunable laser source features an internal variable output attenuator to maintain constant output power. The non-tunable laser source will be used for most scanning photovoltage studies, while the tunable laser is mostly used for the

photomixing measurements. Other laser sources, such as a pulsed 1550 nm laser or a CW 640 nm laser were use only occasionally.

We describe the optical setup based on scanning photovoltage measurements. The non-tunable, CW laser source is fibre-coupled into a programmable optical attenuator (JGR OA1) and is then out-coupled to free space using a fiber mount with a collimation package. A half-wave plate (Thorlabs WPMH05M) is placed right after to set the polarization axis of the laser beam parallel to the optical table. The collimated laser spot at this stage is approximately 2 mm in diameter. Then, the laser beam is modulated through a dual-slot (5:7) optical chopper (Thorlabs MC2F57B). The laser beam is modulated through the inner slot of the optical chopper. The outer slot will be used for the modulation of the laser beam from the tunable source. The beam then goes through a 50:50 broadband beam splitter (Thorlabs

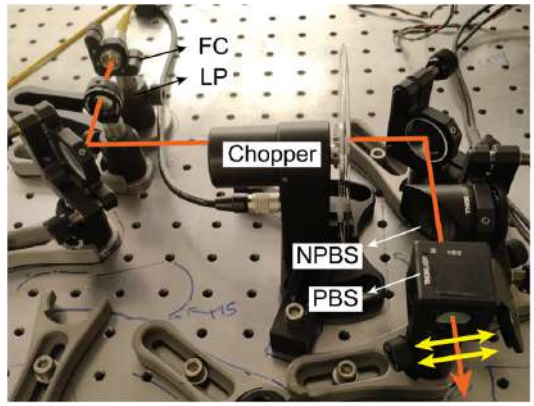

Figure 2.21: a) Modulation stage of the optical path. The laser is coupled to free space through a fiber collimator (FC) and a linear polarizer (LP) and is then modulated in the inner slot of the chopper wheel. Then, the laser beam passes through two different beam splitters, a non-polarizing beam splitter (NPBS) and a polarizing beam splitter (PBS). Afterwards, the beam propagates towards the scanning galvo mirrors.

BSW12) and then a polarizing beam splitter (Thorlabs CCM5-PBS204). These elements are not crucial for the single-laser photovoltage scanning measurements but are central to the laser mixing we will describe in a later section. We select the output corresponding to the in-plane polarization and direct it towards the 2D galvanic mirror scanning system. The other outputs for both the beam splitters are blocked using threaded SM1 caps. The optics for modulation are pictured in Fig. 2.21.

Scanning the laser beam

Accurate scanning photovoltage (or photocurrent) measurements on mesoscale and nanoscale samples rely on the use of a reliable, precise and repeatable scanning system. Often, the system of choice is the 2D galvanometer, based on 2 electronically-drive mirrors in the X and Y planes which deflect the input laser beam to scan the laser spot at the sample plane. However, along a long optical path a small change in the deflection angle from the 2 mirrors will result in very drastic displacement of the laser spot in the sample plane. Therefore, the 2D galvanometer scanning system requires the use of a proper microscopy system. Figure 2.22 depicts the optical path of the scanning microscope system. We use two plano-convex lenses with

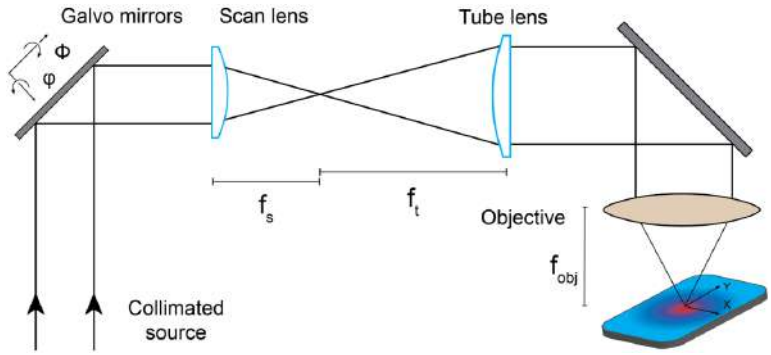

Figure 2.22: Sketch of the optical path for scanning objective microscopy. Through the appropriate choice of the 'scan' and 'tube' lenses and the objective, small displacements of the galvo mirrors can be translated into small displacements in the focus plane of the objective. Here, f_s, f_t and f_{obj} correspond to the focal lengths of the scan lens, tube lens and objective, respectively.

long focal distances to construct the 'scan' and 'tube' lens system. The 'scan' lens has focal length $f_s = 150$ mm and the 'tube' lens has focal length $f_t = 750$ mm. The scanning microscope includes also the objective used to focus onto the sample, with a focal distance of $f_{obj} = 5$ mm.

The 'scan' lens is placed at the output of the galvanic mirrors, with its planar face facing the mirrors. As the laser input is collimated at the planar face, the laser beam will be maximally focused by this lens at a distance f_s. The beam will start diverging for distances larger than f_s. The 'tube' lens is also aligned with the output of the scanning mirrors, at a distance $f_s + f_t = 900$ mm from the first lens. The convex face of the 'tube' lens faces the 'scan' lens and the scanning mirrors. Thus, the diverging laser beam will be collected by the 'tube' lens and be collimated at its output. Now, the laser beam has been expanded and has an approximate diameter of 5.5 mm. Lastly, the distance between the 'tube' lens and the sample must be

approximately $f_s + f_{obj} \sim 755$ mm to complete the scanning microscope.

This configuration enables us to finely scan the sample surface through small angular deflections of the scanning mirrors. Furthermore, we have expanded the laser spot so as to fill the aperture of the objective and maximize the coupling (in and out) efficiency. A wheel with different neutral density filters is also placed between the 'scan' and 'tube' lenses.

Coupling into the sample space

After the scanning optics, the laser beam is coupled into the sample space. Crucially, the input aperture of the cryostat's shroud is placed on the top. Therefore, we must direct the beam upwards, out of the plane of the optical table. The large focal length of the 'tube' lens gives us some distance to maneuver and manipulate the laser path.

Figure 2.23a depicts the optics used to couple the laser beam into the cryostat's objective. After the 'tube' lens, two consecutive silver mirrors re-direct the beam towards the sample space. The beam is transmitted through a non-polarizing pellicle 92:8 beam splitter (BP208). As it features a single surface, the pellicle beam splitter will minimize ghosting effects in the optics. Then, we use two 45° kinematic cage mounts (Thorlabs KCB1) placed on a vertical pole to deflect the beam upwards and then horizontally again at the target height ($\sim$ 20 cm). Laser alignment is critical in this part of the optical path, as taking the laser beam in the vertical direction makes the alignment procedure harder and more dangerous. At this point, the laser beam is parallel to the optical table, albeit at a larger height, and reaches a 45° on a silver mirror placed on a Gimbal mount (Thorlabs KC45D) just above the cryostat's optical aperture. A motorized rotation mount (Thorlabs K10CR1) is used in conjunction with a quarter-wave plate to control the beam's polarization. The optical aperture of the cryostat features a ZnSe window that blocks most of the visible spectrum. Lastly, a long working-distance, apochromatic 50x objective (Olympus LCPLN50XIR) with numerical aperture NA = 0.64 is mounted inside the shroud of the cryostat (see Fig. 2.23b) and focuses the incident collimated light onto a laser spot of $\sim$ 2 μm. Its focal distance is $\sim$ 5 mm. We use a standard Ge power meter (Thorlabs S122C) placed right before the Gimbal mount mirrors to measure the input optical power.

Collection of reflected near-infrared light

Collecting the near-infrared light reflected from the sample's surface is vital for the correct alignment and focusing of the micron-sized laser spot along the millimeter-scale chip. The reflected light from the surfaces at the

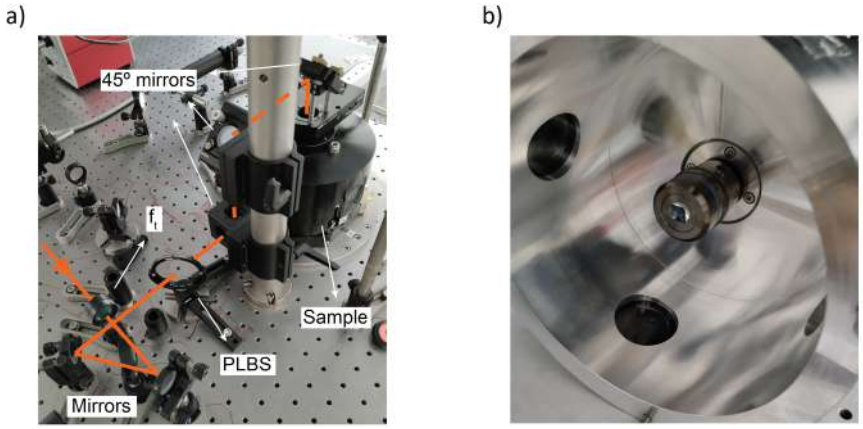

Figure 2.23: a) Optical path for the incident laser beam into the sample space. First optical element in the path is the tube lens (f_t). Afterwards, the bea is re-directed using two mirrors, then passes through a pellicle beam splitter (PLBS) and reaches the vertically-aligned 45° mirrors. Lastly, the beam is to the objective's aperture and to the sample space using a final 45° mirror. b) Image of the objective mounted on the inside of the cryostat's shroud.

focal plane will be out-coupled from the cryostat along the same 'input' optical path, reaching the cage-mounted mirrors and being translated back to the plane of the optical table. Then, the reflected light will be reflected on the pellicle beam splitter (the input beam is being transmitted through it) and re-directed. The reflected beam is transmitted (without any deflection) through a dichroic mirror (Thorlabs DMLP100) and then is focused onto a Ge photodiode (Thorlabs SM05PD6) using a convex lens of focal length $f =$ 50 mm. The photodiode has small active area, so we place it on a kinematic mount and optimize its position. Figure 2.24 depicts the optical path for the reflected near-infrared light, as well as a device image captured by the Ge photodiode.

White light imaging

In addition to the described optical setup for excitation and imaging using near-infrared light, we use a white light source to image the samples. This allows us to pre-align and pre-focus the active area of the chip in a simple and fast way, using a standard CMOS camera. The white light optics follow the same general principes as for near-infrared light, where the pellicle beam splitter enables the coupling of white light in and out of the sample space.

Figure 2.25a shows the excitation and reflection optical paths for white light imaging. The output from a white light fibre-coupled source (Thorlabs

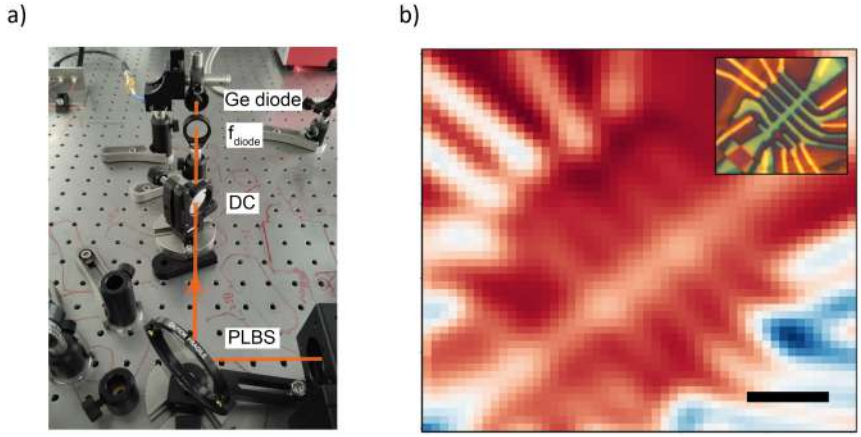

Figure 2.24: a) Optical path for the reflected near-infrared light. After reflecting off the pellicle beam splitter (PLBS), the beam is transmitted through a dichroic mirror (DC) and focused using a lens $f_{diode} = 50$ mm onto the Ge photodiode . b) Reflectivity map of a Hall bar device, captured by scanning the laser beam across the sample and collecting the photodiode intensity. Inset shows an optical image of the same device. The scale bar represents 5 μm.

OSL2) is collimated (inside a tube mount) and then diffused using a piece of translucent scotch tape. The white light beam is then re-directed using the dichroic mirror (which reflects light at optical wavelengths) into the pellicle beam splitter and into the sample space. The reflected light is out-coupled from the sample space, transmitted through the pellicle beam splitter and routed towards a CMOS camera (Thorlabs DCC1645C). The reflected white light hits one of the mirrors used for the in-coupling of the near-infrared light and then an additional mirror which is mounted on a 90^{o} flip mount. Thus, white light imaging requires the flipping of this mirror, which intercepts the optical path for near-infrared excitation. Therefore, it its not possible (also not generally desirable) to perform the scanning photovoltage experiment and the white light imaging simultaneously.

On an additional note, the white light beam is only approximately collimated. Then, in order to form an image of the sample space in our camera, we have to mount a convex lens so that the optical system (lens + camera) is focused at infinity. Placed inside a tube mount, in order to block stray light, we tune the distance between lens and camera to focus an image from 'collimated' light rays. To do this, one should use the optical system to image a distant object. We used the cross at the top of a nearby church to find the infinity-focused distance between lens and camera, obtaining the image shown in the inset of Fig. 2.25b.

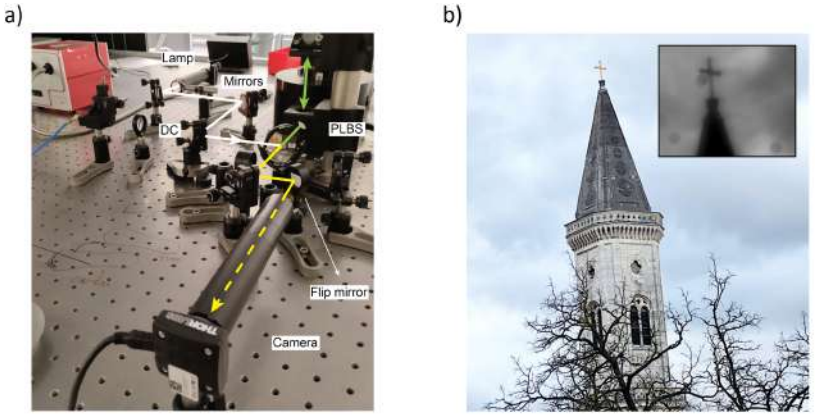

Figure 2.25: a) Optical path for white light input (white line) and imaging (yellow). The white light from the lamp is reflected off the dichroic mirror (DC) and is then coupled in through the pellicle beam splitter (PLBS). On the reflectivity or imaging path, an additional mirror on a 90° flip mount couples the light into the CMOS camera. b) Photograph of nearby church, approximately 200 meters away. Inset shows the infinity-focused image of the church's cross.

2.4.2 Scanning photovoltage measurements

Here we shortly describe the workflow for the scanning photovoltage measurements.

1. Open the cryostat shroud and load the chip carrier or printed circuit board onto the sample space. The piezo stack should not be extended during the loading process to avoid mechanical stress. All electrical connections must be grounded.

2. After loading, close the cryostat shroud and start the cooling down procedure.

3. Turn on the white light source, flip the 90° mount up and start the camera software.

4. Using the white light image, pre-align and pre-focus the chip using the XYZ piezoelectrics on which the sample is mounted. This position will change at cryogenic temperatures, but the pre-alignment will help us find the sample once the system is cold.

5. Once the system reaches base temperature, repeat the alignment and focus the white light image. Afterwards, turn off the fiber illuminator and flip down the 90° mirror mount.

6. Turn on the near-infrared laser and wait for the output power to stabilize (10-30 mins). At this stage, we want to use a high laser power (few mW) and zero or low attenuation. Turn on the optical chopper and reference the lock-in amplifiers to the rotation speed of the inner slot.

7. Read out the Ge photodiode signal from the reflected laser light and perform a coarse reflectivity map using the scanning mirrors. The signal is read out using the lock-in amplifier at the reference frequency of the inner slot of the optical chopper.

8. Identify the key areas of the active area and center it using the XY sample piezos.

9. Improve the focus using knife-edge measurements. Identify a straight , easy-to-resolve feature in the sample and scan the laser perpendicular to the straight edge. Repeat this process while adjusting the Z position of the sample until obtaining the optimal resolution of said feature.

10. Repeat a coarse map and a finer map of the region of interest.

11. Perform the scanning photovoltage measurement by appropriately biasing the optoelectronic device.

2.4.3 Optics for CW photomixing measurements

In addition to the scanning photovoltage measurements, we also use this optical setup to study time-resolved dynamics of the response of the devices. Instead of using pump-probe techniques with very short laser pulses, we perform photomixing between two CW lasers with slight wavelength detuning[169]. Such laser mixing will create an optical beating, analogous to those used in for example in radiofrequency IQ mixers. The envelope frequency of the optical beating will effectively modulate the laser field at very high frequency (few THz), which can be controlled by tuning the wavelength difference between the CW lasers. The laser mixing is implemented at the first stage for laser coupling and modulation. Figure 2.26 shows the modified optical setup for photomixing experiments. A second optical fibre is free space-coupled using a collimation package and passes through an acousto-optic modulator. This modulator can be used to control the power of the beam, as well as generating higher harmonic of the signal. After the modulator, a polarizer sets the beam's polarization to be parallel to that of the other beam (in the XY plane). Then, the laser beam from the tunable source passes through the outer slot of the optical chopper and incides on the the broadband beam splitter.

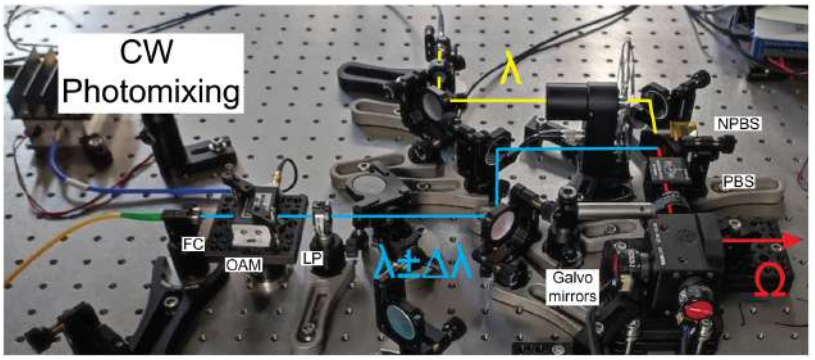

Figure 2.26: Optical path for laser mixing. The second laser (blue line) is coupled-in using a fiber collimator (FC), passes through an acousto-optic modulator (OAM) that can be used to control the beam's intensity, and then through a linear polarizer (LP). Lastly, the laser beam is mixed with the first one (yellow) at the non-polarizing beam splitter (NPBS) and the photomixed signal is then polarized by the polarizing beam splitter (PBS). After the scanning galvo mirrors, the mixed laser signal (red) and the two individual laser beams will follow the optical path described above.

Here, the two laser beams are mixed, as the original laser beam at $\lambda =$ 1550 nm is being transmitted through the beam splitter and the beam at $\lambda =$ 1550 nm $\pm$ $\Delta\lambda$ is being reflected off it. After the beam splitter, the two laser excitations will follow the same optical path and produce the aforementioned optical beating. It's important to maximize the overlap between the two laser spots in the broadband beam splitter, to optimize the photomixing process. From this point on, the optical path and measurement procedure will be identical as described above.

After laser mixing, an optical beating is created, whose envelope frequency is given by the heterodyne difference frequency $\Omega = 2\pi c(\lambda_1^{-1} - \lambda_2^{-1})$ will produce a new component in the device response. Studying the response to the excitation at frequency Ω as a function of the envelope frequency will enable us to gain information on the dynamics of the photoresponse[169]. This response can be isolated by demodulating the device response at the difference frequency between the inner and outer slots of the optical chopper. In the next chapter, we will describe further how one can access the time-dynamics of the device response using the CW photomixing technique.

Chapter 3

Heavy fermion physics in the thermoelectric transport of MATBG

In this chapter, we present an experimental investigation of thermoelectricity in the flat bands of MATBG and illustrate how the observed anomalous response sheds light in the multi-orbital nature of the flat bands. First, we introduce the Seebeck effect, which governs the thermoelectric response in our experiment. We illustrate how thermoelectric transport constitutes a sensitive probe into the electronic structure of condensed matter systems. We then highlight the emergence of particle-hole asymmetry in the MATBG flat bands and introduce the topological heavy fermion (THF) mapping of the system. Next, we present the experiment, based on the measurement of the photo-thermoelectric (PTE) effect on a gate-defined MATBG *pn*-junction, where we observe an anomalous thermoelectric response at integer fillings in two different temperature regimes. Lastly, we discuss the theoretical understanding of our observations in the framework of the THF model.

3.1 Seebeck effect

The Seebeck effect describes the electric field generated in a material subjected to a thermal gradient, arising from the diffusion of charge carriers at the Fermi level from the hot side to the cold side[170, 171](Fig. 3.1). This thermoelectric effect is parametrized by the Seebeck coefficient S, which generally depends on the charge and dispersion of the majority carriers.

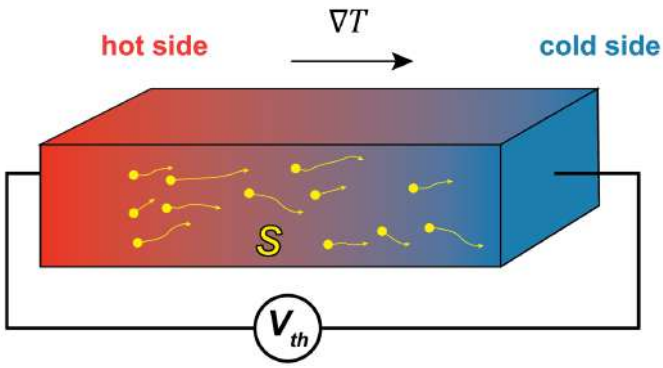

Figure 3.1: Schematic of the Seebeck effect. An electric field develops due to the thermal diffusion of charge carriers from the hot to the cold side of the device.

The thermoelectric voltage appearing between the hot and cold sides of the sample is given by:

$$V = S\Delta T \tag{3.1}$$

, where ΔT is the temperature difference between the hot and cold ends. This expression is valid in the 'linear' regime, where $\Delta T << T$. In our experiment, the sample temperature is $T = 10$ K and the temperature difference is in the range of $\Delta T \leq 1$ K. Thus, we restrict the discussion and the presented results to the linear heating regime.

The Seebeck coefficient depends on the electronic spectrum of the material via its general conductivity function $\sigma(\mu, E)$, according to the Mott relations:

$$\sigma(\mu) = \int_{\infty}^{\infty} dE \, (\frac{\partial n_F(E)}{\partial E}) \, \sigma(\mu, E) \approx \sigma(\mu, 0) \tag{3.2}$$

$$\sigma(\mu)S(\mu) = \int_{\infty}^{\infty} dE \, (\frac{\partial n_F(E)}{\partial E}) \, E \, \sigma(\mu, E) \approx -\frac{\pi^2 T}{3e} \frac{\partial \sigma(\mu, E)}{\partial E}\bigg|_{E=0} \tag{3.3}$$

,where $\sigma(\mu)$ and $S(\mu)$ are the electrical conductivity and Seebeck coefficient at chemical potential μ, e is the electron charge, n_F is the Fermi-Dirac distribution and $\sigma(\mu, E)$ is the general conductivity function. The last approximation corresponds to the Sommerfeld expansion for low temperatures.

The Mott relations establish a complex relation between the Seebeck coefficient S and the general conductivity function $\sigma(\mu, E)$. Therefore, S encodes information about the dispersion of the low-energy charge carriers, as well as the microscopic processes involved in charge transport[172, 173]. At the zeroth order, the sign of S reveals whether electrons or holes dominate transport, via the energy derivative of the Fermi-Dirac distribution ($\frac{\partial n_F(E)}{\partial E}$).

We note that the general conductivity function $\sigma(\mu, E)$ (often not accessible in experiments) will generally depend on the density of states (DoS),

the group velocity of the carriers v_g and their transport lifetime τ (inverse of scattering rate). For a general quadratic band, DoS and v_g are connected by the band's effective mass m^* or bandwidth κ. As we will show, the intricate relation between S and $\sigma(\mu, E)$ can be leveraged to investigate the electronic structure of correlated systems through their thermoelectric transport. It is particularly relevant to study the Seebeck coefficient in semimetals, in systems where multiple bands contribute to transport or near singular points of the Fermi surface.

Given the complexity of the general Mott relations, the Seebeck coefficient is often modeled in its uncorrelated, semiclassical limit. The Seebeck coefficient for a degenerate Fermi gas in the semiclassical limit (no correlations, slowly varying DoS, etc...) is given by the so-called semiclassical Mott formula[174]:

$$S = -\frac{\pi^2 k_b^2 T}{3|e|} \frac{1}{G} \frac{dG}{dV_g} \frac{dV_g}{dE}\bigg|_{E=E_F} \tag{3.4}$$

, where G is the sample conductance and V_g is the applied gate voltage. Note that the use of conductance instead of conductivity only leads to a prefactor dependent on the sample's geometry.

This simple formula, which depends on the (experimentally accessible) conductance G and the DoS, works well for a multitude of systems and conditions. For instance, it can adequately describe the Seebeck coefficient of monolayer graphene[175, 176] (see Figure 3.2a), where S changes sign across charge-neutrality, reflecting the ambipolar transport along the Dirac cones. Furthermore, S vanishes at the Dirac point, where the DoS is zero and the sample's resistance peaks (inset of Figure 3.2a). From the semiclassical Mott formula, one can associate extrema of resistance with zero Seebeck coefficient as $S \propto \frac{dG}{dV_g}$.

In addition to the Seebeck effect, one may also study transversal thermoelectric transport in the presence of an out-of-plane magnetic field, described by the Nernst effect[177]. Figure 3.2b depicts the (photo-)Nersnt effect in monolayer graphene, where a transverse charge current is generated due to the longitudinal thermal gradient and the aforementioned magnetic field. Photocurrents with opposite signs develop in the transverse direction due to an opposite Lorentz force for thermally diffusing electrons and holes[177, 178].

3.1.1 Seebeck coefficient as a probe of the electronic spectrum

As the Seebeck coefficient maps the general conductivity function $\sigma(\mu, E)$, it can serve as an indicator for deviations from single-particle electronic transport, Indeed, thermoelectric transport in strongly-correlated systems often reveals violations of the semiclassical Mott formula[172]. Unconventional

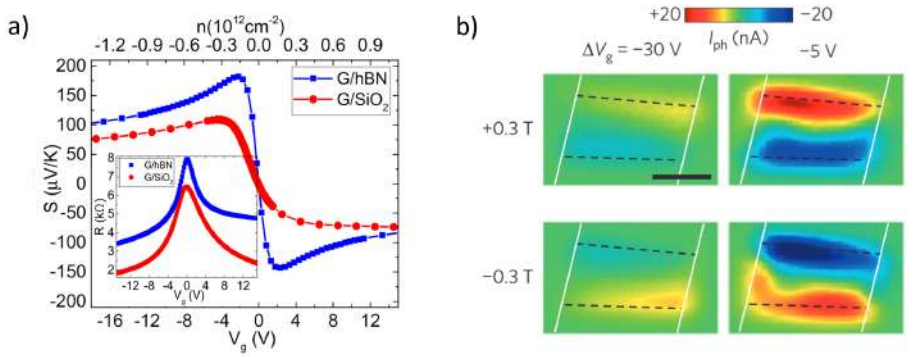

Figure 3.2: a) Seebeck coefficient of graphene near its Dirac point. The sign change of the Seebeck coefficient reflects the change in the majority carriers from holes to electrons. b) Photo-Nernst effect in graphene. Under an applied magnetic field, an electric field transverse to the thermal gradient develops. Reversing the magnetic field changes the polarity of the electric field. Panel (a) adapted from Ref. [175]. Panel (b) adapted from Ref. [178].

thermoelectricity has been associated to interaction-driven phase transitions and modifications to the Fermi surface[179–184], as well as electron-hole asymmetry of transport coefficients and scattering mechanisms in strongly-correlated materials[185–194].

Figure 3.3 depicts some examples of thermoelectric transport beyond the semiclassical picture across various condensed matter systems. In the left panel, an enhancement of the Seebeck coefficient in graphene (compared to the semiclassical Mott formula) appears between $T = 100$-300 K due to an anomaly in the carrier scattering mechanisms. Here, the onset of inelastic carrier scattering and scattering with optical phonons leads to the violation of the Mott formula[190]. In the central panel, the thermoelectricity of a GaAs quantum dot device deviates from the semiclassical expectation due to spin correlations. When the quantum dot hosts an unpaired spin, Kondo screening from the electrons in the reservoir leads to highly asymmetric scattering processes[193]. In the right panel, an anomalous peak of the thermopower appears around $T = 20$ K in Ce-based heavy fermion compounds. This peak arises from asymmetric particle-hole transport when the Kondo resonance develops in the system[189].

In the following, we will investigate the thermoelectric transport of the MATBG flat bands to unveil the particle-hole asymmetry of their low-energy electronic structure. As we will show, the semiclassical Mott formula does not accurately describe the Seebeck coefficient of the MATBG flat bands.

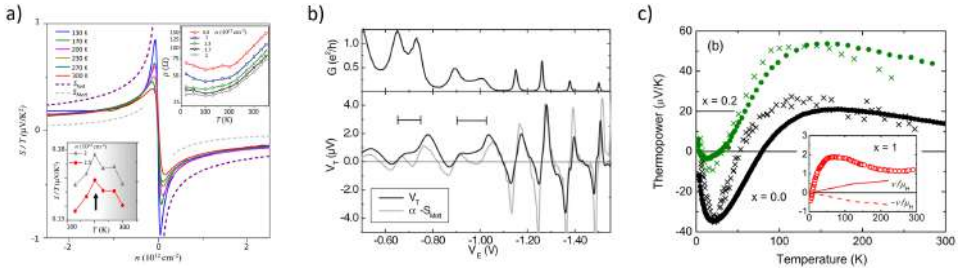

Figure 3.3: a) Deviations from the Mott formula in the thermopower of monolayer graphene. At high temperatures, inelastic carrier-carrier scattering and optical phonon scattering become sizable and lead to this Mott violation. b) Deviation from Mott formula in a GaAs quantum dot. When an unpaired electron resides in the quantum dot, its local moment is screened by the reservoir carriers via the Kondo effect. Then, an excess thermopower appears due to the emergent spin correlations. c) Temperature-dependent thermopower in $Ce_{1-x}La_xCu_2Si_2$ compounds. The enhanced thermopower around $T = 20$ K originates from the marked particle-hole asymmetry of Kondo scattering processes in this material. Panel (a), (b) and (c) adapted from Ref. [190], Ref. [193] and Ref. [189], respectively.

3.2 Particle-hole asymmetry in the MATBG flat bands

The interacting flat bands of MATBG host a plethora of many-body quantum phases, including superconductors[4, 103, 104], correlated insulators[4, 103, 105], topological states[108–111], among others[100]. A great number of transport studies have characterized this phenomenology of the MATBG flat bands, yet the exact role of electron correlations in the formations of these phases remains a central question.

An important aspect of the phenomenology of MATBG is the emergent electron-hole asymmetry in its flat bands. As the flat bands are doped (and electronic interactions kick in), a strong particle-hole asymmetry appears, pervading the entire phase diagram. This is best exemplified by the quantum oscillations emerging at integer fillings upon band reconstruction. Landau fans only appear dispersing away from charge-neutrality (Fig. 3.4a), suggesting strong e-h asymmetry of the phases that appear at the integer fillings[104]. This asymmetry is also observed in thermodynamic probes, such as measurements of the inverse compressibility in the flat bands, which reveal sawtooth filling dependence[195] (see Fig. 3.4a). From a non-zero integer filling $\nu = \mathbb{Z}$, the compressibility of the systems is markedly different when adding one electron or one hole to the correlated state at ν. This observation underscores the distinct character of particle-like and hole-like charge $\pm$ 1 excitations of the correlated ground states of MATBG. In addition to e-h asymmetry,

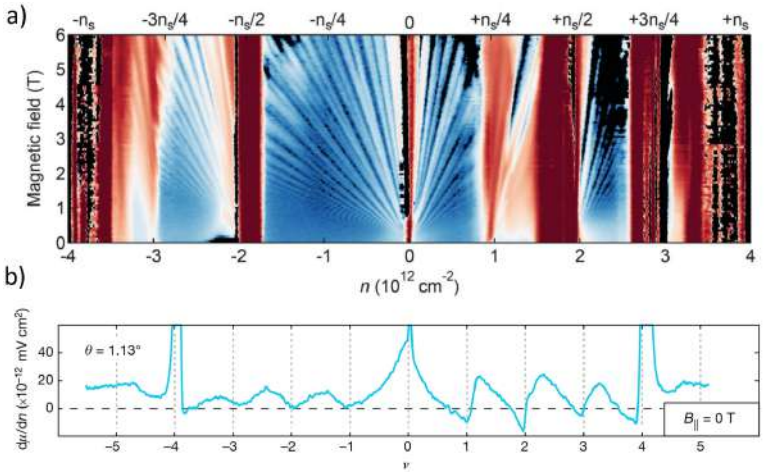

Figure 3.4: a) Magneto-transport characteristics of the MATBG flat bands. Note that the Landau fans (except those coming from the Dirac cone) only disperse away from charge-neutrality, toward the band insulators. b) Inverse compressibility in the MATBG flat bands. Around each integer filling, the inverse compressibility features an asymmetric valley. The sawtooth pattern indicates that the compressibility of the flat bands is particle-hole asymmetric around integer ν. Panel (a) adapted from Ref. [104]. Panel (b) adapted from Ref. [195]

the MATBG flat bands also present an intriguing dichotomy between the properties of itinerant and localized carriers. On the one hand, properties such as metallicity[101, 106, 107], superconductivity[5, 103] or non-trivial topology[110, 111](Fig. 3.5a) indicate the presence of itinerant carriers. On the other hand, strong Mott-like physics including the appearance of correlated insulators and ferromagnets at integer ν[4, 102, 103, 196, 197] and the Pomeranchuk effect[198, 199](Fig. 3.5b), point to the presence of local moments in the system. In addition, the tunneling spectrum on the AA sites of the moiré superlattice revealed quantum-dot-like charging effects[200, 201].

All in all, the strongly-correlated physics of the flat bands feature marked asymmetries between electrons and holes, as well as signatures of fundamentally different orbitals coexisting near the Fermi level. Therefore, the study of thermoelectric transport driven by the Seebeck effect stands out as a powerful tool to study the emergence of these asymmetries in the interacting MATBG flat bands.

3.2.1 Topological Heavy Fermion model of MATBG

The dichotomy between localized and itinerant-like behaviour in MATBG has motivated the development of multi-orbital, 'heavy fermion' models.[202–

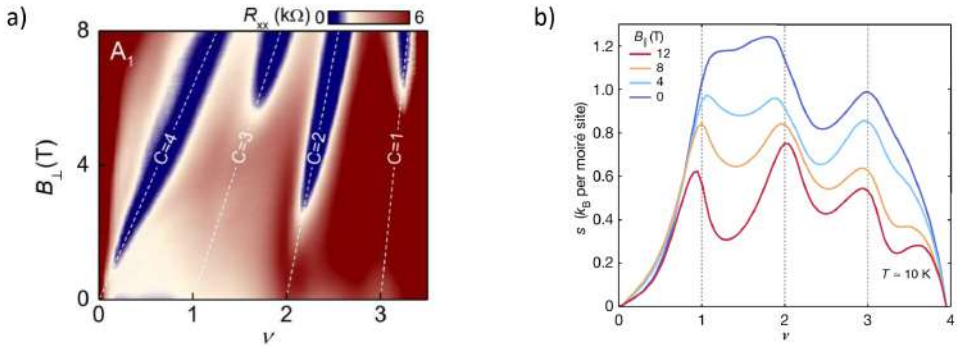

Figure 3.5: a) Magneto-transport of Chern insulators in MATBG. The slope of the linear-in-B dispersion reveals the Chern number of each state. b) Electronic entropy in the MATBG flat bands under different parallel magnetic fields. The decrease in entropy with increasing field suggests the polarization of magnetic local moments. Panels (a) and (b) adapted from Refs. [110, 199], respectively.

206]. These models propose the coexistence of both de-localized, conduction (light) electrons and dispersion-less, localized (heavy) fermions in the flat bands (Fig. 3.6a). From this perspective, the apparent dichotomy in the flat band phenomena can be readily addressed.

The heavy fermion models of MATBG take inspiration from the theoretical framework developed in the study of heavy fermion compounds. As we outlined in Chapter 1, these materials include heavy elements, such as ytterbium or cesium, and feature both localized electrons (coming from f-orbitals) and itinerant electrons (coming from d-orbitals) at the Fermi level. The interplay between the two electron subsystems gives rise to Kondo physics, resulting in a rich, interaction-driven phase diagram. Emergent phenomena include Mott-like physics, superconductivity, and overall non-Fermi liquid behaviour.

In this work, we will focus on the THF mapping of MATBG developed by Song and Bernevig in Ref.[202] and expanded with a focus on the thermoelectric effect in Refs. [207, 208] . We present here a brief introduction into the key aspects of the model and its salient features. Overall, the THF mapping of MATBG is derived from first-principles and offers a simple real-space description of the system, while preserving all the system's symmetries. The starting point for the THF model is the construction of Wannier orbitals for the MATBG active bands, matching those observed in local probe studies[200, 201]. Appropriate Wannier orbitals (respecting the system's symmetries) allowed the authors of Ref. [202] to account for a large majority of the flat bands derived in the original BM model[65].

The non-trivial topology of the flat bands[108] manifests itself near

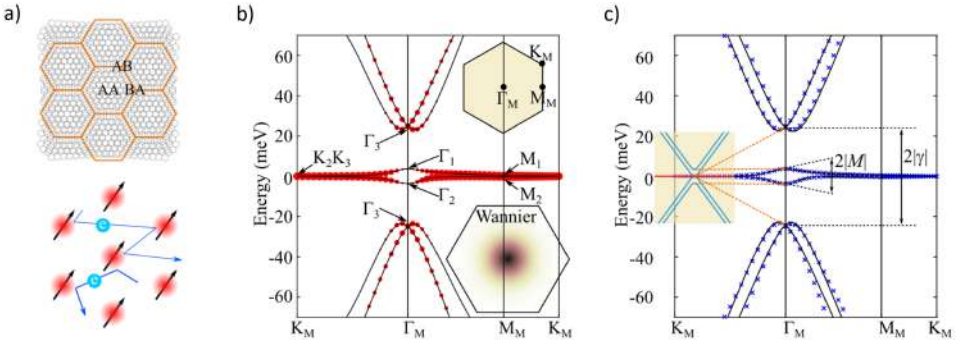

Figure 3.6: a) Illustration of the superlattice in MATBG and the coexistence of light (blue) and heavy electrons (red). b) Comparison between the dispersion from the BM model and that obtained from the Wannier representation of the orbitals at the AA sites (red dots). The agreement is good except near the zone center. c) Dispersion relation in the non-interacting THF model, perfectly reproducing the BM bands. From (b) to (c), the 'flat' electrons populating the Wannier orbitals hybridize with the dispersive electrons from the dispersive bands. Figure adapted from Ref [202].

the Γ point, where the overlap between the Wannier orbitals and the flat bands vanishes. To correctly reproduce the entirety of the MATBG active bands, de-localized carriers from the dispersive bands are hybridized with the localized electrons, giving rise to the missing states near Γ. Thus, the entire non-interacting BM bands could be re-interpreted via the hybridization of coexisting localized (f) and de-localized (c) electronic orbitals (Fig. 3.6b).

Crucially, electronic interactions between the different electronic species can be explicitly computed within the THF model. The interacting Hamiltonian $\hat{H}_I$ in the THF mapping of MATBG is given by:

$$\hat{H}_I = \hat{H}_{U_1} + \hat{H}_J + \hat{H}_{U_2} + \hat{H}_V + \hat{H}_W \tag{3.5}$$

, where $\hat{H}_{U_1}$ represents the on-site interactions between f-electrons, $\hat{H}_J$ represents the exchange coupling between c and f electrons, $\hat{H}_{U_2}$ is the Coulomb repulsion between nearest-neighbours localized electrons, $\hat{H}_V$ is the repulsion between de-localized electrons, and $\hat{H}_W$ is the repulsion between c and f electrons.

Notably, the largest energy scale in terms of electronic interactions is given by the on-site interaction of f-electrons ($U_1 \sim 60$ meV). Akin to the Hubbard model, the large on-site repulsion in the lattice of localized electrons will give rise to interaction-driven quantum phases with spontaneously broken symmetries.

It is important to note that the transport properties will be dominated by the itinerant c-electrons (which also carry the band topology). However,

the strong electronic interactions, experienced by the localized f-electrons, will open gaps in the dispersion of the c-electrons and modify the measured transport properties in the MATBG flat bands.

Figure 3.7 depicts exemplary THF band structure for symmetry-broken ground states of MATBG at different (hole-doped) integer fillings. Here, the bands are color-coded according to their orbital character, where yellow corresponds to localized f-electron states and blue indicates itinerant c-electron states. For the Kramers inter-valley coherent (KIVC) state at charge neutrality (Fig. 3.7a), electronic interactions lead to a drastic modification of the electronic spectrum (compare with the non-interacting case shown in Figure 3.6c). Yet, the spectrum remains particle-hole symmetric at charge-neutrality.

We stress that the band structures shown in Fig. 3.7 are computed using Hartree-Fock methods, in which all the states are infinitely-lived. Therefore, the effects of electronic interactions, which can reduce the lifetime of the quasiparticles, are not captured in the Hartree-Fock computations. In contrast, for non-zero integer fillings ν = -1, -2; the reconstructed bands

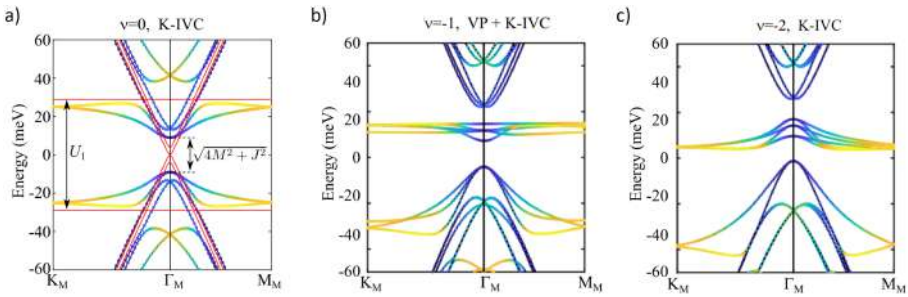

Figure 3.7: a) Self-consistent Hartree-Fock calculation of the band structure for the KIVC ground state at $\nu = 0$. The spectrum is particle-hole symmetric. b)Band structure for the VP + KIVC ground state at ν = -1, calculated via one-shot Hartree Fock method. There is a strong particle-hole asymmetry around the Fermi level. c) THF band structure for the KIVC ground state at ν = -2, calculated via one-shot Hartree Fock method. Like in (b), the low energy bands exhibit marked particle-hole asymmetry. In all panels, yellow and blue correspond to localized and itinerant states, respectively. Figure adapted from Ref. [202]

exhibit marked particle-hole asymmetry near the Fermi level. In both cases, heavy fermions (f-electrons) make up the low-energy electron-like excitations while the hole-like excitations are formed by dispersive, c-electrons. Thus, in addition to a natural account for the apparent dichotomy of the MATBG phenomena; the THF model captures the emergent *e-h* asymmetry of the correlated states.

3.3 Photo-thermoelectric effect in MATBG *pn*-junctions

In our study, we focus on two MATBG *pn*-junctions with twist angles $\theta = 1.14°$ and $\theta = 1.06°$. The fabrication of these samples was outlined in Chapter 2. Figure 3.8 summarizes the device structure and the transport characteristics for the 1.14 ° sample, which exhibits correlated states at integer ν (Fig. 3.8b). The dual gate map of the longitudinal resistance R_{xx} of the junction (Fig. 3.8c) demonstrates that each side of the device hosts correlated states at integer fillings and can be independently addressed. Diagonal features would emerge if there was any cross-talk between the two top gates. The experiment concept is sketched in Figure 3.9a. Leveraging

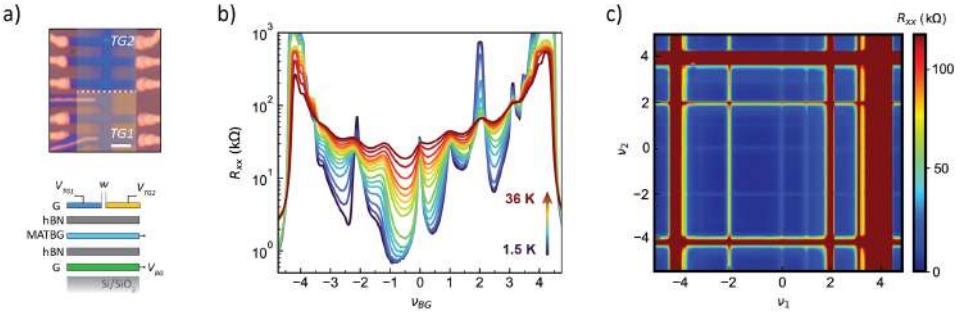

Figure 3.8: a) Upper panel shows an optical image of the MATBG *pn*-junctions. The scale bar corresponds to 1 μm. Lower panel sketches the cross-section of the dual gated *pn*-junction. b) Filling dependence of R_{xx} in the MATBG junction. Multiple correlated states emerge at integer fillings ν. c) Dual-gate map of R_{xx} in the junction. The correlated states from each side of the junction appear as vertical and horizontal resistive features. Lattice temperature is $T = 35$ mK.

the dual gates, we set up a chemical potential difference across the junction and use laser excitation to create a Gaussian thermal profile at the position of the junction. In this configuration, we can study the Seebeck effect, where the hot end now corresponds to the center of the junction and the thermal gradient points away from the junction[209, 210]. As the absorbed laser power is efficiently converted into an increased electronic temperature[210–212], we can selectively heat the charge carriers and study their thermoelectric transport. This offers a significant advantage over commonly employed Joule-heating approaches[176, 184, 190, 213–215], where the applied heat can be coupled to phononic degrees of freedom.

The lower right schematic of Fig. 3.9a illustrates the Seebeck effect in this configuration. Now, the voltage difference across the junction will read $V_{PTE} = -(S_2 - S_1)\Delta T_e$, which we express in terms of the electron

temperature T_e. Note that for uniform gating, no thermoelectric voltage would be observed across the junction, as the response at each side of the junction would cancel out.

In our experiment we do not have direct access to the electronic temperature increase ΔT_e. Electron thermometry is a significant challenge in 2D materials and requires specifically tailored experiments based on, for example, Johnson noise thermometry[213, 216, 217]. Simultaneous study of thermoelectric transport while monitoring the electron temperature through Johnson noise in a twisted bilayer graphene sample is a significant challenge. We avoid the direct readout of the electronic temperature and use the sublinear relation between ΔT_e and the absorbed laser power $P_{abs}$to verify linear heating conditions $\Delta T_e << T_e$ (see Fig. 3.11b).

A steady-state thermal model is used to provide a quantitative estimation of ΔT_e under typical experimental conditions. In short, ΔT_e can be determined through the steady-state relation:

$$\Delta T_e = \frac{P_{abs}}{G_{th}} = \frac{P_{abs}\tau}{C_e} \tag{3.6}$$

,where G_{th} is the thermal conductance of MATBG, τ is the thermal relaxation time for hot carriers and C_e is the electronic heat capacity of MATBG. These quantities are generally dependent on the lattice temperature, but we consider here their values for $T_l = 10$ K. Crucially, we have experimentally determined the thermal relaxation time of $\tau \sim$ 3-4 ps at this temperature (see Chapter 4). Modelling the coupling and absorption efficiency to find P_{abs}, as well as estimating the electronic heat capacity, we can obtain a quantitative estimate for ΔT_e in our experiment[207, 218].

In the low-excitation regime, we estimate P_{abs} in the junction area to range between 50 nW and 5μW. We use optical transfer matrix method on the entire heterostructure to compute the absorption of the MATBG layer and integrate the overlap between the micron-sized Gaussian laser spot and the sample area. Estimating C_e is much more challenging, particularly for MATBG as it will be strongly filling-dependent and sensitive to correlation effects. From the internal energy of the system, we use the THF model to estimate C_e at $T_l = 10$ K to be $C_e \sim$ 0.1-0.4 $\frac{J}{K}$[207]. All together, in the relevant temperature and laser power regime, we find an approximate electronic temperature increase of $\Delta T_e \sim$ 1-2 K $< T_e = T_l = 10$ K. Next, we perform a dual gate sweep around charge-neutrality and record the photovoltage appearing at the modulation frequency of the laser excitation. The dual gate configuration allows us to confirm the thermoelectric nature of the observed response. Figure 3.8b depicts the resulting map, which features a clear 6-fold symmetry of the response[209]. The appearance of multiple sign changes is the hallmark of Seebeck-driven response. Looking at the

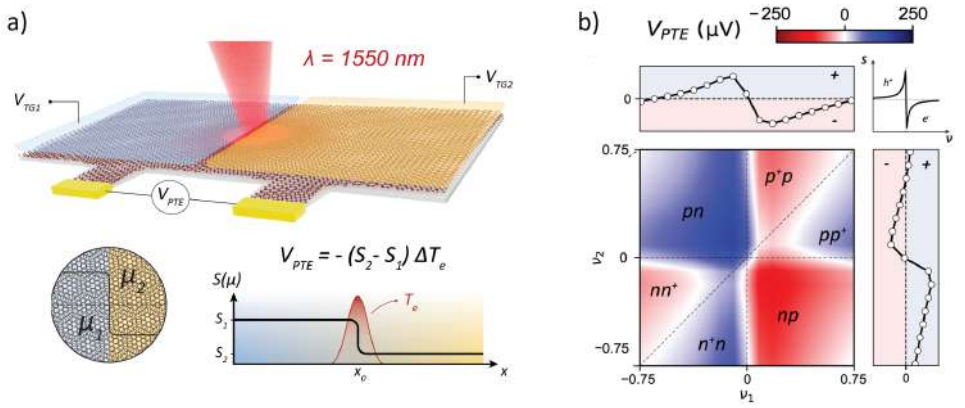

Figure 3.9: a) Illustration of the experimental concept. A CW laser input generates a thermal gradient at the interface of the gate-defined *pn*-junction. Using the two top gates, we define a chemical potential step in the junction, leading to a net thermoelectric voltage. b) Filling dependence of the PTE response around charge neutrality. Lattice temperature is $T = 10$ K. The 6-fold symmetry of the signal confirms the thermoelectric origin of the response. Multiple sign changes appear as a consequence of the non-monotonous gate dependence of the Seebeck coefficient in graphene (see insets and Figs. 3.2a and 3.3a) Panel (b) corresponds to the 1.14° device.

single-gate response (linecuts for $\nu_i = 0$), the characteristic lineshape of the Seebeck coefficient in graphene is recovered. The 6-fold symmetry then arises from the term $S_2 - S_1$ and the non-monotonous gate-dependence of each S_i[209, 210, 219].

Having established the PTE nature of the response, which we label V_{PTE}, we can now use it as a direct proxy the Seebeck coefficient and the electronic spectrum of the MATBG samples. First, we explore the thermoelectric response across the electron-doped flat bands. Figure 3.10 depicts R_{xx} (a) and V_{PTE} (b) as the each top gate is swept between ν_i = -1 and ν_i = +3. Comparing the two maps, one can see that the thermoelectric response acquires a complex gate-dependence; whose main features appear at 'integer' configurations where both ν_1 and ν_2 are integer numbers.

Furthermore, at each 'integer' configuration away the thermoelectric response exhibits its characteristic 6-fold symmetry (see overlayed diagonal lines in Fig. 3.9b). This observation points to a charge-neutral-like response of the junction at the integer fillings, once the low energy bands are reconstructed. Thus, we further confirm that one can utilize V_{PTE} as a proxy of the Seebeck coefficient to study the nature of the interaction-reconstructed flat bands. We note that the appearance of the 6-fold symmetric response does not imply graphene-like or Dirac-like nature of the bands. The 6-fold

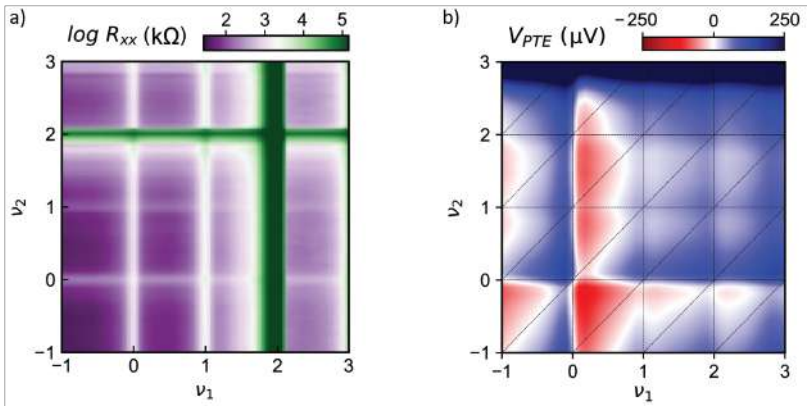

Figure 3.10: a) Dual gate map of R_{xx} in the electron-doped flat bands. Lattice temperature is $T = 35$ mK. b) PTE voltage in the electron-doped flat bands. Multiple sign changes appear around the integer fillings. At crossings between integer fillings from both sides (ν_1,ν_2), the 6-fold symmetry of the response is recovered. Lattice temperature is $T = 10$ K. Both panels correspond to the 1.14° device.

symmetry indicates the thermoelectric origin of the response and the approximately symmetric band structure of the system around the Fermi level. This is true for graphene[175, 210], but also for other semimetals[173, 187] or narrow-gap semiconductors[220].

In the following, we focus on the thermoelectric response from one side of the junction and study its gate dependence to map the Seebeck coefficient (and its electronic spectrum). To do this, we simplify the measurement scheme in order to untangle the response from the two sides of the junction. Figure 3.11a sketches this concept, where the chemical potential for one side of the *pn*-junction is set exactly at its charge neutral point ($\nu_2 = 0$). Due to the perfect band symmetry around $\nu = 0$, the particle and hole currents flowing into that side of the junction will cancel out and the resulting Seebeck coefficient S_2 will be exactly zero. Then, the PTE response will simply read $V_{PTE} = -(S_2 - S_1)\Delta T_e = S_1 \Delta T_e$.

We restrict ourselves to low excitation power in order to avoid overheating. As shown in Figure 3.11b, the power-dependence of the response near charge-neutrality (where we have clearly established the thermoelectric origin of the photovoltage) indicates what is the linear heating regime. For higher laser power, heating effects start to induce sublinearity of the response as the system's heat capacity increases with temperature.

Thus, we fix $S_2 = 0$ and monitor the low-power thermoelectric response as we sweep ν_1 across the flat bands. The response is depicted in the upper panel of Fig. 3.12 for the two devices. At charge-neutrality, the response

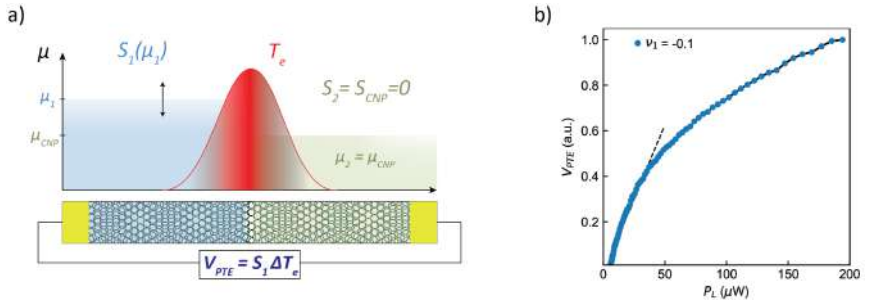

Figure 3.11: a) Illustration of the 1-gate configuration used to map the Seebeck coefficient. The chemical potential for one side of the junction (labeled 2 here) is kept at the Dirac point, where its Seebeck coefficient is zero. Thus, the total thermoelectric response V_{PTE} will be a proxy for the Seebeck coefficient S_1 on one side of the junction. b) PTE response near charge neutrality for increasing laser power. The sublinear power dependence reflects the thermal origin of the signal. All measurements presented here are performed in linear heating conditions, at low laser powers.

exhibits the conventional antisymmetric gate dependence which stems from the form of the Seebeck coefficient. In addition, similar 'oscillating' features emerge at the integer fillings, most notably at $\nu_1 = +1, +2$. As discussed before, these oscillations evidence the reconstruction of the Fermi surface and the appearance of charge-neutral electronic spectra at integer ν_1.

However, the thermoelectric response (and consequently the Seebeck coefficient) does not change sign across this doping range. This striking observation, most noticeable at $\nu_1 = +2$ for the device with $\theta = 1.06°$ (see Fig. 3.12), will be the focus of the following discussion. At surface level, the sign-preserving Seebeck oscillation indicates strong particle-hole asymmetry of the charge-neutral electronic spectrum for the correlated state at $\nu_1 = +2$. In particular, the electronic contributions to thermoelectric transport clearly dominate the hole-like contributions at this filling.

As a first step, we contrast the observed response with the semiclassical Mott formula[174]. While the response at charge-neutrality (where electron correlations are weak) qualitatively matches the Mott formula, at the integer fillings the response strongly deviates from the semiclassical expectation (see lower panel of Fig. 3.12). As discussed before, the Mott formula associates sign-changes of the Seebeck coefficient to extrema of the longitudinal resistance (Fig. 3.13a). However, in our case, the resistance peaks at the integer fillings do not result in zero-crossings of the thermoelectric response. In agreement with the strongly-correlated character of the flat bands, the semiclassical Mott formula does not capture the observed response. The 'Dirac revival' picture[195] is often used to rationalize the Fermi surface

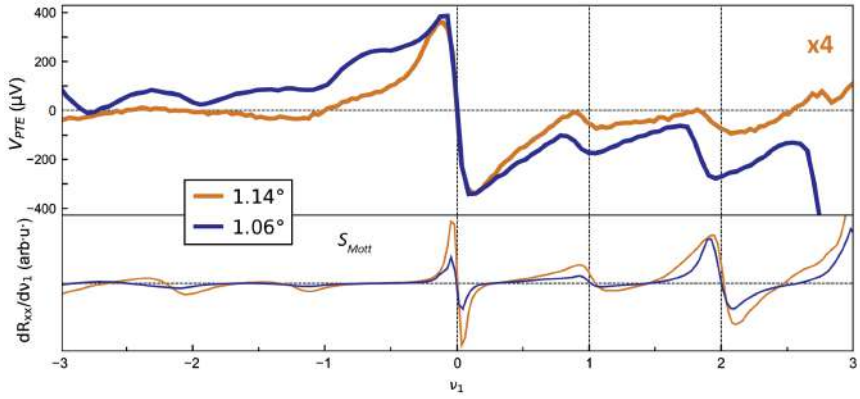

Figure 3.12: Anomalous thermoelectric response in the MATBG flat bands in the one-gate configuration. The sign-preserving oscillations of the Seebeck coefficient observed around $\nu_1 = +1, +2$ evidence strong *e*-*h* asymmetry of the correlated ground states. In the lower panel, we contrast the observed response with that expected from a semiclassical Mott picture.

reconstructions of the MATBG flat bands. This picture hypothesizes that the flat bands can be modeled as degenerate Dirac cones which are doped continuously (all at the same rate). Then, near the integer filling, all the spectral weight is shifted onto a single Dirac cone (of a certain spin-valley flavor) which becomes fully filled, and falls below the Fermi level. All other Dirac bands are reset to charge-neutrality.

Figure 3.13b depicts such a scenario for $\nu = +1$, with one filled Dirac cone below the Fermi energy. All the carriers in these bands are identical, with the same transport lifetime τ and group velocities v_g. However, after the spectral weight re-organization, a strong asymmetry in the DoS appears as the DoS of the unfilled Dirac cones is lower (they are reset to the Dirac point) than that of the filled Dirac cone. Thus, at $\nu = +1$, the DoS is higher for hole-excitations than for electron excitations. In this scenario, the Seebeck coefficient would deviate from the Mott formula and exhibit excess hole-like character.

This picture has been invoked to explain excess positive thermoelectricity observed in previous studies[213] (Fig. 3.13c). Clearly, this scenario cannot account for our experimental observations, as we observe electron-dominated response for $\nu_1 > 0$. We also note that the identification of the flat bands with Dirac cones constitutes an over-simplification of the problem, as it neglects the interaction-driven band reconstruction. We investigate the possible origins for the highly asymmetric transport using a simple two-band model[207]. The low-energy electronic structure for an arbitrary correlated insulator can be modeled using two parabolic bands. This is a reasonable

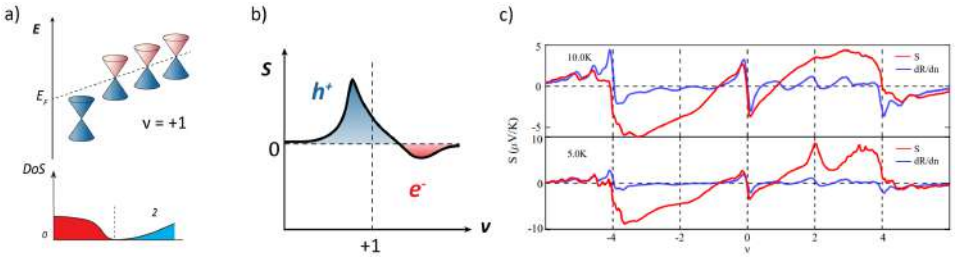

Figure 3.13: a) Schematic representation of the 'Dirac revival' picture. At $\nu = +1$, one of the four Dirac cones is spontaneously filled and pushed below the Fermi level. The remaining Dirac bands are reset to their charge-neutral point. Thus, an asymmetry appears in the DoS of holes and electrons around $\nu = +1$. As the DoS is larger for hole excitations, one expects dominant hole-like Seebeck near this filling. b) Sketch for the expected Seebeck coefficient for a MATBG correlated state according to the 'Dirac revival' picture. c) Observation of excess hole-like thermopower in the electron-doped flat bands of MATBG. At $T = 5$ K, the data features a positive, hole-like peak of the thermoelectric response at $\nu = +2$. Panel (c) adapted from Ref. [213]

approximation for any gapped system at low enough energies. The two-band model, sketched in Fig. 3.14, considers a fixed gap of value Δ and electron and hole bandwidths κ_e, κ_h, as well as independent scattering rates for each band Γ_e, Γ_h. This model aims to mimic the response of a correlated state at integer filling $\nu = \mathbb{Z}$. The bandwidth is inversely proportional to the effective mass of the band, according to $\kappa_i = \frac{\lambda^2}{2m_i}$. For a parabolic band, the bandwidth determines both the DoS and the group velocity of the carriers v_g. At this point, all carriers are modeled with a single, fixed scattering rate Γ. Using this two-band model, we can investigate the role of these transport coefficients, included in the general conductivity function $\sigma(\mu, E)$, on the thermoelectric transport[207]. In the following, we fix $\Delta = 16$ meV, $\kappa_e = 30$ meV, $\Gamma_e = 1$ meV and tune the transport coefficients of the hole band.

Since the observed response points to strong e-h asymmetry dominated by electrons, we consider a scenario where the hole band has a much larger effective mass than the electron band. Therefore, we first set $m_h >> m_e$ or $\kappa_h << \kappa_e$ and compute the Seebeck coefficient from the two-band model. The computed Seebeck coefficient, shown in Fig. 3.14a, exhibits small excess electron-like contributions to thermoelectricity. Notably, the Seebeck coefficient does not deviate significantly from the band-symmetric case even for extreme mass asymmetry, when $\frac{\kappa_h}{\kappa_e} = 150$. This finding indicates that the asymmetry in the bandwidth κ, which determines the group velocity v_g and the DoS of the bands, cannot explain the experimentally observed, fully-negative Seebeck coefficient at the correlated states. We therefore turn

our attention to the role of asymmetry of the scattering rate Γ (or transport lifetime τ).

We now introduce a band-dependent scattering rate Γ_i in the two-band model. We fix the carrier lifetime of the electron band to $\tau_e = 1$ meV^{-1} and explore the effect of decreasing hole carrier lifetime τ_h (increasing Γ_h). In Figures Fig. 3.14d) we present the case where $\tau_h = 8$ meV^{-1} and observe that the transport lifetime asymmetry profoundly affects the computed Seebeck coefficient. The Seebeck oscillation is pushed almost completely to negative values and is also shifted back, it does not occur near the integer filling $\mathbb{Z}$ but rather at finite hole-doping $\mathbb{Z} - \delta$. Therefore, we find that tuning the

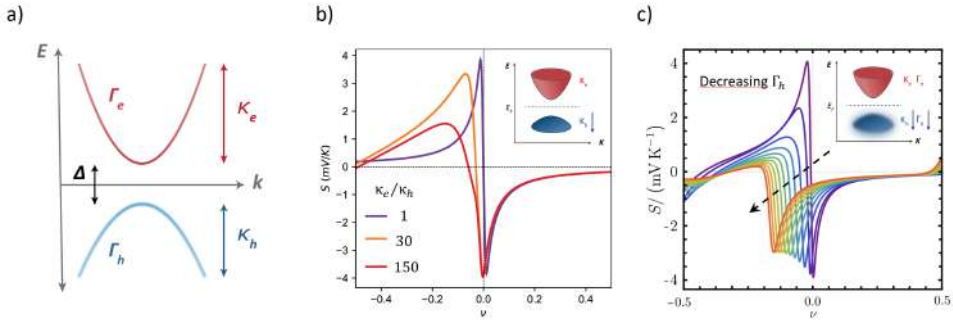

Figure 3.14: a) Band diagram for the two-band model for the correlated insulators in MATBG. Each band has an associated bandwidth κ (inversely proportional to the effective mass) and scattering rate Γ (inverse carrier lifetime). In the simulations, the following parameters are kept constant: $\Delta = 16$ meV, $\kappa_e = 30$ meV, $\Gamma_e = 1$ meV. We study the Seebeck coefficient with respect to changes to the hole band bandwidth (b) and its scattering rate (c). b) Seebeck coefficient computed in the two-band model for increasing band asymmetry via a decrease of the hole bandwidth (increasing mass). Even for extreme band asymmetry, the Seebeck coefficient does not deviate substantially from its conventional behavior. c) Seebeck coefficient computed in the two-band model for increasing Γ_h (decreasing hole transport lifetime). The traces range from $\Gamma_h = \Gamma_e = 1$ meV to $\Gamma_h = 20$ meV. Moderate changes of the scattering drastically modify the resulting Seebeck coefficient. Panel (c) adapted from Ref. [207].

relative carrier lifetime between the electron and hole bands dramatically modifies the Seebeck coefficient (Fig. 3.14c). In this computation, the mass asymmetry was reduced compared to the previous scenario ($\frac{\kappa_h}{\kappa_e} \approx 4$). This observation highlights the crucial role of distinct carrier lifetimes or scattering rates between bands involved in thermoelectricity. This simple two-band model suggests that such lifetime asymmetry is responsible for the observed anomalous, sign-preserving thermoelectric transport.

The effect of energy-dependent carrier lifetime has been observed in other material systems such as $CuFeS_2$[185] or $Co_{1-\delta}Ni_\delta Sb_3$[189], but is

often overlooked. Importantly, the two-band model with mass and lifetime asymmetry constitutes a realization of the light-heavy band structures predicted for the correlated states in the THF model[202] (see Figure 3.7). In the following, we discuss the modelling we performed using the THF model and its agreement with the experimental data.

3.4 Interpretation of the low-temperature thermoelectric response

The interpretation of the Seebeck coefficient in the THF model, done in collaboration with the group of Prof. Andrei Bernevig, is detailed in other publications[207, 208]. Here, we focus on the specific predictions of the model with regards to the band structure and Seebeck coefficient of the 1.06° device in the relevant temperature range ($\sim$ 10 K).

In the following, we present band structure calculated using self-consistent 2^{nd} order perturbation theory, where the electron self-energy $\Sigma(E)$ is computed. This stands in contrast with the Hartree-Fock computations described previously. The electron self-energy contains indicates both the energy of the quasiparticle (its real part) and the lifetime for the excitation (its imaginary part). A nearly-free electron will suffer no interactions, and have a well-defined energy and a long lifetime; while a strongly-correlated, localized electron will have a low lifetime and a significant energy broadening. In the THF computations, the lifetime of the heavy quasiparticles is calculated self-consistently[207] and constitutes the key ingredient in understanding the experimental observations.

Figure 3.15a-c depicts the self-consistent band structures calculated for the 1.06° device and the corresponding Seebeck coefficient at fillings $\nu = 0, +0.8, +2$. Each band structure and thermoelectric response is computed for a given symmetry-broken ground state, indicated in each plot. However, the qualitative features of the electronic spectra and the Seebeck coefficient do not depend on the choice of ground state, as we will show shortly. We choose $\nu = +0.8$ instead of $\nu = +1$ because the salient features of the band structure are more apparent slightly away from the integer filling.

The interacting band structures shown here resemble those presented in Fig. 3.7. However the imaginary part of the self-energy, the carrier lifetime, is now self-consistently assigned to each momentum and energy-resolved state. At charge-neutrality Fig. 3.15a, the bands away from Γ are composed of non-dispersing, heavy fermions while the lower energy states, which lie near the zone center, are dispersive, de-localized carriers. As the spectrum is particle-hole symmetric, we recover a conventional Seebeck coefficient shown in Fig. 3.15d. On the other hand, for the correlated states at $\nu = +0.8$,

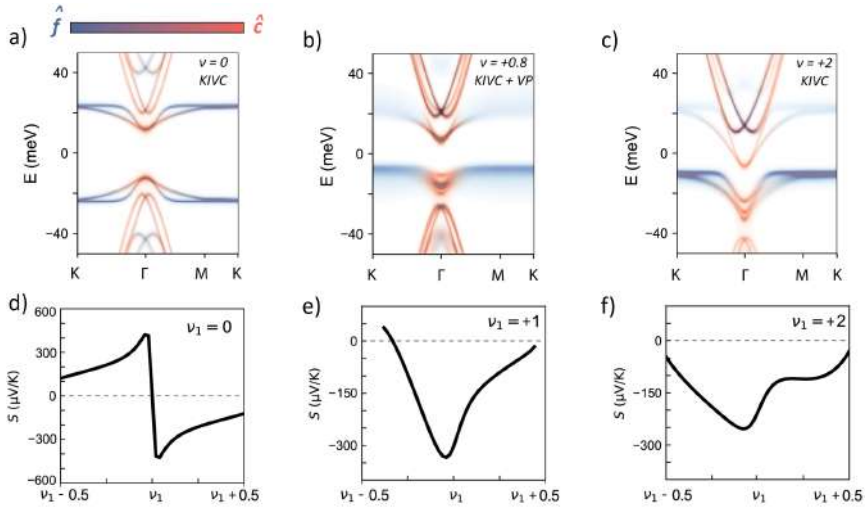

Figure 3.15: a) Band structure for the KIVC correlated insulator at $\nu = 0$. The 2nd order perturbation calculation reproduces the Hartree-Fock results (Fig. 3.7a) while self-consistently computing the k-resolved scattering rate. The low-energy bands are symmetric and dominated by c-electrons. b) Band structure for the KIVC + VP correlated insulator at $\nu = +0.8$. The low-energy states are markedly different for the bands above (dispersive c-states) and below (localized f-states) the Fermi level. Note the large energy broadening (low carrier lifetime) associated with the f-electron states near the Fermi level. c) Band structure for the KIVC correlated insulator at $\nu = +2$. As in (b), the low-energy hole excitations are formed by f-electrons, while the electron excitations are composed of itinerant states. d) Seebeck coefficient computed from the band structure shown in (a). A large, antisymmetric Seebeck coefficient appears as a consequence of the electron-hole symmetric dispersive states near the Fermi level. e) Seebeck coefficient computed from the band structure shown in (b). The vanishing transport contributions of the low energy, hole-like excitations lead to a sign-preserving, negative Seebeck coefficient. f) Seebeck coefficient computed from the band structure shown in (c). As in (e), the marked band and lifetime asymmetry shown in (c) give rise to the electron-like Seebeck coefficient near $\nu_1 = +2$. Panels (d), (e) and (f) show data from the 1.14° device.

+2, the band structure is highly particle-hole asymmetric (Fig. 3.15b-c). The low-energy states below the Fermi level (hole-like states) are incoherent, low lifetime f-electron states with minor contributions to thermoelectric transport. Note the large energy broadening of the non-dispersing states close to the chemical potential. Instead, the available states just above the Fermi level are coherent c-states for both correlated states. Therefore, the electron-like contributions will dominate the transport and lead to a fully-negative Seebeck coefficient as depicted in Fig. 3.15e-f). We note that the Seebeck coefficient in this symmetry-broken correlated state is not always

well-defined in the entire range between ν_1-0.5 and ν_1+0.5. Further doping of the correlated ground state at ν_1 makes it unstable and the symmetry-broken solution diverges.

The computed self-consistent thermoelectric response from correlated ground states in the THF model agrees remarkably with our experimental observations. In Figure 3.16a we make a direct comparison between the experimental data and theoretical simulations to highlight their resemblance. As mentioned before, the choice of symmetry-broken ground state does not change the overall findings. In Fig. 3.16b we depict the computed thermoelectric response for the valley-polarized (VP) correlated states in the same filling range. All in all, based on the natural explanation of the observed response in terms of coexisting light and heavy fermions (Fig. 3.16c), we posit that our observation demonstrates heavy fermion physics in the strongly-interacting flat bands of MATBG.

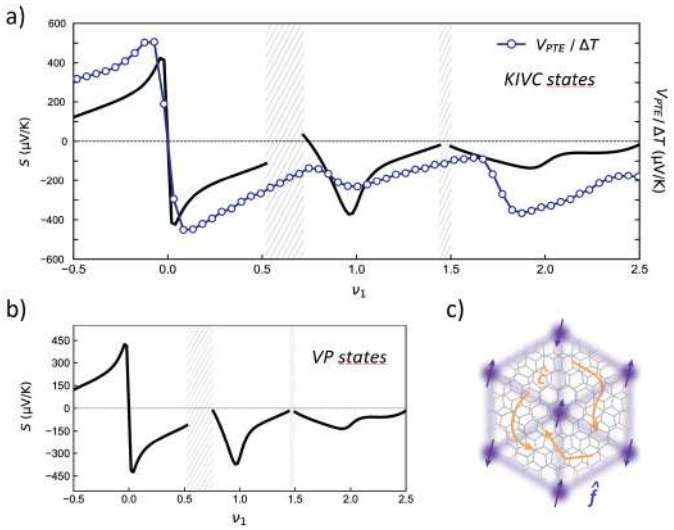

Figure 3.16: a) Direct comparison of the measured thermoelectric response and the Seebeck coefficient predicted by the THF model for the KIVC correlated insulators. b) Seebeck coefficient computed in the same theoretical framework for the VP correlated insulators. c) Schematic illustration of itinerant and localized electronic orbitals in MATBG. The circles in panel (a) correspond to the 1.14° device.

3.5 Strong electron correlations in the unordered, high-temperature state of MATBG

At high enough temperatures, the interaction-driven, flavor-polarized ground states of MATBG are expected to melt, giving way to ground states where all the system's symmetries are preserved[204]. Although this regime has not been explored as extensively as the low-temperature regime, there is entropic evidence for the presence of strong electron correlations at higher temperatures. This includes the persistent cascade of spectral weight reorganization in the flat bands[195, 201], the sawtooth filling dependence of the electronic entropy at temperatures $\sim$ 50 K along with the Pomeranchuk effect[198, 199](Fig. 3.4b).

As an alternative to these spectroscopic and thermodynamic probes, we study the thermoelectric transport of the MATBG flat bands at higher lattice temperatures. We note that the Seebeck coefficient can be regarded as the entropy carried by each charge carrier in the absence of a thermal gradient[221]. Thus, the Seebeck coefficient also constitutes a fundamental thermodynamic magnitude that quantifies the entropy per charge carrier.

The thermoelectric transport at lattice temperatures of T_l = 30 K, 50 K is measured using the simplified scheme described above. We fix $S_2 = 0$ and record V_{PTE} (ν_1) at a low excitation power. Figure 3.17a shows the observed thermoelectric response. First, near $\nu_1 = 0$ we identify the conventional graphene-like oscillation of the Seebeck coefficient. At 50 K, the lineshape is washed out due to the increased participation of higher-energy bands at higher temperatures. Doping away from charge neutrality, the overall trend of the signal is now reversed compared to the low-temperature data. Electron (hole) doping of the flat bands leads to an overall positive (negative) response. In addition, clear oscillations of the Seebeck coefficient develop around the integer fillings, most notably for $\nu_1 = +2$ (see Fig. 3.17b). These observations stand in clear contrast with those for low temperatures, where the order of the correlated ground states is stabilized. We aim to rationalize the measured high temperature response within the THF model[202, 207]. As the ordering (symmetry-breaking) in the MATBG flat bands is mediated by the electronic interactions, we make a rough approximation to the unordered state of MATBG by turning off all the interactions in the model[202]. We note that all microscopic parameters used for the low temperature modelling are kept unchanged. The resulting non-interacting Seebeck coefficient $S_{Non-Int}$, shown in Figure 3.18a, agrees well with the overall trend of the signal.

Still, the oscillatory behaviour of the Seebeck coefficient at the integer fillings evidences the presence of correlated-driven minima in the DoS of the spectrum. The large magnitude of these features, particularly for $\nu_1 = +2$,

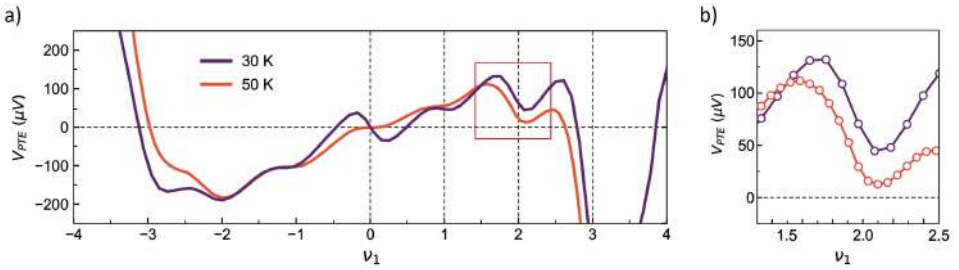

Figure 3.17: a) Thermoelectric response of the MATBG flat bands at high lattice temperature. Marked oscillations of the thermoelectric voltage appear at integer fillings. The overall trend of the response is positive (negative) for $\nu_1 > 0$ ($\nu_1 < 0$). b) Zoom-in of the sign-preserving, positive oscillation of the thermoelectric response at $\nu_1 = +2$. The experimental data corresponds to the 1.14° device.

suggests that the DoS minima correspond to the opening of a thermodynamic gap. Therefore, we must account for electron correlations in order to model the thermoelectric response of the unordered, high-temperature state. We

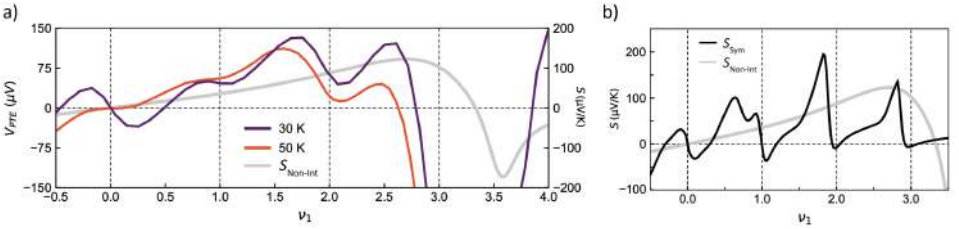

Figure 3.18: a) V_{PTE} at higher lattice temperatures and Seebeck coefficient in the non-interacting limit of the THF model $S_{Non-Int}$. b) Computed Seebeck coefficient for the symmetry-preserving solution of the full THF model.

return to the full, self-consistent THF model and keep all its microscopic parameters and interaction terms[207]. To mimic the non-ordered MATBG ground state, we search for symmetric solutions of the model. In other words, we impose that the ansatz in the THF model must preserve all the symmetries of the system and they cannot be broken by electron correlations. The computed Seebeck coefficient from such a 'symmetric' solution is depicted in Figure 3.18b along with $S_{Non-Int}$. Remarkably, the symmetric Seebeck coefficient S_{Symm} qualitatively reproduces the experimental data. Clear oscillations of the Seebeck coefficient appear at the integer fillings $\nu_1 = \mathbb{Z}$ while the overall sign of the response remains positive for $\nu_1 > 0$.

All in all, the thermoelectric transport of the unordered state of MATBG at high-temperatures can be understood as a combination of non-interacting thermoelectricity and a symmetric, unordered state in which electronic correlations induce gaps in the spectrum without symmetry breaking. The

measured thermoelectric transport further confirms the persistence of strong electron interactions in the MATBG flat bands beyond the ordering temperatures of the flavor-polarized ground states.

Chapter 4

Ultrafast carrier cooling MATBG *pn*-junctions

In this chapter, we describe the experimental study of the electronic thermal relaxation time in MATBG *pn*-junction samples. This study was done in collaboration with the group of Prof. Klaas Jan Tielrooij, who performed time-resolved photocurrent measurements of the MATBG *pn*-junctions. We performed complementary measurements of the electron cooling time through the CW photomixing technique described in the Experimental methods chapter.

Motivation

We have previously discussed MATBG in the context of the electronic properties of its strongly correlated flat bands [100]. The flat bands emerge due to the large moiré superlattice potential (with wavelength $\lambda \sim 14$ nm). In addition, the presence of the superlattice potential will also affect the phonon spectrum creating phonon mini bands[222, 223], akin to the band folding that appears, for example, when a charge density wave is formed. In this section, we will demonstrate how the moiré phonon bands can significantly affect the low-temperature electronic properties of the system, namely through its electron-phonon (*e-ph*) coupling.

The nature and origin of the superconducting state of MATBG remains an outstanding question in the field. Despite intensive theoretical and experimental efforts, no consensus has been reached on the underlying symmetries of the superconducting state or the coupling mechanism behind its formation. As the MATBG phenomenology resembles that of other strongly correlated superconducting systems, unconventional coupling mechanisms driven by electronic interactions have been proposed[224–227]. More conventional mechanisms, driven by *e-ph* interactions, also remain as possible

candidates[228–230]. As the coupling mechanism remains an open question, the investigation of *e-ph* coupling in the system is highly relevant. Particularly, the moiré-induced modification of *e-ph* coupling (otherwise weak in monolayer graphene) could affect the low-temperature scattering pathways for electrons (Figure 4.1).

Theoretical reports predict that the formation of the moiré superlattice could strongly modify *e-ph* coupling in MATBG[222, 223]. At surface level, the moiré phonon mini bands could increase the available phonon density for electron scattering. The study of such effects could shed light on some of the correlated phases in MATBG. In addition to a possible phonon-driven coupling mechanism of the superconducting state, the strange metal phase remains one of the open questions in the field[101, 106, 107]. In this phase, momentum-relaxing electron scattering remains efficient down to very low temperatures, as evidenced by the linear-in-temperature resistivity. At present, it is not clear whether an enhancement of the low temperature *e-ph* interactions could give rise to the observed $\rho \propto T$ behaviour[222]; in contrast to the strange metal picture. All in all, exploring *e-ph* coupling in the MATBG flat bands can help elucidate the scattering processes available for electrons at low temperatures.

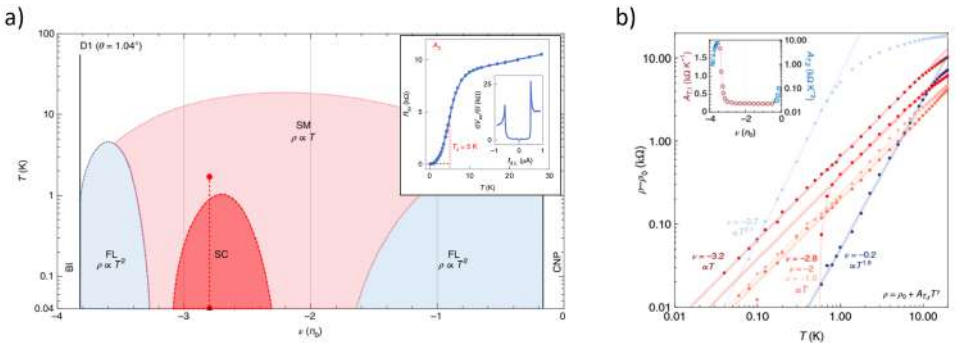

Figure 4.1: a) Phase diagram of the temperature-dependent resistivity in MATBG samples. The resistivity decreases linearly with temperature (outside the superconducting state) around half-filling of the superlattice. b) Linear-in-temperature and quadratic temperature dependence of the resistivity. The prefactor in the T^2 dependence increases around the magic angle. Figures adapted from Ref.[107]. Inset in (a) is adapted from Ref. [110].

The cooling dynamics of a system provide valuable insight into its *e-ph* coupling and scattering mechanisms overall. While the cooling dynamics of hot carriers in graphene have been widely explored, such studies do not exist for MATBG. As we discuss next, long-lived and controllable hot carriers in graphene are of fundamental and technological relevance[130]. Hot carriers can be efficiently generated in graphene in an ultrafast timescale[212, 231,

232] and the hot carrier distribution is long-lived[130]. Thus, low-temperature optoelectronic studies of the cooling dynamics of hot carriers in MATBG are highly desirable. These studies can not only reveal the strength of *e-ph* coupling and the dominant scattering mechanisms but also shed light on the, largely unexplored, dynamics of light-matter interaction in magic-angle graphene.

First, we will introduce the concept of hot carriers and their dynamics in graphene systems. This will serve as a solid starting point for the discussion of the cooling dynamics of MATBG. We will describe the general equation for the evolution of the electronic temperature, as well as the main cooling pathways for electrons in graphene. The aim of this section is not to provide a complete discussion of hot carrier dynamics in graphene. We direct the reader to a recent review article on this topic[130]. Instead, the goal is to provide a self-contained, qualitative picture of the hot carrier dynamics of graphene to put in context our findings in MATBG. Therefore, we will restrict the discussion to the scenarios relevant to this experiment, in terms of the type and energy of the excitation as well as the studied temperature regime.

We then describe and contrast the two optoelectronic techniques employed to access the time dynamics of hot carrier cooling in MATBG. Next, we will present the main findings of this work, namely the ultrafast cooling of electrons in MATBG down to cryogenic temperatures ($\sim$ 5 K). We discuss the dependence of the cooling time as a function of several parameters, such as temperature or optical power. Lastly, we present the novel mechanism behind this effect and model the observed response.

4.1 Hot carrier physics in graphene

Hot carriers are charge carriers (electrons and holes) that have excess kinetic energy and lie above the chemical potential μ in a thermalized Fermi-Dirac distribution. Hot carriers in graphene can be generated through optical, electrica, or thermal excitation[130]. Photo-generation of hot carriers is particularly efficient in graphene, thanks to its gapless dispersion, fast carrier-carrier scattering[212, 231, 232] and weak electron-phonon coupling[233]. Thus, a carrier distribution with higher temperature than the thermal (phonon) bath ($T_e > T_l$) can be established. In this section, we will focus the discussion on the case of steady state heating.

Studying the hot carrier transport in graphene[130, 209] can provide both fundamental insights and be harnessed for future optoelectronic devices. From a fundamental standpoint, hot carrier transport can be used to study the electronic dispersion or electron-phonon coupling in the system. From

an application standpoint, the efficient generation, control and collection of hot carriers in graphene enables the design of novel devices, such as photodetectors, modulators or absorbers[77].

General heat equation

As the salient feature of hot carriers is the presence of a carrier distribution at elevated temperature, it is informative to establish a general equation for the evolution of the (elevated) electronic temperature $T_e(t)$:

$$C_e \frac{\partial T_e}{\partial t} = \frac{dQ_{ext}}{dt} + \kappa_e \nabla^2 T_e - \nabla[(V + ST_e)J] \tag{4.1}$$

, where C_e is the electronic heat capacity, $\frac{dQ_{ext}}{dt}$ is the rate of heat added or removed from the system, $\kappa_e \nabla^2 T_e$ represents the diffusion of heat according to Fourier's law (κ_e is the electronic thermal conductivity) and the last term represents the heat carried by electrical currents. Here, V is the local voltage, S is the Seebeck coefficient which parametrizes thermoelectric transport and J is the current density, written in terms of the electrical conductivity σ as:

$$J = \sigma(-\nabla V - S\nabla T_e) \tag{4.2}$$

In this chapter, we will be focusing on the novel cooling pathways that can appear in graphene-like systems in the presence of a moiré superlattice. Such an effect would be captured in the first term of the right-hand side of Eq. 4.1. In this experiment, we provide heat to the electron subsystem via photoexcitation. It's still important to consider the thermoelectric effect (third term on the right-hand side of Eq. 4.1.) as it will be responsible for the observed electronic response.

Hot carrier dynamics

The dynamics of hot carriers in graphene can be separated into three (subsequent) stages: excitation, thermalization and cooling (Figure 4.2). In the first stage, charge carriers in the system will absorb heat Q_{ext} from an external source. For excitation with near-infrared photons, with energies $\hbar\omega >> E_F$, photoexcitation will lead to the generation of high-energy electron-hole pairs (Fig. 4.2b). These carriers, often called primary photoexcited carriers, acquire energies in the order of $\hbar\omega/2$ above the Fermi level. At this stage, the high energy carriers (not to be mistaken with the hot carriers that will participate in transport) do not form a thermal distribution and therefore cannot be assigned a carrier temperature. Instead, the original, at-equilibrium Fermi-Dirac distribution coexists with a small number of carriers at very high energies.

Thermalization

The thermalization of the high energy carriers will take place shortly after the photoexcitation, typically in a femtosecond scale[212]. The primary photoexcited carriers transfer their kinetic energy to carriers near the Fermi level via intraband, inelastic carrier-carrier scattering. On average, a high energy carrier will transfer an energy $\epsilon \sim E_F$ to an in-equilibrium carrier. Therefore, a single primary photoexcited carrier can share its energy with many carriers, which themselves can scatter with more carriers and reduce their kinetic energy further. Through this cascade, the initial non-thermal distribution of primary photoexcited carriers quickly evolves into a thermalized Fermi-Dirac distribution with elevated temperature (Fig. c). Increasing the excitation power leads to an increase in the steady state temperature of the hot carrier distribution[211].

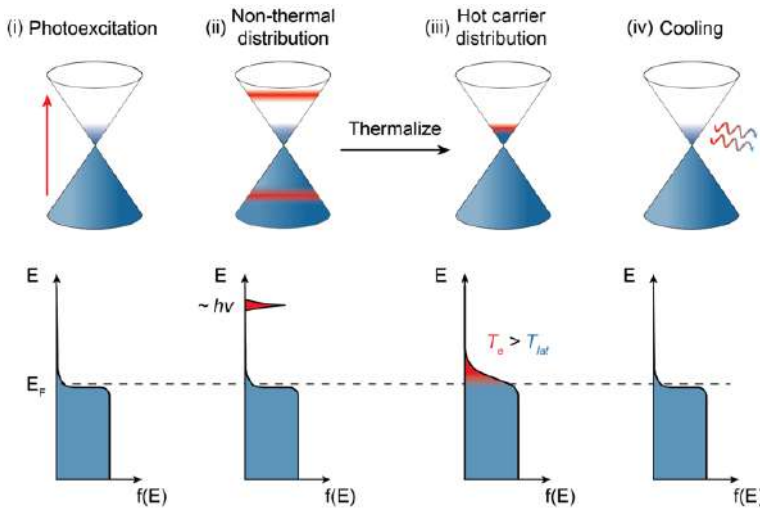

Figure 4.2: Schematic dynamics for hot carriers in monolayer graphene. (i) Graphene absorbs a photon in its equilibrium state at chemical potential μ. (ii) The absorbed energy excites a few electrons to very high energies, of the order of the photon energy. At this stage, the distribution is not thermal. (iii) The primary photoexcited carriers undergo carrier-carrier scattering processes, sharing their energy with the carriers at equilibrium. After a few femtoseconds, a 'hot' Fermi-Dirac distribution is established at the Fermi level. d) The 'hot' carriers relax back to the equilibrium temperature through diffusion, electron-phonon scattering and other mechanisms.

The speed of this thermalization cascade can be controlled through the carrier density (lower carrier densities restrict the number of scattering processes) and the excitation power (higher powers lead to slower and less efficient thermalization)[130, 211]. Note that we refer to thermalization as

the generation of a thermalized carrier distribution in the electron subsystem, not to the equilibration of temperature between the electronic subsystem and the lattice phonons in the sample.

Hot carrier cooling

After thermalization, assuming that the excitation is turned off, the electronic subsystem can equilibrate with the lattice through a variety of microscopic processes (Fig. a). Generally, electron-phonon coupling (either optical or acoustic, from graphene or the substrate) is the main mechanism for cooling the electronic subsystem. As the *e-ph* coupling in graphene is weak, the hot carrier distribution can be long-lived and can be efficiently exploited in devices. Before listing the main cooling mechanisms in graphene, we note that the cooling time at room temperature is ultrafast (few picoseconds) and increases significantly at cryogenic temperatures[130]. This effect can be assigned to the reduced phonon phase space at temperatures below the so-called Bloch-Grüneisen temperature T_{BG}. We also note that primary photoexcited carriers with very high energy may cool down through coupling to optical phonons before thermalization. However, in most cases $\tau_{cool} >> \tau_{therm}$ and cooling takes place after thermalization is complete. We note that we refer to τ_{cool} in other chapters as τ_{th} or simply τ. In this chapter, we use τ_{cool} to avoid confusion with the thermalization time $\tau_{therm} \sim 1$ fs.

Carrier cooling mechanisms in graphene

Here we outline the main cooling mechanisms for hot carriers in graphene. It's important to note that multiple cooling pathways can be active simultaneously. In the end, the measured thermal relaxation time is often agnostic to the cooling pathway and reflects the most efficient process under the given experimental conditions. We also note that a back-flow of energy can happen during the cooling process, i.e. the phonons may feed back energy to the electron subsystem[234]. This effect is most prominent for very high-energy excitations at low sample temperatures.

- **Optical phonons**: Charge carriers with sufficiently high energy can emit an optical phonon, relaxing their excess energy. This process is highly efficient and can compete with the thermalization cascade in a sub-picosecond window. Hot phonons can then relax into lower energy, acoustic phonons. If this cooling process is not fast enough, the optical phonon may be re-absorbed by the electron subsystem. Overall, optical phonon emission is relevant for very large excitation powers that lead to primary photoexcited carriers with very high energies[235, 236] (Fig. 4.3a).

- **Acoustic phonons**: Charge carriers whose energy is not high enough to emit an optical phonon may relax their energy by emission of acoustic phonons. Momentum-conserving scattering between hot carriers and acoustic phonons is much less efficient than optical phonon emission, due to the large momentum mismatch between carriers and acoustic phonons. As momentum is conserved, this scattering process involves acoustic phonons near the Brillouin zone center which can only relax an energy $k_B T_{BG}$ per scattering event. Therefore, many consecutive scattering events are required to relax the energy of the hot carriers (Fig. 4.3a)[237]. All in all, purely momentum-preserving scattering with acoustic phonons should lead to cooling times in the order of nanoseconds[233].

- **Disorder-assisted cooling**: In the presence of disorder, the cooling time determined by acoustic phonon emission can be significantly reduced. In this scenario, often called 'supercollision cooling', the presence of a defect density can overcome the large momentum difference between carriers and phonons, allowing each scattering event to relax more energy (Fig. 4.3a). Through 'supercollisions', scattering between carriers and acoustic phonons becomes much more efficient, leading to picosecond cooling times at room temperature[237, 238].

- **Substrate phonons**: Graphene samples are often encapsulated by hBN layers, which can increase their carrier mobility and act as high-quality gating dielectrics. Hot carriers in graphene can also cool down coupling to phonons in the surrounding hBN layers. In particular, the hyperbolic phonon dispersion of hBN enables efficient near-field coupling of hot carriers to phonon-polaritons at the graphene-hBN interface. This mechanism can be highly efficient, reaching picosecond timescales at room temperature[239].

- **Diffusion cooling**: Hot carrier cooling can also take place through lateral diffusion of the hot carriers away from the local 'hot' area. This process, described by the Wiedemann-Franz law, is only significant for high-mobility samples at extremely low temperatures where nearly all phonon modes are frozen. This cooling mechanism, unlike the ones discussed above, is not encompassed by the term $\frac{dQ_{ext}}{dt}$ in Eq. 4.1. Instead, it will be captured by the term describing current-mediated cooling[72].

- **Other cooling mechanisms**: Additional cooling pathways for hot carriers have been identified in graphene. These include coupling to graphene plasmon modes[240] and direct radiative heat transfer from

the hot carrier system[241]. These cooling pathways are generally inefficient and become only relevant under very specific experimental conditions or in device structures specifically tailored to exploit said effects.

Hot carriers dynamics for MATBG

In the case of magic-angle twisted bilayer graphene, the hot carrier dynamics could differ from those of graphene.MATBG features dispersionless bands at the Fermi energy with bandwidths between 10-20 meV. At larger energy scales, the dispersive bands (both valence and conduction) are separated from the flat bands by a small gap comparable to their bandwidth. The higher energy dispersive bands are less affected by the moiré superlattice and can be roughly modeled as those of intrinsic, AB bilayer graphene. We

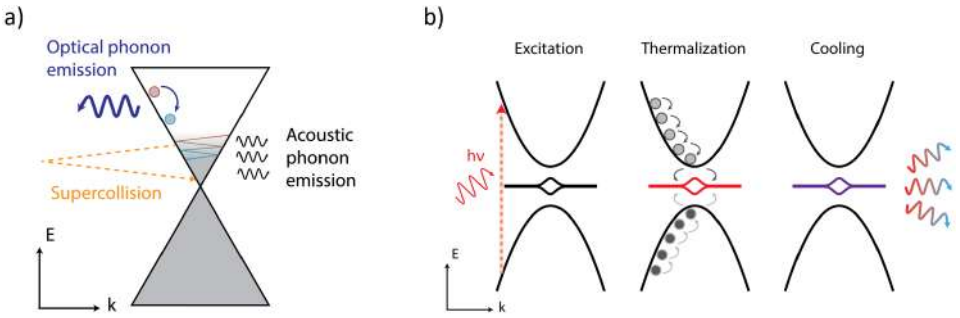

Figure 4.3: a) Schematic for the main phonon-mediated cooling mechanisms in graphene. Supercollisions and optical phonon emission can relax much more energy per scattering event compared to acoustic phonon emission. b) General picture for hot carrier dynamics in MATBG through near-infrared excitation.

excite the samples with near-infrared photons at telecom wavelength (λ = 1550 nm). The energy of these photons (800 meV) is much larger than the energy scales associated with the correlated phenomena in MATBG. Therefore, we expect the fundamental dynamics of the hot carrier cascade in MATBG to be similar to that of (bilayer) graphene (see Figs 4.2 and 4.3b). This assumption is experimentally supported by previous reports[143, 242–245]. Their observations were consistent with the appearance of an elevated temperature of the flat band carriers after above-gap excitation.

Despite the overall cascade being graphene-like, the cooling dynamics may still be significantly affected by the moiré superlattice. As mentioned before, the superlattice potential is expected to fold the phonon bands from bilayer graphene into phononic minibands, which would increase the density of low-energy phonons available for *e-ph* scattering processes[222]. In the

following, we will show that this is indeed the case for hot carrier cooling in MATBG (Fig. 4.3b).

4.2 Complementary techniques to study hot carrier cooling

In this study, we combined two complementary optoelectronic techniques to study the dynamics of hot carrier cooling: time-resolved photovoltage measurements (tr-PV) and continuous-wave (CW-PM) photomixing measurements[169]. We first describe the latter method, which was shortly introduced in the previous chapter. As we exclusively study the cooling time of hot carriers τ_{cool}, from now on we refer to this timescale simply as $\tau_{cool} = \tau$.

After laser mixing, the light intensity reaching the sample will be given by $I(t) = I_1 + I_2 + 2\sqrt{I_1 I_2}\cos\Omega t$, where $I_{1,2}$ represents the intensity from each CW laser and $\Omega = 2\pi c(\lambda_1^{-1} - \lambda_2^{-1}) = 2\pi c(\Delta\lambda)^{-1}$.

Continuous-wave photomixing

The CW-PM technique relies on the optical mixing of two CW lasers which are slightly wavelength-detuned. Here, the central wavelength of both lasers is $\lambda = 1550$ nm and the tunable laser can be detuned by approximately $\Delta\lambda \approx \pm$ 25 nm. The laser mixing will produce an optical beating with envelope frequency $\Omega = 2\pi c(\lambda_1^{-1} - \lambda_2^{-1})$. Thus, the light intensity reaching the sample after photomixing is given by $I(t) = I_1 + I_2 + 2\sqrt{I_1 I_2}\cos\Omega t$, where $I_{1,2}$ represent the intensity from each CW laser and Ω is the heterodyne difference frequency between the two lasers. Then, a new frequency component appears

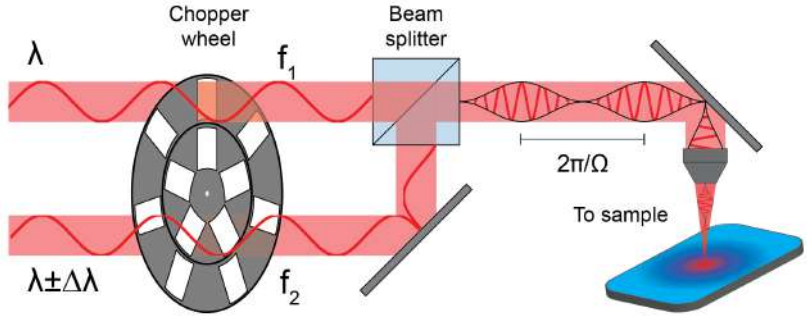

Figure 4.4: Schematic representation of the continuous-wave photomixing process. An optical beating of frequency $\Omega = 2\pi c(\lambda_1^{-1} - \lambda_2^{-1})$ is generated after the laser mixing at the beam splitter.

in the excitation, at the heterodyne difference frequency Ω (Fig.). As mentioned before, the response of the samples to the photomixed laser excitation can be isolated by referencing the lock-in amplifier at the difference frequency between the inner and outer slots of the chopper wheel. It's important to discern between the frequency that characterizes the envelope of the photomixing signal (in the GHz-THz range) and the difference frequency of the chopper (< 1 KHz).

The modulation of the laser field at frequency Ω will effectively provide us with a frequency-resolved technique, which we then translate into the time domain. It is important to note that this technique (as well as the time-resolved photovoltage microscopy) relies on the nonlinear response of the sample. Here, the nonlinearity will arise from the sublinear relation between absorbed power P_{abs} and the increase of electronic temperature T_e. For high excitation powers, the heat absorbed by the system will cause its temperature to increase. We consider here only the electron subsystem and the steady state hot carrier distribution. As the electronic subsystem heats up, its heat capacity C_e will increase accordingly, causing a decrease in the temperature increase ΔT_eproduced by subsequent heat absorption. Thus, the temperature-driven optoelectronic response will depend sublinearly on the absorbed power. This nonlinearity can be exploited to study the cooling dynamics of a system through its optoelectronic response.

We sketch here the origin of the time resolution in the CW photomixing scheme. In terms of the modulation speed, when both lasers have the same frequency $(\Delta\lambda) = 0$ the photomixed signal has a very slow modulation. Then, the sample will be able to relax the acquired energy before absorbing more power in the next cycle of the modulated signal. In this situation, the increase in heat capacity C_e will not take place and the signal will be maximal. As the two lasers are further detuned, the modulation frequency increases and the window for the thermal relaxation of the device τ shortens. Eventually, for fast enough modulation the response of the device will be reduced due to heating effects, as its cooling dynamics cannot follow the modulation speed.

This technique was presented in Ref. [169] and constitutes a simple, yet powerful method to study the cooling dynamics of hot carriers. It has been previously used to study the thermal relaxation time in monolayer graphene[246], as well as the speed of bolometric response in superconducting devices[167]. We provide here a succint mathematical description of the device response under the CW photomixing signal. Ignoring the effects of heat diffusion and current-driven cooling, Eq. 4.1 can be rewritten as:

$$C_e \frac{\partial T_e}{\partial t} = \frac{dQ_{in}}{dt} - \frac{dQ_{out}}{dt} \tag{4.3}$$

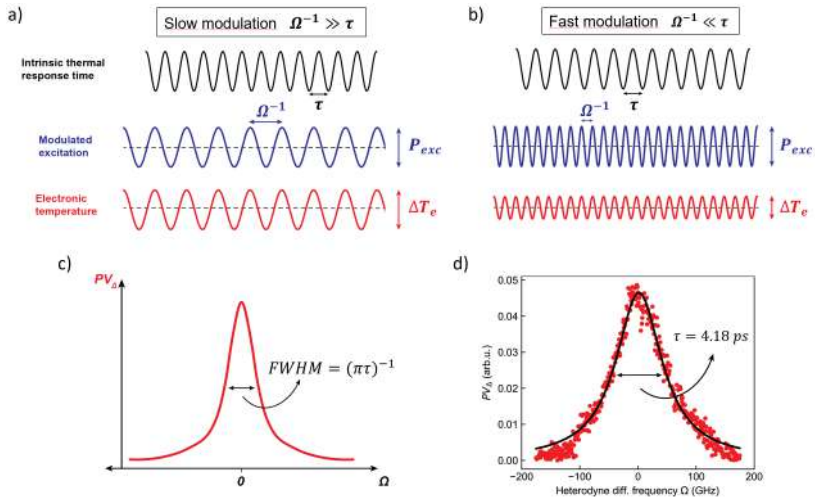

Figure 4.5: a) Time evolution of the electronic temperature T_e for different frequencies of the photomixing signal. When the modulation is slower than the intrinsic relaxation time of the electrons ($\Omega >> \tau_{th}$), T_e can follow the oscillating signal giving raise to a maximal (positive or negative) electron temperature and photoresponse. As Ω is increased, the electron gas does not react fast enough to the modulated excitation and the amplitude of the response is reduced. b) Illustration of the frequency-resolved CW photomixing measurements. Colored dots correspond to the scenarios shown in (a). c) Measurement of τ_{th} in a MATBG sample at two different lattice temperatures.

, where we have explicitly separated the rate of heat added (Q_{in}) and removed (Q_{out}) from the electronic subsystem. The added heat to the system will come from the excitation intensity $I(t) = I_1 + I_2 + 2\sqrt{I_1 I_2}\cos\Omega t$ while Q_{out} will be mediated by carrier cooling through phonons. This equation describes the rate of change in the electronic temperature T_e of the hot carrier distribution after thermalization.

For low-energy excitations, we consider cooling via conventional, momentum-conserving emission of acoustic phonons and 'supercollision' cooling. Then, one can express the evolution of the electronic temperature under photomixing excitation as:

$$C_e \frac{\partial T_e}{\partial t} - \beta_1(T_e - T_l) + \beta_2(T_e^3 - T_l^3) = I_1 + I_2 + 2\sqrt{I_1 I_2}\cos\Omega t \qquad (4.4)$$

, where β_1 and β_2 parametrize the conventional and 'supercollision' cooling rates, respectively. Considering additional phonon-driven cooling mechanisms in this expression does not change the obtained results significantly[169]. As we demonstrate later, this technique is agnostic to the dominant cooling mechanism and can be used to unveil novel cooling pathways.

To establish the connection with the experimental observables, we sort out what is the relation between the measured photothermal response and the electronic temperature in the system T_e. In this experiment, as we established before in 3, the main voltage generation mechanism is the thermoelectric effect where $V(T_e) = S(T_e)(T_e - T_l)$. Considering a fixed lattice temperature T_l, we can find an expression for the intensity-dependent DC photovoltage response. Remember that despite the photomixing scheme, the measurement is performed in DC after demodulating the photomixing response at the chopper's difference frequency. We are interested in the nonlinear components of the resulting DC photovoltage, which are sensitive to the presence of both laser fields. The nonlinear components can be shown to be proportional to:

$$V(I_1, I_2) \propto I_1 I_2 \ (1 + \frac{\gamma^2}{\Omega^2 + \gamma^2}) \tag{4.5}$$

, where $\gamma \equiv (\beta_1 + 3\beta_2 T_l^2)T_e/C_e T_l$ is the linearized cooling rate. This cooling rate quantifies the total relaxation rate, independent of the cooling mechanisms involved. Crucially, from Eq. 4.5 one can see that isolating the response to the photomixing signal (through the appropriate demodulation strategy) yields a DC signal with a Lorentzian dependence on the envelope frequency Ω[169]. The width of the response will be then given by the linearized cooling rate of the system γ. Thus, we can extract the cooling rate of the sample by studying its response to the nonlinear, photomixed excitation as we tune its envelope frequency. The thermal relaxation time will be then given by $(\pi\tau)^{-1}$ = FWHM, where FWHM is defined as the full width at half maximum of the Lorentzian lineshape.

Time-resolved photovoltage microscopy

We now describe the basic principle of tr-PV microscopy[238, 247]. This technique utilizes very short laser pulses (their duration can vary from $\sim$ ps to $\sim$ fs) which are separated by a user-controlled time delay *dt*. Tuning the time delay between the two pulses, one can access the time-resolved dynamics of the system's response. The experiment, performed in Prof. Tielrooij's laboratory, makes use of a Ti:Sapphire laser with a central wavelength of λ = 886 nm and 76 MHz repetition rate. Each laser pulse has an approximate duration of $\sim$ 100 fs. The laser beam is split in two paths and the temporal offset is set by a mechanical delay line for one of the beam paths. Each beam is modulated with an optical chopper. Finally, both beams are combined and focused onto the sample. Scanning mirrors are used to scan the laser beam(s) over the sample (Fig. 2.6a). The electrical readout of the signal is also based on the low-frequency lock-in technique. As previously discussed

for the CW photomixing technique, this technique relies on the nonlinear relation between the absorbed power P_{abs} and the increase in the electronic temperature T_e (Fig. 4.6b). We note that any nonlinearity, not only that associated with photo-thermal response, can be used in these techniques. As illustrated in Figure 4.6c, for vanishing time delays $dt \approx 0$ the generated photovoltage $PV \propto T_e$ is reduced due to heating effects (which increases the sample's heat capacity C_e). Instead, for longer time delays, PV recovers its maximum value. Thus, sweeping the time delay between pulses allows us to resolve the dynamics of hot carrier cooling, i.e. how much time does the system take to relax back to equilibrium upon photoexcitation[238, 247, 248]. The tr-PV response can be modeled through an exponential decay to obtain the thermal relaxation time τ.

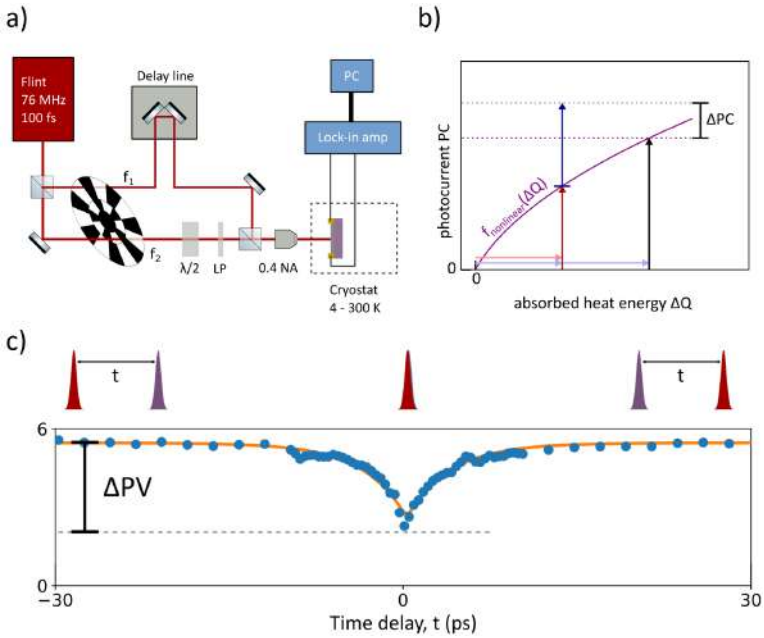

Figure 4.6: a) Optical setup for time-resolved photovoltage microscopy at optical wavelengths. The two pulses are separated in a beam splitter and doubly modulated using a chopper wheel. A delay line is used to controllably delay one of the pulses. Polarization is controlled using a $\lambda/2$ plate and a linear polarizer (LP). Lastly, the two beams are focused onto the sample (inside the cryostat) using an objective with numerical aperture NA = 0.4. b) Sublinear relation between the photothermal response and the absorbed energy. c) Exemplary tr-PV measurement in a bilayer graphene sample. The magnitude of the response decreases when the delay between the pulses is comparable to τ_{th}. Credit images: Jake Mehew.

Differences between the two techniques

The two techniques described above can both access the intrinsic thermal relaxation time of graphene (and moiré graphene) samples. However, they present highly contrasting characteristics, which we summarize here:

- tr-PV resolves the response in the time domain, while CW-PM obtains the response in the frequency domain. Using tr-PV, the delay between pulses can be made arbitrarily large so long cooling dynamics can be easily studied. However, very short dynamics can only be resolved with ultrashort pulses with precisely controlled time delay and spectral characteristics. On the other hand, as CW-PM works in the frequency domain, short cooling dynamics will result in broad features in the detuning axis. Thus, CW-PM can easily access ultrafast dynamics, only limited by the tunability range of the laser source[169]. Conversely, long dynamics are hard to resolve as they require very accurate control of the wavelength detuning, often limited by the laser's bandwidth and spectral width.

- tr-PV utilizes ultrashort laser pulses (below picoseconds) which induce 'transient heating' of the sample, where the sample's electronic temperature will change over time. The electronic peak temperature will decay exponentially. On the other hand, CW-PM works under steady state conditions where the sample is continuously excited. Then, a steady state can form through the interplay between laser heating and electronic cooling. The frequency resolution is achieved through the isolation of the response to the nonlinear photomixing signal.

- As tr-PV uses ultrashort pulses, the power density absorbed by the sample will be quite large and the electronic subsystem can easily reach temperatures in the order of $T_e \sim 1000$ K. Conversely, the CW-PM technique can work at low excitation powers enabling the study of cooling dynamics for $T_e \sim T_l$. Therefore, each technique can access a different regime of electronic temperature after thermalization.

4.3 Studied samples and experimental method

In this work, we study the thermal relaxation time τ of magic-angle twisted bilayer graphene *pn*-junctions using both tr-PV and CW-PM. We explore the dependence of τ with respect to sample temperature, laser power, spot size and filling of the moiré unit cell. Our temperature-dependent studies range from room temperature, where graphene systems exhibit ultrafast cooling times (few picoseconds)[130], down to cryogenic temperatures (∼

5 K) where the cooling time of intrinsic graphene systems slows down significantly[233].

We compare multiple twisted devices with an untwisted AB bilayer graphene sample that does not feature any moiré superlattice or correlated electronic states. All our samples feature a split top graphite gate that is used to define a *pn*-junction (see Figure 4.7). The role of the *pn*-junction is two-fold. First, independent control of the two sides of the junction can help determine the mechanism of photovoltage generation[209, 210]. Second, 'symmetric' doping of the junction, where one side is biased at $+V$ and the other is biased at $-V$, will provide a large, localized photoresponse that can be used to selectively study the photovoltage at the junction. We also choose relatively thin top graphite gates to minimize their light absorption. Panels (c) and (f) in Figure 4.7 show the longitudinal resistance R_{xx} of the AB bilayer sample and the MATBG sample (with twist angle $\theta = 1.24°$, respectively. The low-temperature resistance establishes the emergence of correlated resistive states at integer fillings in the twisted device[4] and the uniform nature of the non-twisted sample.

We note that the focus of this project does not lie in the study of the photoresponse at the correlated states of the MATBG samples. Thus, when doping the *pn*-junctions we do not target integer fillings ν of the moiré flat bands. As we will show, the observed cooling dynamics are largely insensitive to the underlying symmetry-breaking ground states at integer ν.

We study the time- and frequency-dependent response of the *pn*-junctions for 'symmetric' doping conditions under zero applied bias (no source-drain current is applied). Shining with pulsed or continuous laser excitation at the junction interface, we measure the thermal relaxation time under different experimental conditions. For both tr-PV and CW-PM, despite their vastly different peak power density, we maintain a relatively low incident fluence (~ 60 nJ/cm^{-2})

4.4 Temperature-independent carrier cooling in MATBG

Figure 4.8 summarizes the main finding of this study and the starting point for the exploration of hot carrier cooling in MATBG. At a lattice temperature of 25 K, we observe strongly contrasting cooling times between the MATBG and AB samples, where the twisted device has a much faster cooling time. While the AB bilayer device exhibits a cooling time $\tau \sim 25$ ps, consistent with the values found in the literature at this temperature, electron cooling in MATBG is ultrafast and we observe $\tau \sim 3$ ps. While the traces shown in Fig. 4.8 correspond to tr-PV measurements, the same

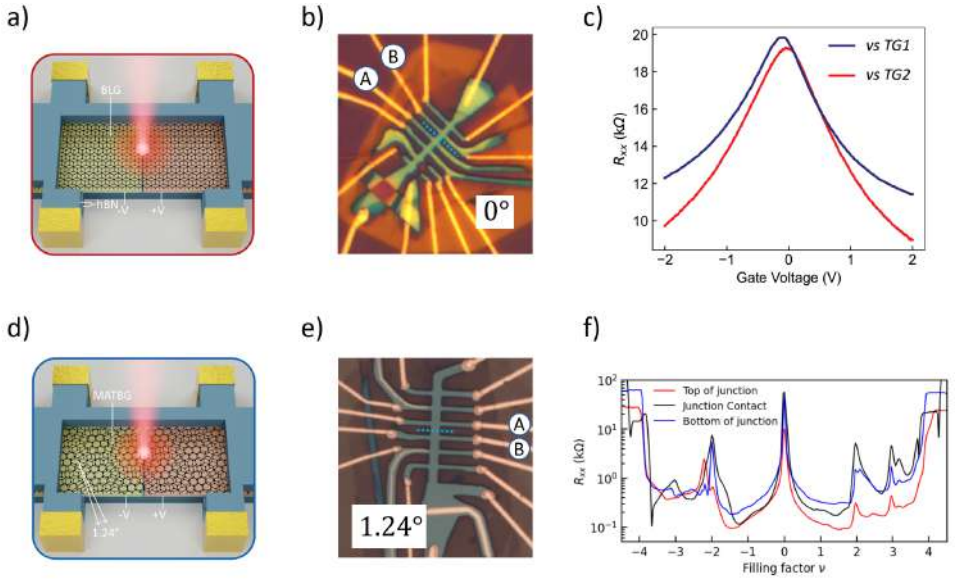

Figure 4.7: (a) and (d) sketch the experimental concept, where we study the optoelectronic response of two *pn*-junctions: one in AB bilayer graphene (a) and one in MATBG (d). (b) and (e) present optical images of the two *pn*-junctions. The contacts at the junction are labeled A and B. (c) and (f) show the gate-dependence of R_{xx} on the non-twisted and MATBG samples, respectively. After splitting the top gate, we also check the transport characteristics at each side of the junction. The correlated states in (f), which exhibit virtually no changes between adjacent contacts, demonstrate the homogeneous twist angle (1.24°) in the MATBG device. Credit for panel (f): Jaime Díez Mérida.

behaviour was also observed in the CW-PM measurements.

This striking difference in electron thermal relaxation time, nearly a full order of magnitude, calls for the examination of the possible mechanisms for hot electron relaxation in MATBG. From this observation, we hypothesize that the moiré superlattice plays a central role in the enhanced low-temperature cooling time. In the following, we will contrast the experimental observations with the different cooling mechanisms we have introduced. First, we probe the evolution of τ as a function of lattice temperature.

Figure 4.9a shows the temperature-dependent cooling time for hot carriers in the AB graphene sample and one MATBG device (twist angle 1.24°). For the non-twisted sample τ increases as the temperature is decreased, from $\sim$ 3 ps at room temperature to $\sim$ 25 ps at 5 K. This is consistent with less efficient *e-ph* scattering due to a reduced phonon phase space at low temperatures[249]. Notably, for the magic-angle samples, the electron

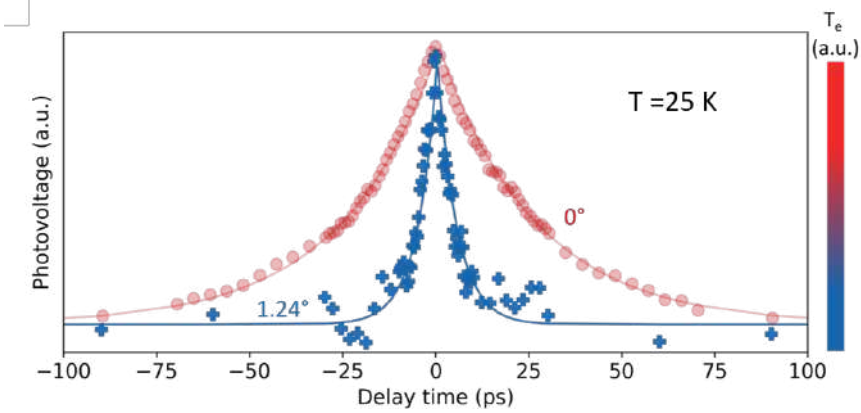

Figure 4.8: Cooling time for twisted and non-twisted bilayer graphene samples at $T = 25$ K. The cooling time in MATBG is markedly faster than in the non-twisted sample.

cooling time remains ultrafast (about 3 ps) from room temperature to 5 K. It becomes apparent that an additional cooling pathway is present in MATBG samples when compared to the intrinsic bilayer. This pathway remains efficient down to the lowest temperatures in our experiment. A natural candidate for this scattering mechanism is the coupling to moiré phonons, which result from the formation of phononic minibands in the presence of the superlattice potential[222].

As shown in Figure 4.9b, all conventional phonon-driven cooling mechanisms slow down appreciably at low temperatures. In the case of optical phonon emission, a very large electronic temperature (thousands of Kelvins) is required to couple to these high-energy phonons[235, 236, 250]. This process is highly inefficient at cryogenic temperatures. Acoustic phonon emission is also quenched due to the reduced phonon space at T_l and should yield cooling times which are orders of magnitude slower ($\sim$ ns)[233]. While disorder-assisted cooling and coupling to the hyperbolic phonons of hBN are more efficient at intermediate temperatures ($\sim$ 100 K), these mechanisms should also slow down when approaching cryogenic temperatures[234, 238]. At the lowest temperature of $T = 5$ K, supercollision cooling would yield $\tau \sim 100$ ps - 10 ns and cooling through hBN phonons is already slower than the observed τ at 200 K.

Thus, we conclude that the observed ultrafast thermal relaxation in MATBG cannot be accounted for by these conventional phonon-driven mechanisms. We note, however, that the observed cooling time for AB graphene at 5 K is lower than the expectation from these cooling pathways. We therefore explore diffusive cooling which does not rely on phonon emission

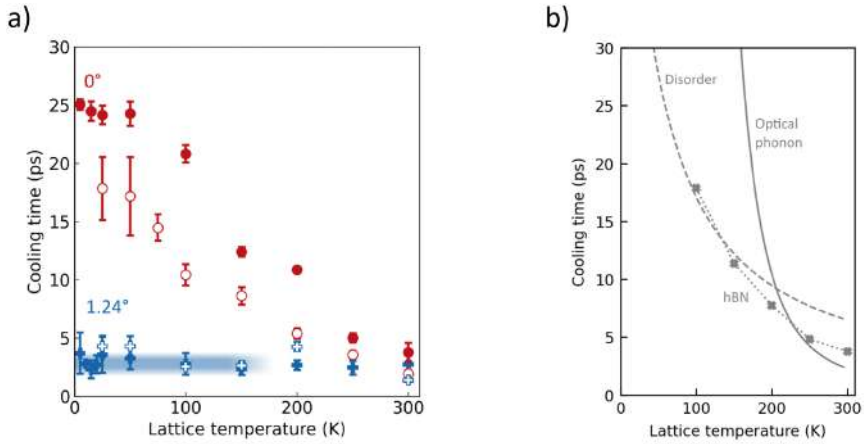

Figure 4.9: a) Temperature dependence of the cooling time. Strikingly, the cooling time for both MATBG samples remains ultrafast at cryogenic temperatures. Empty symbols correspond to CW-PM data. b) Calculated temperature dependence of the main phonon cooling mechanisms.

and can be more efficient at low temperatures[72, 251].

Diffusive cooling describes the motion of hot carriers away from the excitation spot, effectively lowering the local electronic temperature. Experimentally, we can vary the size of the laser spot to check for diffusive cooling. If the dominant cooling mechanism is diffusive, larger spot sizes would lead to longer thermal relaxation times, as the hot carriers need to diffuse longer distances to exit the excitation spot. Figure 4.10 presents the spot size dependence of the carrier cooling time.

For the AB bilayer sample, τ increases with increasing laser spot size at temperatures below 100 K. We find that its cooling dynamics, particularly at 25 K and 50 K, are well explained by a diffusive mechanism 4.10b. For 100 K, the spot size dependence is less pronounced as the carrier mobility is decreased and the diffusion process slows down. Even then, we observe an increase in the thermal relaxation time with increasing size of the excitation spot.

In the MATBG samples, τ remains ultrafast and unchanged by the increasing spot size. This finding strongly suggests that diffusive cooling is not the main mechanism for the energy relaxation of the hot carriers in MATBG. Thus, within the micron-scale laser spot, heat will not spread in space. Instead, our observations indicate that hot carriers in MATBG can relax their energy before diffusion takes place.

Next, we study the dependence of the thermal relaxation time on electronic temperature. Tuning the power of the laser excitation, we can control the initial temperature of the primary photoexcited electrons which in turn

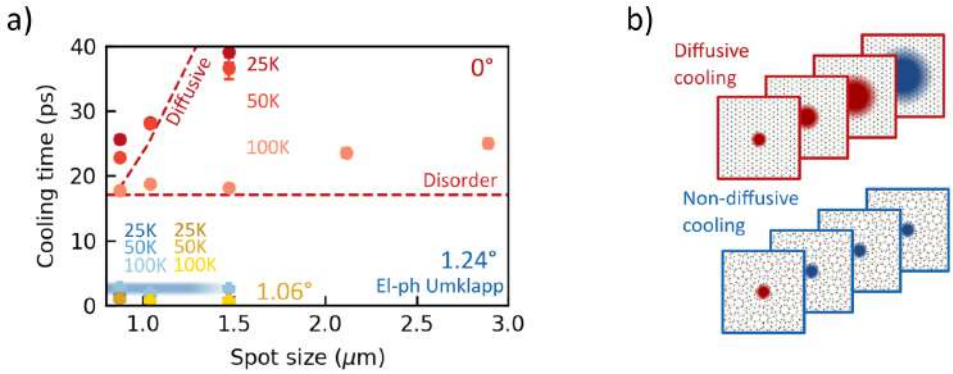

Figure 4.10: a) Cooling time vs. laser spot size at different temperatures. For MATBG, we verify the results with a second device (twist angle 1.06°) The cooling dynamics of the twisted samples are unaffected by the laser spot size. For the AB bilayer sample, τ increases at larger spot sizes, suggesting that diffusion cooling plays a role in its dynamics. b) Visual representation of the diffusive cooling in AB bilayer graphene and its absence in MATBG.

will determine the density of hot carriers in the dispersive bands[130]. As we described before, the tr-PV measurements utilize much higher excitation powers than for CW-PM.

Increasing the hot carrier population in the dispersive band could lead to bottleneck effects that slow down the cooling process. Bottleneck effects could appear for *e-ph* scattering processes (if the hot carrier population saturates the available cooling channels) or for phonon-phonon processes (typically involving the relaxation from optical to acoustic phonons)[234]. Re-thermalization of the electrons can occur in these circumstances, leading to slower τ.

Figure 4.11 the power dependence of the cooling time for the MATBG and untwisted samples. The AB graphene sample exhibits a weak power dependence, where the cooling time increases by 20 % between the CW-PM and the tr-PV datasets. Note that the change in power is of several orders of magnitude. For MATBG we do not observe any power dependence, suggesting that there are no bottleneck effects and the cooling remains ultrafast independent of lattice and electronic temperature. This observation also indicates that at partial filling of the flat bands, the interband transition between the dispersive and the low-energy flat bands does not limit the rate of cooling (Fig. 4.11). This interband transition must take place on a faster timescale than the observed τ, even when the hot carrier population in the dispersive bands is increased.

As the cooling mechanism appears to be driven by the moiré superlattice, we now explore its dependence on the filling ν of the moiré unit cell. We

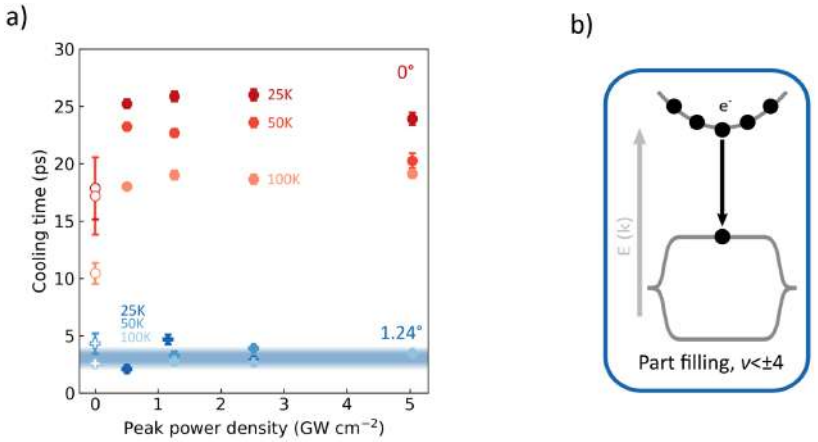

Figure 4.11: a) Carrier cooling time for increasing power density. Both samples exhibit a weak dependence on optical power. Note that the power is markedly different between the CW-PM (low power) and tr-PV measurements (high power). Empty symbols correspond to CW-PM data. b) Interband relaxation process between the dispersive and flat bands. For partial filling of the flat band, no bottleneck effect was observed.

define $\nu = \pm 4n/n_s$, where n_s is the carrier density corresponding to a fully filled moiré band. As previously discussed, we gate the *pn*-junctions in a symmetric configuration so each filling factor ν corresponds to gate voltages $V(\pm\nu)$ for each gate. At full filling of the bands ($\nu = \pm 4$), the system is expected to behave as a conventional narrow gap semiconductor as all the states below (above) the dispersive conduction (valence) band would be occupied (empty).

Figure 4.12a illustrates the cooling time τ across the entire doping range of the flat bands. The thermal relaxation time remains nearly constant when the flat bands are partially filled. This suggests that the correlated electronic ground states that emerge at integer ν do not affect the cooling dynamics. Near charge-neutrality ($\nu \sim 0$), the error bars grow larger because the response of the junction in this configuration is smaller in magnitude.

For full filling of the bands, either with electrons or holes, the cooling time exhibits a five-fold increase. As demonstrated by the highly resistive behaviour (see R_{xx} data), at $\nu = \pm 4$ the moiré unit cell is fully filled and the chemical potential lies in the band insulators. Then, hot carriers in the dispersive bands cannot relax into the flat bands due to the Pauli blockade and their cooling becomes slower (Fig. 4.12b). Furthermore, at full filling of the moiré unit cell, we observe a strong dependence of τ with excitation power (see Figure 4.12c). In contrast to the case of partial filling, a bottleneck exists for the relaxation of hot carriers into low-energy bands where efficient

scattering mechanisms are available.

All in all, the findings described here strongly suggest that the moiré superlattice potential and the enhanced density of low-energy phonons (arising from the phonon band folding) are responsible for the observed ultrafast carrier cooling. Next, we will describe a novel electron-phonon scattering mechanism, electron-phonon Umklapp scattering[252], which explains the experimental observations and is unique to moiré graphene systems.

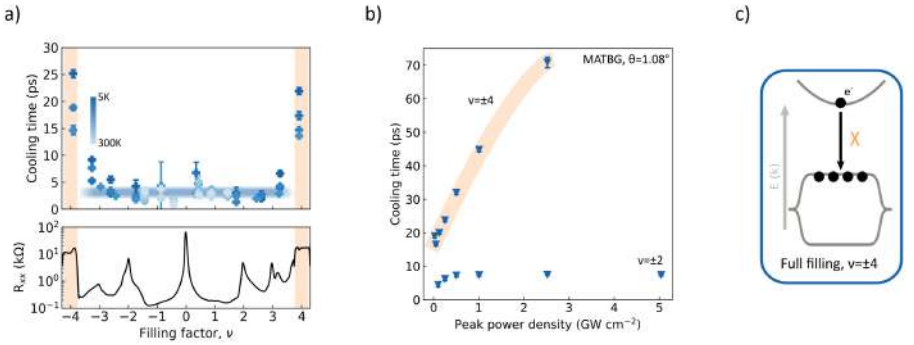

Figure 4.12: a) Cooling time across the flat bands for the 1.06º MATBG device. τ remains nearly constant for a partially-filled flat band. The cooling time rapidly increases when the bands are nearly full. No features were observed at integer filling factors ν. b) Bottleneck for hot carrier cooling for full filling of the flat bands. c) Band diagram illustrating the cooling bottleneck due to Pauli blockade in the flat bands.

4.5 Ultrafast cooling via novel Umklapp *e-ph* scattering

Here, we describe the modelling of the experimental observations based on a novel mechanism for energy relaxation, electron-phonon Umklapp scattering[252]. This mechanism naturally accounts for the highly efficient, temperature-independent hot carrier cooling we observe. Umklapp *e-ph* cooling is enabled by the coalescence of three different effects in magic-angle graphene: (1) the increased density of low-energy moiré phonons at the superlattice scale (Fig. 4.13a), (2) the reduced Fermi surface from the moiré mini-Brillouin zones (Fig. 4.13b) and (3) the presence of highly localized Wannier orbitals at the AA sites (Fig. 4.13c). First, we describe the two relevant regimes in the model.

The theoretical modelling is based on Boltzmann transport theory. At high lattice temperatures, we consider a minimal model for MATBG consisting of four bands, two flat bands with bandwidth W and two dispersive

bands whose band edges lie at energy $\pm\Delta$ (Fig. 4.14a). This temperature regime is defined by the condition $T_l > \Delta$, where the electron population at the dispersive bands cannot be neglected. For realistic parameters in MATBG, this high-temperature regime corresponds to 150 K $< T_l <$ 300 K. In this regime, intra-dispersive band scattering processes dominate the cooling rate τ^{-1}, while interband (between dispersive and flat bands) and intra-flat band scattering processes have negligible contributions (Fig. 4.14a). For intra-dispersive band scattering mediated by Umklapp *e-ph* processes, we estimate the thermal relaxation time using this expression:

$$\tau^{-1} = \frac{6\rho_1}{\pi T_e} \sum_m \omega_m^2 (\left\| g_m^{1,1} \right\|^2 + \left\| g_m^{-1,-1} \right\|^2) \tag{4.6}$$

, where ρ_1 is the density of states in the dispersive hole or electron band, $g_m^{n,n}$ is the *e-ph* coupling in the nth band and ω_m is the phonon frequency at the mth band. From this formula, we directly estimate the cooling time τ in the high-temperature regime. We find a cooling rate that is independent of the lattice temperature T_l, in agreement with the experimental observations (see Fig. 4.9a). For low lattice temperatures, we can neglect the dispersive

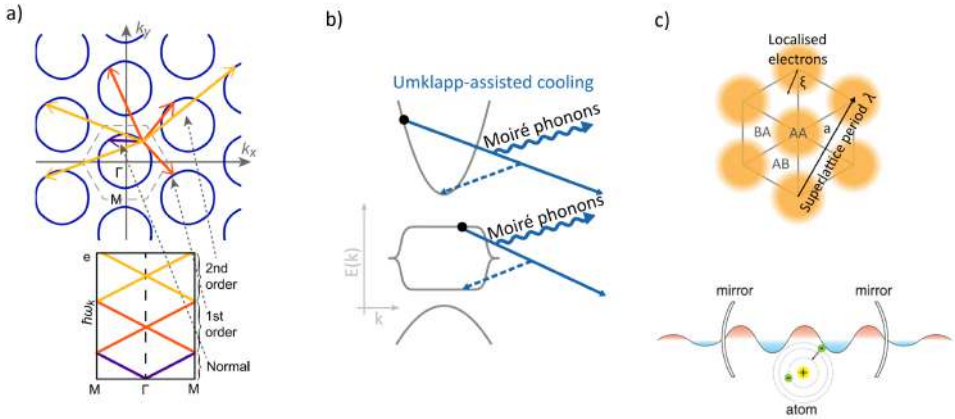

Figure 4.13: a) Higher-order moiré phonons and the allowed *e-ph* scatterings. As shown in the lower panel, the superlattice formation folds the phononic spectrum and increases the density of low-energy modes. b) Umklapp-assisted cooling represented in a schematic band diagram. The superlattice modulation creates moiré phonons that can provide the momentum kick to enable more efficient cooling. c) Upper panel: Orbital localization in the AA sites of the moiré superlattice. The Wannier orbitals are tightly confined in the moiré length scale. Lower panel: Schematic for the Purcell effect in atomic physics. Panel (a) adapted from Ref. [222]. Lower figure in panel (c) adapted from Ref. [253].

bands in the cooling process as now $T_l < \Delta$ (Fig. 4.14a). Then, as electron cooling will take place from the low-energy flat bands, we must account for

the localized Wannier orbitals that compose most of the flat band electronic states. Strong localization of these Wannier orbitals (in the scale of the superlattice potential) has been observed in local probe measurements. The radius of the Wannier orbitals is therefore much smaller than the superlattice period λ. In the calculations, we assume the radius of the Wannier orbitals to be $\xi \sim a/6$.

The presence of localized electron orbitals will modulate the *e-ph* coupling strength in the system. Now, the average momentum transfer q for an *e-ph* scattering event involving the localized orbitals will be $q \sim 1/\xi >> 1/a$. Thus, the localized electron orbitals enable the scattering with phonons of large momentum, which would be prohibited in the absence of the orbital localization on the superlattice scale. Therefore, flat band electrons can undergo Umklapp-scattering with these large momentum phonons, being coupled outside the first Brillouin zone.

It's important to note that the Umklapp electron-phonon mechanism differs from supercollision cooling[238], which relies on a significant density of defects. The superlattice period can provide the required large momentum scattering for efficient cooling, without the need for defects. Therefore, the system can exhibit simultaneously ultrafast relaxation time and high mobility in the absence of defects. In this temperature regime, we compute

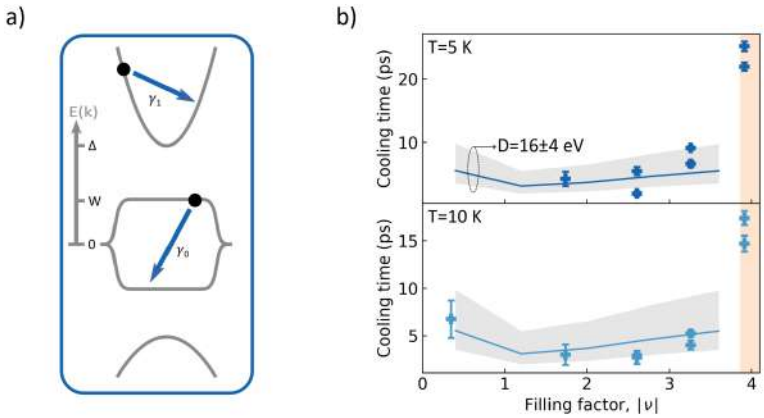

Figure 4.14: a) Band diagram for the two intra-band scattering processes considered in the four-band model. b) Calculation of the Umklapp-assisted cooling time for MATBG at low lattice temperatures. The model successfully captures the speed of the cooling process and its weak filling factor dependence.

the thermal relaxation time τ from the equation describing the cooling rate in the steady state:

$$\tau = \frac{C_e(T_e - T_l)}{J} \tag{4.7}$$

, where J is the cooling power in the system. For the calculated cooling

times, one needs to assume a deformation potential that parametrizes the *e-ph* coupling in the system. We used a deformation potential $D \sim 16$ eV, compatible with previously reported values in graphene. Figure 4.14b depicts the results of the calculations for the thermal relaxation time at low lattice temperatures. Indeed, we observe ultrafast cooling times both for 5 K and 10 K which remains nearly constant as a function of filling, as long as the flat bands are not fully occupied. Therefore, we conclude that our experimental observations are consistent with electron-phonon Umklapp scattering, enabled by the moiré superlattice. For further information on the theory model and the explicit calculations, we refer the reader to Refs [222, 252].

It is informative to draw an analogy between the scattering mechanism discussed here and the Purcell effect from atomic optics. In the Purcell effect, a single atom embedded in an optical cavity will exhibit an enhancement of its spontaneous emission rate (upper panel Fig. 4.13c)[254]. This enhancement stems from the localization of the optical modes inside the cavity, which leads to stronger interaction between the optical modes and the electron orbitals in the atom.

In MATBG, we can conceptually replace the electron orbitals (bound to the atom) with the tightly localized Wannier orbitals in the AA sites of the superlattice, and the photonic modes with phonon modes. Then, an increased phonon emission rate would be expected from the enhanced interaction between phonon modes and localized Wannier orbitals (Fig. 4.13c)[200, 255]. It is precisely this enhancement in the phonon emission rate that leads to the ultrafast, low-temperature cooling observed in the experiment.

It's worth noting that the *e-ph* Umklapp mechanism is fundamentally different from phonon-phonon Umklapp scattering (which sets the thermal conductivity in low-mobility systems) and electron-electron Umklapp scattering[256, 257] (predicted but often obscured in the low-temperature resistivity of ultraclean metallic systems). The *e-ph* Umklapp scattering discussed here is uniquely enabled by the combination of a long-range superlattice, small Fermi surfaces, and localized electron orbitals. As we have shown, this mechanism remains efficient across a very wide range of temperatures.

Chapter 5

Telecom photodetectors based on 2D high-T_C superconducting devices

In this chapter, we will describe our efforts to advance the technology of superconducting photodetectors by employing a high-T_C superconductor. In particular, we will focus on the layered cuprate superconductor BSCCO-2212, whose superconducting transition temperature reaches ∼90 K even in the 2D limit[89]. Cuprate-based devices could be operated at liquid nitrogen temperature (77 K), drastically reducing the cryogenic requirements for the operation of superconducting devices[145]. Although this prospect has been a topic of discussion since the discovery of high-T_C superconductors, it has faced a multitude of challenges that precluded its realization. The main bottleneck in the development of HTS devices is their chemical instability[151], as they quickly degrade under ambient conditions. The strategies we developed to avoid degradation are extensively described in the fabrication methodology.

Here, we first outline the concept of superconducting photodetectors and their technological relevance, as well as describe the main photoresponse mechanisms that underlie these devices. Next, we describe the transport characterization of the superconducting nanostructures based on exfoliated thin flakes of BSCCO-2212. Then, we will present and characterize two different BSCCO-2212 photodetectors that operate under different photoresponse mechanisms. The device characteristics (sensitivity, operation conditions, speed) of each photodetector are also presented.

5.1 Superconducting photodetectors and photoresponse mechanisms

Superconducting photodetectors in technology

The superconducting state, characterized by zero electrical resistance and perfect screening of magnetic fields, is separated from the 'normal' phase by a phase boundary characterized by a critical temperature T_c, supercurrent density J_c and magnetic field B_c (see Fig. 5.1a). The transition between these two states across this phase boundary is extremely sharp, regardless of which of the critical magnitudes is exceeded. This forms the basis for a variety of quantum sensing devices. Superconducting photodetectors in particular rely on light absorption to trigger a transition across this phase boundary[258]. The main advantage of superconducting photodetectors over those based on semiconductors is their broadband sensitivity, only limited by small superconducting gaps $\Delta \sim$ meV. In addition, they don't dissipate as much energy as semiconducting devices and exhibit faster response times[258]. While the concept of superconducting photodetectors dates back several

Figure 5.1: a) Schematic phase diagram of the superconducting phase in low-temperature superconductors (LTS) and high-temperature superconductors (HTS). b) Illustration of high-speed optical communications. Credit: TELESAT. c) Concept for on-chip photonics in a planar waveguide platform. Credit: R.J. Shiue and D. Englund.

decades, it came into focus with the demonstration in 2001 by Goltsmann *et al* of single-photon detection by absorption in a biased superconducting nanowire[259, 260]. The remarkable performance and conceptual simplicity of these devices kickstarted the 'modern' generation of superconducting single-photon detectors. Today, superconducting single-photon detectors based on calorimetric or avalanche-type response are widely used in technologies for the detection of faint signals[258]. Their applications range from detection of faint photon sources in astronomy[261] and deep-space optical communications[262](Fig. 5.1b), all the way to photonic quantum computing in free space or on-chip photonic circuits[263, 264] (Fig. 5.1c). Extensive

research efforts aim not only to optimize the device performance for these applications but also to provide cheaper and more flexible detection systems that extend single-photon detection to other areas[265].

Bolometric photodetectors

Superconducting bolometers (or transition edge sensors) are photodetectors based on the large dR/dT in a superconductor near its critical temperature T_c (Fig. 5.2a). A low-T_c superconducting film acts as the active element with a very low heat capacity C. Thanks to their minute heat capacity, the absorption of low amounts of energy can induce a large temperature increase in the device, whose resistance will then change as dR/dT[261]. Figure 5.2b sketches a two-temperature model for a bolometric system. The active element (with temperature T and heat capacity C) is thermally isolated from the environment (at temperature T_{bath}) by a weak thermal link. The rate at which the active element and the bath exchange energy is characterized by the thermal conductance G_{th} and thermal relaxation time τ.

Ultimately, the sensitivity of the bolometer is set by the sharpness of the superconducting transition and the thermal properties of the active element[261]. To maximize the device responsivity, one must carefully engineer the thermal link between the active element and the environment. Increased thermal isolation leads to higher sensitivity but slower recovery times.

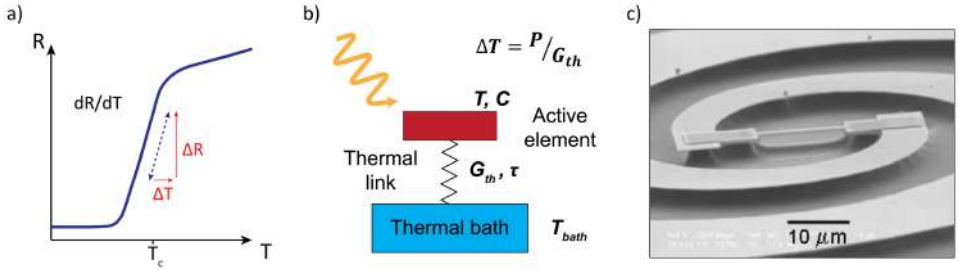

Figure 5.2: a) Superconducting transition with large dR/dT value. b) Schematic of the bolometric detection principle. Here, T, C, G_{th}, τ and T_{bath} represent the temperature of the active element, its heat capacity, the thermal conductance between the bolometer and the thermal bath, the thermal relaxation time of the system and the bath temperature, respectively. c) SEM image of a suspended bolometer embedded in a THz antenna. Credit: Ortolani, M. at CNR-IFN

The optimal readout circuit for a superconducting bolometer is based on a superconducting quantum interference device (SQUID) that inductively senses the current flowing through the bolometer. As the absorbed energy

breaks Cooper pairs in the active element, its temperature and resistance increase. The consequent decrease of the current flowing through the device is accurately sensed by the SQUID. Thus, superconducting bolometers can be operated in a free-running, continuous operation mode. We note that in our studies, the bolometric response does not require a complete breakdown of superconductivity in the device. It's worth noting that bolometers are calorimetric detectors, as they are sensitive to the total amount of deposited energy. This enables bolometers to discern the number of absorbed photons for a given wavelength λ. The main drawbacks of bolometers are often their slow response time ($\sim$ ms) and the need for very low cryogenic temperatures ($\sim$ mK). In addition, they must be carefully designed to engineer the thermal link (see Fig. 5.2c).

Current-driven avalanche photoresponse

Superconducting nanowire single-photon detectors (SNSPD) constitute the state-of-the-art technology in terms of single-photon detection[266]. SNSPD's are based on a non-bolometric detection mechanism that relies on an avalanche process driven by the photon absorption. They consist of long superconducting nanowires (widths $\sim$ 50 - 300 nm) which are often patterned into a meandering shape to maximize the active area of the photodetector (Fig. 5.3a). The SNSPD is current-biased close to its critical current $I_b \approx I_c$ and is operated below its T_c. We briefly describe a general picture of the detection mechanism in a current-biased SNSPD.

Photoabsorption leads to Cooper pair breaking, generating a local hotspot of quasiparticles in the nanowire. In the hotspot, the superconducting phase is suppressed and the device becomes locally resistive, dissipating energy. Due to the current bias I_b, a fixed amount of current is now being pushed through a smaller (superconducting) cross-section of the nanowire. Thus, the critical current density J_c may be exceeded, leading to an avalanche effect in which the entire nanowire cross-section turns resistive and blocks the supercurrent flow[267–269]. After the avalanche process, whose exact dynamics are still an open question, no supercurrent can flow through the nanowire and the device behaves as a resistor of value R_N. These dynamics are sketched in Figure 5.3b.

From a circuit perspective, the SNSPD can be simply modeled as a variable resistor that switches from $R_{SC} = 0$ to R_N if a photon is absorbed. Due to the photo-induced change of resistance, a voltage peak will appear in the readout circuit of the SNSPD (see Fig. 5.3c). As we will show next, the voltage peak is not measured directly across the SNSPD terminals. After amplification of the voltage signal, this simple device concept enables the transduction of a microscopic excitation into a macroscopic, measurable

signal.

Unlike in a bolometer, superconductivity is quenched across the entire SNSPD so one must reset the device to keep detecting photons. This can be simply done through the use of a shunt resistor, connected in parallel with the nanowire[266]. Once the SNSPD becomes resistive, the bias current is shunted to said resistor, Joule heating is quenched in the nanowire and it can be cooled back to its superconducting state. The voltage spike resulting from the resistive switching of the SNSPD is measured across this load resistor, which abruptly receives an increased current flow. The readout circuit of

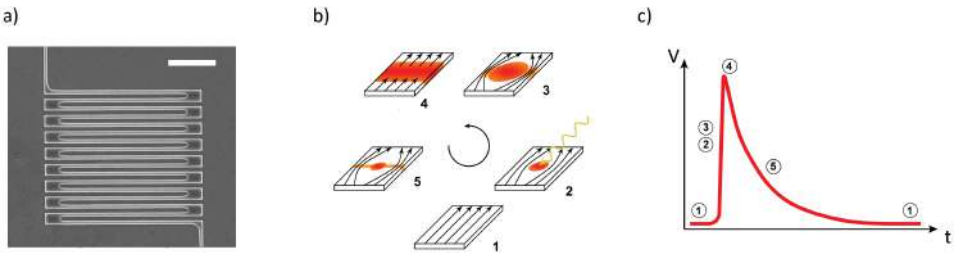

Figure 5.3: a) Exemplary SNSPD formed by a long meandering nanowire. Scale bar represents 1 μm. Credit: NIST. b) Schematic of dynamics of Cooper pair breaking and hotspot creating in a biased superconducting nanowire. Numbering of the different stages corresponds to subfigure (c). Adapted from Ref. [270].c) Illustrative voltage pulse generated by the hotspot avalanche effect in an SNSPD. Initially (1), the device is superconducting and no voltage drops across the shunt resistor. In stages (2) and (3), Cooper pair breaking from the absorbed photon creates a resistive hotspot and the nanowire's effective superconducting area is reduced. Thus, the voltage at the shunt resistor grows. (4) Superconductivity is fully destroyed in the nanowire cross-section, and all current flows to the shunt resistor. (5) As Joule heating decreases, the bias current returns to the nanowire and the detector returns to stage (1).

the SNSPD can be optimized to minimize the reset time, which is set by the relative values of the shunt and device resistance, as well as the kinetic inductance of the nanowire L_k. We refer the reader to extensive literature on the reset dynamics of these devices[271–274]. Further discussion of the readout circuit will be presented in a later section. One further advantage of SNSPD's is their very low jitter time, which sets the timing information for the arrival of the absorbed photon. An optimized SNSPD can detect a photon with $\sim$ ps resolution on its arrival time[275], which is highly desirable for applications in quantum communications[276, 277]. Overall, SNSPD's have high detection efficiency, low dark count rate, high detection speed and low jitter time[258].

Other photoresponse mechanisms

We note here other superconducting photodetectors besides superconducting bolometers and SNSPD's, which are based on alternative detection principles. Namely, superconducting tunnel junctions[278] (STJ) and microwave kinetic inductance detectors (MKID)[279], STJ's are voltage-biased superconducting junctions in which photo-absorption leads to a finite tunnel current in the direction of the applied voltage. The magnitude of the tunnel current is proportional to the absorbed photon energy. STJ's have been primarily employed for the detection of high-energy X-ray photons[280].

MKID's are based on high-quality factor superconducting resonators with a characteristic resonant frequency f_0[279]. When a photon is absorbed in the resonator Cooper pair breaking leads to a decrease of the superconducting carrier density, which in turn increases L_k in the resonator. Thus, the internal quality factor of the resonator decreases and its resonant frequency f_0 is shifted. These photo-induced changes can be read out by embedding the MKID into a resonant microwave circuit. MKID's are mainly used in astrophysics applications[279] as a compact and lower-cost alternative to superconducting bolometers.

Two-dimensional High T_c superconductors for photodetection

The motivation behind the design of superconducting photodetectors based on high T_c materials is clear: extending their operation temperature beyond liquid helium temperature ($\sim$ 4.2 K). A BSCCO-2212 photodetector could, in principle, be operated up to its critical temperature of about $T_c =$ 90 K. This would drastically reduce the cryogenic constraints for the use of superconducting photodetectors[145], allowing the design of cheaper, more flexible photodetection systems which could be used in a wider range of applications[265].

Current bolometer and SNSPD technologies are based on low T_c superconducting thin films such as NbTiN, WSi or Al. These materials can be readily grown and patterned into various nanostructures using standard cleanroom fabrication. However, superconductivity in these films is intrinsically three-dimensional, implying that for ultra-thin films the superconducting behaviour would be lost. This limits the design of low-heat capacity, two-dimensional superconducting devices. Here, we adopt an alternative strategy based on the cuprate superconductor BSCCO-2212 whose layered crystal structure, pictured in Fig. 5.4a, allows the mechanical exfoliation of high T_c superconducting flakes. Remarkably, the superconducting properties of a pristine monolayer of BSCCO-2212 were found to be nearly identical to the bulk superconducting properties[89, 282] (Fig. 5.4b). The study of few-layer

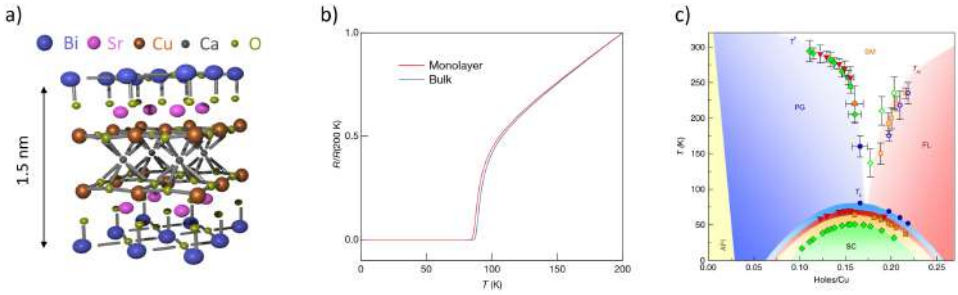

Figure 5.4: a) Crystal structure of a BSCCO-2212 monolayer (half unit cell). Each atomic species is color-labeled. The crystal always cleaves at the BiO layer. b) Superconducting transition for a BSCCO-2212 monolayer and the bulk crystal. c) Phase diagram for few-layer BSCCO flakes. These ultra-thin flakes can be doped electrostatically to access different regions of the phase diagram within a single device. Comparing this phase diagram with that of Fig. 1.4c, we can see how the essential physics of cuprate superconductivity can be accessed in the 2D limit. Panels (b) and (c) adapted from Refs. [89] and [281]

BSCCO-2212 samples allows for unprecedented control of its properties, which can be explored in a single device via electrostatic gating[281] (Fig. 5.4c). One can use the fabrication techniques of van der Waals assembly of 2D layers to build functional superconducting devices based on high-quality BSCCO-2212 flakes. As described in the Methods, we developed a fabrication strategy for BSCCO-2212 hBN heterostructures tailored to avoid the degradation of the thin superconducting flakes. Furthermore, we leveraged the sensitivity of the superconducting state to the oxygen doping level (see Figs. 1.4c and 5.4b) to directly pattern nanostructures on the BSCCO-2212 flakes without any etching or milling process. The He-FIB patterning process enables us to locally modify the hole concentration in the 2D BSCCO-2212 layer.

5.2 Transport characteristics of 2D BSCCO-2212 nanostructures

In this section, we describe the transport measurements performed on our 2D BSCCO-2212 nanostructures. The aim of these studies is the characterization of their superconducting properties for their use as superconducting photodetectors. We focus on BSCCO-2212 as it has a layered crystal structure, from which we can exfoliate thin flakes and assemble van der Waals heterostructures.

Depending on their transport characteristics, the devices may be used in a bolometric or an SNSPD-like detection scheme. The initial characterization

of the devices before He-FIB patterning in the inert atmosphere probe station was previously described in the fabrication chapter. After the patterning, we repeat said measurements now inside the Attodry800 cryostat before cooling down the sample to cryogenic temperatures.

Superconducting transitions

As the sample cools down from 300 K to the base temperature of $\sim$ 6 K, we measure its resistance (in either 2-probe or 4-probe configuration) as a function of temperature. From this one can confirm the superconductivity in exfoliated BSCCO-2212 flakes, as well as evaluate the quality of the electrical contacts or the damage induced by the patterning process. While most devices are operated as detectors in a 2-probe configuration, we present 4-probe data of unpatterned devices to highlight the zero resistance state of the intrinsic thin BSCCO-2212 flakes below T_c.

Figure 5.5a depicts the 4-probe (or sheet) resistance of an unpatterned BSCCO-2212 flake of thickness $d = 10$ nm. Between 300 K and $\sim$ 150 K, the resistance decreases linearly with temperature. This behavior is consistent with optimally doped BSCCO-2212 crystals that exhibit a strange metal behaviour at elevated temperatures[41, 43] (see Fig. 1.4c). Between $\sim$ 150 K and T_c, the sample enters a Berezinskii-Kosterlitz-Thouless (BKT) phase fluctuation regime[283], where the resistance decreases nonlinearly down to the zero-resistance state at $\sim$ 75 K. We define the superconducting critical temperature from the middle of the transition and obtain $T_c = 82$ K. The large value of T_c confirms that the superconducting flakes are optimally doped and that degradation can be minimized in our assembly process.

We typically use a low AC excitation current ($\leq$ 100 nA) to measure R vs. T to avoid strong electric fields across these fragile devices. We find, however, that often the electrical bottom contact results in a non-Ohmic contact with a Schottky barrier. This behaviour likely stems from the insulating nature of the outer layers (BiO, SrO) of the BSCCO-2212 unit cell (see Fig. 5.4a). The contact resistance due to the Schottky barrier increases rapidly with decreasing temperature and can sometimes conceal the evolution of the flake resistance.

Pushing an additional DC current on top of the low AC excitation, which can be done directly from the output of the lock-in amplifier, helps overcome the contact resistance and obtain a cleaner R vs. T curve. Figure 5.5b shows the superconducting transition of a flake of thickness $d = 10$ nm for these two different configurations. For low excitation current, the superconducting transition appears around 60 K but is measured in series with a significant resistive background. The large resistive tail appearing below T_c reflects the temperature dependence of the contact resistance.

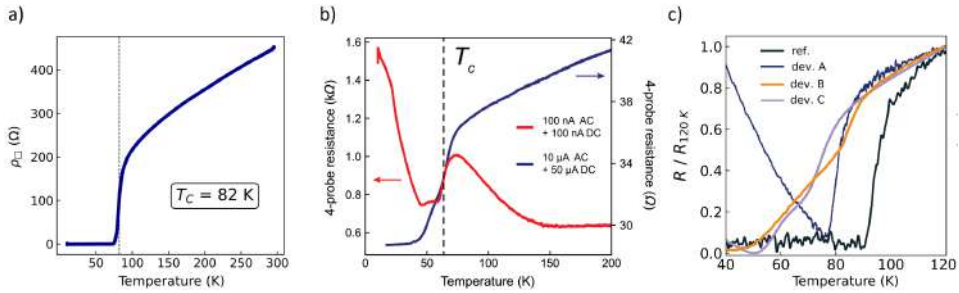

Figure 5.5: a) Sheet resistance versus temperature for a 10 nm thick BSCCO-2212 flake after exfoliation and encapsulation. b) Superconducting transition for low and high applied bias current. The applied DC offset quenches the contact resistance and reveals a clean superconducting transition. c) Superconducting transition for a reference bulk sample (black) and several other patterned nanostructures of varying dimensions.

Lastly, in Figure Fig. 5.5c we compare the superconducting transition in several nano-patterned devices with that of a bulk BSCCO-2212 crystal measured in 4-probe configuration. Nanostructures were measured in 2-probe. For the nanostructures (devices A, B and C), the superconducting critical temperature is somewhat reduced to values between 60 K and 80 K while the bulk crystal reaches the zero-resistance state around 90 K. All in all, the combined effects of the exfoliation, assembly and subsequent He-FIB patterning can slightly degrade the superconducting properties of the cuprate thin flakes. Yet, high-temperature superconductivity can be retained in these nanostructures, paving the way for the development of functional superconducting detectors based on two-dimensional BSCCO-2212.

Current-Voltage characteristics

Having identified T_c for the superconducting nanostructures, we study their current-voltage (IV) characteristics. Using the lock-in amplifier, one may also study the differential resistance in a dV/dI measurement. Conventional resistors exhibit linear IV curves following Ohm's law. Instead, IV characteristics of superconductors are non-linear and reflect the transition from the superconducting state to the normal state upon exceeding I_c. In the ideal case, a 4-probe measurement in a sample with sharply defined superconductivity, no voltage drop appears for $|I_b| < I_c$ and the IV curve abruptly jumps to a finite voltage value when reaching I_c. Once in the resistive state, the voltage increases linearly with bias current as for a normal resistor.

The superconducting nanostructures for photodetection were designed as 2-terminal devices (see Fig. 2.18). Therefore, in practice, the IV curves

display a finite voltage when the device is superconducting due to the contact resistance R_c. Upon exceeding the critical current, the slope of the IV curve will change according to the total resistance R_c+R_N. Figures 5.6a-b depict the 2-probe IV and dV/dI curves obtained for a nanochannel with 300 nm width in a flake with 27 nm thickness. The curves exhibit a clear non-linear behaviour, where the device jumps to the resistive state at $I_c \sim 200$ μA. Such smooth, nonlinear IV curves are commonly known as flux-flow behaviour of a superconducting nanowire. Although the transition is not extremely sharp in the IV curve, it becomes apparent in the dV/dI plot, in which one can also confirm the reduction of the Schottky barrier dominating R_c as the DC current is increased. The sharpness of the IV curves is reduced by disorder

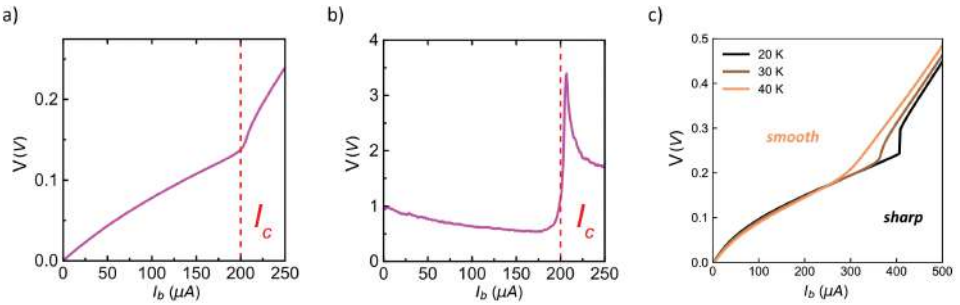

Figure 5.6: a) IV curve at $T = 15$ K for a 300 nm wide BSCCO-2212 nanochannel. In the flux-flow characteristics, there is not a sharp, vertical voltage jump at I_c. b) Differential resistance for the same device in (a). The superconducting transition, as well as the decreasing contact resistance, are visible. c) Evolution of IV characteristics with temperature for a 250 nm wide nanochannel. The transition gradually smoothens with increasing temperatures.

in the superconducting channel, due to slight degradation of the flakes or the patterning process. Still, even for a flake of BSCCO-2212 with pristine properties, the transition in the IV characteristics will become smoother as the sample temperature increases. As shown in Figure 5.6c, a device with a sharp, vertical voltage jump at $T = 20$ K will exhibit a smoother transition at higher temperatures. Altogether, the IV curves confirm the superconductivity of the nano-structured thin flakes of BSCCO-2212. As we will show next, devices with smooth transitions at I_c can be used for very sensitive bolometric photodetection in a large range of temperatures below T_c.

First, we conclude the transport characterization of the device by measuring the temperature-dependent transport characteristics. Figures 5.7a-b show the differential resistance of the BSCCO nanochannel pictured in Figs. 5.6a-b for increasing lattice temperatures. At the lowest temperatures, a sharp boundary separates the superconducting and normal states. As the

temperature increases, I_c and the transition becomes gradually smoother. Between 30 K and the critical temperature ($\sim$ 84 K), the superconducting phase persists but its phase space is reduced and not sharply separated from the normal state. This dV/dI map indicates the optimal bias position for bolometric detection at every temperature, where dR/dT is maximal.

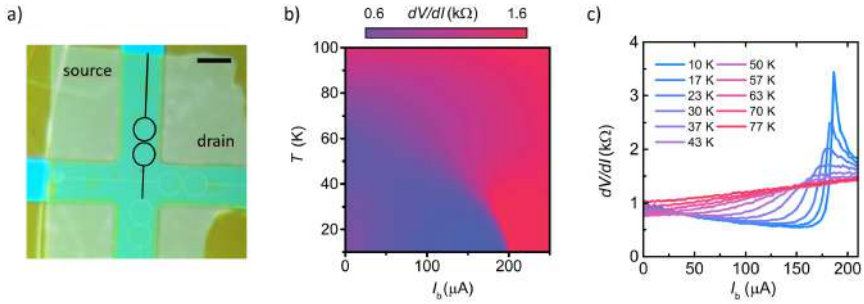

Figure 5.7: a) Differential resistance versus bias current and sample temperature for the 300 nm wide nanochannel. Above 30 K, the boundary between superconducting and resistive states is smeared out. b) Linecuts of differential resistance for the map depicted in (a).

5.3 Characterization of BSCCO-2212 bolometers

Here, we study the bolometric response of the two-dimensional BSCCO-2212 nanostructures. The optoelectronic setup for telecom wavelengths is described in the Methods chapter. We start by spatially locating the nanochannel or nanowire that constitutes the active area of our bolometer. We bias the device close to its critical current (extracted from the previous transport characterization) and record the voltage drop across the device as we scan the laser spot. A large photovoltage signal will appear in the device's active area (see Fig. 5.8a). Note that the I_c we measure must correspond to a constriction within the supercurrent flow in the flake, i.e. in the patterned nanostructure. Therefore, we expect the photovoltage response when $I_b \sim I_c$ to be largest in the active area.

Next, we park the laser spot on the active area of the device and study its bolometric response. To do this, the voltage drop across the nanostructure is measured as a function of bias current I_b and sample temperature I_b. The resulting current and temperature-dependent response is shown in Figure 5.8b. The device response is presented in terms of its responsivity $\mathcal{R}$, which quantifies the photovoltage signal normalized by the incident laser power.

At $T = 10$ K, the response is negligible below $I_b \sim 100$ μA and increases rapidly as $I_b \sim I_c$. The signal develops a strong peak at I_c, where dR/dT

is largest, confirming the bolometric nature of the observed photoresponse. Thus, the largest response takes place at the phase boundary between the superconducting and resistive states. This can be confirmed by comparing the current-dependent bolometric response with the transport characteristics in 5.7b.

The device responsivity at I_c is extremely large, reaching 1.67 x10^6 V/W at T = 10 K. As the lattice temperature increases, the position of the response peak shifts to lower currents (I_c decreases). The smoother phase transition at higher temperatures results in lower peak values of V_{ph} with a broader current dependence. Around 60 K, the bolometric response ceases to have a maximum around I_c and increases monotonically (albeit not linearly) with I_b. Even at 77 K, the bolometric response is remarkably large, in the order of 2 x10^5 V/W[167]. The device performance is quantified in

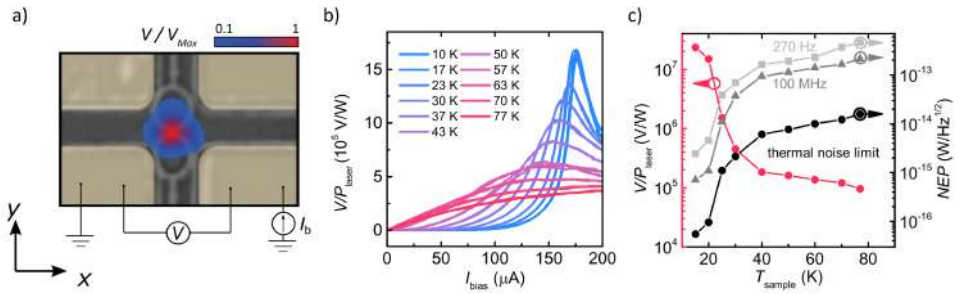

Figure 5.8: a) Schematic of the device configuration and spatially-resolved photovoltage response of the BSCCO-2212 nanochannel. The image presents an overlay of an optical image and the response map. b) Device responsivity versus bias current for different lattice temperatures. Bolometric photoresponse peaks at the temperature-dependent critical current. At higher temperatures, the transition is smeared and the photoresponse peak is not well-defined. c) Summary of the bolometer performance, in terms of $\mathcal{R}$ and NEP for different temperatures. The NEP is shown for two different sampling speeds, along with the theoretical limit for the NEP in our setup (only limited by thermal noise).

terms of its responsivity $\mathcal{R}$ and noise equivalent power (NEP). The NEP is defined as the incident power for which the device registers a signal equal to its noise floor in a 1 Hz bandwidth. Thus, the NEP can be expressed as NEP = $\sqrt{PSD}/\mathcal{R} = 1$, where PSD is the power spectral density of the system. In Figure 5.8c we summarize the device performance for a different bolometer based on BSCCO-2212, whose peak responsivity and NEP (at T = 15 K) reached 2.33 x10^7 V/W and 707 aW/Hz$^{1/2}$, respectively[167]. Note that the NEP value will also depend on the bandwidth used in the measurement. Slower measurements of the bolometric response will yield a higher responsivity and a lower NEP. We find that the measured NEP is

limited by the noise floor in the setup. With an ideal thermal noise floor, limited only by Johnson noise, the NEP may be reduced by one order of magnitude (see black trace in Fig. 5.8c).

All in all, the BSCCO-2212 bolometers presented here achieve record performance in terms of responsivity when compared to previous reports of HTS bolometers[284]. They also exhibit comparable performance to many of the well-established, low-T_c bolometers; albeit at much higher temperatures. Next, we will explore the detection speed of the BSCCO-2212 bolometric photodetectors.

Studying the response time through CW photo-mixing

Next, we discuss the speed of the bolometric detection in these devices. As the bolometric response is proportional to the temperature increase in the sample, we can use the CW-photomixing technique[169] to study the cooling time of the system, i.e. the time dynamics of the bolometric response. The photomixing measurements are summarized in Figure 5.9a-b. The response of the bolometer to the photomixing signal as a function of heterodyne frequency Ω is best described by two overlapping Lorentzians. We find a fast ($\sim$ 200 ps) and a slow ($\sim$ 2 ns) timescale with weak temperature dependence[167]. The intrinsic gap dynamics in bulk BSCCO-2212 were found to be much faster, in the order of few picoseconds[285]. Thus, we believe the observed timescales are related to the diffusion of heat through the insulating barriers defined with the He-FIB. The nanosecond timescale

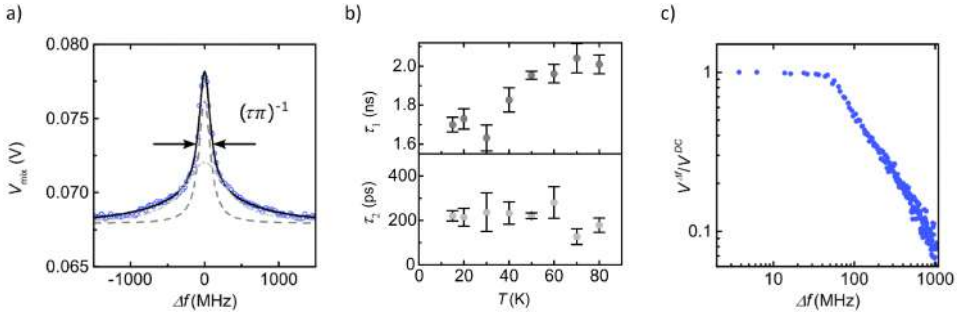

Figure 5.9: a) Photomixing response V_{mix} as a function of heterodyne difference frequency Ω. The thermal relaxation timescale(s) can be deduced from the FWHM of the Lorentzian lineshape(s). b) Temperature-dependent thermal relaxation times extracted from the photomixing study of a BSCCO-2212 bolometer. The slower timescale limits the detection speed to a few nanoseconds. c) Bode plot of the normalized photomixing response as a function of heterodyne modulation frequency.

sets the maximum operating speed of the bolometric detector at around 175 MHz. In Figure 5.9c we show the normalized response to the photomixing

signal as a function of the modulation frequency. The magnitude of the response is nearly unchanged up to $\sim$ 100 MHz, all the way from 15 K to 77 K. Faster operation speeds ($\sim$ 0.1 GHz) can be achieved at the expense of a decrease of one order of magnitude in the response. These findings demonstrate that bolometric detectors based on BSCCO-2212 offer ultra-sensitive detection at telecom wavelengths, with nanosecond relaxation times and operating temperatures up to 77 K[167].

Integration of 2D BSCCO-2212 bolometers on planar waveguides

Lastly, we demonstrate the integration of the HTS bolometers in planar photonic circuits based on SiN waveguides. The prospect of on-chip photonics relies on the development of efficient ways to emit, manipulate and detect light that travels inside a waveguide using suitable components[263, 264]. Due to the two-dimensional nature of the BSCCO-2212 bolometer, it is natural to explore their use in integrated photonic circuits (Fig. 5.1c).

The chips used in this study feature grating couplers, which can take focused laser light as input and couple it in-plane and a long waveguide channel where the light is confined. The waveguide chips were produced at CNIT, Pisa by the group of Marco Romagnoli. To bias the integrated device, we simply fabricate two-probe electrical contacts along the waveguide and perform our standard stacking and nano-patterning process for a device placed on the waveguide (see Fig. 5.10a).

The lower panel of Figure 5.10b demonstrates the response of the bolometer integrated on the waveguide in two different configurations. In both images, we overlay optical images of the waveguide chip to clarify the scan position. On the left, we illuminate directly on top of the bolometer using the focused laser beam and observe standard bolometric response when $I_b \sim I_c$. The response maximum appears at the narrowest point of the patterned nanostructure. Therefore, the waveguide-integrated bolometer still can be operated directly without using the in-plane waveguide coupling. On the lower right panel of Fig. 5.10b, we show the bolometric response when the flake is not directly illuminated. Instead, we park the laser spot at the grating coupler and couple the light into the waveguide. As before, we observe a clear photovoltage response that arises from the coupling between the light traveling along the waveguide and the BSCCO-2212 bolometer. Note that the device is located millimeters away from the grating coupler, evidencing that indeed we observe response from the light confined on the waveguide. The observed response is much lower in this configuration, but we attribute this to large losses ($\sim$ 35 dB) from the grating coupler. Our experiment is restricted to perpendicular incidence, while the grating coupler

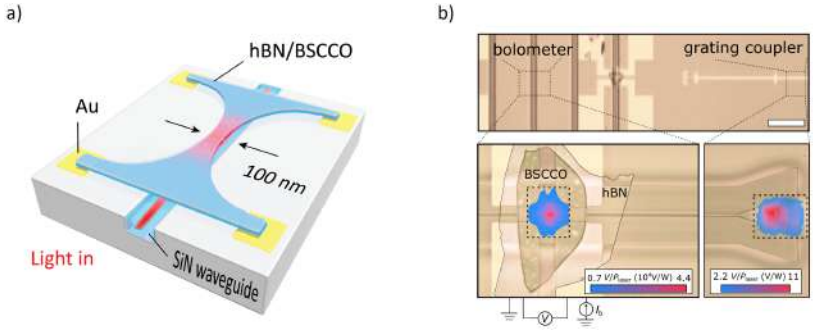

Figure 5.10: a) Schematic of the device concept for waveguide-coupled 2D bolometer based on an hBN/BSCCO-2212 nanostructure. b) Upper panel: Overview of the main parts of the SiN chip, including a grating coupler and electrical contacts for the bolometer along the waveguide. Lower panel: (Left) Overlayed optical image of the BSCCO-2212 flake and its photoresponse under direct illumination. (Right) Image of the grating coupler and photoresponse signal from the bolometer when illuminating only the grating coupler. Credit panel (a): Paul Seifert.

is optimized for oblique incidence.

Here, we have demonstrated the possibility of integrating the high-T_c bolometers with fast response, high responsivity and operating temperatures into planar architectures for photonic circuits[167]. We highlight that, potentially, the coupling through the evanescent modes of the waveguide could yield higher coupling efficiencies with the ultra-thin superconducting flakes. Further engineering of photonic circuits and integrated devices could boost various photonic quantum technologies.

5.4 Single-photon detection in hysteretic 2D BSCCO-2212 nanowires

In this section, we focus on the non-bolometric, avalanche response observed in high-quality BSCCO-2212 nanostructures with hysteretic IV characteristics. As we will show, the observed avalanche response allowed us to reach single-photon sensitivity at a remarkable temperature of $T = 20$ K[168]. First, we will explain the connection between the hysteresis observed in transport and the appearance of an avalanche response upon photo-absorption. Next, we underscore the need for a shunting circuit of the device and discuss how we construct it. Then, we show the emergence of SNSPD-like response in our devices and discuss the statistics of the photo-induced clicks- Finally, we demonstrate the single-photon sensitivity in these devices and put forward possible avenues for the improvement and scalable implementation of such high T_c superconducting single-photon detectors.

Hysteretic IV characteristics in high-quality samples

For some of the highest quality BSCCO-2212 samples, whose critical current densities exceed 10^6 A/cm^2, we observe markedly different IV characteristics. Their IV curves, shown in Figure 5.11a, are characterized by a sharp, vertical voltage jump at the critical current I_c and the appearance of hysteretic behaviour. After switching onto the resistive state, when the bias current is ramped down the device does not recover its superconducting state at the expected value I_c. Instead, the device remains resistive until the current is lowered further to a value known as the retrapping current $I_r < I_c$. Therefore, a hysteresis loop appears in the IV curves between I_r and I_c. This behaviour persists at higher lattice temperatures, as shown in Figure 5.11b for T = 20 K. The hysteresis indicates the existence of a bistable state[286–288] for bias currents $I_r < I_b < I_c$ that can be exploited for highly sensitive, non-bolometric photodetection as that found in SNSPD's[258, 267, 268].

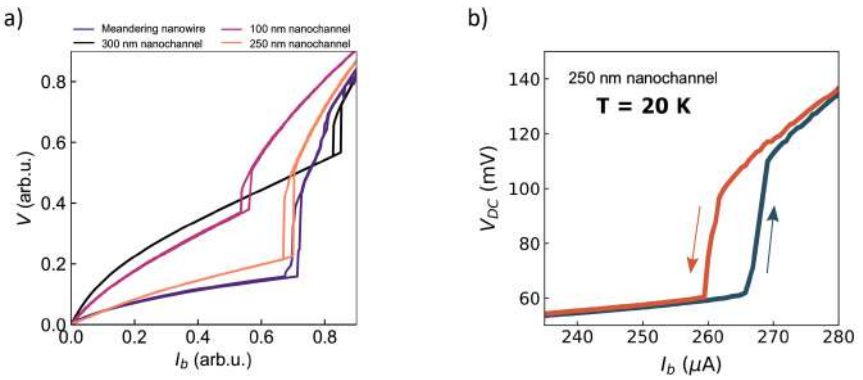

Figure 5.11: a) Hysteretic IV characteristics for various devices with different dimensions and nanostructure designs at T = 10 K. The bias current and voltage of each curve have been normalized for visual clarity. b) Hysteretic IV behaviour persisting at T = 20 K for a 250 nm wide nanochannel.

Microscopic origin of the hysteresis, avalanche response

The bistability of the IV curve originates from Joule heating. When the device is resistive, it dissipates power P according to $P = I_b^2 R_N$ due to the applied bias current I_b, which continues to flow after superconductivity is broken. Thus, for $I_r < I_b < I_c$ the power being dissipated in the nanowire precludes it from recovering the superconducting state and the bistable condition is reached[267–269]. This bistability is generally attributed to the presence of a self-heating hotspot. Further decrease of the bias current below I_r allows the cooling power of the cryostat to counter the Joule heating effect

and the device switches back to the superconducting state (see Fig. 5.12a).

The hysteresis depends on the electro-thermal balance of the nanowire, which is set by its transport characteristics (critical current density, normal state resistance and dimensions) and the thermal conductance between the nanowire and its environment[271, 272]. As shown in Figure 5.12b, the hysteresis loop in our devices closed around 30 K, likely due to a combined effect between lower Joule heating and increased thermal conductance in the nanowire. We also note that a decrease in the thermal conductance of the nanostructures, perhaps favoring the stabilization of self-heating hotspots, could be due to slight amorphization of the nanostructure edges[158].

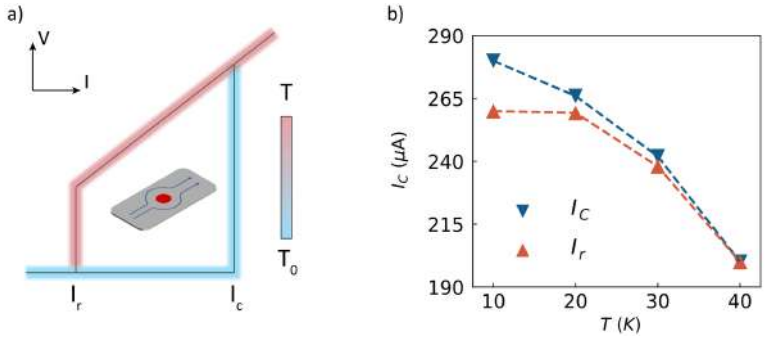

Figure 5.12: a) Illustration of the hysteresis loop arising from the stabilization of a self-heating hotspot in the nanowire. The device can exhibit bistability between the superconducting (blue) and dissipative states (red). c) Temperature dependence of the critical and retrapping current in the 250 nm wide nanochannel. The hysteresis loop remains finite up to $\sim$ 30 K.

Crucially, the hysteretic transport properties are the basis for SNSPD-like avalanche photodetection when $I_b \sim I_c$. After photoabsorption, a local hotspot of quasiparticles can expand and create an avalanche effect upon which the entire nanowire turns resistive[266]. The bistability of the transport characteristics of a superconducting nanowire (without any optical input) can be exploited in an SNSPD if one can trigger the creation of a self-heating hotspot via optical excitation.

We highlight here the feasibility of switching the entire nanowire through optical excitation by demonstrating latching behaviour. At a constant bias current I_b, the device will not transition back to the superconducting state once it turns resistive, as the Joule heating cannot be countered. This permanent switch is known as latching[271–274]. The bias current through the device is fixed at $I_b \sim 0.95 I_c$ and we read out the source voltage needed to source I_b. If the device turns resistive, the necessary source voltage to maintain constant current flow will increase.

We now scan the laser spot across the sample, near the active area of the

biased nanostructure (a meandering nanowire in this case). See Figure 5.13a for the location of the nanowire and the directionality of the scan. As shown in Figure 5.13b, the nanowire is initially in the superconducting state (low source voltage applied) as the laser spot is scanned several microns away from the biased nanowire. This confirms that illuminating the unpatterned BSCCO-2212 areas does not trigger any response from the nanowire, even though Cooper-pair-breaking is taking place. As soon as the laser spot

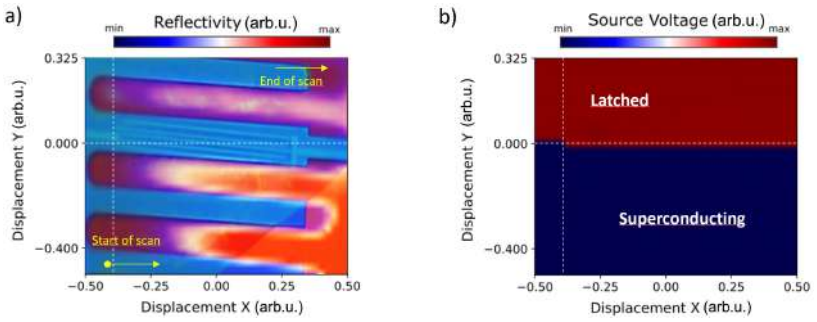

Figure 5.13: a) Overlayed optical image and reflectivity from a BSCCO-2212 meander nanostructure. The yellow arrows indicate the direction of the scan, while the white dashed line indicates the first point where the laser spot overlaps with the nanowire. b) Applied source voltage for the current-biasing of the meander device. As soon as the laser spot is incident on the device's active area, the nanowire becomes resistive and the applied source voltage increases. As the device latches after photodetection, the source voltage remains high even when the laser spot is away from the nanowire.

overlaps with the biased nanowire, the device turns resistive and the source voltage increases. As the bias current is fixed, the device does not recover superconductivity even when the laser excitation does not overlap with the nanowire. Thus, it is possible to 'latch' BSCCO-2212 devices with hysteretic transport behavior. In the following, we will include a shunt circuit that allows the detector to self-reset after switching. It is hard to pin down what constitutes a 'high quality' BSCCO-2212 device that would exhibit hysteresis. In literature, the critical current density J_c was found to be a good predictor of the device quality[289, 290]. For reference, in Fig. 5.14 we summarize the main characteristics of the studied hysteretic devices.

Choosing a shunting circuit

A crucial aspect of an SNSPD is its free-running operation, i.e. the SNSPD can reset itself without external input after every detection event. For this, an electrothermal feedback circuit[271] is used, which is based on modeling the SNSPD as a variable resistor. In Figure 5.15a, we depict

	Structure	Length (μm)	Width (nm)	I_c (μA)	J_c (A/cm^2)	d (nm)
Device A	Nanochannel	2.7	250	280 (10 K)	6.79×10^6	16.5
Device B	Meander	120	500	214 (10.8 K)	2.85×10^6	15
Device C	Nanochannel	4	300	422 (15 K)	6.70×10^6	21
Device D	Nanochannel	3	100	270 (10 K)	1.69×10^7	16.5

Figure 5.14: Table summarizing the device characteristics for the hysteretic BSCCO-2212 nanostructures reported in this study.

the basic principle of the resetting circuit. On the left side, the SNSPD is sketched as a circuit element with 2 parallel paths: one is non-dissipative (closed switch) and represents the superconducting state, and the other represents the normal state resistance R_N.

Crucially, the superconductivity can be destroyed if a photon is absorbed (open switch), forcing the bias current to flow through R_N and produce Joule heating. In this condition, superconductivity will not be recovered. Thus, a shunt or load resistor R_{Load} is connected in parallel to the SNSPD so that I_b is re-directed once the switch opens and the Joule heating is rapidly reduced. As the switch closes, the detector is reset and can detect absorbed radiation once again. In the SNSPD branch, we include a series resistor R_C that represents the non-negligible contact resistance in our devices. The

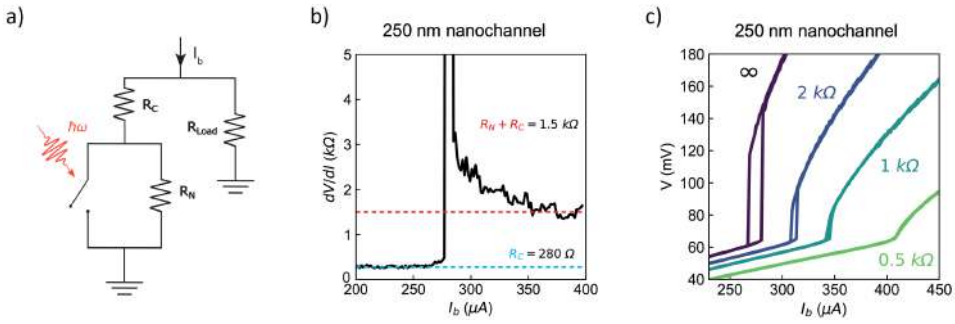

Figure 5.15: a) Schematic of the central elements of the reset circuit. The SNSPD is modeled as a superconducting switch in parallel with the device normal state resistance R_N. In series with both paths, the contact resistance is represented as R_c. A load resistor R_{Load} is connected in parallel with the SNSPD to shunt away the current once the superconducting switch is opened due to photoabsorption. b) Differential resistance of a 250 nm wide BSCCO-2212 nanochannel at T = 20 K. The extracted resistances for each state of the device inform the choice of R_{Load}. c) IV curves for the same device for different choices of the load resistor. The 1 kΩ load resistor provides an ideal tradeoff between closing the hysteresis loop and retaining a vertical voltage jump at I_c.

suitability of the shunting circuit depends on the resistances involved. One should choose a load resistor such that $R_C < R_{Load} < R_N$. We measure the

2-probe differential resistance dV/dI of the device (Fig. 5.15b) to determine the values of $R_C = 280\ \Omega$ and $R_N + R_N = 1.5\ \text{k}\Omega$. Therefore, we choose a load resistor $R_{Load} = 1\ \text{k}\Omega$ which satisfies the condition state above. In Figure 5.15c we depict the IV characteristics for the 250 nm nanochannel device using different parallel load resistors.

In the absence of the load resistor (∞), the full hysteresis loop is observed and the optical response would lead to latching. Adding R_{Load} shifts the total bias current to higher values and decreases the size of the hysteresis loop, both in voltage and current. For $R_{Load} = 0.5\ \text{k}\Omega$, the device does not exhibit a well-defined voltage jump at the superconducting transition. However, $R_{Load} = 1\ \text{k}\Omega$, the hysteresis loop is nearly closed, implying that the electrothermal feedback is improved, while the IV curve still features a sharp transition. In the following, we focus on the optoelectronic response of the BSCCO-2212 SNSPD with this load resistor.

Click response of the shunted device

The full circuit used for the self-resetting SNSPD operation of these devices is sketched in Fig. 5.16a. The bias current is applied over a 10 kΩ resistor. The voltage spikes arising from the sudden re-direction of the bias current (upon photoabsorption) are first amplified with a room-temperature low-noise amplifier (LNA) and then measured by a high-speed lock-in amplifier with input impedance of 10 MΩ. The SNSPD also has an intrinsic kinetic inductance L_k which affects the dynamics of the circuit. We estimated L_k from the reported magnetic penetration depth of BSCCO-2212. Our circuit differs from the standard SNSPD readout, which involves the use

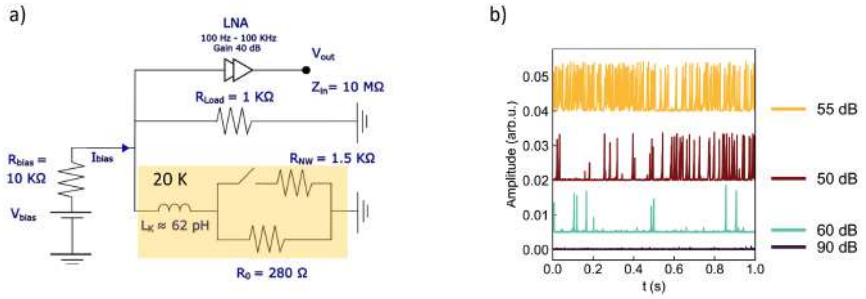

Figure 5.16: a) Full shunting circuit for the SNSPD operation of the BSCCO-2212 nanostructures. In addition to the elements described in Fig. 5.14a, the bias branch and the voltage readout are shown. LNA stands for low-noise amplifier, whose configuration is specified in the sketch. The voltage output is monitored using a high-speed lock-in amplifier represented as an input impedance of 10 MΩ. b) Appearance of voltage spikes at the voltage output as the attenuation of laser input is reduced.

of a bias tee for DC bias and AC readout of the detector[266]. Unfortunately, not all the circuitry in the setup is RF-compatible. The use of an RF bias tee in our circuit did not lead to reproducible detection of photo-induced clicks. Instead, we opted to use low-frequency AC instruments for the readout. Thus, the detection speed in our devices suffered from the non-optimal readout circuit. Shortly, we will discuss the observed reset time and highlight other studies that managed to optimize the readout circuitry for BSCCO-2212 devices.

Due to the low yield of hysteretic BSCCO-2212 nanostructures, we could not tailor the nanostructure design or readout circuit for each device. Furthermore, the chemical instability of the thin cuprate layer[151] also sets a time constraint in the photodetection experiments.

In Figure 5.16.b we depict the voltage measured at the circuit output over a 1-second window for different levels of optical power. The device was biased at $I_b \sim 0.98 I_c$. For very high attenuation (90 dB) no spikes were observed, implying that the bias condition is stable and superconductivity is not broken in the absence of photon input. As the attenuation is lowered, more and more voltage spikes appear over this time window. Thus, we conclude that we can indeed observe SNSPD-like response to telecom photons in the BSCCO-2212 devices. In the following, we will explore the statistics of these 'detection events' as a function of applied bias and laser power. First, we verify that the clicks stem from the active area of the device and inspect its characteristic timescale.

To confirm that the detection events arise from the nanochannel, we monitor the voltage output as we scan the laser spot near the device (Fig. 5.17.a). Unlike in Figure 5.13, the device does not latch after a detection event, thanks to the shunting circuit. We can correlate the position of maximum response (or switching rate) to the constriction in the nanostructure, which sets the measured I_c. Absorption of photons one micron away from the constriction does not lead to a significant switching rate. As mentioned before, the dynamics of current shunting (that take place once the device turns resistive) are not optimized in this experiment. Consequently, the time traces of the detection events (measured using an oscilloscope) reveal a rather slow resetting of the device (Fig. 5.18a). Photoabsorption at $t = 0$ rapidly leads to the avalanche effect and the complete switching of the device. This takes place on a sub-microsecond timescale, reflected in the rise time of the time trace. Then, the detector relaxes and the bias current returns to it on a longer timescale, with a reset time of $\tau \sim 700$ μs.

This slow reset time likely stems from the non-optimal readout circuitry. The intrinsic thermal relaxation time for BSSCO-2212 in the absence of the avalanche response was found to be in the nanosecond regime[167]. Therefore, these devices could operate at much higher detection speeds if the circuit is

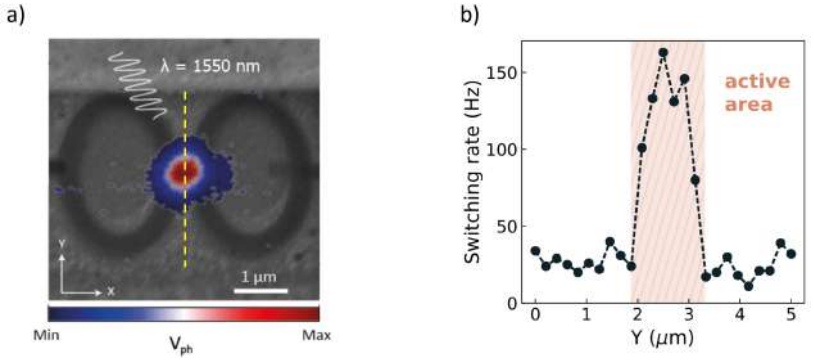

Figure 5.17: a) Spatially resolved response of the BSCCO-2212 nanochannel. To avoid latching, we over-shunt the device for this measurement and then repeat the same measurement with the proper SNSPD readout circuit. b) Switching rate of the BSCCO-2212 SNSPD along the yellow dashed line in (a).

optimized. Even then, understanding the electrical and thermal properties of these complex devices is important for the optimal engineering of their readout. In fact, a different group demonstrated $\sim$ ns reset times of similar devices using a bias tee circuit[288], see Fig. 5.18b. Perhaps most notably, they included a series inductor in the shunting branch of the circuit. This element helps block the high-frequency voltage spikes from re-entering the DC branch of the circuit, which could cause latching effects.

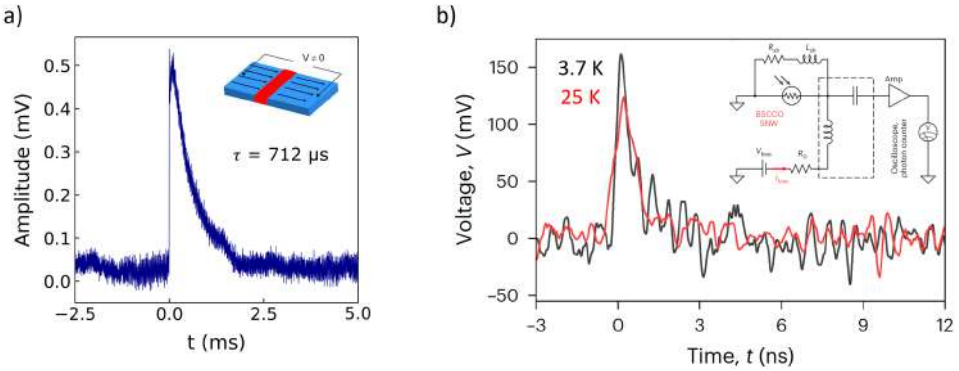

Figure 5.18: a) Trace for an individual voltage spike using the circuit depicted in Fig. 5.16a. The inset sketches the full resistive switching across the nanowire's cross-section. The extracted relaxation time is $\tau = 712$ μs. b) Time traces from the photoresponse of a BSCCO-2212 meander at two different temperatures, revealing nanosecond reset times. The improved readout circuit used in this experiment is shown as an inset. Panel (b) adapted from Ref. [288]

Counting detection events

To gather statistics about the detection events, one needs to define a criterion for what constitutes a detection event or photon click. Often in commercial SNSPD's, the voltage spikes are easily distinguishable from the noise floor and this criterion can be defined right away. Looking at the voltage spikes (Fig. 5.19a), it becomes clear that not all the detection events have the same magnitude and that the noise floor may exhibit some small spikes on its own. Therefore, we must define a consistent criterion to build detection statistics.

We used the following protocol. At each bias current I_b, we record the output voltage for 5 minutes under no illumination (laser off, optical window blocked). This helps us characterize the noise floor and the number of dark counts (voltage spikes unrelated to the intended input). Then, we construct a histogram of all the recorded voltages over this time window (see Fig. 5.19b) and fit it to a (skewed) Gaussian distribution, obtaining its mean μ and standard deviation σ. As the photo-induced voltage spikes appear

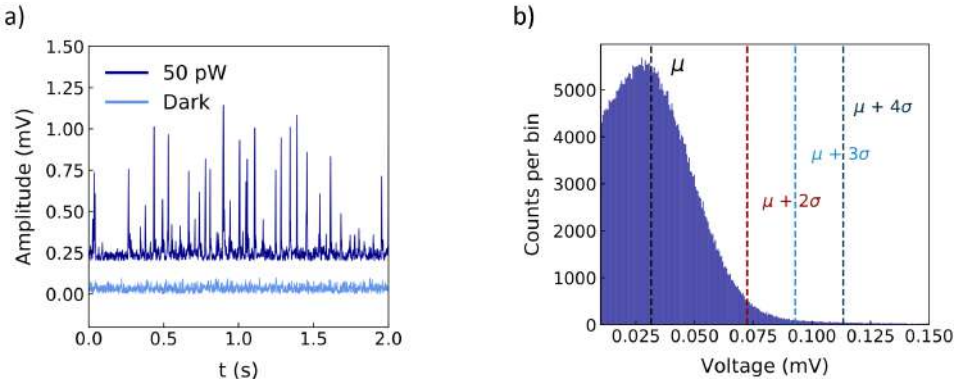

Figure 5.19: a) Exemplary voltage output over a 2-second window. The voltage spikes only appear when the device is illuminated by the telecom laser. Note that not all the voltage spikes have the same amplitude. b) Histogram of the recorded voltages over 5 minutes for the BSCCO-2212 SNSPD in dark conditions. The mean and standard deviation of the distribution at each bias current are used to define a threshold voltage at each I_b value.

clearly above the noise floor, we must define a 'trigger' or threshold voltage for what constitutes a detection event. We define an I_b-dependent trigger voltage as $V_{trig}(I_b) = \mu(I_b) + \mathrm{N}\sigma(I_b)$. Thus, we set the detection events to constitute a certain percentile of the tail of the distribution of voltage values during a 5-minute window. In Figure 5.19b, the vertical dashed lines indicate the position of the threshold voltage for different values of N. In the results we show next, we have counted the detection events using N =

3.5. However, we will also show how the main experimental observation in this study is independent of the choice of this trigger voltage.

Bias current dependence

We first examine the device's switching rate (number of detection events in a 1-second window) as a function of the applied bias current. As mentioned before, if I_b is much lower than the device's critical or switching current, no detection events should take place as the condition for the avalanche response is not fulfilled[288]. On the other hand, we expect the switching rate to increase as I_b approaches I_c.

As shown in Figure 5.20a, the BSCCO-2212 SNSPD follows the expected trend. Below $I_b \sim 0.8I_c$, the rate of detection events is negligible. Above $I_b \sim 0.9I_c$, the switching rate rapidly increases. If the device is biased at I_c or above it, it enters a regime of fluctuations where it switches between the superconducting and resistive state without any optical input. It is therefore not a viable bias regime for the SNSPD. The grey squares in Fig. 5.20a depict the dark count rate measured under the same experimental conditions. The dark count rate increases as we approach the device instability at I_c but remains lower than the total count rate under illumination.

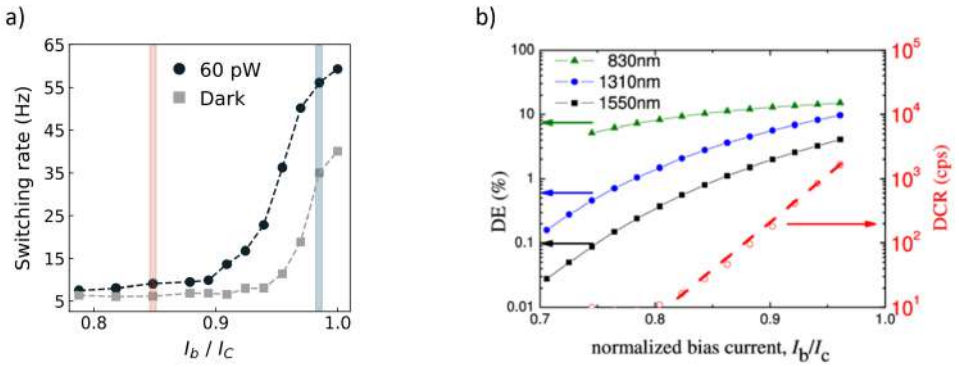

Figure 5.20: a) Bias current dependence of the switching rate for the 250 nm wide nanochannel under low power illumination and dark conditions. Shaded rectangles highlight the two bias conditions for the results in Fig. 5.22a. b) Representative bias current dependence for the photon and dark count rate of a standard, low-temperature SNSPD device. Panel (b) adapted from Ref.[266]

We contrast this behaviour with the I_b dependence of the count rate for a representative SNSPD device (Fig. 5.20b). The trend of the response is qualitatively similar between our device and the standard SNSPD[258, 266]. However, two main differences stand out: (1) the switching rate in our device does not saturate and (2) the dark count rate of our device has a similar I_b

dependence as the total switching rate. The lack of saturation indicates that the internal efficiency of the device is not 100%, i.e. not all absorbed photons in the active area will lead to a detection event. Commercial SNSPD's often display a saturated detection efficiency around $0.95I_c$. We note that the nanochannel devices can have a position-dependent I_c, as the device cross-section is not uniform[291]. Then, as I_b changes, the active area (the area where the intended bias condition is fulfilled) will change its size and the device sensitivity changes. This has been connected to non-saturating switching rates in nanochannel devices[291].

Regarding the dark count rate, these false detection events often arise due to thermal fluctuations that can trigger the detector when $I_b \approx I_c$. Thermally activated dark counts are known to exhibit an exponential I_b dependence, different from the switching rate that has a sigmoidal bias dependence (Fig. 5.20). In our devices, however, both rates exhibit very similar evolutions. This observation suggests that the dark counts in this experiment are not of thermal origin. Instead, we hypothesize that the observed dark counts originate from the absorption of stray photons at other wavelengths. In particular, we make use of a room-temperature objective that sits millimeters away from the sample. It's likely that thermal photons from the 'hot' objective reach the detector even when the laser is blocked, leading to the observed dark count rate with 'photon-like' bias dependence.

Poissonian statistics of the click response

In the previous discussion, we explored the appearance of photo-induced voltage spikes, their timescales and their I_b-dependence. Nevertheless, we have not yet investigated the sensitivity of the device. In other words, the SNSPD-like response could be originated by the absorption of a single-photon or a thousand photons. We address the device's photon sensitivity by looking at the statistics of the switching events as a function of laser power. For a highly attenuated laser source, the absorption (and detection) of a photon in a current-carrying superconducting nanostructure constitutes a rare and uncorrelated event[292]. The SNSPD, provided that it's fully reset, does not retain information about previous detection events and consecutive photodetection processes are uncorrelated. The photo-induced clicks are rare due to the low photon fluence incident on the nanowire. Thus, the statistics of the detection events in an SNSPD are governed by Poissonian statistics[292].

The Poisson distribution is a discrete probability function describing the probability of an event happening k times over a certain time window, given that the mean number of events in that frame is λ. The probability for k

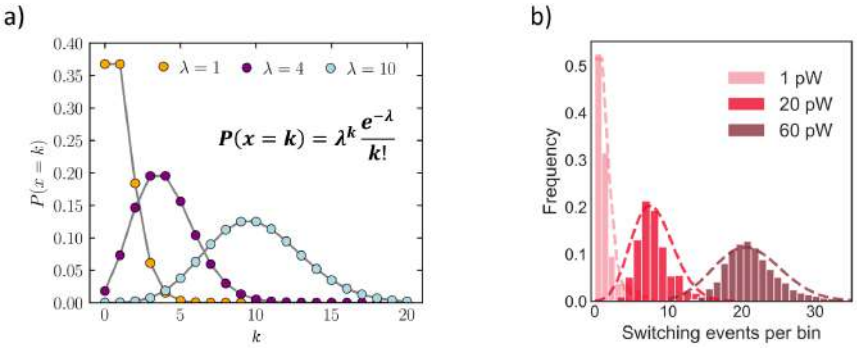

Figure 5.21: a) Poissonian probability function for increasing mean number of events λ. b) Poissonian distribution of the power-dependent switching rate for a BSCCO-2212 SNSPD. Panel (a) adapted from Wikipedia.

events is then given by:

$$P(X = k) = \lambda^k \frac{e^{-\lambda}}{k!} \tag{5.1}$$

Figure 5.21a depicts the Poisson probability distribution for different values of λ. For large values of λ (for which the events are no longer rare), the Poisson distribution is equal to the Gaussian distribution.

In terms of photodetection in an SNSPD, the number of events k can be associated with the simultaneous absorption and detection of k photons and λ can be linked to the mean photon number, i.e. the laser power[292]. As such, when λ is very low, one expects to mostly observe no detection events and some events due to a single-photon being absorbed. As the optical power is increased, the probability of no detection events in a time window is lowered and the probability for multiple photons to be detected at once $k > 1$ increases. The device response will only follow Poissonian statistics if it's triggered by a few photons.

To inspect the switching statistics, we fix the bias current at $I_b = 0.97 I_c$, record the voltage output at different laser powers and count the spikes per time bin. The bins are chosen according to the device reset time, to avoid counting a single spike multiple times. As we show in Figure 5.21b, the switching statistics of the BSCCO-2212 devices are well described by Poissonian statistics at low laser powers. This finding indicates that indeed the observed response corresponds to single or few-photon events.

Single-photon sensitivity at $T = 20$ K

The sensitivity of these SNSPD-like detectors can be further characterized through their Poissonian distribution. Inspecting Eq. 5.1, one can formulate

what is the probability (given that the incident power is low, $\lambda << 1$) for a k-photon event, i.e. to detect k incident photons in the superconducting nanowire. For instance, for a single-photon event ($k = 1$), the probability is given by $P(k = 1) \approx \lambda$. Thus, the detection probability (or switching rate) for single-photon events should evolve linearly with the mean photon number or input laser power.

We focus on the device sensitivity at a temperature of $T = 20$ K, far beyond what's attainable with standard SNSPD's. As the device sensitivity is largest when $I_b \approx I_c$ and the superconducting nanowire is closest to the transition, we apply a bias $I_b = 0.97I_c$ and study the evolution of the switching rate with increasing laser power. Figure 5.22a depicts a log-log plot of the power dependence of the switching rate in this bias condition (blue circles). The switching rate evolves linearly ($k = 0.95 \pm 0.03$ from the best fit) with increasing optical power, demonstrating the single-photon sensitivity of the BSCCO-2212 nanostructures. We have verified such single-photon sensitivity across multiple devices and at temperatures of $T = 15$ K and $T = 20$ K.

It's important to note that the observation of single-photon sensitivity is robust with respect to the choice of threshold voltage. For any reasonable value of the trigger (above the noise level), the linear power dependence of the switching rate is observed (Fig. 5.22b). Note that for a lower threshold (N = 2), the switching rate at lower optical powers is increased (due to false counts not far from the noise floor) and the overall slope of the curve is sub-linear. This non-physical sublinear dependence indicates that this threshold voltage is not discriminating properly the detection events from the noise floor.

One may also ask what is the sensitivity of the detector to multi-photon events (when $k > 1$). In large-area SNSPD's based on meandering nanowires, multi-photon events are extremely rare. The large active area of the device makes simultaneous absorption of multiple photons (within the size of a hotspot) highly unlikely. However, in nanochannel devices where the active area is smaller, statistics from multi-photon detection events can be observed[291].

The Poissonian probability function helps us identify the signatures of multi-photon events. For 2-photon events, we expect a quadratic power dependence of the switching rate; while for 3-photon events, this dependence is expected to be cubic. In a log-log plot, these would correspond to lines of slope m = 2 and m = 3, respectively. To investigate the appearance of multi-photon events, we inspect the photodetection statistics of the device at lower bias currents (see red rectangle in Fig. 5.20a). The hypothesis is the following: while a single-photon may not efficiently lead to a detection event at a given bias current I_b, the absorption of two photons might be

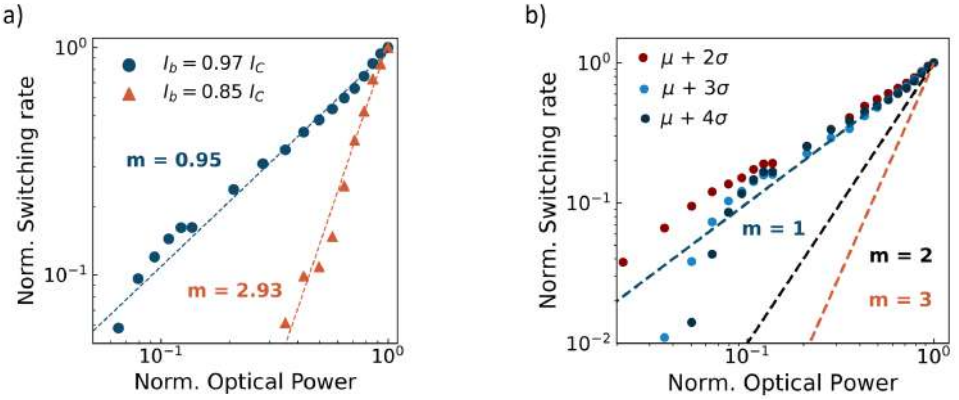

Figure 5.22: a) Log-log plot of the power dependence of the switching rate for a BSCCO-2212 nanochannel at T = 20 K. Blue circles (red triangles) correspond to the high (low) bias condition and demonstrate the single (multi) photon sensitivity of the device. b) Robustness of the single-photon sensitivity with respect to the choice of a threshold voltage.

sufficient to trigger the resistive switching of the device[291].

The red triangles in Figure 5.22a illustrate the power dependence of the switching rate at $I_b = 0.85I_c$. The number of switching events evolves in a drastically different way than at $I_b = 0.97I_c$. First, they appear at higher laser powers overall, as the probability for multiple incident photons grows. Second, the switching rate grows much faster than for single-photons. The best power law fit yields a slope in the log-log plot of $k = 2.93 \pm 0.13$, strongly suggesting that 3-photon detection events dominate the switching rate at this bias condition. We also observe a regime for 2-photon sensitivity between the two discussed bias conditions. However, our experimental data from that regime is not comprehensive enough.

We have therefore demonstrated the single-photon sensitivity of BSCCO-2212 SNSPD's to single telecom photons at a temperature of $T = 20$ K[168]. This extreme sensitivity was enabled by the high quality of the nanopatterned devices, which exhibit large critical current densities along with sharp voltage jumps and hysteresis loops in their IV characteristics. Lastly, we observed clear signatures of multi-photon detection, further confirming their SNSPD characteristics[168]. The speed and efficiency of these HTS devices should be examined more thoroughly in future work. Improvements in the readout circuit and benchmarking of the devices in pulsed and time-correlated measurements stand out as the next steps to characterize the device's performance.

Chapter 6

Outlook

In this closing chapter, we discuss future prospects of the overall research field and the concrete topics presented in this thesis. The study of 2D materials and vdW heterostructures, now two decades old, keeps attracting extensive interest and producing remarkable physical phenomena. Its technological impact, which is not significant yet, may very well arise in the coming decades. The expansive library of 2D materials, nowadays expanded via large-scale computations[250, 293, 294], ensures that vdW heterostructures may constitute the material foundry of the future.

Furthermore, moiré physics has reinvigorated the study of correlated phenomena in 2D materials[3]. The study of 2D moiré quantum matter is only now in its infancy but has already proven to be a singularly powerful tool. While hundreds of different 2D heterostructures have been reported, the next step in the field seems to lie in the development of new measurement techniques for these atomically thin, artificial materials. As we have discussed in this work, current and novel optoelectronic techniques can be powerful probes into the complex phenomena found in (moiré) vdW heterostructures[131].

Here, we summarize our findings and comment on possible advancements in the specific research directions we have explored. We have described various experimental studies of fundamental and technological relevance, involving different material platforms and experimental techniques. Therefore, we provide separate discussions on each topic.

Thermoelectricity and heavy fermion physics in 2D materials

In Chapter 3, we studied the thermoelectric transport generated by the Seebeck effect in the MATBG flat bands. Using a gate-defined *pn*-junction, we were able to demonstrate the thermoelectric nature of the photovoltage response of MATBG (for above-gap excitation). We then

leveraged the Seebeck-driven thermoelectric response to directly map the electronic structure of the correlated states in the flat bands[218].

The low-temperature thermoelectricity featured an anomalous behaviour, where the gap-like oscillations of the signal remained negative across the correlated states for $\nu > 0$. The observed response, indicative of strong *e*-*h* asymmetry of the correlated states, was microscopically modeled using the topological heavy fermion mapping of MATBG. All in all, we found remarkable agreement between theory and experiment, which can be linked directly to the coexistence of light and heavy electrons within the flat bands[218]. We believe our findings provide, for the first time, direct evidence of the interplay between these light and heavy electronic species in MATBG.

The concept of heavy fermion physics in 2D materials constitutes an important research direction in the field and is not unique to MATBG. In the case of the MATBG flat bands, this notion naturally accounts for many of the contrasting electronic ground states of the strongly correlated flat bands. Other twisted graphene multilayers also exhibit behaviours characteristic of the interaction between electron orbitals localized at the superlattice scale and a free electron sea[295]. Anomalous thermoelectricity in twisted trilayer graphene[296] (see Fig. 6.1a) and the electronic ratchet effect in twisted-untwisted configurations of graphene-hBN[297] stand out as prime examples.

Heavy fermion phenomena were also expected to emerge in twisted TMD heterostructures[298, 299], where the bandwidth (or degree of localization) in each layer is different. When the layer with localized orbitals is doped to one carrier per moiré site, they effectively form a lattice of local unpaired moments (Fig. 6.1b). Then, the nearly-free carriers of the adjacent layers screen out the local moments via the Kondo effect[300].

In contrast with conventional heavy fermion compounds, these effects can be easily tuned via electrostatic gating in these moiré heterostructures. As shown in Fig. 6.1c, the Kondo temperature in the twisted TMD heterostructure can vary significantly for small changes in the doping[300].

Thus, moiré-engineered heterostructures can simulate the Hubbard model in an effective and flexible manner, including heavy fermion physics. We note that recently, an intrinsic heavy fermion compound was isolated in its 2D form for the first time[301] (Fig. 6.1d). The electronic and thermal properties observed in CeSiI evidence the existence of intrinsic heavy fermions in exfoliable 2D materials (Fig. 6.1e), opening the door for further studies of this material and its heterostructures.

Regarding thermoelectric studies of MATBG, the Nernst effect which describes transverse thermoelectric transport under an applied magnetic field, stands out as a natural extension of this work. Similar to the Seebeck effect, the Nernst effect can provide insight into a material's electronic structure

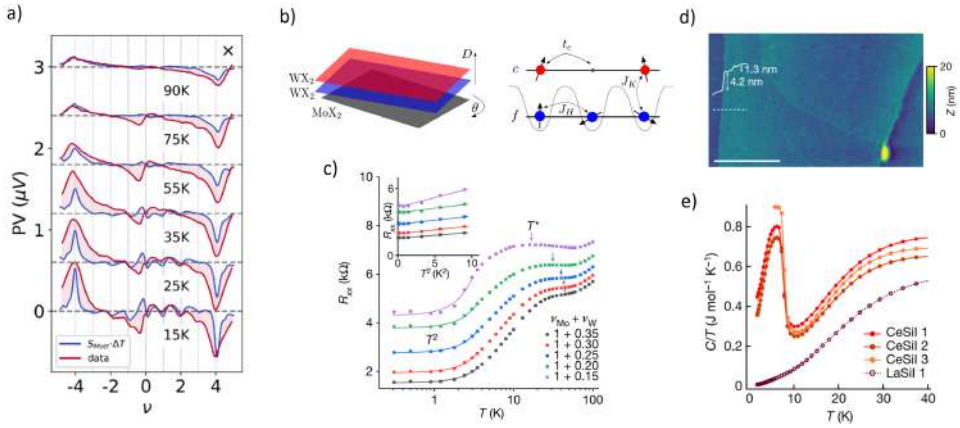

Figure 6.1: a) Violation of the Mott formula in the photo-thermoelectric voltage of twisted trilayer graphene. b) Illustration of a TMD heterotrilayer, where the strength of the moiré potential is layer-dependent. Controlling the moiré potential and filling factor of each layer, an interlayer Kondo effect can be realized. c) Filling-dependent Kondo temperature in a TMD homobilayer. The Kondo temperature ranges between $T = 5$ - 45 K in the relevant filling range. d) AFM map of a 2D layer of heavy fermion compound CeSiI. e) Temperature-dependent specific heat of CeSiI thin flakes. The pronounced peak of the specific heat around $T = 5$ K indicates the emergence of a Kondo resonance. Panels (a), (b), (c), (d-e) are adapted from Refs. [296], [299], [300] and [301], respectively.

that remains hidden in direct electrical transport[177]. Previous studies revealed the presence of Weyl points and quantum critical points in 2D WTe_2[302, 303].

Furthermore, the Nernst effect is particularly sensitive to superconducting fluctuations and vortex matter, as demonstrated in (bulk) cuprate superconductors[177]. Thus, studying the Nernst effect in 2D superconductors (below and above their T_c) could provide unique insight into the formation of Cooper pairs and the role of superconducting fluctuations in the superconducting pairing. We note that heavy fermions are also expected to leave distinct fingerprints in the transverse thermoelectricity[177].

Local probe techniques also constitute a promising avenue for the study of thermoelectric (and thermal) effects in 2D materials. Unlike global transport and diffraction-limited optical studies, local thermal probes can provide spatial insight into these phenomena. Recent examples include the spatial mapping of the Seebeck coefficient in monolayer graphene using a scanning thermal gate[304] or the direct observation of the Ettingshausen effect in WTe_2 using the SQUID-on-tip technique[305]. The recently developed quantum twisting microscope[306] could also provide new and unique insight into the thermoelectricity of (twisted) 2D materials.

These studies of thermoelectric effects mainly focus on probing the electronic spectrum governing the hot carrier transport, in a regime where phonons do not play a significant role. However, we must highlight that a comprehensive understanding of the role of phonon transport for 2D materials is lacking. How phonons behave in systems of reduced dimensionality or how phonons propagate across the vdW interfaces constitute essential questions for thermal transport in vdW heterostructures. Furthermore, the small sample size makes thermal transport experiments challenging in these systems[217]. We note that an optomechanical technique to probe the thermal properties of 2D materials has been recently reported[307].

On the cooling dynamics of MATBG

In Chapter 4, we studied the cooling time of a hot carrier distribution in MATBG, revealing ultrafast carrier cooling down to cryogenic temperatures[252]. In contrast to the cooling time of AB bilayer graphene, the cooling time in MATBG remains ultrafast when decreasing the lattice temperature (above 5 K); indicating the existence of an efficient cooling pathway connected to the moiré superlattice. We modeled the cooling pathways in MATBG and found evidence of a novel Umklapp electron-phonon scattering mechanism[252].

The new insights into the low-temperature cooling time in MATBG raise some intriguing points. From a fundamental perspective, this study motivates the inspection of Umklapp electron-phonon scattering and its consequences on the device resistivity. As mentioned before, the origin of the linear-in-T resistivity or the large prefactor of the T^2 remain open questions[101, 106, 107]. It has been proposed that an enhanced electron-phonon coupling in the MATBG flat bands could be related to these observations[223]. In addition, one may consider whether the enhancement of the *e-ph* coupling plays a role in the 'pairing glue' of the superconducting state. So far, no conclusive experimental insight points towards either *e-ph* driven superconductivity[228–230] or a more exotic *e-e* driven pairing[224–227]. Many aspects about the phonon spectrum and the strength of *e-ph* coupling in MATBG remain unresolved.

This study of the electron cooling dynamics supports the current picture of light-matter interaction in MATBG for above-gap excitation (see Fig. 4.3b). As put forward in previous reports[143, 242–245], the excitation and thermalization processes for 'high-energy' photons (much larger than the energy scale of the flat bands) appear to be insensitive to the flat bands and the correlated states. The main consequence of the photo-absorption is the generation of a hot carrier distribution in the flat bands with $T_e > T_l$.

However, we note that hot carrier physics in MATBG has not been

comprehensively explored. Many of the experimental signatures of hot carrier transport in graphene[130, 209, 210] have not been reported yet for MATBG. For instance, we have hypothesized here that the thermalization time in MATBG is similar to that of intrinsic graphene. To date, the thermalization dynamics of this system have not been directly observed. Experiments with higher temporal resolution ($\sim$ fs) are required to resolve these dynamics[212].

Future studies may also look closer into the role of the correlated ground states in the hot carrier dynamics. Would they change dramatically for a correlated insulator compared to a 'trivial' metallic state? Are the hot carrier dynamics sensitive to the symmetries of the underlying ground state? In our study, at temperatures of $T \geq 5$ K and with $\sim$ 100 fs temporal resolution, we didn't observe such effects

Studying the cooling dynamics of MATBG in different conditions is also an enticing prospect. First, one may study them at lower lattice temperatures. Will the cooling time remain ultrafast down to mK temperatures? Are there other scattering mechanisms beyond the Umklapp *e-ph* scattering? What role do the hBN phonons play in these MATBG samples? Could one engineer moiré phonons in surrounding layers, for example in the hBN substrate?[308]

Another promising research direction is the use of longer excitation wavelengths. To fully unravel light-matter interaction in the flat bands, one needs to match the energy scale of the flat bands, which corresponds to a photon energy of a few THz. Terahertz excitation could be used to study optical transitions within the MATBG flat bands[139, 309, 310], perhaps unveiling intricate selection rules. A bulk photovoltaic effect is also expected to occur in MATBG under THz illumination[311]. We note that terahertz optics experiments are challenging, particularly when the size of the MATBG samples is comparable to or smaller than the wavelength. The possibility of performing on-chip THz spectroscopy[312] or Fourier-transform infrared spectroscopy[313] stands out as a possible avenue to address these challenges.

From an applied perspective, the central question is how can one leverage the ultrafast cooling in MATBG for the design of novel devices. One immediate possibility is the development of ultrafast photodetectors operating at low temperatures[137, 314], with applications in space communications[266] or quantum photonic circuits[315]. The ultrafast, low-temperature cooling could also be leveraged in conjunction with the ultra-low carrier density superconductivity in MATBG, which has been proven to be extremely sensitive to optical excitations[140, 143]. Furthermore, the combination of the unique thermoelectric response demonstrated in Chapter 3 and the ultrafast electron cooling time could enable the development of novel thermoelectric devices based on MATBG[316].

The ultrafast carrier cooling observed in MATBG is also appealing for

heat management in low-temperature electronics. Modern electronic circuits are characterized by high-density packing of miniaturized components that will dissipate heat[317]. Thermal engineering of these circuits becomes increasingly challenging as the device dimensions shrink and the operation temperature decreases. However, 2D materials including MATBG generally exhibit excellent thermal properties. Thus, implementing 2D materials in commercial cryogenic electronics can help alleviate the thermal load in these circuits[318].

On high-T_c superconducting devices for quantum technologies

Lastly, in Chapter 5, we described the development of superconducting photodetectors based on an exfoliated, high-T_c superconductor. We demonstrated bolometric photodetection that leverages the large dR/dT values in the BSCCO-2212 samples, obtaining record performance in terms of device responsivity up to liquid nitrogen temperatures (77 K)[167]. Furthermore, we showed that for high-quality devices with hysteretic, bistable IV curves, it is possible to exploit an SNSPD-like avalanche response. Through this non-bolometric mechanism, we were able to reach single-photon sensitivity at $\lambda = 1550$ nm at $T = 20$ K[168].

The results presented here constitute a significant first step towards the practical use of HTS's in sensing applications. Indeed, the group of Karl Berggren demonstrated very similar devices with improved performance shortly after[288]. Notably, they reported single photon detection at a slightly higher temperature (25 K) and were able to read out the device response in a nanosecond timescale (comparable to commercial SNSPD's).

Here, we discuss possible avenues for improvement in the specific devices explored in this thesis, as well as recent efforts to scale the fabrication and integration of HTS devices. While the mechanical exfoliation of BSCCO-2212 flakes does not offer much scalability, so far it has proven to be an effective way to harness HTS in ultra-thin samples[86, 89, 167, 168, 281, 282, 288, 319].

Regarding the improvement of the BSCCO-2212/hBN heterostructures, the clear goal is realizing superconducting single-photon detectors that operate at liquid nitrogen temperature. In principle, hysteretic IV characteristics at higher temperatures should be attainable in pristine BSCCO-2212 nanostructures. We highlight two areas for improvement towards this prospect: 1. improving the electrical contact to the superconducting flake and 2. reducing the degradation of the non-irradiated layers.

In this work, we used a bottom contact strategy to minimize the fabrication steps after exfoliation and stacking. However, the bottom contacts create a Schottky barrier at low temperatures and can be unstable over long periods. While the Schottky barrier can be overcome, it may complicate

the impedance matching of these devices, which could ultimately limit the overall performance of such detectors[320].

The superconducting properties of the BSCCO-2212 flakes ultimately depend on the degradation due to the exposure to ambient conditions[151]. While we attempted to minimize this effect, the bottleneck for hysteretic transport above 30 K remains the material's chemical instability. In the fabrication process, one may minimize degradation further using a better encapsulation strategy [321, 322] or through an improvement of the nanopatterning process.

Top-encapsulated devices with bottom electrical contacts may suffer some degradation once they are outside the glovebox, as air can creep in through the roughness of the SiO_2 substrate and the gaps at the electrode edge. In our fabrication workflow, this can take place during the brief exposure of the sample when wire bonding the chip. An alternative is the double encapsulation of the BSCCO-2212 flake with hBN. Such a device could retain high-quality superconducting properties at high temperatures, including the hysteretic IV characteristics. New strategies for electrical contact would be required for double-encapsulated devices[322]. One possibility would be the use of larger flakes in which the active area of the device is doubly encapsulated, while the electrical contact lies away from the active area. Vertical access through pre-patterned gold contacts on the encapsulating hBN, known as VIA contacts, is also an appealing strategy[323].

In this work, we used an inert atmosphere glovebox for the exfoliation and assembly of BSCCO-2212 heterostructures. Exfoliation of BSCCO-2212 using a cold plate (liquid nitrogen cooled) can help preserve the flake doping level[89, 319]. Direct evaporation of metallic contacts using a stencil mask was also demonstrated as a viable strategy for BSCCO-2212 devices[282, 319, 321]. Ideally, the entire exfoliation, stacking, contact evaporation, wire-bonding and nanopatterning of the devices would be performed without any exposure to ambient conditions. This prospect requires highly specialized setups, like those shown in Refs. [89, 324–326].

The nanopatterning process can also be optimized to reduce further any damage from the He^+ ion beam. Outside the patterned area, some (unwanted) disorder can appear due to the ion irradiation, reducing the sample quality. From simulations of the beam-sample interaction, the backscattering of helium ions was found to be the main source of unwanted disorder[167]. Collisions from backscattered He-ions reduce the nominal width of the nanowires and make the doping profile less sharp, with the edges of the nanowire likely being away from optimal doping[158].

A way to reduce ion back-scattering is the fabrication of suspended devices where the active area of the BSCCO-2212 flake has no underlying substrate (see Fig. 2.16c). One could even envision a doubly-encapsulated BSCCO-

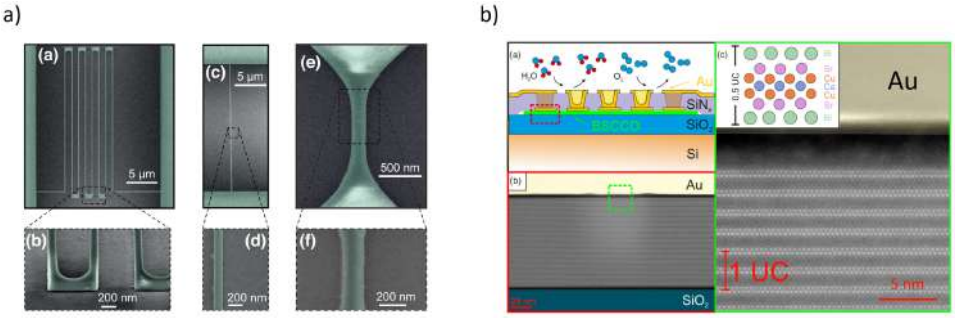

Figure 6.2: a) SEM images of different nanostructures on a YBCO film of 30 nm thickness. Both meandering nanowires and nanochannel devices exhibited hysteretic transport characteristics. b) Illustration of the cross-section for a BSCCO flake integrated in a printed circuit board, which serves as electrical contact and encapsulating layer. The lower and right panels show general and detailed TEM images of the interface between BSCCO-2212 and the gold layer. Panels (a) and (b) are adapted from [290] and [322].

2212 device where the active area is free-standing. Such a design could enable even higher patterning precision ($\sim$ nm scale) and sharp superconducting features at higher temperatures.

Regarding the scalability of high-T_c devices, the growth of cuprate thin films (specifically $YBa_2Cu_3O_7$ or YBCO) stands out as a promising avenue for large-scale fabrication of these devices[145]. The demonstration of single-photon control of the switching dynamics in a YBCO nanowire illustrates the potential for next-generation HTS-based quantum devices[327]. Extensive research efforts have tried to obtain YBCO nanowires with hysteretic transport and potential for single-photon detection [286, 287, 328–330]. Recently, the scalable fabrication of high-quality YBCO nanostructures with hysteretic IV's was reported[290] (Fig. 6.2b).

Another possibility is the direct integration of exfoliated HTS flakes into different device architectures, as we explored with the waveguide-integrated bolometer. Recent work demonstrated an approach for scalable integration of exfoliated BSCCO-2212 flakes into CMOS circuits[322]. The method relies on the PDMS-assisted transfer of printed circuit boards directly on the exfoliated BSCCO-2212 flakes (see Fig. 6.2b). The printed circuit boards lie on a thin SiN membrane which also encapsulates the superconducting flake as the circuit is transferred. These devices are very promising, as they exhibit excellent and stable transport characteristics[322].

The appeal of cuprate-based 2D devices goes beyond the prospect of designing better superconducting sensors. From a fundamental standpoint, several aspects of cuprate phenomena are still under debate, including the

pairing mechanism and the symmetry of the order parameter. Early studies of exfoliated BSCCO-2212 explored its phase diagram via electrostatic doping[281]. Unlike its bulk counterpart, 2D layers of BSCCO-2212 can be doped continuously via ionic liquid gating (see Fig. 5.4c).

Other studies have investigated junctions of twisted BSCCO-2212 layers, where the twist angle controls the overlap between the anisotropic d-wave superconducting gaps of each layer[319, 321, 331, 332]. Theoretical proposals predicted that a topological superconducting state would emerge at a twist angle of 45°[333]. Recent experimental studies unveiled a suppression of the tunneling for 45° junctions[319], a direct consequence of the symmetry of the d-wave symmetry of the order parameter, as well as a superconducting diode effect [334]. Josephson junctions based on twisted d-wave superconductors have also been proposed as a platform for novel hybrid qubits with enhanced coherence times[335].

All in all, the work comprised in this thesis illustrates the wide-ranging possibilities that lie in the physics of correlated 2D materials; both in terms of fundamental physics and the development of new technologies. Hopefully, the results and discussion presented here motivate future research that pushes science, and therefore society, forward.

Bibliography

[1] K. S. Novoselov, A. Mishchenko, A. Carvalho, and A. H. Castro Neto, "2D materials and van der Waals heterostructures," *Science*, vol. 353, no. 6298, p. aac9439, Jul. 2016. [Online]. Available: https://www.science.org/doi/10.1126/science.aac9439

[2] Y. Liu, N. O. Weiss, X. Duan, H.-C. Cheng, Y. Huang, and X. Duan, "Van der Waals heterostructures and devices," *Nature Reviews Materials*, vol. 1, no. 9, p. 16042, Jul. 2016. [Online]. Available: https://www.nature.com/articles/natrevmats201642

[3] E. Y. Andrei, D. K. Efetov, P. Jarillo-Herrero, A. H. MacDonald, K. F. Mak, T. Senthil, E. Tutuc, A. Yazdani, and A. F. Young, "The marvels of moiré materials," *Nature Reviews Materials*, vol. 6, no. 3, pp. 201–206, Mar. 2021. [Online]. Available: https://www.nature.com/articles/s41578-021-00284-1

[4] Y. Cao, V. Fatemi, A. Demir, S. Fang, S. L. Tomarken, J. Y. Luo, J. D. Sanchez-Yamagishi, K. Watanabe, T. Taniguchi, E. Kaxiras, R. C. Ashoori, and P. Jarillo-Herrero, "Correlated insulator behaviour at half-filling in magic-angle graphene superlattices," *Nature*, vol. 556, no. 7699, pp. 80–84, Apr. 2018. [Online]. Available: http://www.nature.com/articles/nature26154

[5] Y. Cao, V. Fatemi, S. Fang, K. Watanabe, T. Taniguchi, E. Kaxiras, and P. Jarillo-Herrero, "Unconventional superconductivity in magic-angle graphene superlattices," *Nature*, vol. 556, no. 7699, pp. 43–50, 2018, publisher: Nature Publishing Group.

[6] P. Drude, "Zur Elektronentheorie der Metalle," *Annalen der Physik*, vol. 306, no. 3, pp. 566–613, Jan. 1900. [Online]. Available: https://onlinelibrary.wiley.com/doi/10.1002/andp.19003060312

[7] E. H. Hall, "Sommerfeld's Electron-Theory of Metals," *Proceedings of the National Academy of Sciences*, vol. 14, no. 5, pp. 370–377, May 1928. [Online]. Available: https://pnas.org/doi/full/10.1073/pnas.14.5.370

[8] F. Bloch, “Uber die Quantenmechanik der Elek~ronen in Kristallgittern.” *Zeitschrift für Physik*, vol. 52, pp. 555–600, 1928.

[9] T. Zandt, H. Dwelk, C. Janowitz, and R. Manzke, “Quadratic temperature dependence up to 50 K of the resistivity of metallic MoTe 2,” *Journal of Alloys and Compounds*, vol. 442, no. 1-2, pp. 216–218, Sep. 2007. [Online]. Available: https://linkinghub.elsevier.com/retrieve/pii/S0925838807002800

[10] I. Landau, L.D.; Pomeranchuk, “On the properties of metals at very low temperatures,” in *Collected Papers of L.D. Landau*, 1965, pp. 171–183. [Online]. Available: https://linkinghub.elsevier.com/retrieve/pii/B9780080105864500304

[11] W. G. Baber, “The contribution to the electrical resistance of metals from collisions between electrons,” 1936.

[12] J. Hubbard, “Electron correlations in narrow energy bands,” *Proc. R. Soc. Lond. A*, vol. 276, pp. 238–257, 1963.

[13] M. C. Gutzwiller, “Effect of Correlation on the Ferromagnetism of Transition Metals,” *Physical Review Letters*, vol. 10, no. 5, pp. 159–162, Mar. 1963. [Online]. Available: https://link.aps.org/doi/10.1103/PhysRevLett.10.159

[14] J. Kanamori, “Electron Correlation and Ferromagnetism of Transition Metals,” *Progress of Theoretical Physics*, vol. 30, no. 3, pp. 275–289, Sep. 1963. [Online]. Available: https://academic.oup.com/ptp/article-lookup/doi/10.1143/PTP.30.275

[15] Y. Yang, F. Yu, X. Wen, Z. Gui, Y. Zhang, F. Zhan, R. Wang, J. Ying, and X. Chen, “Pressure-induced transition from a Mott insulator to a ferromagnetic Weyl metal in La2O3Fe2Se2,” *Nature Communications*, vol. 14, no. 1, p. 2260, Apr. 2023. [Online]. Available: https://www.nature.com/articles/s41467-023-37971-2

[16] J. Hubbard, “Electron correlations in narrow energy bands III. An improved solution,” *Proc. R. Soc. Lond. A*, vol. 281, no. 1386, pp. 401–419, Sep. 1964. [Online]. Available: https://royalsocietypublishing.org/doi/10.1098/rspa.1964.0190

[17] T. Vojta, “Quantum phase transitions in electronic systems,” *Annalen der Physik*, vol. 512, no. 6, pp. 403–440, Jun. 2000. [Online]. Available: https://onlinelibrary.wiley.com/doi/10.1002/andp.20005120601

[18] "The Hubbard model at half a century," *Nature Physics*, vol. 9, no. 9, pp. 523–523, Sep. 2013. [Online]. Available: https://www.nature.com/articles/nphys2759

[19] G. R. Stewart, "Heavy-fermion systems," *Reviews of Modern Physics*, vol. 56, no. 4, pp. 755–787, Oct. 1984. [Online]. Available: https://link.aps.org/doi/10.1103/RevModPhys.56.755

[20] S. Wirth and F. Steglich, "Exploring heavy fermions from macroscopic to microscopic length scales," *Nature Reviews Materials*, vol. 1, no. 10, p. 16051, Aug. 2016. [Online]. Available: https://www.nature.com/articles/natrevmats201651

[21] W. De Haas and G. Van Den Berg, "The electrical resistance of gold and silver at low temperatures," *Physica*, vol. 3, no. 6, pp. 440–449, Jun. 1936. [Online]. Available: https://linkinghub.elsevier.com/retrieve/pii/S0031891436800093

[22] J. Kondo, "Resistance Minimum in Dilute Magnetic Alloys," *Progress of Theoretical Physics*, vol. 32, no. 1, pp. 37–49, Jul. 1964. [Online]. Available: https://academic.oup.com/ptp/article-lookup/doi/10.1143/PTP.32.37

[23] M. Lavagna and C. Pépin, "The Kondo lattice model," *Acta Physica Polonica B*, vol. 29, 1998.

[24] M. A. Ruderman and C. Kittel, "Indirect Exchange Coupling of Nuclear Magnetic Moments by Conduction Electrons," *Physical Review*, vol. 96, no. 1, pp. 99–102, Oct. 1954. [Online]. Available: https://link.aps.org/doi/10.1103/PhysRev.96.99

[25] T. Kasuya, "A Theory of Metallic Ferro- and Antiferromagnetism on Zener's Model," *Progress of Theoretical Physics*, vol. 16, no. 1, pp. 45–57, Jul. 1956. [Online]. Available: https://academic.oup.com/ptp/article-lookup/doi/10.1143/PTP.16.45

[26] K. Yosida, "Magnetic Properties of Cu-Mn Alloys," *Physical Review*, vol. 106, no. 5, pp. 893–898, Jun. 1957. [Online]. Available: https://link.aps.org/doi/10.1103/PhysRev.106.893

[27] E. D. Isaacs, P. Zschack, C. L. Broholm, C. Burns, G. Aeppli, A. P. Ramirez, T. T. M. Palstra, R. W. Erwin, N. Stücheli, and E. Bucher, "Antiferromagnetism and Its Relation to the Superconducting Phases of UP t 3," *Physical Review Letters*, vol. 75, no. 6, pp. 1178–1181, Aug. 1995. [Online]. Available: https://link.aps.org/doi/10.1103/PhysRevLett.75.1178

[28] S. A. M. Mentink, A. Drost, G. J. Nieuwenhuys, E. Frikkee, A. A. Menovsky, and J. A. Mydosh, "Magnetic Ordering and Frustration in Hexagonal U Ni 4 B," *Physical Review Letters*, vol. 73, no. 7, pp. 1031–1034, Aug. 1994. [Online]. Available: https://link.aps.org/doi/10.1103/PhysRevLett.73.1031

[29] K. Andres, J. E. Graebner, and H. R. Ott, "4 f -Virtual-Bound-State Formation in Ce Al 3 at Low Temperatures," *Physical Review Letters*, vol. 35, no. 26, pp. 1779–1782, Dec. 1975. [Online]. Available: https://link.aps.org/doi/10.1103/PhysRevLett.35.1779

[30] W. Simeth, Z. Wang, E. A. Ghioldi, D. M. Fobes, A. Podlesnyak, N. H. Sung, E. D. Bauer, J. Lass, S. Flury, J. Vonka, D. G. Mazzone, C. Niedermayer, Y. Nomura, R. Arita, C. D. Batista, F. Ronning, and M. Janoschek, "A microscopic Kondo lattice model for the heavy fermion antiferromagnet CeIn3," *Nature Communications*, vol. 14, no. 1, p. 8239, Dec. 2023. [Online]. Available: https://www.nature.com/articles/s41467-023-43947-z

[31] F. Steglich, J. Aarts, C. D. Bredl, W. Lieke, D. Meschede, W. Franz, and H. Schäfer, "Superconductivity in the Presence of Strong Pauli Paramagnetism: Ce Cu 2 Si 2," *Physical Review Letters*, vol. 43, no. 25, pp. 1892–1896, Dec. 1979. [Online]. Available: https://link.aps.org/doi/10.1103/PhysRevLett.43.1892

[32] P. Coleman, C. Pépin, Q. Si, and R. Ramazashvili, "How do Fermi liquids get heavy and die?" *Journal of Physics: Condensed Matter*, vol. 13, no. 35, pp. R723–R738, Sep. 2001. [Online]. Available: https://iopscience.iop.org/article/10.1088/0953-8984/13/35/202

[33] B. B. Zhou, S. Misra, E. H. Da Silva Neto, P. Aynajian, R. E. Baumbach, J. D. Thompson, E. D. Bauer, and A. Yazdani, "Visualizing nodal heavy fermion superconductivity in CeCoIn5," *Nature Physics*, vol. 9, no. 8, pp. 474–479, Aug. 2013. [Online]. Available: https://www.nature.com/articles/nphys2672

[34] M. P. Allan, F. Massee, D. K. Morr, J. Van Dyke, A. W. Rost, A. P. Mackenzie, C. Petrovic, and J. C. Davis, "Imaging Cooper pairing of heavy fermions in CeCoIn5," *Nature Physics*, vol. 9, no. 8, pp. 468–473, Aug. 2013. [Online]. Available: https://www.nature.com/articles/nphys2671

[35] T. Park, E. D. Bauer, and J. D. Thompson, "Probing the Nodal Gap in the Pressure-Induced Heavy Fermion Superconductor CeRhIn 5,"

Physical Review Letters, vol. 101, no. 17, p. 177002, Oct. 2008. [Online]. Available: https://link.aps.org/doi/10.1103/PhysRevLett.101.177002

[36] M. Taupin and S. Paschen, "Are Heavy Fermion Strange Metals Planckian?" *Crystals*, vol. 12, no. 2, p. 251, Feb. 2022. [Online]. Available: https://www.mdpi.com/2073-4352/12/2/251

[37] A. Menth, E. Buehler, and T. H. Geballe, "Magnetic and Semiconducting Properties of Sm B 6," *Physical Review Letters*, vol. 22, no. 7, pp. 295–297, Feb. 1969. [Online]. Available: https://link.aps.org/doi/10.1103/PhysRevLett.22.295

[38] J. G. Bednorz and K. A. Mülleer, "Possible High Tc Superconductivity in the Ba - La- Cu- 0 System," *Z. Phys.B- CondensedMatter*, vol. 64, pp. 189–193, 1986.

[39] M. K. Wu, J. R. Ashburn, C. J. Torng, P. H. Hor, R. L. Meng, L. Gao, Z. J. Huang, Y. Q. Wang, and C. W. Chu, "Superconductivity at 93 K in a new mixed-phase Y-Ba-Cu-O compound system at ambient pressure," *Physical Review Letters*, vol. 58, no. 9, pp. 908–910, Mar. 1987. [Online]. Available: https://link.aps.org/doi/10.1103/PhysRevLett.58.908

[40] H. Maeda, Y. Tanaka, M. Fukutomi, and T. Asano, "A New High-Tc Oxide Superconductor without a Rare Earth Element," *Jpn. J. Appl. Phys.*, vol. 27, no. L209, 1988.

[41] C. Proust and L. Taillefer, "The Remarkable Underlying Ground States of Cuprate Superconductors," *Annual Review of Condensed Matter Physics*, vol. 10, no. 1, pp. 409–429, Mar. 2019. [Online]. Available: https://www.annualreviews.org/doi/10.1146/annurev-conmatphys-031218-013210

[42] B. Michon, C. Girod, S. Badoux, J. Kačmarčík, Q. Ma, M. Dragomir, H. A. Dabkowska, B. D. Gaulin, J.-S. Zhou, S. Pyon, T. Takayama, H. Takagi, S. Verret, N. Doiron-Leyraud, C. Marcenat, L. Taillefer, and T. Klein, "Thermodynamic signatures of quantum criticality in cuprate superconductors," *Nature*, vol. 567, no. 7747, pp. 218–222, Mar. 2019. [Online]. Available: https://www.nature.com/articles/s41586-019-0932-x

[43] G. Mirarchi, G. Seibold, C. Di Castro, M. Grilli, and S. Caprara, "The Strange-Metal Behavior of Cuprates," *Condensed Matter*, vol. 7, no. 1, p. 29, Mar. 2022. [Online]. Available: https://www.mdpi.com/2410-3896/7/1/29

[44] T. Timusk and B. Statt, "The pseudogap in high-temperature superconductors: an experimental survey," *Reports on Progress in Physics*, vol. 62, no. 1, pp. 61–122, Jan. 1999. [Online]. Available: https://iopscience.iop.org/article/10.1088/0034-4885/62/1/002

[45] N. Doiron-Leyraud, O. Cyr-Choinière, S. Badoux, A. Ataei, C. Collignon, A. Gourgout, S. Dufour-Beauséjour, F. F. Tafti, F. Laliberté, M.-E. Boulanger, M. Matusiak, D. Graf, M. Kim, J.-S. Zhou, N. Momono, T. Kurosawa, H. Takagi, and L. Taillefer, "Pseudogap phase of cuprate superconductors confined by Fermi surface topology," *Nature Communications*, vol. 8, no. 1, p. 2044, Dec. 2017. [Online]. Available: https://www.nature.com/articles/s41467-017-02122-x

[46] B. Keimer, S. A. Kivelson, M. R. Norman, S. Uchida, and J. Zaanen, "From quantum matter to high-temperature superconductivity in copper oxides," *Nature*, vol. 518, no. 7538, pp. 179–186, Feb. 2015. [Online]. Available: https://www.nature.com/articles/nature14165

[47] W. L. McMillan, "Transition Temperature of Strong-Coupled Superconductors," *Physical Review*, vol. 167, no. 2, pp. 331–344, Mar. 1968. [Online]. Available: https://link.aps.org/doi/10.1103/PhysRev.167.331

[48] D. J. Van Harlingen, "Phase-sensitive tests of the symmetry of the pairing state in the high-temperature superconductors—Evidence for d x 2 y 2 symmetry," *Reviews of Modern Physics*, vol. 67, no. 2, pp. 515–535, Apr. 1995. [Online]. Available: https://link.aps.org/doi/10.1103/RevModPhys.67.515

[49] K. A. Moler, D. L. Sisson, J. S. Urbach, M. R. Beasley, A. Kapitulnik, D. J. Baar, R. Liang, and W. N. Hardy, "Specific heat of YBa 2Cu 3O 7," *PHYSICAL REVIEW B*, vol. 55, 1997.

[50] Y. Kamihara, H. Hiramatsu, M. Hirano, R. Kawamura, H. Yanagi, T. Kamiya, and H. Hosono, "Iron-Based Layered Superconductor: LaOFeP," *Journal of the American Chemical Society*, vol. 128, no. 31, pp. 10 012–10 013, Aug. 2006. [Online]. Available: https://pubs.acs.org/doi/10.1021/ja063355c

[51] W. Ruan and Y. Zhang, "Strong correlations in two-dimensional transition metal dichalcogenides," *Science China Physics, Mechanics & Astronomy*, vol. 66, no. 11, p. 117506, Nov. 2023. [Online]. Available: https://link.springer.com/10.1007/s11433-023-2141-9

[52] D. Jérome, "Organic Superconductors: When Correlations and Magnetism Walk in," *Journal of Superconductivity and Novel Magnetism*, vol. 25, no. 3, pp. 633–655, Apr. 2012. [Online]. Available: http://link.springer.com/10.1007/s10948-012-1475-7

[53] D. C. Tsui, H. L. Stormer, and A. C. Gossard, "Two-Dimensional Magnetotransport in the Extreme Quantum Limit," *Physical Review Letters*, vol. 48, no. 22, pp. 1559–1562, May 1982. [Online]. Available: https://link.aps.org/doi/10.1103/PhysRevLett.48.1559

[54] D. Jaksch, C. Bruder, J. I. Cirac, C. W. Gardiner, and P. Zoller, "Cold Bosonic Atoms in Optical Lattices," *Physical Review Letters*, vol. 81, no. 15, pp. 3108–3111, Oct. 1998. [Online]. Available: https://link.aps.org/doi/10.1103/PhysRevLett.81.3108

[55] M. Greiner, O. Mandel, and T. Esslinger, "Quantum phase transition from a superfluid to a Mott insulator in a gas of ultracold atoms," *Nature*, vol. 415, 2002.

[56] M. Köhl, H. Moritz, T. Stöferle, K. Günter, and T. Esslinger, "Fermionic Atoms in a Three Dimensional Optical Lattice: Observing Fermi Surfaces, Dynamics, and Interactions," *Physical Review Letters*, vol. 94, no. 8, p. 080403, Mar. 2005. [Online]. Available: https://link.aps.org/doi/10.1103/PhysRevLett.94.080403

[57] S. Baier, M. J. Mark, D. Petter, K. Aikawa, L. Chomaz, Z. Cai, M. Baranov, P. Zoller, and F. Ferlaino, "Extended Bose-Hubbard models with ultracold magnetic atoms," *Science*, vol. 352, no. 6282, pp. 201–205, Apr. 2016. [Online]. Available: https://www.science.org/doi/10.1126/science.aac9812

[58] S. Ospelkaus, C. Ospelkaus, O. Wille, M. Succo, P. Ernst, K. Sengstock, and K. Bongs, "Localization of Bosonic Atoms by Fermionic Impurities in a Three-Dimensional Optical Lattice," *Physical Review Letters*, vol. 96, no. 18, p. 180403, May 2006. [Online]. Available: https://link.aps.org/doi/10.1103/PhysRevLett.96.180403

[59] K. Günter, T. Stöferle, H. Moritz, M. Köhl, and T. Esslinger, "Bose-Fermi Mixtures in a Three-dimensional Optical Lattice," *Physical Review Letters*, vol. 96, no. 18, p. 180402, May 2006.

[60] D. Jaksch and P. Zoller, "The cold atom Hubbard toolbox," *Annals of Physics*, vol. 315, no. 1, pp. 52–79, Jan. 2005. [Online]. Available: https://linkinghub.elsevier.com/retrieve/pii/S0003491604001782

[61] T. Esslinger, "Fermi-Hubbard Physics with Atoms in an Optical Lattice," *Annual Review of Condensed Matter Physics*, vol. 1, no. 1, pp. 129–152, Aug. 2010. [Online]. Available: https://www.annualreviews.org/doi/10.1146/annurev-conmatphys-070909-104059

[62] K. S. Novoselov, A. K. Geim, S. . Morozov., D. Jiang, Y. Zhang, S. V. Dubonos, I. V. Grigorieva, and A. A. Firsov, "Electric Field Effect in Atomically Thin Carbon Films," *Science*, vol. 306, no. 5696, pp. 666–669, 2016.

[63] G. Li, A. Luican, J. M. B. Lopes Dos Santos, A. H. Castro Neto, A. Reina, J. Kong, and E. Y. Andrei, "Observation of Van Hove singularities in twisted graphene layers," *Nature Physics*, vol. 6, no. 2, pp. 109–113, Feb. 2010. [Online]. Available: https://www.nature.com/articles/nphys1463

[64] A. Luican, G. Li, A. Reina, J. Kong, R. R. Nair, K. S. Novoselov, A. K. Geim, and E. Y. Andrei, "Single-Layer Behavior and Its Breakdown in Twisted Graphene Layers," *Physical Review Letters*, vol. 106, no. 12, p. 126802, Mar. 2011. [Online]. Available: https://link.aps.org/doi/10.1103/PhysRevLett.106.126802

[65] R. Bistritzer and A. H. MacDonald, "Moiré bands in twisted double-layer graphene," *Proceedings of the National Academy of Sciences of the United States of America*, vol. 108, no. 30, pp. 12 233–12 237, Jul. 2011.

[66] L. A. Ponomarenko, R. V. Gorbachev, G. L. Yu, D. C. Elias, R. Jalil, A. A. Patel, A. Mishchenko, A. S. Mayorov, C. R. Woods, J. R. Wallbank, M. Mucha-Kruczynski, B. A. Piot, M. Potemski, I. V. Grigorieva, K. S. Novoselov, F. Guinea, V. I. Fal'ko, and A. K. Geim, "Cloning of Dirac fermions in graphene superlattices," *Nature*, vol. 497, no. 7451, pp. 594–597, May 2013. [Online]. Available: https://www.nature.com/articles/nature12187

[67] C. R. Dean, L. Wang, P. Maher, C. Forsythe, F. Ghahari, Y. Gao, J. Katoch, M. Ishigami, P. Moon, M. Koshino, T. Taniguchi, K. Watanabe, K. L. Shepard, J. Hone, and P. Kim, "Hofstadter's butterfly and the fractal quantum Hall effect in moiré superlattices," *Nature*, vol. 497, no. 7451, pp. 598–602, May 2013. [Online]. Available: https://www.nature.com/articles/nature12186

[68] B. Hunt, J. D. Sanchez-Yamagishi, A. F. Young, M. Yankowitz, B. J. LeRoy, K. Watanabe, T. Taniguchi, P. Moon, M. Koshino,

P. Jarillo-Herrero, and R. C. Ashoori, "Massive Dirac Fermions and Hofstadter Butterfly in a van der Waals Heterostructure," *Science*, vol. 340, no. 6139, pp. 1427–1430, Jun. 2013. [Online]. Available: https://www.science.org/doi/10.1126/science.1237240

[69] P. R. Wallace, "The Band Theory of Graphite," *Physical Review*, vol. 71, no. 9, pp. 622–634, May 1947. [Online]. Available: https://link.aps.org/doi/10.1103/PhysRev.71.622

[70] A. H. Castro Neto, F. Guinea, N. M. R. Peres, K. S. Novoselov, and A. K. Geim, "The electronic properties of graphene," *Reviews of Modern Physics*, vol. 81, no. 1, pp. 109–162, Jan. 2009. [Online]. Available: https://link.aps.org/doi/10.1103/RevModPhys.81.109

[71] K. S. Novoselov, A. K. Geim, S. V. Morozov, D. Jiang, M. I. Katsnelson, I. V. Grigorieva, S. V. Dubonos, and A. A. Firsov, "Two-dimensional gas of massless Dirac fermions in graphene," *Nature*, vol. 438, no. 7065, pp. 197–200, 2005.

[72] J. Crossno, J. K. Shi, K. Wang, X. Liu, A. Harzheim, A. Lucas, S. Sachdev, P. Kim, T. Taniguchi, K. Watanabe, T. A. Ohki, and K. C. Fong, "Observation of the Dirac fluid and the breakdown of the Wiedemann-Franz law in graphene," *Science*, vol. 351, no. 6277, pp. 1058–1061, Mar. 2016. [Online]. Available: https://www.science.org/doi/10.1126/science.aad0343

[73] K. S. Novoselov, Z. Jiang, Y. Zhang, S. V. Morozov, H. L. Stormer, U. Zeitler, J. C. Maan, G. S. Boebinger, P. Kim, and A. K. Geim, "Room-temperature quantum hall effect in graphene," *Science*, vol. 315, no. 5817, p. 1379, 2007.

[74] X. Cui, G.-H. Lee, Y. D. Kim, G. Arefe, P. Y. Huang, C.-H. Lee, D. A. Chenet, X. Zhang, L. Wang, F. Ye, F. Pizzocchero, B. S. Jessen, K. Watanabe, T. Taniguchi, D. A. Muller, T. Low, P. Kim, and J. Hone, "Multi-terminal transport measurements of MoS2 using a van der Waals heterostructure device platform," *Nature Nanotechnology*, vol. 10, no. 6, pp. 534–540, Jun. 2015. [Online]. Available: https://www.nature.com/articles/nnano.2015.70

[75] K. F. Mak, L. Ju, F. Wang, and T. F. Heinz, "Optical spectroscopy of graphene: From the far infrared to the ultraviolet," *Solid State Communications*, vol. 152, no. 15, pp. 1341–1349, Aug. 2012. [Online]. Available: https://linkinghub.elsevier.com/retrieve/pii/S0038109812002700

[76] R. R. Nair, P. Blake, A. N. Grigorenko, K. S. Novoselov, T. J. Booth, T. Stauber, N. M. R. Peres, and A. K. Geim, "Fine Structure Constant Defines Visual Transparency of Graphene," *Science*, vol. 320, no. 5881, pp. 1308–1308, Jun. 2008. [Online]. Available: https://www.science.org/doi/10.1126/science.1156965

[77] Q. Bao and K. P. Loh, "Graphene Photonics, Plasmonics, and Broadband Optoelectronic Devices," *ACS Nano*, vol. 6, no. 5, pp. 3677–3694, May 2012. [Online]. Available: https://pubs.acs.org/doi/10.1021/nn300989g

[78] E. McCann and V. I. Fal'ko, "Landau-Level Degeneracy and Quantum Hall Effect in a Graphite Bilayer," *Physical Review Letters*, vol. 96, no. 8, p. 086805, Mar. 2006. [Online]. Available: https://link.aps.org/doi/10.1103/PhysRevLett.96.086805

[79] Y. Zhang, T.-T. Tang, C. Girit, Z. Hao, M. C. Martin, A. Zettl, M. F. Crommie, Y. R. Shen, and F. Wang, "Direct observation of a widely tunable bandgap in bilayer graphene," *Nature*, vol. 459, no. 7248, pp. 820–823, Jun. 2009. [Online]. Available: https://www.nature.com/articles/nature08105

[80] H. Yan, "Bilayer graphene: physics and application outlook in photonics," *Nanophotonics*, vol. 4, no. 1, pp. 115–127, May 2015. [Online]. Available: https://www.degruyter.com/document/doi/10.1515/nanoph-2014-0019/html

[81] Y. Huang, E. Sutter, N. N. Shi, J. Zheng, T. Yang, D. Englund, H. J. Gao, and P. Sutter, "Reliable Exfoliation of Large-Area High-Quality Flakes of Graphene and Other Two-Dimensional Materials," *ACS Nano*, vol. 9, no. 11, pp. 10 612–10 620, 2015.

[82] K. F. Mak, C. Lee, J. Hone, J. Shan, and T. F. Heinz, "Atomically Thin MoS 2 : A New Direct-Gap Semiconductor," *Physical Review Letters*, vol. 105, no. 13, p. 136805, Sep. 2010. [Online]. Available: https://link.aps.org/doi/10.1103/PhysRevLett.105.136805

[83] Q. H. Wang, K. Kalantar-Zadeh, A. Kis, J. N. Coleman, and M. S. Strano, "Electronics and optoelectronics of two-dimensional transition metal dichalcogenides," *Nature Nanotechnology*, vol. 7, no. 11, pp. 699–712, Nov. 2012. [Online]. Available: https://www.nature.com/articles/nnano.2012.193

[84] C. R. Dean, A. F. Young, I. Meric, C. Lee, L. Wang, S. Sorgenfrei, K. Watanabe, T. Taniguchi, P. Kim, K. L. Shepard, and J. Hone,

"Boron nitride substrates for high-quality graphene electronics," *Nature Nanotechnology*, vol. 5, no. 10, pp. 722–726, Oct. 2010. [Online]. Available: https://www.nature.com/articles/nnano.2010.172

[85] B. Huang, G. Clark, E. Navarro-Moratalla, D. R. Klein, R. Cheng, K. L. Seyler, D. Zhong, E. Schmidgall, M. A. McGuire, D. H. Cobden, W. Yao, D. Xiao, P. Jarillo-Herrero, and X. Xu, "Layer-dependent ferromagnetism in a van der Waals crystal down to the monolayer limit," *Nature*, vol. 546, no. 7657, pp. 270–273, Jun. 2017. [Online]. Available: https://www.nature.com/articles/nature22391

[86] K. Lee, A. H. Dismukes, E. J. Telford, R. A. Wiscons, J. Wang, X. Xu, C. Nuckolls, C. R. Dean, X. Roy, and X. Zhu, "Magnetic Order and Symmetry in the 2D Semiconductor CrSBr," *Nano Letters*, vol. 21, no. 8, pp. 3511–3517, Apr. 2021. [Online]. Available: https://pubs.acs.org/doi/10.1021/acs.nanolett.1c00219

[87] J. T. Ye, Y. J. Zhang, R. Akashi, M. S. Bahramy, R. Arita, and Y. Iwasa, "Superconducting Dome in a Gate-Tuned Band Insulator," *Science*, vol. 338, no. 6111, pp. 1193–1196, Nov. 2012. [Online]. Available: https://www.science.org/doi/10.1126/science.1228006

[88] X. Xi, Z. Wang, W. Zhao, J.-H. Park, K. T. Law, H. Berger, L. Forró, J. Shan, and K. F. Mak, "Ising pairing in superconducting NbSe2 atomic layers," *Nature Physics*, vol. 12, no. 2, pp. 139–143, Feb. 2016. [Online]. Available: https://www.nature.com/articles/nphys3538

[89] Y. Yu, L. Ma, P. Cai, R. Zhong, C. Ye, J. Shen, G. Gu, C. Xian Hui, and Y. Zhang, "High-temperature superconductivity in monolayer Bi2Sr2CaCu2O8+," *Nature*, vol. 575, no. April, pp. 156–163, 2019.

[90] D. Teweldebrhan, V. Goyal, and A. A. Balandin, "Exfoliation and Characterization of Bismuth Telluride Atomic Quintuples and Quasi-Two-Dimensional Crystals," *Nano Letters*, vol. 10, no. 4, pp. 1209–1218, Apr. 2010. [Online]. Available: https://pubs.acs.org/doi/10.1021/nl903590b

[91] H. B. Heersche, P. Jarillo-Herrero, J. B. Oostinga, L. M. K. Vandersypen, and A. F. Morpurgo, "Bipolar supercurrent in graphene," *Nature*, vol. 446, no. 7131, pp. 56–59, Mar. 2007. [Online]. Available: https://www.nature.com/articles/nature05555

[92] C. Li, Q. Cao, F. Wang, Y. Xiao, Y. Li, J.-J. Delaunay, and H. Zhu, "Engineering graphene and TMDs based van der Waals heterostructures for photovoltaic and photoelectrochemical solar energy conversion,"

Chemical Society Reviews, vol. 47, no. 13, pp. 4981–5037, 2018. [Online]. Available: http://xlink.rsc.org/?DOI=C8CS00067K

[93] V. Elings and F. Wudl, "Tunneling microscopy on various carbon materials," *Journal of Vacuum Science & Technology A: Vacuum, Surfaces, and Films*, vol. 6, no. 2, pp. 412–414, Mar. 1988. [Online]. Available: https://pubs.aip.org/jva/article/6/2/412/97134/Tunneling-microscopy-on-various-carbon

[94] J. Xhie, K. Sattler, M. Ge, and N. Venkateswaran, "Giant and supergiant lattices on graphite," *Physical Review B*, vol. 47, no. 23, pp. 15 835–15 841, Jun. 1993. [Online]. Available: https://link.aps.org/doi/10.1103/PhysRevB.47.15835

[95] Z. Y. Rong and P. Kuiper, "Electronic effects in scanning tunneling microscopy: Moiré pattern on a graphite surface," *Physical Review B*, vol. 48, no. 23, pp. 17 427–17 431, Dec. 1993. [Online]. Available: https://link.aps.org/doi/10.1103/PhysRevB.48.17427

[96] J. Hass, F. Varchon, J. E. Millán-Otoya, M. Sprinkle, N. Sharma, W. A. De Heer, C. Berger, P. N. First, L. Magaud, and E. H. Conrad, "Why Multilayer Graphene on 4 H SiC (000 1 $^{-}$) Behaves Like a Single Sheet of Graphene," *Physical Review Letters*, vol. 100, no. 12, p. 125504, Mar. 2008. [Online]. Available: https://link.aps.org/doi/10.1103/PhysRevLett.100.125504

[97] F. Guinea, A. H. Castro Neto, and N. M. R. Peres, "Electronic states and Landau levels in graphene stacks," *Physical Review B*, vol. 73, no. 24, p. 245426, Jun. 2006. [Online]. Available: https://link.aps.org/doi/10.1103/PhysRevB.73.245426

[98] J. M. B. Lopes dos Santos, N. M. R. Peres, and A. H. Castro Neto, "Graphene Bilayer with a Twist: Electronic Structure," *Physical Review Letters*, vol. 99, no. 25, p. 256802, Dec. 2007. [Online]. Available: https://link.aps.org/doi/10.1103/PhysRevLett.99.256802

[99] A. Uri, S. Grover, Y. Cao, J. Crosse, K. Bagani, D. Rodan-Legrain, Y. Myasoedov, K. Watanabe, T. Taniguchi, P. Moon, M. Koshino, P. Jarillo-Herrero, and E. Zeldov, "Mapping the twist-angle disorder and Landau levels in magic-angle graphene," *Nature*, vol. 581, no. 7806, pp. 47–52, May 2020. [Online]. Available: https://www.nature.com/articles/s41586-020-2255-3

[100] L. Balents, C. R. Dean, D. K. Efetov, and A. F. Young, "Superconductivity and strong correlations in moiré flat bands,"

Nature Physics, vol. 0, no. 0, pp. 1–9, 2020. [Online]. Available: http://dx.doi.org/10.1038/s41567-020-0906-9

[101] H. Polshyn, M. Yankowitz, S. Chen, Y. Zhang, K. Watanabe, T. Taniguchi, C. R. Dean, and A. F. Young, "Large linear-in-temperature resistivity in twisted bilayer graphene," *Nature Physics*, vol. 15, no. 10, pp. 1011–1016, 2019. [Online]. Available: http://dx.doi.org/10.1038/s41567-019-0596-3

[102] A. L. Sharpe, E. J. Fox, A. W. Barnard, J. Finney, K. Watanabe, T. Taniguchi, M. A. Kastner, and D. Goldhaber-Gordon, "Emergent ferromagnetism near three-quarters filling in twisted bilayer graphene," *Science*, vol. 365, no. 6453, pp. 605–608, Aug. 2019. [Online]. Available: http://arxiv.org/abs/1901.03520

[103] X. Lu, P. Stepanov, W. Yang, M. Xie, M. A. Aamir, I. Das, C. Urgell, K. Watanabe, T. Taniguchi, G. Zhang, A. Bachtold, A. H. MacDonald, and D. K. Efetov, "Superconductors, orbital magnets and correlated states in magic-angle bilayer graphene," *Nature*, vol. 574, no. 7780, pp. 653–657, 2019.

[104] M. Yankowitz, S. Chen, H. Polshyn, Y. Zhang, K. Watanabe, T. Taniguchi, D. Graf, A. F. Young, and C. R. Dean, "Tuning superconductivity in twisted bilayer graphene," *Science*, vol. 363, no. 6431, pp. 1059–1064, Mar. 2019. [Online]. Available: https://www.science.org/doi/10.1126/science.aav1910

[105] N. Bultinck, E. Khalaf, S. Liu, S. Chatterjee, A. Vishwanath, and M. P. Zaletel, "Ground State and Hidden Symmetry of Magic-Angle Graphene at Even Integer Filling," *Physical Review X*, vol. 10, no. 3, p. 031034, Aug. 2020. [Online]. Available: https://link.aps.org/doi/10.1103/PhysRevX.10.031034

[106] Y. Cao, D. Chowdhury, D. Rodan-Legrain, O. Rubies-Bigorda, K. Watanabe, T. Taniguchi, T. Senthil, and P. Jarillo-Herrero, "Strange Metal in Magic-Angle Graphene with near Planckian Dissipation," *Physical Review Letters*, vol. 124, no. 7, p. 076801, Feb. 2020. [Online]. Available: https://link.aps.org/doi/10.1103/PhysRevLett.124.076801

[107] A. Jaoui, I. Das, G. Di Battista, J. Díez-Mérida, X. Lu, K. Watanabe, T. Taniguchi, H. Ishizuka, L. Levitov, and D. K. Efetov, "Quantum critical behaviour in magic-angle twisted bilayer graphene," *Nature Physics*, vol. 18, no. 6, pp. 633–638, Jun. 2022. [Online]. Available: https://www.nature.com/articles/s41567-022-01556-5

[108] Z. Song, Z. Wang, W. Shi, G. Li, C. Fang, and B. A. Bernevig, "All Magic Angles in Twisted Bilayer Graphene are Topological," *Physical Review Letters*, vol. 123, no. 3, p. 036401, Jul. 2019. [Online]. Available: https://link.aps.org/doi/10.1103/PhysRevLett.123.036401

[109] M. Serlin, C. L. Tschirhart, H. Polshyn, Y. Zhang, J. Zhu, K. Watanabe, T. Taniguchi, L. Balents, and A. F. Young, "Intrinsic quantized anomalous Hall effect in a moire heterostructure," *Science*, vol. 367, no. 6480, pp. 900–903, Feb. 2020. [Online]. Available: http://arxiv.org/abs/1907.00261

[110] I. Das, X. Lu, J. Herzog-Arbeitman, Z.-D. Song, K. Watanabe, T. Taniguchi, B. A. Bernevig, and D. K. Efetov, "Symmetry-broken Chern insulators and Rashba-like Landau-level crossings in magic-angle bilayer graphene," *Nature Physics*, vol. 17, no. 6, pp. 710–714, Jun. 2021. [Online]. Available: https://www.nature.com/articles/s41567-021-01186-3

[111] Y. Xie, A. T. Pierce, J. M. Park, D. E. Parker, E. Khalaf, P. Ledwith, Y. Cao, S. H. Lee, S. Chen, P. R. Forrester, K. Watanabe, T. Taniguchi, A. Vishwanath, P. Jarillo-Herrero, and A. Yacoby, "Fractional Chern insulators in magic-angle twisted bilayer graphene," *Nature*, vol. 600, no. 7889, pp. 439–443, Dec. 2021. [Online]. Available: https://www.nature.com/articles/s41586-021-04002-3

[112] J. M. Park, Y. Cao, L.-Q. Xia, S. Sun, K. Watanabe, T. Taniguchi, and P. Jarillo-Herrero, "Robust superconductivity in magic-angle multilayer graphene family," *Nature Materials*, vol. 21, no. 8, pp. 877–883, Aug. 2022. [Online]. Available: https://www.nature.com/articles/s41563-022-01287-1

[113] N. R. Finney, M. Yankowitz, L. Muraleetharan, K. Watanabe, T. Taniguchi, C. R. Dean, and J. Hone, "Tunable crystal symmetry in graphene–boron nitride heterostructures with coexisting moiré superlattices," *Nature Nanotechnology*, vol. 14, no. 11, pp. 1029–1034, Nov. 2019. [Online]. Available: https://www.nature.com/articles/s41565-019-0547-2

[114] M. Anđelković, S. P. Milanović, L. Covaci, and F. M. Peeters, "Double Moiré with a Twist: Supermoiré in Encapsulated Graphene," *Nano Letters*, vol. 20, no. 2, pp. 979–988, 2020.

[115] X. Sun, S. Zhang, Z. Liu, H. Zhu, J. Huang, K. Yuan, Z. Wang, K. Watanabe, T. Taniguchi, X. Li, M. Zhu, J. Mao, T. Yang,

J. Kang, J. Liu, Y. Ye, Z. V. Han, and Z. Zhang, "Correlated states in doubly-aligned hBN/graphene/hBN heterostructures," *Nature Communications*, vol. 12, no. 1, p. 7196, Dec. 2021. [Online]. Available: https://www.nature.com/articles/s41467-021-27514-y

[116] Y. Xu, S. Liu, D. A. Rhodes, K. Watanabe, T. Taniguchi, J. Hone, V. Elser, K. F. Mak, and J. Shan, "Correlated insulating states at fractional fillings of moiré superlattices," *Nature*, vol. 587, no. 7833, pp. 214–218, Nov. 2020.

[117] F. Wu, Q. Xu, Q. Wang, Y. Chu, L. Li, J. Tang, J. Liu, J. Tian, Y. Ji, L. Liu, Y. Yuan, Z. Huang, J. Zhao, X. Zan, K. Watanabe, T. Taniguchi, D. Shi, G. Gu, Y. Xu, L. Xian, W. Yang, L. Du, and G. Zhang, "Giant Correlated Gap and Possible Room-Temperature Correlated States in Twisted Bilayer MoS 2," *Physical Review Letters*, vol. 131, no. 25, p. 256201, Dec. 2023. [Online]. Available: https://link.aps.org/doi/10.1103/PhysRevLett.131.256201

[118] K. Kang, B. Shen, Y. Qiu, K. Watanabe, T. Taniguchi, J. Shan, and K. F. Mak, "Observation of the fractional quantum spin Hall effect in moiré MoTe2," *arXiv:2402.03294*, 2023.

[119] K. Kang, Y. Qiu, K. Watanabe, T. Taniguchi, J. Shan, and K. F. Mak, "Observation of the double quantum spin Hall phase in moiré WSe2," *arXiv:2402.04196*, 2023.

[120] F. Wu, T. Lovorn, E. Tutuc, and A. MacDonald, "Hubbard Model Physics in Transition Metal Dichalcogenide Moiré Bands," *Physical Review Letters*, vol. 121, no. 2, p. 026402, Jul. 2018. [Online]. Available: https://link.aps.org/doi/10.1103/PhysRevLett.121.026402

[121] N. Götting, F. Lohof, and C. Gies, "Moiré-Bose-Hubbard model for interlayer excitons in twisted transition metal dichalcogenide heterostructures," *Physical Review B*, vol. 105, no. 16, p. 165419, Apr. 2022. [Online]. Available: https://link.aps.org/doi/10.1103/PhysRevB.105.165419

[122] D. Huang, J. Choi, C.-K. Shih, and X. Li, "Excitons in semiconductor moiré superlattices," *Nature Nanotechnology*, vol. 17, no. 3, pp. 227–238, Mar. 2022. [Online]. Available: https://www.nature.com/articles/s41565-021-01068-y

[123] P. X. Nguyen, R. Chaturvedi, L. Ma, P. Knuppel, K. Watanabe, T. Taniguchi, K. F. Mak, and J. Shan, "A degenerate trion liquid in atomic double layers," *arXiv:2312.12571*, 2023.

[124] T. Smoleński, P. E. Dolgirev, C. Kuhlenkamp, A. Popert, Y. Shimazaki, P. Back, X. Lu, M. Kroner, K. Watanabe, T. Taniguchi, I. Esterlis, E. Demler, and A. Imamoğlu, "Signatures of Wigner crystal of electrons in a monolayer semiconductor," *Nature*, vol. 595, no. 7865, pp. 53–57, Jul. 2021. [Online]. Available: https://www.nature.com/articles/s41586-021-03590-4

[125] Q. Shi, E.-M. Shih, M. V. Gustafsson, D. A. Rhodes, B. Kim, K. Watanabe, T. Taniguchi, Z. Papić, J. Hone, and C. R. Dean, "Odd- and even-denominator fractional quantum Hall states in monolayer WSe2," *Nature Nanotechnology*, vol. 15, no. 7, pp. 569–573, Jul. 2020. [Online]. Available: https://www.nature.com/articles/s41565-020-0685-6

[126] Y. Jia, P. Wang, C.-L. Chiu, Z. Song, G. Yu, B. Jäck, S. Lei, S. Klemenz, F. A. Cevallos, M. Onyszczak, N. Fishchenko, X. Liu, G. Farahi, F. Xie, Y. Xu, K. Watanabe, T. Taniguchi, B. A. Bernevig, R. J. Cava, L. M. Schoop, A. Yazdani, and S. Wu, "Evidence for a monolayer excitonic insulator," *Nature Physics*, vol. 18, no. 1, pp. 87–93, Jan. 2022. [Online]. Available: https://www.nature.com/articles/s41567-021-01422-w

[127] S. Mañas-Valero, B. M. Huddart, T. Lancaster, E. Coronado, and F. L. Pratt, "Quantum phases and spin liquid properties of 1T-TaS2," *npj Quantum Materials*, vol. 6, no. 1, p. 69, Jul. 2021. [Online]. Available: https://www.nature.com/articles/s41535-021-00367-w

[128] T. Li, S. Jiang, L. Li, Y. Zhang, K. Kang, J. Zhu, K. Watanabe, T. Taniguchi, D. Chowdhury, L. Fu, J. Shan, and K. F. Mak, "Continuous Mott transition in semiconductor moiré superlattices," *Nature*, vol. 597, no. 7876, pp. 350–354, Sep. 2021. [Online]. Available: https://www.nature.com/articles/s41586-021-03853-0

[129] D. N. Basov, R. D. Averitt, D. Van Der Marel, M. Dressel, and K. Haule, "Electrodynamics of correlated electron materials," *Reviews of Modern Physics*, vol. 83, no. 2, pp. 471–541, Jun. 2011. [Online]. Available: https://link.aps.org/doi/10.1103/RevModPhys.83.471

[130] M. Massicotte, G. Soavi, A. Principi, and K.-J. Tielrooij, "Hot carriers in graphene – fundamentals and applications," *Nanoscale*, vol. 13, no. 18, pp. 8376–8411, 2021. [Online]. Available: http://xlink.rsc.org/?DOI=D0NR09166A

[131] Q. Ma, R. Krishna Kumar, S.-Y. Xu, F. H. L. Koppens, and J. C. W. Song, "Photocurrent as a multiphysics diagnostic of quantum

materials," *Nature Reviews Physics*, vol. 5, no. 3, pp. 170–184, Feb. 2023. [Online]. Available: https://www.nature.com/articles/s42254-022-00551-2

[132] A. Cavalleri, C. Tóth, C. W. Siders, J. A. Squier, F. Ráksi, P. Forget, and J. C. Kieffer, "Femtosecond Structural Dynamics in VO 2 during an Ultrafast Solid-Solid Phase Transition," *Physical Review Letters*, vol. 87, no. 23, p. 237401, Nov. 2001. [Online]. Available: https://link.aps.org/doi/10.1103/PhysRevLett.87.237401

[133] J. Shi, Y. Zhou, and S. Ramanathan, "Colossal resistance switching and band gap modulation in a perovskite nickelate by electron doping," *Nature Communications*, vol. 5, no. 1, p. 4860, Sep. 2014. [Online]. Available: https://www.nature.com/articles/ncomms5860

[134] K. Ramadoss, F. Zuo, Y. Sun, Z. Zhang, J. Lin, U. Bhaskar, S. H. Shin, M. A. Alam, S. Guha, D. Weinstein, and S. Ramanathan, "Proton-doped strongly correlated perovskite nickelate memory devices," *IEEE Electron Device Letters*, pp. 1–1, 2018. [Online]. Available: https://ieeexplore.ieee.org/document/8438481/

[135] Z. Zhang, D. Schwanz, B. Narayanan, M. Kotiuga, J. A. Dura, M. Cherukara, H. Zhou, J. W. Freeland, J. Li, R. Sutarto, F. He, C. Wu, J. Zhu, Y. Sun, K. Ramadoss, S. S. Nonnenmann, N. Yu, R. Comin, K. M. Rabe, S. K. R. S. Sankaranarayanan, and S. Ramanathan, "Perovskite nickelates as electric-field sensors in salt water," *Nature*, vol. 553, no. 7686, pp. 68–72, Jan. 2018. [Online]. Available: https://www.nature.com/articles/nature25008

[136] A. Shahsafi, P. Roney, Y. Zhou, Z. Zhang, Y. Xiao, C. Wan, R. Wambold, J. Salman, Z. Yu, J. Li, J. T. Sadowski, R. Comin, S. Ramanathan, and M. A. Kats, "Temperature-independent thermal radiation," *Proceedings of the National Academy of Sciences*, vol. 116, no. 52, pp. 26 402–26 406, Dec. 2019. [Online]. Available: https://pnas.org/doi/full/10.1073/pnas.1911244116

[137] P. Seifert, X. Lu, P. Stepanov, J. R. Durán Retamal, J. N. Moore, K.-C. Fong, A. Principi, and D. K. Efetov, "Magic-Angle Bilayer Graphene Nanocalorimeters: Toward Broadband, Energy-Resolving Single Photon Detection," *Nano Letters*, vol. 20, no. 5, pp. 3459–3464, May 2020. [Online]. Available: https://pubs.acs.org/doi/10.1021/acs.nanolett.0c00373

[138] J. Díez-Mérida, A. Díez-Carlón, S. Y. Yang, Y.-M. Xie, X.-J. Gao, J. Senior, K. Watanabe, T. Taniguchi, X. Lu, A. P. Higginbotham,

K. T. Law, and D. K. Efetov, "Symmetry-broken Josephson junctions and superconducting diodes in magic-angle twisted bilayer graphene," *Nature Communications*, vol. 14, no. 1, p. 2396, Apr. 2023. [Online]. Available: https://www.nature.com/articles/s41467-023-38005-7

[139] H. Agarwal, K. Nowakowski, A. Forrer, A. Principi, R. Bertini, S. Batlle-Porro, A. Reserbat-Plantey, P. Prasad, L. Vistoli, K. Watanabe, T. Taniguchi, A. Bachtold, G. Scalari, R. Krishna Kumar, and F. H. L. Koppens, "Ultra-broadband photoconductivity in twisted graphene heterostructures with large responsivity," *Nature Photonics*, vol. 17, no. 12, pp. 1047–1053, Dec. 2023. [Online]. Available: https://www.nature.com/articles/s41566-023-01291-0

[140] G. D. Battista, K. C. Fong, A. Díez-Carlón, K. Watanabe, T. Taniguchi, and D. K. Efetov, "Ultra-low carrier density superconducting bolometers with single photon sensitivity based on magic-angle twisted bilayer graphene," *arXiv:2403.02049*, 2024.

[141] D. C. Larbalestier, J. Jiang, U. P. Trociewitz, F. Kametani, C. Scheuerlein, M. Dalban-Canassy, M. Matras, P. Chen, N. C. Craig, P. J. Lee, and E. E. Hellstrom, "Isotropic round-wire multifilament cuprate superconductor for generation of magnetic fields above 30 T," *Nature Materials*, vol. 13, no. 4, pp. 375–381, Apr. 2014. [Online]. Available: https://www.nature.com/articles/nmat3887

[142] E. Portolés, S. Iwakiri, G. Zheng, P. Rickhaus, T. Taniguchi, K. Watanabe, T. Ihn, K. Ensslin, and F. K. De Vries, "A tunable monolithic SQUID in twisted bilayer graphene," *Nature Nanotechnology*, vol. 17, no. 11, pp. 1159–1164, Nov. 2022. [Online]. Available: https://www.nature.com/articles/s41565-022-01222-0

[143] G. Di Battista, P. Seifert, K. Watanabe, T. Taniguchi, K. C. Fong, A. Principi, and D. K. Efetov, "Revealing the Thermal Properties of Superconducting Magic-Angle Twisted Bilayer Graphene," *Nano Letters*, vol. 22, no. 16, pp. 6465–6470, Aug. 2022. [Online]. Available: https://pubs.acs.org/doi/10.1021/acs.nanolett.1c04512

[144] P. Rickhaus, G. Zheng, J. L. Lado, Y. Lee, A. Kurzmann, M. Eich, R. Pisoni, C. Tong, R. Garreis, C. Gold, M. Masseroni, T. Taniguchi, K. Wantanabe, T. Ihn, and K. Ensslin, "Gap Opening in Twisted Double Bilayer Graphene by Crystal Fields," *Nano Letters*, vol. 19, no. 12, pp. 8821–8828, Dec. 2019. [Online]. Available: https://pubs.acs.org/doi/10.1021/acs.nanolett.9b03660

[145] D. F. Santavicca, "Prospects for faster, higher-temperature superconducting nanowire single-photon detectors," *Superconductor Science and Technology*, vol. 31, no. 4, 2018.

[146] L. Wang, I. Meric, P. Y. Huang, Q. Gao, Y. Gao, H. Tran, T. Taniguchi, K. Watanabe, L. M. Campos, D. A. Muller, J. Guo, P. Kim, J. Hone, K. L. Shepard, and C. R. Dean, "One-Dimensional Electrical Contact to a Two-Dimensional Material," *Science*, vol. 342, no. 6158, pp. 614–617, Nov. 2013. [Online]. Available: http://www.sciencemag.org/cgi/doi/10.1126/science.1244358

[147] F. Pizzocchero, L. Gammelgaard, B. S. Jessen, J. M. Caridad, L. Wang, J. Hone, P. Bøggild, and T. J. Booth, "The hot pick-up technique for batch assembly of van der Waals heterostructures," *Nature Communications*, vol. 7, no. 1, p. 11894, Jun. 2016. [Online]. Available: https://www.nature.com/articles/ncomms11894

[148] A. Castellanos-Gomez, M. Buscema, R. Molenaar, V. Singh, L. Janssen, H. S. Van Der Zant, and G. A. Steele, "Deterministic transfer of two-dimensional materials by all-dry viscoelastic stamping," *2D Materials*, vol. 1, no. 1, pp. 1–34, 2014.

[149] Y. Cao, A. Mishchenko, G. L. Yu, E. Khestanova, A. P. Rooney, E. Prestat, A. V. Kretinin, P. Blake, M. B. Shalom, C. Woods, J. Chapman, G. Balakrishnan, I. V. Grigorieva, K. S. Novoselov, B. A. Piot, M. Potemski, K. Watanabe, T. Taniguchi, S. J. Haigh, A. K. Geim, and R. V. Gorbachev, "Quality Heterostructures from Two-Dimensional Crystals Unstable in Air by Their Assembly in Inert Atmosphere," *Nano Letters*, vol. 15, no. 8, pp. 4914–4921, 2015.

[150] D. G. Purdie, N. M. Pugno, T. Taniguchi, K. Watanabe, A. C. Ferrari, and A. Lombardo, "Cleaning interfaces in layered materials heterostructures," *Nature Communications*, vol. 9, no. 1, p. 5387, Dec. 2018. [Online]. Available: https://www.nature.com/articles/s41467-018-07558-3

[151] L. J. Sandilands, A. A. Reijnders, A. H. Su, V. Baydina, Z. Xu, A. Yang, G. Gu, T. Pedersen, F. Borondics, and K. S. Burch, "Origin of the insulating state in exfoliated high-Tc two-dimensional atomic crystals," *Physical Review B - Condensed Matter and Materials Physics*, vol. 90, no. 8, pp. 1–5, 2014.

[152] D. C. Bell, "Contrast Mechanisms and Image Formation in Helium Ion Microscopy," *Microscopy and Microanalysis*, vol. 15,

no. 2, pp. 147–153, Apr. 2009. [Online]. Available: https://academic.oup.com/mam/article/15/2/147/6919682

[153] D. C. Bell, M. C. Lemme, L. A. Stern, J. R. Williams, and C. M. Marcus, "Precision cutting and patterning of graphene with helium ions," *Nanotechnology*, vol. 20, p. 455301, 2009.

[154] B. W. Ward, J. A. Notte, N. P. Economou, B. W. Ward, J. A. Notte, and N. P. Economou, "Helium ion microscope : A new tool for nanoscale microscopy and metrology Advertisement : Helium ion microscope : A new tool for nanoscale microscopy and metrology," *JVSTB*, vol. 2871, no. 2006, pp. 1–5, 2013.

[155] F. Fang, N. Zhang, D. Guo, K. Ehmann, B. Cheung, K. Liu, and K. Yamamura, "Towards atomic and close-to-atomic scale manufacturing," *International Journal of Extreme Manufacturing*, vol. 1, no. 1, p. 012001, Apr. 2019. [Online]. Available: https://iopscience.iop.org/article/10.1088/2631-7990/ab0dfc

[156] S. A. Cybart, E. Y. Cho, T. J. Wong, B. H. Wehlin, M. K. Ma, C. Huynh, and R. C. Dynes, "Nano Josephson superconducting tunnel junctions in YBa2Cu3O7- directly patterned with a focused helium ion beam," *Nature Nanotechnology*, vol. 10, no. 7, pp. 598–602, 2015.

[157] E. Y. Cho, M. K. Ma, C. Huynh, K. Pratt, D. N. Paulson, V. N. Glyantsev, R. C. Dynes, and S. A. Cybart, "YBa2Cu3O7- superconducting quantum interference devices with metallic to insulating barriers written with a focused helium ion beam," *Applied Physics Letters*, vol. 106, no. 25, 2015.

[158] B. Müller, M. Karrer, F. Limberger, M. Becker, B. Schröppel, C. J. Burkhardt, R. Kleiner, E. Goldobin, and D. Koelle, "Josephson Junctions and SQUIDs Created by Focused Helium-Ion-Beam Irradiation of YBa2Cu3 O7," *Physical Review Applied*, vol. 11, no. 4, pp. 1–12, 2019.

[159] F. Couëdo, P. Amari, C. Feuillet-Palma, C. Ulysse, Y. K. Srivastava, R. Singh, N. Bergeal, and J. Lesueur, "Dynamic properties of high-Tc superconducting nano-junctions made with a focused helium ion beam," *Scientific Reports*, vol. 10, no. 1, p. 10256, Jun. 2020. [Online]. Available: https://www.nature.com/articles/s41598-020-66882-1

[160] B. Aichner, B. Müller, M. Karrer, V. R. Misko, F. Limberger, K. L. Mletschnig, M. Dosmailov, J. D. Pedarnig, F. Nori, R. Kleiner,

D. Koelle, and W. Lang, "Ultradense Tailored Vortex Pinning Arrays in Superconducting YBa2Cu3O7- Thin Films Created by Focused He Ion Beam Irradiation for Fluxonics Applications," *ACS Applied Nano Materials*, vol. 2, no. 8, pp. 5108–5115, 2019.

[161] L. Kasaei, T. Melbourne, V. Manichev, L. C. Feldman, T. Gustafsson, K. Chen, X. X. Xi, and B. A. Davidson, "MgB2 Josephson junctions produced by focused helium ion beam irradiation," *AIP Advances*, vol. 8, no. 7, 2018.

[162] G. D. Martinez, D. Buckley, I. Charaev, A. Dane, D. E. Dow, and K. K. Berggren, "Superconducting Nanowire Fabrication on Niobium Nitride using Helium Ion Irradiation," pp. 1–4, 2020, arXiv: 2003.02898. [Online]. Available: http://arxiv.org/abs/2003.02898

[163] E. Y. Cho, Y. W. Zhou, J. Y. Cho, and S. A. Cybart, "Superconducting nano Josephson junctions patterned with a focused helium ion beam," *Applied Physics Letters*, vol. 113, no. 2, pp. 1–5, 2018.

[164] E. Y. Cho, H. Li, J. C. Lefebvre, Y. W. Zhou, R. C. Dynes, and S. A. Cybart, "Direct-coupled micro-magnetometer with Y-Ba-Cu-O nano-slit SQUID fabricated with a focused helium ion beam," *Applied Physics Letters*, vol. 113, no. 16, 2018.

[165] A. Gozar, N. E. Litombe, J. E. Hoffman, and I. Božović, "Optical Nanoscopy of High Tc Cuprate Nanoconstriction Devices Patterned by Helium Ion Beams," *Nano Letters*, vol. 17, no. 3, pp. 1582–1586, 2017.

[166] H. Li, H. Cai, E. Y. Cho, S. J. McCoy, Y. T. Wang, J. C. Lefebvre, Y. W. Zhou, and S. A. Cybart, "High-transition-temperature nanoscale superconducting quantum interference devices directly written with a focused helium ion beam," *Applied Physics Letters*, vol. 116, no. 7, 2020.

[167] P. Seifert, J. R. D. Retamal, R. L. Merino, H. H. Sheinfux, J. N. Moore, M. A. Aamir, T. Taniguchi, K. Watanabe, K. Kadowaki, M. Artiglia, M. Romagnoli, and D. K. Efetov, "A high-T c van der Waals superconductor based photodetector with ultra-high responsivity and nanosecond relaxation time," *2D Materials*, vol. 8, no. 3, p. 035053, 2021.

[168] R. L. Merino, P. Seifert, J. D. Retamal, R. K. Mech, T. Taniguchi, K. Watanabe, K. Kadowaki, R. H. Hadfield, and D. K. Efetov, "Two-dimensional cuprate nanodetector with single telecom photon sensitivity at T = 20 K," *2D Materials*,

vol. 10, no. 2, p. 021001, Apr. 2023. [Online]. Available: https://iopscience.iop.org/article/10.1088/2053-1583/acb4a8

[169] M. M. Jadidi, R. J. Suess, C. Tan, X. Cai, K. Watanabe, T. Taniguchi, A. B. Sushkov, M. Mittendorff, J. Hone, H. Dennis Drew, M. S. Fuhrer, and T. E. Murphy, "Tunable Ultrafast Thermal Relaxation in Graphene Measured by Continuous-Wave Photomixing," *Physical Review Letters*, vol. 117, p. 257401, 2016.

[170] C. Herring, "Theory of the Thermoelectric Power of Semiconductors," *Physical Review*, vol. 96, no. 5, pp. 1163–1187, Dec. 1954. [Online]. Available: https://link.aps.org/doi/10.1103/PhysRev.96.1163

[171] X. Zhang and L.-D. Zhao, "Thermoelectric materials: Energy conversion between heat and electricity," *Journal of Materiomics*, vol. 1, no. 2, pp. 92–105, Jun. 2015. [Online]. Available: https://linkinghub.elsevier.com/retrieve/pii/S2352847815000258

[172] K. Behnia, D. Jaccard, and J. Flouquet, "On the thermoelectricity of correlated electrons in the zero-temperature limit," *Journal of Physics: Condensed Matter*, vol. 16, no. 28, pp. 5187–5198, Jul. 2004. [Online]. Available: https://iopscience.iop.org/article/10.1088/0953-8984/16/28/037

[173] M. Markov, S. E. Rezaei, S. N. Sadeghi, K. Esfarjani, and M. Zebarjadi, "Thermoelectric properties of semimetals," *Physical Review Materials*, vol. 3, no. 9, p. 095401, Sep. 2019. [Online]. Available: https://link.aps.org/doi/10.1103/PhysRevMaterials.3.095401

[174] M. Cutler and N. F. Mott, "Observation of Anderson Localization in an Electron Gas," *Physical Review*, vol. 181, no. 3, pp. 1336–1340, May 1969. [Online]. Available: https://link.aps.org/doi/10.1103/PhysRev.181.1336

[175] J. Duan, X. Wang, X. Lai, G. Li, K. Watanabe, T. Taniguchi, M. Zebarjadi, and E. Y. Andrei, "High thermoelectricpower factor in graphene/hBN devices," *Proceedings of the National Academy of Sciences*, vol. 113, no. 50, pp. 14 272–14 276, Dec. 2016. [Online]. Available: https://pnas.org/doi/full/10.1073/pnas.1615913113

[176] Y. M. Zuev, W. Chang, and P. Kim, "Thermoelectric and Magnetothermoelectric Transport Measurements of Graphene," *Physical Review Letters*, vol. 102, no. 9, p. 096807, Mar. 2009. [Online]. Available: https://link.aps.org/doi/10.1103/PhysRevLett.102.096807

[177] K. Behnia and H. Aubin, "Nernst effect in metals and superconductors: a review of concepts and experiments," *Reports on Progress in Physics*, vol. 79, no. 4, p. 046502, Apr. 2016. [Online]. Available: https://iopscience.iop.org/article/10.1088/0034-4885/79/4/046502

[178] H. Cao, G. Aivazian, Z. Fei, J. Ross, D. H. Cobden, and X. Xu, "Photo-Nernst current in graphene," *Nature Physics*, vol. 12, no. 3, pp. 236–239, Mar. 2016. [Online]. Available: https://www.nature.com/articles/nphys3549

[179] S. Hartmann, N. Oeschler, C. Krellner, C. Geibel, and F. Steglich, "Low-temperature thermopower study of YbRh $_2$ Si $_2$," *Journal of Physics: Conference Series*, vol. 150, no. 4, p. 042049, Mar. 2009. [Online]. Available: https://iopscience.iop.org/article/10.1088/1742-6596/150/4/042049

[180] F. Laliberté, J. Chang, N. Doiron-Leyraud, E. Hassinger, R. Daou, M. Rondeau, B. Ramshaw, R. Liang, D. Bonn, W. Hardy, S. Pyon, T. Takayama, H. Takagi, I. Sheikin, L. Malone, C. Proust, K. Behnia, and L. Taillefer, "Fermi-surface reconstruction by stripe order in cuprate superconductors," *Nature Communications*, vol. 2, no. 1, p. 432, Aug. 2011. [Online]. Available: https://www.nature.com/articles/ncomms1440

[181] K. Wang, A. Wang, A. Tomic, L. Wang, A. M. Abeykoon, E. Dooryhee, S. J. Billinge, and C. Petrovic, "Enhanced thermoelectric power and electronic correlations in RuSe2," *APL Materials*, vol. 3, no. 4, Apr. 2015, publisher: American Institute of Physics Inc.

[182] A. Jaoui, G. Seyfarth, C. W. Rischau, S. Wiedmann, S. Benhabib, C. Proust, K. Behnia, and B. Fauqué, "Giant Seebeck effect across the field-induced metal-insulator transition of InAs," *npj Quantum Materials*, vol. 5, no. 1, p. 94, Dec. 2020. [Online]. Available: https://www.nature.com/articles/s41535-020-00296-0

[183] A. Jayaraman, K. Hsieh, B. Ghawri, P. S. Mahapatra, K. Watanabe, T. Taniguchi, and A. Ghosh, "Evidence of Lifshitz Transition in the Thermoelectric Power of Ultrahigh-Mobility Bilayer Graphene," *Nano Letters*, vol. 21, no. 3, pp. 1221–1227, Feb. 2021. [Online]. Available: https://pubs.acs.org/doi/10.1021/acs.nanolett.0c03586

[184] V. H. Guarochico-Moreira, C. R. Anderson, V. Fal'ko, I. V. Grigorieva, E. Tóvári, M. Hamer, R. Gorbachev, S. Liu, J. H. Edgar, A. Principi, A. V. Kretinin, and I. J. Vera-Marun,

"Thermopower in hBN/graphene/hBN superlattices," *Physical Review B*, vol. 108, no. 11, p. 115418, Sep. 2023. [Online]. Available: https://link.aps.org/doi/10.1103/PhysRevB.108.115418

[185] H. Xie, X. Su, T. P. Bailey, C. Zhang, W. Liu, C. Uher, X. Tang, and M. G. Kanatzidis, "Anomalously Large Seebeck Coefficient of CuFeS $_2$ Derives from Large Asymmetry in the Energy Dependence of Carrier Relaxation Time," *Chemistry of Materials*, vol. 32, no. 6, pp. 2639–2646, Mar. 2020. [Online]. Available: https://pubs.acs.org/doi/10.1021/acs.chemmater.0c00388

[186] A. Gourgout, G. Grissonnanche, F. Laliberté, A. Ataei, L. Chen, S. Verret, J.-S. Zhou, J. Mravlje, A. Georges, N. Doiron-Leyraud, and L. Taillefer, "Seebeck Coefficient in a Cuprate Superconductor: Particle-Hole Asymmetry in the Strange Metal Phase and Fermi Surface Transformation in the Pseudogap Phase," *Physical Review X*, vol. 12, no. 1, p. 011037, Feb. 2022. [Online]. Available: https://link.aps.org/doi/10.1103/PhysRevX.12.011037

[187] Y. Pan, F. Fan, X. Hong, B. He, C. Le, W. Schnelle, Y. He, K. Imasato, H. Borrmann, C. Hess, B. Büchner, Y. Sun, C. Fu, G. J. Snyder, and C. Felser, "Thermoelectric Properties of Novel Semimetals: A Case Study of YbMnSb $_2$," *Advanced Materials*, vol. 33, no. 7, p. 2003168, Feb. 2021. [Online]. Available: https://onlinelibrary.wiley.com/doi/10.1002/adma.202003168

[188] A. Bentien, S. Johnsen, G. K. H. Madsen, B. B. Iversen, and F. Steglich, "Colossal Seebeck coefficient in strongly correlated semiconductor FeSb $_2$," *Europhysics Letters (EPL)*, vol. 80, no. 1, p. 17008, Oct. 2007. [Online]. Available: https://iopscience.iop.org/article/10.1209/0295-5075/80/17008

[189] P. Sun, B. Wei, J. Zhang, J. M. Tomczak, A. M. Strydom, M. Søndergaard, B. B. Iversen, and F. Steglich, "Large Seebeck effect by charge-mobility engineering," *Nature Communications*, vol. 6, Jun. 2015.

[190] F. Ghahari, H.-Y. Xie, T. Taniguchi, K. Watanabe, M. S. Foster, and P. Kim, "Enhanced Thermoelectric Power in Graphene: Violation of the Mott Relation by Inelastic Scattering," *Physical Review Letters*, vol. 116, no. 13, p. 136802, Mar. 2016. [Online]. Available: https://link.aps.org/doi/10.1103/PhysRevLett.116.136802

[191] P. Sun and F. Steglich, "Nernst effect: Evidence of local kondo scattering in heavy fermions," *Physical Review Letters*, vol. 110, no. 21, May 2013.

[192] S. Goswami, C. Siegert, M. Baenninger, M. Pepper, I. Farrer, D. A. Ritchie, and A. Ghosh, "Highly Enhanced Thermopower in Two-Dimensional Electron Systems at Millikelvin Temperatures," *Physical Review Letters*, vol. 103, no. 2, p. 026602, Jul. 2009. [Online]. Available: https://link.aps.org/doi/10.1103/PhysRevLett.103.026602

[193] R. Scheibner, H. Buhmann, D. Reuter, M. N. Kiselev, and L. W. Molenkamp, "Thermopower of a kondo spin-correlated quantum dot," *Physical Review Letters*, vol. 95, no. 17, Oct. 2005.

[194] Wang, Y., Rogado, N.S., Cava, R. J., and Ong, N.P., "Spin entropy as the likely sourceof enhanced thermopower inNaxCo2O," *Nature*, vol. 423, no. 6938, pp. 422–425, May 2003.

[195] U. Zondiner, A. Rozen, D. Rodan-Legrain, Y. Cao, R. Queiroz, T. Taniguchi, K. Watanabe, Y. Oreg, F. von Oppen, A. Stern, E. Berg, P. Jarillo-Herrero, and S. Ilani, "Cascade of phase transitions and Dirac revivals in magic-angle graphene," *Nature*, vol. 582, no. 7811, pp. 203–208, 2020. [Online]. Available: https://doi.org/10.1038/s41586-020-2373-y

[196] G. Chen, A. L. Sharpe, E. J. Fox, Y.-H. Zhang, S. Wang, L. Jiang, B. Lyu, H. Li, K. Watanabe, T. Taniguchi, Z. Shi, T. Senthil, D. Goldhaber-Gordon, Y. Zhang, and F. Wang, "Tunable correlated Chern insulator and ferromagnetism in a moiré superlattice," *Nature*, vol. 579, no. 7797, pp. 56–61, Mar. 2020. [Online]. Available: https://www.nature.com/articles/s41586-020-2049-7

[197] Y. Saito, J. Ge, L. Rademaker, K. Watanabe, T. Taniguchi, D. A. Abanin, and A. F. Young, "Hofstadter subband ferromagnetism and symmetry-broken Chern insulators in twisted bilayer graphene," *Nature Physics*, vol. 17, no. 4, pp. 478–481, Apr. 2021. [Online]. Available: https://www.nature.com/articles/s41567-020-01129-4

[198] Y. Saito, F. Yang, J. Ge, X. Liu, T. Taniguchi, K. Watanabe, J. I. A. Li, E. Berg, and A. F. Young, "Isospin Pomeranchuk effect in twisted bilayer graphene," *Nature*, vol. 592, no. 7853, pp. 220–224, 2021. [Online]. Available: https://doi.org/10.1038/s41586-021-03409-2

[199] A. Rozen, J. M. Park, U. Zondiner, Y. Cao, D. Rodan-Legrain, T. Taniguchi, K. Watanabe, Y. Oreg, A. Stern,

E. Berg, P. Jarillo-Herrero, and S. Ilani, "Entropic evidence for a Pomeranchuk effect in magic-angle graphene," *Nature*, vol. 592, no. 7853, pp. 214–219, Apr. 2021. [Online]. Available: https://www.nature.com/articles/s41586-021-03319-3

[200] Y. Xie, B. Lian, B. Jäck, X. Liu, C.-L. Chiu, K. Watanabe, T. Taniguchi, B. A. Bernevig, and A. Yazdani, "Spectroscopic signatures of many-body correlations in magic-angle twisted bilayer graphene," *Nature*, vol. 572, no. 7767, pp. 101–105, Aug. 2019. [Online]. Available: http://www.nature.com/articles/s41586-019-1422-x

[201] D. Wong, K. P. Nuckolls, M. Oh, B. Lian, Y. Xie, S. Jeon, K. Watanabe, T. Taniguchi, B. A. Bernevig, and A. Yazdani, "Cascade of electronic transitions in magic-angle twisted bilayer graphene," *Nature*, vol. 582, no. 7811, pp. 198–202, 2020. [Online]. Available: https://doi.org/10.1038/s41586-020-2339-0

[202] Z. D. Song and B. A. Bernevig, "Magic-Angle Twisted Bilayer Graphene as a Topological Heavy Fermion Problem," *Physical Review Letters*, vol. 129, no. 4, Jul. 2022.

[203] H. Hu, G. Rai, L. Crippa, J. Herzog-Arbeitman, D. Călugăru, T. Wehling, G. Sangiovanni, R. Valentí, A. M. Tsvelik, and B. A. Bernevig, "Symmetric Kondo Lattice States in Doped Strained Twisted Bilayer Graphene," *Physical Review Letters*, vol. 131, no. 16, p. 166501, Oct. 2023. [Online]. Available: https://link.aps.org/doi/10.1103/PhysRevLett.131.166501

[204] G. Rai, L. Crippa, B. A. Bernevig, R. Valentı, G. Sangiovanni, and T. Wehling, "Dynamical correlations and order in magic-angle twisted bilayer graphene," 2024, arXiv:2309.08529v1.

[205] L. L. H. Lau and P. Coleman, "Topological Mixed Valence Model for Twisted Bilayer Graphene," Mar. 2023, arXiv:2303.02670 [cond-mat]. [Online]. Available: http://arxiv.org/abs/2303.02670

[206] Y.-J. Wang, G.-D. Zhou, S.-Y. Peng, B. Lian, and Z.-D. Song, "Molecular Pairing in Twisted Bilayer Graphene Superconductivity," Feb. 2024, arXiv:2402.00869 [cond-mat]. [Online]. Available: http://arxiv.org/abs/2402.00869

[207] D. Călugăru, H. Hu, R. L. Merino, N. Regnault, D. K. Efetov, and B. A. Bernevig, "The Thermoelectric Effect and Its Natural Heavy Fermion Explanation in Twisted Bilayer and

Trilayer Graphene," Feb. 2024, arXiv:2402.14057 [cond-mat]. [Online]. Available: http://arxiv.org/abs/2402.14057

[208] D. Călugăru and e. al, "DMFT Seebeck," 2024, arXiv:1907.12338 [cond-mat].

[209] J. C. Song, M. S. Rudner, C. M. Marcus, and L. S. Levitov, "Hot carrier transport and photocurrent response in graphene," *Nano Letters*, vol. 11, no. 11, pp. 4688–4692, Nov. 2011.

[210] N. M. Gabor, J. C. W. Song, Q. Ma, N. L. Nair, T. Taychatanapat, K. Watanabe, T. Taniguchi, L. S. Levitov, and P. Jarillo-Herrero, "Hot Carrier–Assisted Intrinsic Photoresponse in Graphene," *Science*, vol. 334, no. 6056, pp. 648–652, Nov. 2011. [Online]. Available: https://www.science.org/doi/10.1126/science.1211384

[211] K. J. Tielrooij, J. C. W. Song, S. A. Jensen, A. Centeno, A. Pesquera, A. Zurutuza Elorza, M. Bonn, L. S. Levitov, and F. H. L. Koppens, "Photoexcitation cascade and multiple hot-carrier generation in graphene," *Nature Physics*, vol. 9, no. 4, pp. 248–252, Apr. 2013. [Online]. Available: https://www.nature.com/articles/nphys2564

[212] K. J. Tielrooij, L. Piatkowski, M. Massicotte, A. Woessner, Q. Ma, Y. Lee, K. S. Myhro, C. N. Lau, P. Jarillo-Herrero, N. F. Van Hulst, and F. H. Koppens, "Generation of photovoltage in graphene on a femtosecond timescale through efficient carrier heating," *Nature Nanotechnology*, vol. 10, no. 5, pp. 437–443, 2015.

[213] A. K. Paul, A. Ghosh, S. Chakraborty, U. Roy, R. Dutta, K. Watanabe, T. Taniguchi, A. Panda, A. Agarwala, S. Mukerjee, S. Banerjee, and A. Das, "Interaction-driven giant thermopower in magic-angle twisted bilayer graphene," *Nature Physics*, vol. 18, no. 6, pp. 691–698, Jun. 2022.

[214] B. Ghawri, P. S. Mahapatra, M. Garg, S. Mandal, S. Bhowmik, A. Jayaraman, R. Soni, K. Watanabe, T. Taniguchi, H. R. Krishnamurthy, M. Jain, S. Banerjee, U. Chandni, and A. Ghosh, "Breakdown of semiclassical description of thermoelectricity in near-magic angle twisted bilayer graphene," *Nature Communications*, vol. 13, no. 1, Dec. 2022.

[215] S. Bhowmik, B. Ghawri, N. Leconte, S. Appalakondaiah, M. Pandey, P. S. Mahapatra, D. Lee, K. Watanabe, T. Taniguchi, J. Jung, A. Ghosh, and U. Chandni, "Broken-symmetry states at half-integer band fillings in twisted bilayer graphene," *Nature Physics*, vol. 18, no. 6, pp. 639–643, Jun. 2022.

[216] M. A. Aamir, J. N. Moore, X. Lu, P. Seifert, D. Englund, K. C. Fong, and D. K. Efetov, "Ultrasensitive Calorimetric Measurements of the Electronic Heat Capacity of Graphene," *Nano Letters*, vol. 21, no. 12, pp. 5330–5337, Jun. 2021. [Online]. Available: https://pubs.acs.org/doi/10.1021/acs.nanolett.1c01553

[217] J. Waissman, L. E. Anderson, A. V. Talanov, Z. Yan, Y. J. Shin, D. H. Najafabadi, M. Rezaee, X. Feng, D. G. Nocera, T. Taniguchi, K. Watanabe, B. Skinner, K. A. Matveev, and P. Kim, "Electronic thermal transport measurement in low-dimensional materials with graphene non-local noise thermometry," *Nature Nanotechnology*, vol. 17, no. 2, pp. 166–173, Feb. 2022. [Online]. Available: https://www.nature.com/articles/s41565-021-01015-x

[218] R. L. Merino, D. Călugăru, H. Hu, J. Díez-Mérida, A. Díez, T. Taniguchi, K. Watanabe, P. Seifert, and B. A. Bernevig, "Evidence of heavy fermion physics in the thermoelectric transport of magic angle twisted bilayer graphene," 2024, arXiv:2402.11749 [cond-mat].

[219] X. Xu, N. M. Gabor, J. S. Alden, A. M. Van Der Zande, and P. L. McEuen, "Photo-Thermoelectric Effect at a Graphene Interface Junction," *Nano Letters*, vol. 10, no. 2, pp. 562–566, Feb. 2010. [Online]. Available: https://pubs.acs.org/doi/10.1021/nl903451y

[220] T. Hong, B. Chamlagain, W. Lin, H.-J. Chuang, M. Pan, Z. Zhou, and Y.-Q. Xu, "Polarized photocurrent response in black phosphorus field-effect transistors," *Nanoscale*, vol. 6, no. 15, pp. 8978–8983, 2014. [Online]. Available: http://xlink.rsc.org/?DOI=C4NR02164A

[221] K. Behnia, "What is measured when measuring a thermoelectric coefficient?" *Comptes Rendus. Physique*, vol. 23, no. S2, pp. 25–40, Jun. 2023. [Online]. Available: http://arxiv.org/abs/2204.04429

[222] H. Ishizuka, A. Fahimniya, F. Guinea, and L. Levitov, "Purcell-like Enhancement of Electron–Phonon Interactions in Long-Period Superlattices: Linear-Temperature Resistivity and Cooling Power," *Nano Letters*, vol. 21, no. 18, pp. 7465–7471, Sep. 2021. [Online]. Available: https://pubs.acs.org/doi/10.1021/acs.nanolett.1c00565

[223] H. Ishizuka and L. Levitov, "Wide-range T^2 resistivity and umklapp scattering in moiré graphene," *New Journal of Physics*, vol. 24, no. 5, p. 052001, May 2022. [Online]. Available: https://iopscience.iop.org/article/10.1088/1367-2630/ac688c

[224] D. M. Kennes, J. Lischner, and C. Karrasch, "Strong correlations and d + id superconductivity in twisted bilayer graphene," *Physical Review B*, vol. 98, no. 24, p. 241407, Dec. 2018. [Online]. Available: https://link.aps.org/doi/10.1103/PhysRevB.98.241407

[225] E. Khalaf, S. Chatterjee, N. Bultinck, M. P. Zaletel, and A. Vishwanath, "Charged skyrmions and topological origin of superconductivity in magic-angle graphene," *Science Advances*, vol. 7, no. 19, p. eabf5299, May 2021. [Online]. Available: https://www.science.org/doi/10.1126/sciadv.abf5299

[226] H. Isobe, N. F. Yuan, and L. Fu, "Unconventional Superconductivity and Density Waves in Twisted Bilayer Graphene," *Physical Review X*, vol. 8, no. 4, p. 041041, Dec. 2018. [Online]. Available: https://link.aps.org/doi/10.1103/PhysRevX.8.041041

[227] A. Julku, T. J. Peltonen, L. Liang, T. T. Heikkilä, and P. Törmä, "Superfluid weight and Berezinskii-Kosterlitz-Thouless transition temperature of twisted bilayer graphene," *Physical Review B*, vol. 101, no. 6, p. 060505, Feb. 2020. [Online]. Available: https://link.aps.org/doi/10.1103/PhysRevB.101.060505

[228] F. Wu, A. MacDonald, and I. Martin, "Theory of Phonon-Mediated Superconductivity in Twisted Bilayer Graphene," *Physical Review Letters*, vol. 121, no. 25, p. 257001, Dec. 2018. [Online]. Available: https://link.aps.org/doi/10.1103/PhysRevLett.121.257001

[229] B. Lian, Z. Wang, and B. A. Bernevig, "Twisted Bilayer Graphene: A Phonon-Driven Superconductor," *Physical Review Letters*, vol. 122, no. 25, p. 257002, Jun. 2019. [Online]. Available: https://link.aps.org/doi/10.1103/PhysRevLett.122.257002

[230] C. Lewandowski, D. Chowdhury, and J. Ruhman, "Pairing in magic-angle twisted bilayer graphene: Role of phonon and plasmon umklapp," *Physical Review B*, vol. 103, no. 23, p. 235401, Jun. 2021. [Online]. Available: https://link.aps.org/doi/10.1103/PhysRevB.103.235401

[231] J. C. Johannsen, S. Ulstrup, F. Cilento, A. Crepaldi, M. Zacchigna, C. Cacho, I. C. E. Turcu, E. Springate, F. Fromm, C. Raidel, T. Seyller, F. Parmigiani, M. Grioni, and P. Hofmann, "Direct View of Hot Carrier Dynamics in Graphene," *Physical Review Letters*, vol. 111, no. 2, p. 027403, Jul. 2013. [Online]. Available: https://link.aps.org/doi/10.1103/PhysRevLett.111.027403

[232] J. C. W. Song, K. J. Tielrooij, F. H. L. Koppens, and L. S. Levitov, "Photoexcited carrier dynamics and impact-excitation cascade in graphene," *Physical Review B*, vol. 87, no. 15, p. 155429, Apr. 2013. [Online]. Available: https://link.aps.org/doi/10.1103/PhysRevB.87.155429

[233] R. Bistritzer and A. H. MacDonald, "Electronic Cooling in Graphene," *Physical Review Letters*, vol. 102, no. 20, p. 206410, May 2009. [Online]. Available: https://link.aps.org/doi/10.1103/PhysRevLett.102.206410

[234] E. A. Pogna, X. Jia, A. Principi, A. Block, L. Banszerus, J. Zhang, X. Liu, T. Sohier, S. Forti, K. Soundarapandian, B. Terrés, J. D. Mehew, C. Trovatello, C. Coletti, F. H. Koppens, M. Bonn, H. I. Wang, N. Van Hulst, M. J. Verstraete, H. Peng, Z. Liu, C. Stampfer, G. Cerullo, and K. J. Tielrooij, "Hot-Carrier Cooling in High-Quality Graphene Is Intrinsically Limited by Optical Phonons," *ACS Nano*, vol. 15, no. 7, pp. 11 285–11 295, 2021.

[235] H. Wang, J. H. Strait, P. A. George, S. Shivaraman, V. B. Shields, M. Chandrashekhar, J. Hwang, F. Rana, M. G. Spencer, C. S. Ruiz-Vargas, and J. Park, "Ultrafast relaxation dynamics of hot optical phonons in graphene," *Applied Physics Letters*, vol. 96, no. 8, p. 081917, Feb. 2010. [Online]. Available: https://pubs.aip.org/apl/article/96/8/081917/237866/Ultrafast-relaxation-dynamics-of-hot-optical

[236] A. Laitinen, M. Kumar, M. Oksanen, B. Plaçais, P. Virtanen, and P. Hakonen, "Coupling between electrons and optical phonons in suspended bilayer graphene," *Physical Review B*, vol. 91, no. 12, p. 121414, Mar. 2015. [Online]. Available: https://link.aps.org/doi/10.1103/PhysRevB.91.121414

[237] Q. Ma, N. M. Gabor, T. I. Andersen, N. L. Nair, K. Watanabe, T. Taniguchi, and P. Jarillo-Herrero, "Competing Channels for Hot-Electron Cooling in Graphene," *Physical Review Letters*, vol. 112, no. 24, p. 247401, Jun. 2014. [Online]. Available: https://link.aps.org/doi/10.1103/PhysRevLett.112.247401

[238] M. W. Graham, S.-F. Shi, D. C. Ralph, J. Park, and P. L. McEuen, "Photocurrent measurements of supercollision cooling in graphene," *Nature Physics*, vol. 9, no. 2, pp. 103–108, Feb. 2013. [Online]. Available: https://www.nature.com/articles/nphys2493

[239] K. J. Tielrooij, N. C. Hesp, A. Principi, M. B. Lundeberg, E. A. Pogna, L. Banszerus, Z. Mics, M. Massicotte, P. Schmidt, D. Davydovskaya,

D. G. Purdie, I. Goykhman, G. Soavi, A. Lombardo, K. Watanabe, T. Taniguchi, M. Bonn, D. Turchinovich, C. Stampfer, A. C. Ferrari, G. Cerullo, M. Polini, and F. H. Koppens, "Out-of-plane heat transfer in van der Waals stacks through electron-hyperbolic phonon coupling," *Nature Nanotechnology*, vol. 13, no. 1, pp. 41–46, 2018. [Online]. Available: http://dx.doi.org/10.1038/s41565-017-0008-8

[240] L. Kim, S. Kim, P. K. Jha, V. W. Brar, and H. A. Atwater, "Mid-infrared radiative emission from bright hot plasmons in graphene," *Nature Materials*, vol. 20, no. 6, pp. 805–811, Jun. 2021. [Online]. Available: https://www.nature.com/articles/s41563-021-00935-2

[241] R.-J. Shiue, Y. Gao, C. Tan, C. Peng, J. Zheng, D. K. Efetov, Y. D. Kim, J. Hone, and D. Englund, "Thermal radiation control from hot graphene electrons coupled to a photonic crystal nanocavity," *Nature Communications*, vol. 10, no. 1, p. 109, Jan. 2019. [Online]. Available: https://www.nature.com/articles/s41467-018-08047-3

[242] T. V. Alencar, D. Von Dreifus, M. Gabriela Cota Moreira, G. S. N. Eliel, C.-H. Yeh, P.-W. Chiu, M. A. Pimenta, L. M. Malard, and A. Maria De Paula, "Twisted bilayer graphene photoluminescence emission peaks at van Hove singularities," *Journal of Physics: Condensed Matter*, vol. 30, no. 17, p. 175302, May 2018. [Online]. Available: https://iopscience.iop.org/article/10.1088/1361-648X/aab64b

[243] H. Patel, L. Huang, C.-J. Kim, J. Park, and M. W. Graham, "Stacking angle-tunable photoluminescence from interlayer exciton states in twisted bilayer graphene," *Nature Communications*, vol. 10, no. 1, p. 1445, Mar. 2019. [Online]. Available: https://www.nature.com/articles/s41467-019-09097-x

[244] E. A. A. Pogna, X. Miao, D. Von Dreifus, T. V. Alencar, M. V. O. Moutinho, P. Venezuela, C. Manzoni, M. Ji, G. Cerullo, and A. M. De Paula, "Angle-tunable intersubband photoabsorption and enhanced photobleaching in twisted bilayer graphene," *Nano Research*, vol. 14, no. 8, pp. 2797–2804, Aug. 2021. [Online]. Available: https://link.springer.com/10.1007/s12274-021-3288-0

[245] J. Nathawat, I. Mansaray, K. Sakanashi, N. Wada, M. D. Randle, S. Yin, K. He, N. Arabchigavkani, R. Dixit, B. Barut, M. Zhao, H. Ramamoorthy, R. Somphonsane, G.-H. Kim, K. Watanabe, T. Taniguchi, N. Aoki, J. E. Han, and J. P. Bird, "Signatures of hot carriers and hot phonons in the re-entrant metallic and semiconducting states of Moiré-gapped graphene," *Nature*

Communications, vol. 14, no. 1, p. 1507, Mar. 2023. [Online]. Available: https://www.nature.com/articles/s41467-023-37292-4

[246] M. A. Aamir, J. N. Moore, X. Lu, P. Seifert, D. Englund, K.-C. Fong, and D. K. Efetov, *Ultrafast and sensitive calorimetry of Dirac electrons*, 2020, arXiv: 2007.14280. [Online]. Available: http://arxiv.org/abs/2007.14280

[247] A. Urich, K. Unterrainer, and T. Mueller, "Intrinsic Response Time of Graphene Photodetectors," *Nano Letters*, vol. 11, no. 7, pp. 2804–2808, Jul. 2011. [Online]. Available: https://pubs.acs.org/doi/10.1021/nl2011388

[248] K. J. Tielrooij, M. Massicotte, L. Piatkowski, A. Woessner, Q. Ma, P. Jarillo-Herrero, N. F. V. Hulst, and F. H. L. Koppens, "Hot-carrier photocurrent effects at graphene–metal interfaces," *Journal of Physics: Condensed Matter*, vol. 27, no. 16, p. 164207, Apr. 2015. [Online]. Available: https://iopscience.iop.org/article/10.1088/0953-8984/27/16/164207

[249] D. K. Efetov and P. Kim, "Controlling Electron-Phonon Interactions in Graphene at Ultrahigh Carrier Densities," *Physical Review Letters*, vol. 105, no. 25, p. 256805, Dec. 2010. [Online]. Available: https://link.aps.org/doi/10.1103/PhysRevLett.105.256805

[250] N. Mounet and N. Marzari, "First-principles determination of the structural, vibrational and thermodynamic properties of diamond, graphite, and derivatives," *Physical Review B*, vol. 71, no. 20, p. 205214, May 2005. [Online]. Available: https://link.aps.org/doi/10.1103/PhysRevB.71.205214

[251] A. C. Betz, F. Vialla, D. Brunel, C. Voisin, M. Picher, A. Cavanna, A. Madouri, G. Fève, J.-M. Berroir, B. Plaçais, and E. Pallecchi, "Hot Electron Cooling by Acoustic Phonons in Graphene," *Physical Review Letters*, vol. 109, no. 5, p. 056805, Aug. 2012. [Online]. Available: https://link.aps.org/doi/10.1103/PhysRevLett.109.056805

[252] J. D. Mehew, R. L. Merino, H. Ishizuka, A. Block, J. D. Mérida, A. D. Carlón, K. Watanabe, T. Taniguchi, L. S. Levitov, D. K. Efetov, and K.-J. Tielrooij, "Ultrafast Umklapp-assisted electron-phonon cooling in magic-angle twisted bilayer graphene," *Science Advances*, vol. 10, no. 6, p. eadj1361, Feb. 2024. [Online]. Available: https://www.science.org/doi/10.1126/sciadv.adj1361

[253] M. V. Rybin, S. F. Mingaleev, M. F. Limonov, and Y. S. Kivshar, "Purcell effect and Lamb shift as interference phenomena," *Scientific Reports*, vol. 6, no. 1, p. 20599, Feb. 2016. [Online]. Available: https://www.nature.com/articles/srep20599

[254] Purcell, E.M., "Spontaneous emission probabilities at radio frequencies," *Physical Review*, vol. 69, no. 11-12, pp. 674–674, Jun. 1946. [Online]. Available: https://link.aps.org/doi/10.1103/PhysRev.69.674

[255] A. Kerelsky, L. J. McGilly, D. M. Kennes, L. Xian, M. Yankowitz, S. Chen, K. Watanabe, T. Taniguchi, J. Hone, C. Dean, A. Rubio, and A. N. Pasupathy, "Maximized electron interactions at the magic angle in twisted bilayer graphene," *Nature*, vol. 572, no. 7767, pp. 95–100, Aug. 2019. [Online]. Available: https://www.nature.com/articles/s41586-019-1431-9

[256] J. R. Wallbank, R. Krishna Kumar, M. Holwill, Z. Wang, G. H. Auton, J. Birkbeck, A. Mishchenko, L. A. Ponomarenko, K. Watanabe, T. Taniguchi, K. S. Novoselov, I. L. Aleiner, A. K. Geim, and V. I. Fal'ko, "Excess resistivity in graphene superlattices caused by umklapp electron–electron scattering," *Nature Physics*, vol. 15, no. 1, pp. 32–36, Jan. 2019.

[257] C. Moulsdale and V. Fal'ko, "Umklapp electron-electron scattering in bilayer graphene moiré superlattice," *Physical Review B*, vol. 107, no. 14, p. 144111, Apr. 2023. [Online]. Available: https://link.aps.org/doi/10.1103/PhysRevB.107.144111

[258] D. V. Morozov, A. Casaburi, and R. H. Hadfield, "Superconducting photon detectors," *Contemporary Physics*, vol. 62, no. 2, pp. 69–91, Apr. 2021. [Online]. Available: https://www.tandfonline.com/doi/full/10.1080/00107514.2022.2043596

[259] G. N. Gol'tsman, O. Okunev, G. Chulkova, A. Lipatov, A. Semenov, K. Smirnov, B. Voronov, A. Dzardanov, C. Williams, and R. Sobolewski, "Picosecond superconducting single-photon optical detector," *Applied Physics Letters*, vol. 79, no. 6, pp. 705–707, 2001.

[260] A. D. Semenov, G. N. Gol'tsman, and A. A. Korneev, "Quantum detection by current carrying superconducting film," *Physica C: Superconductivity*, vol. 351, no. 4, pp. 349–356, Apr. 2001. [Online]. Available: https://www-sciencedirect-com.recursos.biblioteca.upc.edu/science/article/pii/S0921453400016373?via%3Dihub

[261] P. L. Richards, "Bolometers for infrared and millimeter waves," *Journal of Applied Physics*, vol. 76, no. 1, pp. 1–24, 1994.

[262] H. Hemmati, A. Biswas, and I. B. Djordjevic, "Deep-Space Optical Communications: Future Perspectives and Applications," *Proceedings of the IEEE*, vol. 99, no. 11, pp. 2020–2039, Nov. 2011. [Online]. Available: http://ieeexplore.ieee.org/document/5985459/

[263] J. M. Arrazola, V. Bergholm, K. Brádler, T. R. Bromley, M. J. Collins, I. Dhand, A. Fumagalli, T. Gerrits, A. Goussev, L. G. Helt, J. Hundal, T. Isacsson, R. B. Israel, J. Izaac, S. Jahangiri, R. Janik, N. Killoran, S. P. Kumar, J. Lavoie, A. E. Lita, D. H. Mahler, M. Menotti, B. Morrison, S. W. Nam, L. Neuhaus, H. Y. Qi, N. Quesada, A. Repingon, K. K. Sabapathy, M. Schuld, D. Su, J. Swinarton, A. Száva, K. Tan, P. Tan, V. D. Vaidya, Z. Vernon, Z. Zabaneh, and Y. Zhang, "Quantum circuits with many photons on a programmable nanophotonic chip," *Nature*, vol. 591, no. 7848, pp. 54–60, Mar. 2021. [Online]. Available: https://www.nature.com/articles/s41586-021-03202-1

[264] F. Najafi, J. Mower, N. C. Harris, F. Bellei, A. Dane, C. Lee, X. Hu, P. Kharel, F. Marsili, S. Assefa, K. K. Berggren, and D. Englund, "On-chip detection of non-classical light by scalable integration of single-photon detectors," *Nature Communications*, vol. 6, no. 1, p. 5873, Jan. 2015. [Online]. Available: https://www.nature.com/articles/ncomms6873

[265] T. Polakovic, W. Armstrong, G. Karapetrov, Z. E. Meziani, and V. Novosad, "Unconventional applications of superconducting nanowire single photon detectors," *Nanomaterials*, vol. 10, no. 6, pp. 1–20, 2020.

[266] C. M. Natarajan, M. G. Tanner, and R. H. Hadfield, "Superconducting nanowire single-photon detectors: Physics and applications," *Superconductor Science and Technology*, vol. 25, no. 6, 2012.

[267] A. Engel, J. J. Renema, K. Il'In, and A. Semenov, "Detection mechanism of superconducting nanowire single-photon detectors," *Superconductor Science and Technology*, vol. 28, no. 11, 2015.

[268] R. Gaudio, J. J. Renema, Z. Zhou, V. B. Verma, A. E. Lita, J. Shainline, M. J. Stevens, R. P. Mirin, S. W. Nam, M. P. Van Exter, M. J. De Dood, and A. Fiore, "Experimental investigation of the detection mechanism in WSi nanowire superconducting single photon detectors," *Applied Physics Letters*, vol. 109, no. 3, 2016.

[269] M. Caloz, B. Korzh, N. Timoney, M. Weiss, S. Gariglio, R. J. Warburton, C. Schönenberger, J. Renema, H. Zbinden, and F. Bussières, "Optically probing the detection mechanism in a molybdenum silicide superconducting nanowire single-photon detector," *Applied Physics Letters*, vol. 110, no. 8, 2017. [Online]. Available: http://dx.doi.org/10.1063/1.4977034

[270] I. Holzman and Y. Ivry, "Superconducting Nanowires for Single-Photon Detection: Progress, Challenges, and Opportunities," *Advanced Quantum Technologies*, vol. 2, no. 3-4, p. 1800058, Apr. 2019. [Online]. Available: https://onlinelibrary.wiley.com/doi/abs/10.1002/qute.201800058

[271] A. J. Kerman, J. K. Yang, R. J. Molnar, E. A. Dauler, and K. K. Berggren, "Electrothermal feedback in superconducting nanowire single-photon detectors," *Physical Review B - Condensed Matter and Materials Physics*, vol. 79, no. 10, pp. 1–4, 2009.

[272] A. J. Annunziata, O. Quaranta, D. F. Santavicca, A. Casaburi, L. Frunzio, M. Ejrnaes, M. J. Rooks, R. Cristiano, S. Pagano, A. Frydman, and D. E. Prober, "Reset dynamics and latching in niobium superconducting nanowire single-photon detectors," *Journal of Applied Physics*, vol. 108, no. 8, 2010.

[273] D. K. Liu, S. J. Chen, L. X. You, Y. L. Wang, S. Miki, Z. Wang, X. M. Xie, and M. H. Jiang, "Nonlatching superconducting nanowire single-photon detection with quasi-constant-voltage bias," *Applied Physics Express*, vol. 5, no. 12, pp. 1–14, 2012.

[274] D. K. Liu, L. X. You, S. J. Chen, X. Y. Yang, Z. Wang, Y. L. Wang, X. M. Xie, and M. H. Jiang, "Electrical characteristics of superconducting nanowire single photon detector," *IEEE Transactions on Applied Superconductivity*, vol. 23, no. 3, pp. 3–6, 2013.

[275] B. Korzh, Q. Y. Zhao, J. P. Allmaras, S. Frasca, T. M. Autry, E. A. Bersin, A. D. Beyer, R. M. Briggs, B. Bumble, M. Colangelo, G. M. Crouch, A. E. Dane, T. Gerrits, A. E. Lita, F. Marsili, G. Moody, C. Peña, E. Ramirez, J. D. Rezac, N. Sinclair, M. J. Stevens, A. E. Velasco, V. B. Verma, E. E. Wollman, S. Xie, D. Zhu, P. D. Hale, M. Spiropulu, K. L. Silverman, R. P. Mirin, S. W. Nam, A. G. Kozorezov, M. D. Shaw, and K. K. Berggren, "Demonstration of sub-3 ps temporal resolution with a superconducting nanowire single-photon detector," *Nature Photonics*, vol. 14, no. 4, pp. 250–255, 2020. [Online]. Available: http://dx.doi.org/10.1038/s41566-020-0589-x

[276] O. Kahl, S. Ferrari, P. Rath, A. Vetter, C. Nebel, and W. H. Pernice, "High Efficiency On-Chip Single-Photon Detection for Diamond Nanophotonic Circuits," *Journal of Lightwave Technology*, vol. 34, no. 2, pp. 249–255, 2016.

[277] L. You, "Superconducting nanowire single-photon detectors for quantum information," *Nanophotonics*, vol. 9, no. 9, pp. 2673–2692, 2020.

[278] C. A. Mears, Q. Hu, P. L. Richards, A. H. Worsham, D. E. Prober, and A. V. Räisänen, "Quantum-limited heterodyne detection of millimeter waves using superconducting tantalum tunnel junctions," *Applied Physics Letters*, vol. 57, no. 23, pp. 2487–2489, 1990.

[279] B. A. Mazin, P. K. Day, H. G. LeDuc, A. Vayonakis, and J. Zmuidzinas, "Superconducting kinetic inductance photon detectors," *Highly Innovative Space Telescope Concepts*, vol. 4849, p. 283, 2002.

[280] D. Twerenbold, "Superconducting tunneling junctions as X-ray detectors and their possible applications in astrophysics," *Nuclear Instruments and Methods in Physics Research Section A: Accelerators, Spectrometers, Detectors and Associated Equipment*, vol. 273, no. 2-3, pp. 575–582, Dec. 1988. [Online]. Available: https://linkinghub.elsevier.com/retrieve/pii/0168900288900599

[281] E. Sterpetti, J. Biscaras, A. Erb, and A. Shukla, "Comprehensive phase diagram of two-dimensional space charge doped Bi2Sr2CaCu2O8+x," *Nature Communications*, vol. 8, no. 1, p. 2060, Dec. 2017. [Online]. Available: http://www.nature.com/articles/s41467-017-02104-z

[282] S. Y. Zhao, N. Poccia, M. G. Panetta, C. Yu, J. W. Johnson, H. Yoo, R. Zhong, G. D. Gu, K. Watanabe, T. Taniguchi, S. V. Postolova, V. M. Vinokur, and P. Kim, "Sign-Reversing Hall Effect in Atomically Thin High-Temperature Bi2.1Sr1.9CaCu2.0 O8+ Superconductors," *Physical Review Letters*, vol. 122, no. 24, pp. 1–6, 2019.

[283] J. M. Kosterlitz and D. J. Thouless, "Ordering, metastability and phase transitions in two-dimensional systems," *Journal of Physics C: Solid State Physics*, vol. 6, p. 1181, 1973.

[284] A. J. Kreisler and A. Gaugue, "Recent progress in high-temperature superconductor bolometric detectors: from the mid-infrared to the far-infrared (THz) range," *Superconductor Science and Technology*, vol. 13, no. 8, pp. 1235–1245, Aug. 2000. [Online]. Available: https://iopscience.iop.org/article/10.1088/0953-2048/13/8/321

[285] S. Parham, H. Li, T. J. Nummy, J. A. Waugh, X. Q. Zhou, J. Griffith, J. Schneeloch, R. D. Zhong, G. D. Gu, and D. S. Dessau, "Ultrafast gap dynamics and electronic interactions in a photoexcited cuprate superconductor," *Physical Review X*, vol. 7, no. 4, pp. 1–11, 2017.

[286] R. Arpaia, M. Ejrnaes, L. Parlato, F. Tafuri, R. Cristiano, D. Golubev, R. Sobolewski, T. Bauch, F. Lombardi, and G. P. Pepe, "High-temperature superconducting nanowires for photon detection," *Physica C: Superconductivity and its Applications*, vol. 509, pp. 16–21, 2015. [Online]. Available: http://dx.doi.org/10.1016/j.physc.2014.09.017

[287] C. Cirillo, M. Caputo, L. Parlato, M. Ejrnaes, D. Salvoni, R. Cristiano, G. P. Pepe, and C. Attanasio, "Ultrathin superconducting NbRe microstrips with hysteretic voltage-current characteristic," *Fizika Nizkikh Temperatur*, vol. 46, no. 4, pp. 457–461, 2020.

[288] I. Charaev, D. A. Bandurin, A. T. Bollinger, I. Y. Phinney, I. Drozdov, M. Colangelo, B. A. Butters, T. Taniguchi, K. Watanabe, X. He, O. Medeiros, I. Božović, P. Jarillo-Herrero, and K. K. Berggren, "Single-photon detection using high-temperature superconductors," *Nature Nanotechnology*, vol. 18, no. 4, pp. 343–349, Apr. 2023. [Online]. Available: https://www.nature.com/articles/s41565-023-01325-2

[289] R. Arpaia, D. Golubev, R. Baghdadi, R. Ciancio, G. DraŽić, P. Orgiani, D. Montemurro, T. Bauch, and F. Lombardi, "Transport properties of ultrathin YBa2Cu3 O7- nanowires: A route to single-photon detection," *Physical Review B*, vol. 96, no. 6, pp. 1–11, 2017.

[290] P. Amari, S. Kozlov, E. Recoba-Pawlowski, Z. Velluire-Pellat, A. Jouan, F. Couëdo, C. Ulysse, J. Briatico, D. Roditchev, N. Bergeal, J. Lesueur, and C. Feuillet-Palma, "Scalable nanofabrication of high-quality YBa 2 Cu 3 O 7 nanowires for single-photon detectors," *Physical Review Applied*, vol. 20, no. 4, p. 044025, Oct. 2023. [Online]. Available: https://link.aps.org/doi/10.1103/PhysRevApplied.20.044025

[291] D. Bitauld, F. Marsili, A. Gaggero, F. Mattioli, R. Leoni, S. J. Nejad, F. Lévy, and A. Fiore, "Nanoscale optical detector with single-photon and multiphoton sensitivity," *Nano Letters*, vol. 10, no. 8, pp. 2977–2981, 2010.

[292] R. H. Hadfield, "Single-photon detectors for optical quantum information applications," *Nature Photonics*, vol. 3, no. 12, pp. 696–705, Dec. 2009. [Online]. Available: http://www.nature.com/articles/nphoton.2009.230

[293] D. Wang, F. Tang, J. Ji, W. Zhang, A. Vishwanath, H. C. Po, and X. Wan, "Two-dimensional topological materials discovery by symmetry-indicator method," *Physical Review B*, vol. 100, no. 19, p. 195108, Nov. 2019. [Online]. Available: https://link.aps.org/doi/10.1103/PhysRevB.100.195108

[294] J. Björk, J. Zhou, P. O. Persson, and J. Rosen, "Two-dimensional materials by large-scale computations and chemical exfoliation of layered solids," *Science*, vol. 383, no. 6688, pp. 1210–1215, Mar. 2024. [Online]. Available: https://www.science.org/doi/10.1126/science.adj6556

[295] A. Ramires and J. L. Lado, "Emulating Heavy Fermions in Twisted Trilayer Graphene," *Physical Review Letters*, vol. 127, no. 2, p. 026401, Jul. 2021. [Online]. Available: https://link.aps.org/doi/10.1103/PhysRevLett.127.026401

[296] S. Batlle-Porro, D. Calugaru, H. Hu, R. K. Kumar, N. C. H. Hesp, K. Watanabe, T. Taniguchi, B. A. Bernevig, P. Stepanov, and F. H. L. Koppens, "Cryo-Near-Field Photovoltage Microscopy of Heavy-Fermion Twisted Symmetric Trilayer Graphene," Feb. 2024, arXiv:2402.12296 [cond-mat]. [Online]. Available: http://arxiv.org/abs/2402.12296

[297] Z. Zheng, X. Wang, Z. Zhu, S. Carr, T. Devakul, S. de la Barrera, N. Paul, Z. Huang, A. Gao, Y. Zhang, D. Bérubé, K. N. Evancho, K. Watanabe, T. Taniguchi, L. Fu, Y. Wang, S.-Y. Xu, E. Kaxiras, P. Jarillo-Herrero, and Q. Ma, "Electronic ratchet effect in a moir\'e system: signatures of excitonic ferroelectricity," Jun. 2023, arXiv:2306.03922 [cond-mat]. [Online]. Available: http://arxiv.org/abs/2306.03922

[298] V. Vaňo, M. Amini, S. C. Ganguli, G. Chen, J. L. Lado, S. Kezilebieke, and P. Liljeroth, "Artificial heavy fermions in a van der Waals heterostructure," *Nature*, vol. 599, no. 7886, pp. 582–586, Nov. 2021. [Online]. Available: https://www.nature.com/articles/s41586-021-04021-0

[299] A. Kumar, N. C. Hu, A. H. MacDonald, and A. C. Potter, "Gate-tunable heavy fermion quantum criticality in a moiré Kondo lattice," *Physical Review B*, vol. 106, no. 4, p. L041116, Jul. 2022. [Online]. Available: https://link.aps.org/doi/10.1103/PhysRevB.106.L041116

[300] W. Zhao, B. Shen, Z. Tao, Z. Han, K. Kang, K. Watanabe, T. Taniguchi, K. F. Mak, and J. Shan, "Gate-tunable heavy fermions

in a moiré Kondo lattice," *Nature*, vol. 616, no. 7955, pp. 61–65, Apr. 2023. [Online]. Available: https://www.nature.com/articles/s41586-023-05800-7

[301] V. A. Posey, S. Turkel, M. Rezaee, A. Devarakonda, A. K. Kundu, C. S. Ong, M. Thinel, D. G. Chica, R. A. Vitalone, R. Jing, S. Xu, D. R. Needell, E. Meirzadeh, M. L. Feuer, A. Jindal, X. Cui, T. Valla, P. Thunström, T. Yilmaz, E. Vescovo, D. Graf, X. Zhu, A. Scheie, A. F. May, O. Eriksson, D. N. Basov, C. R. Dean, A. Rubio, P. Kim, M. E. Ziebel, A. J. Millis, A. N. Pasupathy, and X. Roy, "Two-dimensional heavy fermions in the van der Waals metal CeSiI," *Nature*, vol. 625, no. 7995, pp. 483–488, Jan. 2024. [Online]. Available: https://www.nature.com/articles/s41586-023-06868-x

[302] K. G. Rana, F. K. Dejene, N. Kumar, C. R. Rajamathi, K. Sklarek, C. Felser, and S. S. P. Parkin, "Thermopower and Unconventional Nernst Effect in the Predicted Type-II Weyl Semimetal WTe $_2$," *Nano Letters*, vol. 18, no. 10, pp. 6591–6596, Oct. 2018. [Online]. Available: https://pubs.acs.org/doi/10.1021/acs.nanolett.8b03212

[303] T. Song, Y. Jia, G. Yu, Y. Tang, P. Wang, R. Singha, X. Gui, A. J. Uzan-Narovlansky, M. Onyszczak, K. Watanabe, T. Taniguchi, R. J. Cava, L. M. Schoop, N. P. Ong, and S. Wu, "Unconventional superconducting quantum criticality in monolayer WTe2," *Nature Physics*, vol. 20, no. 2, pp. 269–274, Feb. 2024. [Online]. Available: https://www.nature.com/articles/s41567-023-02291-1

[304] A. Harzheim, C. Evangeli, O. V. Kolosov, and P. Gehring, "Direct mapping of local Seebeck coefficient in 2D material nanostructures via scanning thermal gate microscopy," *2D Materials*, vol. 7, no. 4, p. 041004, Aug. 2020. [Online]. Available: https://iopscience.iop.org/article/10.1088/2053-1583/aba333

[305] T. Völkl, A. Aharon-Steinberg, T. Holder, E. Alpern, N. Banu, A. K. Pariari, Y. Myasoedov, M. E. Huber, M. Hücker, and E. Zeldov, "Demonstration and imaging of cryogenic magneto-thermoelectric cooling in a van der Waals semimetal," *Nature Physics*, Mar. 2024. [Online]. Available: https://www.nature.com/articles/s41567-024-02417-z

[306] A. Inbar, J. Birkbeck, J. Xiao, T. Taniguchi, K. Watanabe, B. Yan, Y. Oreg, A. Stern, E. Berg, and S. Ilani, "The quantum twisting microscope," *Nature*, vol. 614, no. 7949, pp. 682–687,

Feb. 2023. [Online]. Available: https://www.nature.com/articles/s41586-022-05685-y

[307] H. Liu, H. Brahmi, C. Boix-Constant, H. S. J. Van Der Zant, P. G. Steeneken, and G. J. Verbiest, "Optomechanical methodology for characterizing the thermal properties of 2D materials," *APL Materials*, vol. 12, no. 2, p. 021126, Feb. 2024. [Online]. Available: https://pubs.aip.org/apm/article/12/2/021126/3267327/Optomechanical-methodology-for-characterizing-the

[308] L. P. A. Krisna and M. Koshino, "Moiré phonons in graphene/hexagonal boron nitride moiré superlattice," *Physical Review B*, vol. 107, no. 11, p. 115301, Mar. 2023. [Online]. Available: https://link.aps.org/doi/10.1103/PhysRevB.107.115301

[309] X. Zou, J. Shang, J. Leaw, Z. Luo, L. Luo, C. La-o vorakiat, L. Cheng, S. A. Cheong, H. Su, J.-X. Zhu, Y. Liu, K. P. Loh, A. H. Castro Neto, T. Yu, and E. E. M. Chia, "Terahertz Conductivity of Twisted Bilayer Graphene," *Physical Review Letters*, vol. 110, no. 6, p. 067401, Feb. 2013. [Online]. Available: https://link.aps.org/doi/10.1103/PhysRevLett.110.067401

[310] J. W. Zuber and C. Zhang, "Nonlinear optical response of twisted bilayer graphene," *Physical Review B*, vol. 103, no. 24, p. 245417, Jun. 2021. [Online]. Available: https://link.aps.org/doi/10.1103/PhysRevB.103.245417

[311] S. Chaudhary, C. Lewandowski, and G. Refael, "Shift-current response as a probe of quantum geometry and electron-electron interactions in twisted bilayer graphene," *Physical Review Research*, vol. 4, no. 1, p. 013164, Feb. 2022. [Online]. Available: https://link.aps.org/doi/10.1103/PhysRevResearch.4.013164

[312] A. M. Potts, A. K. Nayak, M. Nagel, K. Kaj, B. Stamenic, D. D. John, R. D. Averitt, and A. F. Young, "On-Chip Time-Domain Terahertz Spectroscopy of Superconducting Films below the Diffraction Limit," *Nano Letters*, vol. 23, no. 9, pp. 3835–3841, May 2023. [Online]. Available: https://pubs.acs.org/doi/10.1021/acs.nanolett.3c00412

[313] J. Yang, G. Chen, T. Han, Q. Zhang, Y.-H. Zhang, L. Jiang, B. Lyu, H. Li, K. Watanabe, T. Taniguchi, Z. Shi, T. Senthil, Y. Zhang, F. Wang, and L. Ju, "Spectroscopy signatures of electron correlations in a trilayer graphene/hBN moiré superlattice," *Science*, vol. 375, no. 6586, pp. 1295–1299, Mar. 2022. [Online]. Available: https://www.science.org/doi/10.1126/science.abg3036

[314] Y. Han and A. Zhang, "Cryogenic technology for infrared detection in space," *Scientific Reports*, vol. 12, no. 1, p. 2349, Feb. 2022. [Online]. Available: https://www.nature.com/articles/s41598-022-06216-5

[315] S. Gyger, J. Zichi, L. Schweickert, A. W. Elshaari, S. Steinhauer, S. F. Covre Da Silva, A. Rastelli, V. Zwiller, K. D. Jöns, and C. Errando-Herranz, "Reconfigurable photonics with on-chip single-photon detectors," *Nature Communications*, vol. 12, no. 1, p. 1408, Mar. 2021. [Online]. Available: https://www.nature.com/articles/s41467-021-21624-3

[316] M. Polini, F. Giazotto, K. C. Fong, I. M. Pop, C. Schuck, T. Boccali, G. Signorelli, M. D'Elia, R. H. Hadfield, V. Giovannetti, D. Rossini, A. Tredicucci, D. K. Efetov, F. H. L. Koppens, P. Jarillo-Herrero, A. Grassellino, and D. Pisignano, "Materials and devices for fundamental quantum science and quantum technologies," Jan. 2022, arXiv:2201.09260. [Online]. Available: http://arxiv.org/abs/2201.09260

[317] A. R. Dhumal, A. P. Kulkarni, and N. H. Ambhore, "A comprehensive review on thermal management of electronic devices," *Journal of Engineering and Applied Science*, vol. 70, no. 1, p. 140, Dec. 2023. [Online]. Available: https://jeas.springeropen.com/articles/10.1186/s44147-023-00309-2

[318] H. Song, J. Liu, B. Liu, J. Wu, H.-M. Cheng, and F. Kang, "Two-Dimensional Materials for Thermal Management Applications," *Joule*, vol. 2, no. 3, pp. 442–463, Mar. 2018. [Online]. Available: https://linkinghub.elsevier.com/retrieve/pii/S2542435118300345

[319] S. Y. F. Zhao, X. Cui, P. A. Volkov, H. Yoo, S. Lee, J. A. Gardener, A. J. Akey, R. Engelke, Y. Ronen, R. Zhong, G. Gu, S. Plugge, T. Tummuru, M. Kim, M. Franz, J. H. Pixley, N. Poccia, and P. Kim, "Time-reversal symmetry breaking superconductivity between twisted cuprate superconductors," *Science*, vol. 382, no. 6677, pp. 1422–1427, Dec. 2023. [Online]. Available: https://www.science.org/doi/10.1126/science.abl8371

[320] M. Colangelo, B. Korzh, J. P. Allmaras, A. D. Beyer, A. S. Mueller, R. M. Briggs, B. Bumble, M. Runyan, M. J. Stevens, A. N. McCaughan, D. Zhu, S. Smith, W. Becker, L. Narváez, J. C. Bienfang, S. Frasca, A. E. Velasco, E. E. Ramirez, A. B. Walter, E. Schmidt, E. E. Wollman, M. Spiropulu, R. Mirin, S. W. Nam, K. K. Berggren, and M. D. Shaw, "Impedance-Matched

Differential Superconducting Nanowire Detectors," *Physical Review Applied*, vol. 19, no. 4, p. 044093, Apr. 2023. [Online]. Available: https://link.aps.org/doi/10.1103/PhysRevApplied.19.044093

[321] Y. Lee, M. Martini, T. Confalone, S. Sokri, C. N. Saggau, D. Wolf, G. Gu, K. Watanabe, T. Taniguchi, D. Montemurro, V. M. Vinokur, K. Nielsch, and N. Poccia, "Encapsulating High-Temperature Superconducting Twisted van der Waals Heterostructures Blocks Detrimental Effects of Disorder," *Advanced Materials*, vol. 35, p. 2209135, 2023.

[322] C. N. Saggau, S. Shokri, M. Martini, T. Confalone, Y. Lee, D. Wolf, G. Gu, V. Brosco, D. Montemurro, V. M. Vinokur, K. Nielsch, and N. Poccia, "2D High-Temperature Superconductor Integration in Contact Printed Circuit Boards," *ACS Applied Materials & Interfaces*, vol. 15, no. 44, pp. 51 558–51 564, Nov. 2023. [Online]. Available: https://pubs.acs.org/doi/10.1021/acsami.3c10564

[323] E. J. Telford, A. Benyamini, D. Rhodes, D. Wang, Y. Jung, A. Zangiabadi, K. Watanabe, T. Taniguchi, S. Jia, K. Barmak, A. N. Pasupathy, C. R. Dean, and J. Hone, "Via Method for Lithography Free Contact and Preservation of 2D Materials," *Nano Letters*, vol. 18, no. 2, pp. 1416–1420, Feb. 2018. [Online]. Available: https://pubs.acs.org/doi/10.1021/acs.nanolett.7b05161

[324] M. J. Gray, N. Kumar, R. O'Connor, M. Hoek, E. Sheridan, M. C. Doyle, M. L. Romanelli, G. B. Osterhoudt, Y. Wang, V. Plisson, S. Lei, R. Zhong, B. Rachmilowitz, H. Zhao, H. Kitadai, S. Shepard, L. M. Schoop, G. D. Gu, I. Zeljkovic, X. Ling, and K. S. Burch, "A cleanroom in a glovebox," *Review of Scientific Instruments*, vol. 91, no. 7, p. 073909, Jul. 2020. [Online]. Available: https://pubs.aip.org/rsi/article/91/7/073909/966910/A-cleanroom-in-a-glovebox

[325] S. Guo, M. Luo, G. Shi, N. Tian, Z. Huang, F. Yang, L. Ma, N. Z. Wang, Q. Shi, K. Xu, Z. Xu, K. Watanabe, T. Taniguchi, X. H. Chen, D. Shen, L. Zhang, W. Ruan, and Y. Zhang, "An ultra-high vacuum system for fabricating clean two-dimensional material devices," *Review of Scientific Instruments*, vol. 94, no. 1, p. 013903, Jan. 2023. [Online]. Available: https://pubs.aip.org/rsi/article/94/1/013903/2872353/An-ultra-high-vacuum-system-for-fabricating-clean

[326] W. Wang, N. Clark, M. Hamer, A. Carl, E. Tovari, S. Sullivan-Allsop, E. Tillotson, Y. Gao, H. De Latour, F. Selles, J. Howarth, E. G. Castanon, M. Zhou, H. Bai, X. Li, A. Weston, K. Watanabe, T. Taniguchi, C. Mattevi, T. H. Bointon, P. V. Wiper, A. J.

Strudwick, L. A. Ponomarenko, A. V. Kretinin, S. J. Haigh, A. Summerfield, and R. Gorbachev, "Clean assembly of van der Waals heterostructures using silicon nitride membranes," *Nature Electronics*, vol. 6, no. 12, pp. 981–990, Dec. 2023. [Online]. Available: https://www.nature.com/articles/s41928-023-01075-y

[327] M. Lyatti, M. A. Wolff, I. Gundareva, M. Kruth, S. Ferrari, R. E. Dunin-Borkowski, and C. Schuck, "Energy-level quantization and single-photon control of phase slips in YBa2Cu3O7–x nanowires," *Nature Communications*, vol. 11, no. 1, p. 763, Feb. 2020. [Online]. Available: https://www.nature.com/articles/s41467-020-14548-x

[328] G. P. Pepe, L. Parlato, M. Ejrnaes, R. Cristiano, R. Arpaia, F. Tafuri, D. Golubev, T. Bauch, F. Lombardi, and R. Sobolewski, "Y-Ba-Cu-O nanostripes for optical photon detection," *Photon Counting Applications 2015*, vol. 9504, p. 950406, 2015.

[329] L. Parlato, M. Ejrnaes, U. Nasti, R. Arpaia, T. Taino, T. Bauch, H. Myoren, R. Sobolewski, F. Tafuri, F. Lombardi, R. Cristiano, and G. Pepe, "Investigation of dark counts in innovative materials for superconducting nanowire single-photon detector applications," *Photon Counting Applications 2017*, vol. 10229, p. 102290I, 2017.

[330] M. Ejrnaes, L. Parlato, R. Arpaia, T. Bauch, T. Lombardi, R. Cristiano, F. Tafuri, and G. Pepe, "Observation of dark pulses in 10 nm thick YBCO nanostrips presenting hysteretic current voltage characteristics," *Materials Research Express*, pp. 0–12, 2019.

[331] Y. Zhu, M. Liao, Q. Zhang, H.-Y. Xie, F. Meng, Y. Liu, Z. Bai, S. Ji, J. Zhang, K. Jiang, R. Zhong, J. Schneeloch, G. Gu, L. Gu, X. Ma, D. Zhang, and Q.-K. Xue, "Presence of s -Wave Pairing in Josephson Junctions Made of Twisted Ultrathin Bi2Sr2CaCu2O8+x Flakes," *Physical Review X*, vol. 11, no. 3, p. 031011, Jul. 2021. [Online]. Available: https://link.aps.org/doi/10.1103/PhysRevX.11.031011

[332] H. Wang, Y. Zhu, Z. Bai, Z. Wang, S. Hu, H.-Y. Xie, X. Hu, J. Cui, M. Huang, J. Chen, Y. Ding, L. Zhao, X. Li, Q. Zhang, L. Gu, X. J. Zhou, J. Zhu, D. Zhang, and Q.-K. Xue, "Prominent Josephson tunneling between twisted single copper oxide planes of Bi2Sr2-xLaxCuO6+y," *Nature Communications*, vol. 14, no. 1, p. 5201, Aug. 2023. [Online]. Available: https://www.nature.com/articles/s41467-023-40525-1

[333] O. Can, T. Tummuru, R. P. Day, I. Elfimov, A. Damascelli, and M. Franz, "High-temperature topological superconductivity in

twisted double-layer copper oxides," *Nature Physics*, vol. 17, no. 4, pp. 519–524, 2021. [Online]. Available: http://dx.doi.org/10.1038/s41567-020-01142-7

[334] S. Ghosh, V. Patil, A. Basu, Kuldeep, A. Dutta, D. A. Jangade, R. Kulkarni, A. Thamizhavel, J. F. Steiner, F. Von Oppen, and M. M. Deshmukh, "High-temperature Josephson diode," *Nature Materials*, Feb. 2024. [Online]. Available: https://www.nature.com/articles/s41563-024-01804-4

[335] V. Brosco, G. Serpico, V. Vinokur, N. Poccia, and U. Vool, "Superconducting Qubit Based on Twisted Cuprate Van der Waals Heterostructures," *Physical Review Letters*, vol. 132, no. 1, p. 017003, Jan. 2024. [Online]. Available: https://link.aps.org/doi/10.1103/PhysRevLett.132.017003